Palacký University
Olomouc

Palacky University Olomouc

Faculty of Science

Department of Geology

Study programme: Geological Sciences (P0532D330004)

Sequence Stratigraphic Framework and Hydrocarbon Potential of Stylolite Distribution in Upper Cretaceous Kometan Formation, Western Zagros, Iraqi Kurdistan

Doctoral Dissertation

Hussein Suad Hussein M.Sc.

Supervisor: prof. Mgr. Ondřej Bábek, Dr.

Consultant: Dr. Howri Mansurbeg

Olomouc 2024

Declaration

I hereby declare that this dissertation thesis entitled "**Sequence Stratigraphic Framework and Hydrocarbon Potential of Stylolite Distribution in Upper Cretaceous Kometan Formation, Western Zagros, Iraqi Kurdistan**" is entirely the result of my work, except where otherwise acknowledged. All sources used in this thesis have been properly acknowledged. This work has not been submitted in whole or in part for any other degree or qualification in any university or other educational institution. Where information has been derived from other sources, I have provided appropriate acknowledgment in the text and references.

In Olomouc, Czech Republic, April 22, 2024

Hussein Suad Hussein

Acknowledgments

I extend my heartfelt acknowledgment to Professor Ondrej Babek and Howri Mansurbeg for their unwavering support and mentorship throughout my academic journey. Professor Babek's insightful guidance as my supervisor, coupled with Howri Mansurbeg's valuable input as my consultant, significantly enriched my research experience.

I extend my heartfelt appreciation to the Department of Geology at Palacký University for their unwavering support, expertise, and resources throughout our endeavors. Their commitment to excellence in geological research has been instrumental in shaping our academic journey.

The generous support from the Fischer scholarship enabled me to confidently pursue my academic endeavors, and I am deeply thankful for their investment in my studies.

I gratefully acknowledge the North Oil Company in Iraq for their partial provision of data for this dissertation. Their contribution has been invaluable in enriching the research and enhancing its depth and relevance.

I sincerely thank Ms. Dana Gronychová for her exceptional service in Student Affairs for International Students. Her dedication to student well-being and integration has been invaluable. I also extend my gratitude to Ms. Waleria Słowiková for her outstanding contributions as Foreign Relations Officer. Both have played key roles in fostering a welcoming environment and advancing their institution's global presence.

Furthermore, I am immensely grateful to Barcelona University and to Professor Juan Diego Martín-Martín and Associate Professor Enrique Gomez-Rivas at Barcelona University for their assistance during my research stay. Their expertise and encouragement were instrumental in advancing my work.

In addition, Dr. Jaroslav Kapusta's expertise and assistance in the laboratory were indispensable, ensuring the smooth execution of experiments and data measurements.

I also wish to express my gratitude to Mr. Arkan Othman at Soran University for his assistance with field sampling.

Lastly, I extend my appreciation to Brno University for providing essential resources and facilities for the meticulous measurement of samples. Each of these individuals and institutions played a pivotal role in shaping the outcome of my research, and I am profoundly grateful for their contributions to my academic and personal growth.

Dedication

I dedicate this dissertation to my beloved wife, whose unwavering love, support, and understanding have been my guiding light throughout this journey. Her patience, encouragement, and sacrifices have made it possible for me to pursue my academic aspirations. This achievement is as much hers as it is mine, and I am profoundly grateful for her presence in my life.

Abstract

Surface analogues are suitable tools to link reservoir models to real facies, but they require a robust outcrop-to-subsurface correlation. This Dissertation thesis aims to characterize reservoir quality by statistically predicting electrofacies, fracture identification, statistically analyzing stylolite morphology and network distribution, and linking the reservoir to sequence stratigraphy from different Oil Fields in the Upper Cretaceous Kometan Formation, a prolific carbonate reservoir of northern Iraq. Conventional well logs (caliper, gamma ray, neutron, density, and sonic), along with geochemical data, were used in this study. Laboratory spectral gamma-ray measurements were also conducted. A multivariate regression approach was used to analyze electrofacies. Various interpretations, including porosity analysis and fracture identification, were employed. Field sampling quantified stylolite networks, and thin sections with scanning electron microscopy were used for pore estimation. The correlation was done between well logs and geochemical data from surface analogues. The results indicate that the Kometan Formation predominantly comprises limestone, marl, marly limestone, and argillaceous limestone. A statistically significant correlation (R^2 = 0.83–0.85) between described and predicted lithology was established. The model with a higher coefficient of determination (0.85) was tested for further predictions in other wells. Six microfacies composed of mudstones to packstone with planktonic, and benthic foraminifers were identified in the outcrop, and interpreted as middle ramp, outer ramp, and basin deposits. The K+Al logs are correlated for 33 km, and the subsurface GR logs for over 100 km distance, but both reflect detrital admixture in biogenic carbonate. However, the outcrop- and subsurface log patterns show opposite vertical trends across the lower, middle, and upper parts of the formation. Such opposite log trends are interpreted as jointly reflecting landward and seaward shifts of the middle ramp carbonate factory within the mixed carbonate–siliciclastic system during transgressions and regressions, respectively. The inner ramp GR maxima and minima, and the outer ramp K+Al minima and maxima, are interpreted as maximum regression surfaces (mrs) and maximum flooding surfaces (mfs), respectively, in the T-R sequence-stratigraphic model. Neutron-density and sonic logs indicate that the best reservoir quality is achieved in fractured pure carbonates, which are controlled by these T-R cycles. Good secondary porosity has been Identified from the Secondary Porosity Index (SPI), which has reached a maximum value of 17%, and the average is 4% for Kz40. The maximum value is 30%, and the average is 8% for K216. In facies primarily composed of grain-supported packstone with moderate sorting, where grains are dispersed within a finer matrix, predominant stylolites typically exhibit weak connectivity and considerable vertical spacing. Conversely, mud-supported facies, marked by poor sorting and heterogeneity, display well-developed intersection stylolite networks. Stylolites in mud-supported facies demonstrate closer spacing, heightened amplitudes, and intensified junctions, with prevalent morphologies of the suture and sharp-peak varieties. Notably, this study unveils that stylolite significantly enhances porosity and permeability in the studied formation. Dissolution of minerals along stylolite seams forms intricate networks of channels and conduits. The results highlight the importance of the outcrop-to-subsurface correlation of well log data and elemental geochemistry in stratigraphic correlation and reservoir quality.

Keywords: sequence stratigraphy, stylolite, fracture, well logs, element geochemistry, Kometan Formation

Abstrakt

Povrchové analogy jsou vhodnými nástroji pro propojení modelů ropných rezervoárů s reálnými faciemi, avšak tyto vyžadují robustní korelaci mezi výchozy a podpovrchovými výskyty. Tato disertační práce si klade za cíl charakterizovat kvalitu rezervoáru pomocí statistické predikce elektrofacií, identifikací fraktur, statistické analýzy morfologie stylolitů a jejich distribuce a propojením sekvenční stratigrafie s kvalitou rezervoáru z několika ropných polí ve svrchnokřídovém souvrství Kometan, které je vysoce produktivním karbonátovým rezervoárem v severním Iráku. V této studii byly použity konvenční karotážní záznamy (kaliper, gamakarotáž, neutronová karotáž, hustotní karotáž a akustická karotáž) spolu s geochemickými daty. V rámci práce byla rovněž provedena laboratorní měření gamaspektrometrie. K analýze elektrofacií byla použita metoda vícerozměrné regrese. Byly použity různé interpretace, včetně analýzy porozity a identifikace fraktur. Terénní výzkum zahrnoval dokumentaci a kvantifikaci sítě stylolitů, a vzorkování pro analýzu výbrusů a odhad porozity pomocí rastrovací elektronové mikroskopie. Byla provedena korelace mezi vrtnými záznamy a geochemickými daty z povrchových analogů. Výsledky naznačují, že souvrství Kometan tvoří převážně vápence, slínovce, slínité vápence a jílovité vápence. Byla stanovena statisticky významná korelace (R^2 = 0,83–0,85) mezi popsanou a predikovanou litologií. Model s vyšším koeficientem determinace (0,85) byl testován pro další predikce v dalších vrtech. Na výchozech bylo identifikováno šest mikrofacií zahrnující vápence typu mudstone až packstone s planktonními a bentickými foraminiferami, které byly uloženy v prostředí střední části karbonátové rampy (middle ramp), vnější rampy (outer ramp) a pánve. Geochemické záznamy koncentrací K a Al jsou korelovány na vzdálenost 33 km mezi výchozy, a podpovrchové záznamy celkové gamakarotáže na vzdálenost více než 100 km; obě proxy odrážejí detritickou příměs v biogenním karbonátu. Geochemické a karotážní křivky na výchozech a pod povrchem však vykazují opačné vertikální trendy napříč spodní, střední a horní částí souvrství. Tyto opačné trendy křivek jsou společně reflektují posuny zónu maximální karbonátové produkce (carbonate factory) střední rampy v rámci smíšeného karbonát-siliciklastického systému směrem na pevninu během transgresí a směrem do oceánu během regresí. Maxima gamakarotážních hodnot v prostředí vnitřní rampy jsou v transgresivně-regresivním (TR) modelu sekvenční-stratigrafie interpretována jako povrchy maximální regrese (maximum regression surface, mrs) a maxima koncentrací K a Al na vnější rampě jako povrchy maximální záplavy (maximum flooding surface, mfs). Neutronová hustotní karotáž a akustická karotáž naznačují, že nejlepší kvality rezervoár dosahuje v čistých karbonátech s puklinovou porozitou, jejichž distribuce je řízena těmito TR cykly. Dobrá druhotná pórovitost byla identifikována z indexu sekundární porozity (SPI), který dosáhl maximální hodnoty 17 % (průměr 4 %) pro vrt Kz40. Maximální hodnota dosahuje 30 % a průměrná hodnota 8 % pro vrt K216. Ve faciích složených primárně ze středně vytříděných typů packstone s podpůrnou strukturou zrn převládající stylolity, které typicky vykazují slabou konektivitu a značné vertikální rozestupy. Naopak heterogenní facie s podpůrnou strukturou matrix a špatným vytříděním vykazují dobře vyvinuté protínání stylolitů. Ve faciích s podpůrnou strukturou matrix mají stylolity užší rozestupy, zvýšené amplitudy a vyšší četnost propojení, s převládající morfologií švů a variet s ostrými vrcholy. Tato studie zejména odhaluje, že stylolitizace v tomto souvrství významně zvyšuje porozitu a permeabilitu. Rozpouštění minerálů podél tlakových švů vytváří složité sítě kanálů. Výsledky zdůrazňují význam prvkové geochemie na výchozech a karotážních dat z podpovrchových výskytů ve stratigrafické korelaci a analýze kvality rezervoáru.

Table of Contents

List of Figures

List of Tables

1. Introduction

1.1. Preface

The Kometan Formation (Turonian – Campanian), which is a prospective carbonate reservoir for oil and gas in northern Iraq, is composed of fractured, fine-grained, foraminifer-rich carbonate sediments deposited in shallow-water shelf and open marine to pelagic settings (Aqrawi et al., 2010). Depositional facies of the formation are arranged into three stratigraphic units with variable lithology and siliciclastic admixture as indicated by gamma-ray logs. Porosity and permeability are controlled mainly by fracture distribution and modified by pressure dissolution features, particularly stylolites, which may represent potential conduits for hydrocarbon migration (Aqrawi et al., 2010; Rashid et al., 2015; Al-Qayim et al., 2016). Some north Iraqi oil fields produce commercial oil from the fractured Kometan Formation (Aqrawi, 1996). Aqrawi et al. (2010) found that the Kometan Formation produces gas in the Jambur oil field and oil in the Avanah and Baba Domes of the Kirkuk structure and Bai Hassan field. In the Taq Taq oil field, the fractured Kometan Formation produces light oils (41 API) with 700–750 million barrels of recoverable reserves. TTOPCO (2007) anticipated 200,000–250,000 barrels per day from the field when fully developed (Rashid et al., 2015a). The Kometan Formation's fractures increase porosity and permeability, regulating carbonate rock productivity (Rashid et al., 2015a).

1.2. Lithological Controls on Carbonate Reservoir Properties

The lithology of carbonate succession controls porosity and permeability heterogeneity. Thus, understanding spatial and vertical lithological differences is essential for characterizing the petrophysical and mechanical properties of carbonate reservoirs (Li et al., 2006; Sun et al., 2018; Wang et al., 2018; Al-Dujaili et al., 2021). Rock density, strength, and hydraulic fracturing depend on lithology (Vipulanandan and Mohammed, 2018; Mohammed, 2019; Mahmood et al., 2020). The core description is the easiest approach to determine lithology, but it takes time and is limited to well intervals (Chang et al., 2000; Li et al., 2006; Mahmoodi et al., 2016; Tian et al., 2016; Zhang et al., 2017). Thus, lithology identification requires well log analysis. Well logging methods were used to study subsurface reservoir lithology, petrophysics, and facies interpretation (Killeen, 1997; Chang et al., 2000; Sfidari et al., 2014; Abdelmaksoud and Radwan, 2022; Abdullah et al., 2022). Bar graphs and bivariate statistical analysis have been widely used to determine lithology from well log data (Zhang et al., 2014; Guiwen et al., 2015). Qualitative techniques can benefit from geologists' knowledge but have disadvantages such ambiguity, excessive work, ineffectiveness, and geologist-introduced artifacts (Li et al., 2006; Zhang et al., 2017). Recently, computer methods have been used to estimate lithology from well log data. In logging-based lithology categorization, the ANN is commonly used as an unpredictable automated estimator. Supervised (Baldwin, et al., 1989; Rogers, et al., 1992), unsupervised (Kohonen, 1982; Ripley, 2007; Chang et al., 2000), and adaptive resonance theory (Doveton, 1994; Chang et al., 2000) have been used to predict lithology. Back propagation neural networks and Kohonen self-organizing maps are supervised and unsupervised ANNs. Studies examined clustering theory in lithology recognition (Sfidari et al., 2014). Various clustering studies predicted lithology (Tian et al., 2016; Pabakhsh et al., 2012; Nouri-Taleghani et al., 2015).

Computerized well log evaluation has lately used random forest (Cracknell and Reading, 2014; Harris and Grunsky, 2015), support vector machine (Elkatatny and Mahmoud, 2018), deep recurrent neural networks (Wu et al., 2018), and deep convolutional neural networks (Imamverdiyev and Sukhostat, 2019). In the preceding methods, the lithology is established only by examining several log readings at the relevant depth, without considering the combined lithologies' geological properties. The response properties of log curves of different lithologies are difficult to distinguish, especially close to the transition surface, and no mathematical solution can adequately integrate log data to create an accurate underground lithology pattern (Li et al., 2006; Mahmoodi et al., 2016). Accordingly, the results may disagree with accepted geologic principles.

1.3. Carbonate Reservoir Modeling and Sequence Stratigraphy

Outcrop analogues can aid subsurface reservoir modeling. Outcrops allow direct study of facies, stacking patterns, diagenesis, and petrophysical properties, unlike exploratory wells. Even though outcrop research has several benefits, the lack of quantitative logging procedures makes subsurface correlation challenging. Facies stacking patterns and diagenetic traits inherited from sea-level variations during deposition are often linked to reservoir attributes (Fig. 1) (Westphal et al., 2004; Ehrenberg et al., 2006; Stadtműller, 2019; Zhang et al., 2024). Transgressive and regressive cycles may be linked to the primary and secondary porosity of carbonate rock (Morad et al., 2000; Flügel, 2004). Cementation during regression fills significant inter- or intra-particle pores, reducing primary porosity (Read and Horbury, 1993; Tucker, 1993; Flügel, 2004). Sea-level variations affect diagenesis and secondary porosity (Morad et al., 2012). Porosity chemistry differs in near-surface water, hypersaline, brackish, and meteoric depositional situations. At the sediment/water contact, sea-level changes can modify the pore water chemistry in carbonate sediments (Morad et al., 2012). Transgressive/regressive cycles also determine diagenetic process duration and modulation magnitude. Slow sedimentation during transgression exposes sediments to marine pore water diagenesis, while high sedimentation during regression leads to widespread meteoric diagenesis (Morad et al., 2012). Changing sea levels affect organic matter amount and type (Cross, 1988; Whalen et al., 2000). Biochemically generated methane exhalation impacts carbonate matrix dissolution (Flügel, 2004). In sequence stratigraphy, primary and secondary diagenetic porosity are controlled (Tucker and Wright, 1990; Posamentier and Allen, 1999). The Kometan Formation's sedimentology, stratigraphy, paleontology, and structure have been examined by various investigators. Stylolites, chert nodules, and high secondary porosity characterize the Kometan Formation's foraminiferal oligostiginid wackestone to grainstone. It was deposited in an open marine, low energy, middle to outer ramp depositional context partly governed by shallow-water eroded components. Deep burial diagenesis created stylolite and chert nodules, according to Al-Barzinjy (2008). The formation contains transgressive and highstand systems tracts of a complete third-order sequence separated by type-2 sequence boundaries (Haddad and Amin, 2007; Balaky et al., 2016).

Rashid et al. (2015a, 2015b, 2017) examined the surface and subsurface porosity, permeability, and reservoir quality of the Kometan Formation. Although outcrop investigations reveal the Kometan Formation's depositional contexts, sequence stratigraphy, and diagenetic history, its underground production potential is

unknown. To turn well-log lithology data into genetic packages for assessing delicate stratigraphic reservoirs, reservoir basin analysis must use sequence stratigraphy. This approach correlates well lithostratigraphy (Omigie and Alaminiokuma, 2020). However, quantitative procedures in reservoir outcrop analogues and subsurface well log correlation are difficult. Gamma-ray spectrometry can link petrophysical characteristics to facies (Rider, 1999) and enable quantitative sequence-stratigraphic interpretations in outcrop studies (Bábek et al., 2018). One more fast, cheap method for quantifying stratigraphic correlation in outcrop is X-ray fluorescence spectroscopy (XRF) of powdered samples. It can detect changes in lithology and paleoenvironmental conditions in carbonates. Although sediment geochemistry is seldom used in hydrocarbon exploration and production, it is hypothesized here that outcrop geochemistry and subsurface lithology well logs can be mutually correlated and the XRF technique provides a quantitative link between reservoirs and their outcrop analogues.

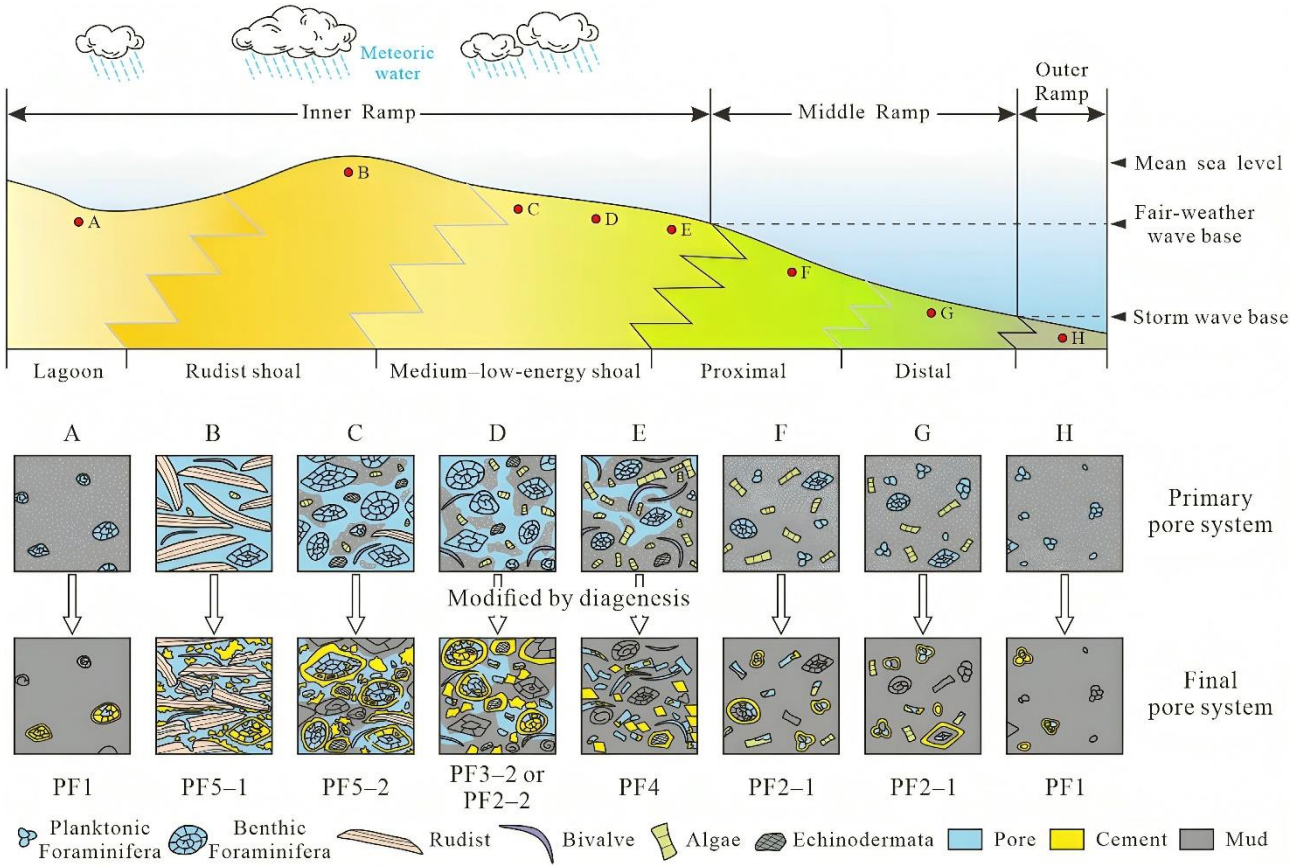

Fig. 1. Pore distribution types of different facies and environments in carbonate ramp (Zhang et al., 2024).

1.4. Stylolites and Fractures in Carbonate Reservoirs

Subsurface reservoir features of carbonate rocks are difficult to predict due to depositional rock textural variability and post-depositional diagenetic overprints. Petrophysical characteristics and carbonate textures fluctuate vertically, laterally, and over time along diagenetic pathways. Therefore, reservoir quality, especially permeability, is hard to assess. In otherwise homogenous carbonate rocks, stylolites are common diagenetic

characteristics (Bathurst et al., 1991). Pressure dissolution can form thin, undulating tooth-like stylolites with concentrated insoluble residue parallel to bedding planes. Stylolites may exaggerate the original bedding planes defined by changes in lithology, or even form new, so-called pseudo-bedding surfaces, which do not coincide with original bedding, and which separate units of the same lithology (Simpson, 1985). Targeted contractional strain affected stylolite orientation (Fletcher and Pollard, 1981; Schultz and Fossen, 2008). According to Groshong (1975), stylolite peaks align with the highest primary stress ($\sigma 1$). Slickolites have skewed stylolite planes when they move (Gratier et al., 2005). Normal sedimentary stylolites are parallel to bedding and perpendicular to burial stress. Pressure-dissolution at grain and crystal interfaces nucleates and grows stylolites. The chemical dissolution of rock-forming minerals and localized physical stress-induced grain compaction at a fluid-filled interface occur. Because it provides the solubility contrast needed to generate stylolite surfaces, rock mineralogical heterogeneity governs this process. On localized less-soluble heterogeneous material, the "proto-stylolite plane" becomes sharp and roughen (Koehn et al., 2012). Stylolites have been shown to affect fluid flow and petrophysical parameters in several research (Paganoni et al., 2016; Martín-Martín et al., 2018; Heap et al., 2018; Toussaint et al., 2018; Bruna et al., 2019; Humphrey et al., 2019; Gomez-Rivas et al., 2022) (Fig. 2). Even though stylolite shaves are prevalent in carbonate rocks, they attracted less attention than fracture networks. Stylolite morphology and orientation can determine compressive stress distribution, amplitude, and orientation in a region (Koehn et al., 2012). Amplitude, wavelength, spacing, and connectivity combine to create a variety of stylolite network designs. Stylolite networks' effects on fluid flow have largely been studied due to their diverse fluid behavior. Based on field and microscopy observations, stylolites and their networks may act as fluid flow barriers (Burgess and Peter, 1985; Finkel and Wilkinson, 1990; Alsharhan and Sadd, 2000; Martín-Martín et al., 2018; Gomez-Rivas et al., 2022). Stylolites may increase permeability parallel to their planes, like in carbonate reservoirs and outcrops (Carozzi and Bergen 1987; Bergen and Carozzi, 1990; Lind et al., 1994; Harris, 2006; Chandra et al., 2015; Barnett et al., 2018; Paganoni et al., 2016; Martín-Martín et al., 2018; Morad et al., 2018; Gomez-Rivas et al., 2022). Preferred dissolving along stylolite planes leads to limited porosity around stylolites (Bergen and Carozzi, 1990) and larger pore throats (Baud et al., 2016). Despite various research on stylolites' significance in local fluid flow, little is known about how depositional facies and carbonate rock components affect stylolite morphology, type, and growth. There is also growing interest in how host rock variety impacts stylolite shape, distribution, and size (Toussaint et al., 2018; Morad et al., 2018; Humphrey et al., 2020). While these authors recognized lithology as the key factor for stylolitization, Koehn et al. (2016) stressed the importance of lithological controls interacting to create stylolite. Fluids' role in stylolite production and evolution is also unclear. Petroleum emplacement could prevent stylolitization (Neilson et al., 1998; Morad, 2018). Many hydrocarbon-bearing limestones include broad lateral stylolite networks that compartmentalize reservoirs and modify fluid movability (Hassan and Wada, 1981; Ehrenberg et al., 2016). The discontinuous shape of stylolites only affects petrophysical properties locally (Heap et al., 2014). Stylolites can also cause permeability heterogeneities, where permeability increases throughout the surface (Heap et al., 2018). Numerous studies have examined stylolites in carbonate rocks (Koehn et al. 2007; Ebner et al. 2010; Paganoni et al., 2016; Martín-Martín et al., 2018; Heap et al., 2018; Toussaint et al., 2018; Bruna et al., 2019; Humphrey et al., 2020;

Gomez-Rivas et al., 2022), as well as sandstones (Baron and Parnell, 2007; Nenna and Aydin, 2011), and evaporites (Bauerle et al., 2000). There is a lack of studies on the formation of stylolites in carbonates with a mixed carbonate/silica composition, which are quite common in carbonate reservoirs and in which the silica enrichment results from the accumulation and diagenesis of siliceous.

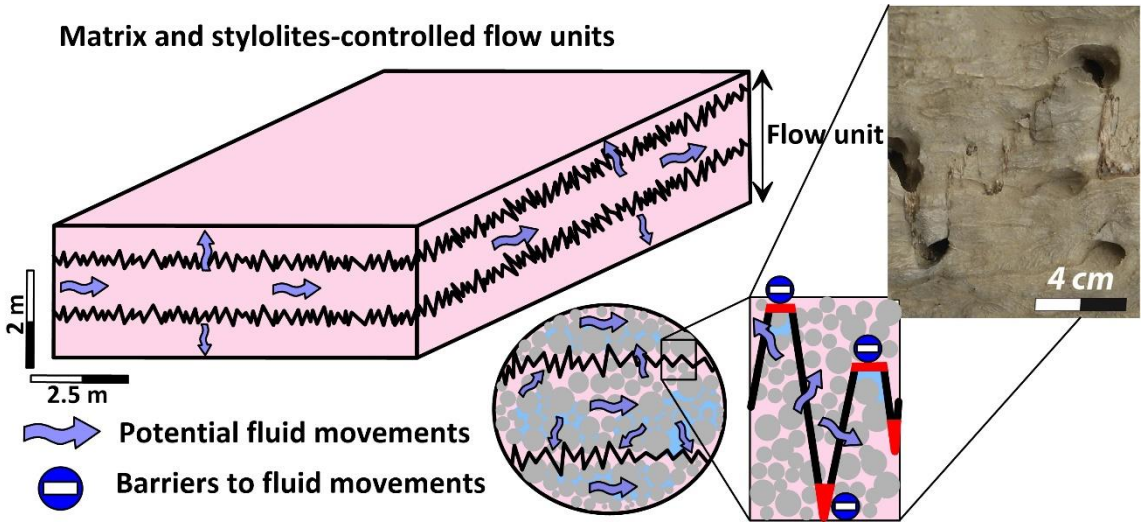

Fig. 2. Stylolite system acting as potential to fluid flow (Adopted from Bruna et al., 2019).

Carbonate reservoirs are fractured and complex due to varied depositional textures and diagenetic effects throughout a wide part of Northern Iraq's geology, making reservoir quality evaluation difficult. Natural fractures cause carbonate rocks' complexity and heterogeneity. Fractures improve reservoir quality, fluid movability, and production (Roehl and Choduette, 1985; Watkins, et al., 2017) (Fig. 3). Fractures can be identified directly from core samples and indirectly from seismic sections, well logs, well tests, and drilling mud losses (Thompson, 2000; Nelson, 2001; Martinez-Torres, 2002; Dutta et al., 2007). The most qualified fracture identification methods are the Borehole Acoustic Televiewer, Formation Micro scanner (FMS), Formation Micro-Imager (FMI), and Electric Micro Imaging (EMI), however, they are pricey and only provide images at defined intervals. On the other hand, the Conventional well log tools can be evaluated without limitations. In addition, open and fluid-filled fractures are also sensitive to conventional logging approaches (Laongsakul and Durrast, 2011). Fractures increase permeability in carbonate reservoirs, especially low-pore Carbonates, hence fracture networks must be identified.

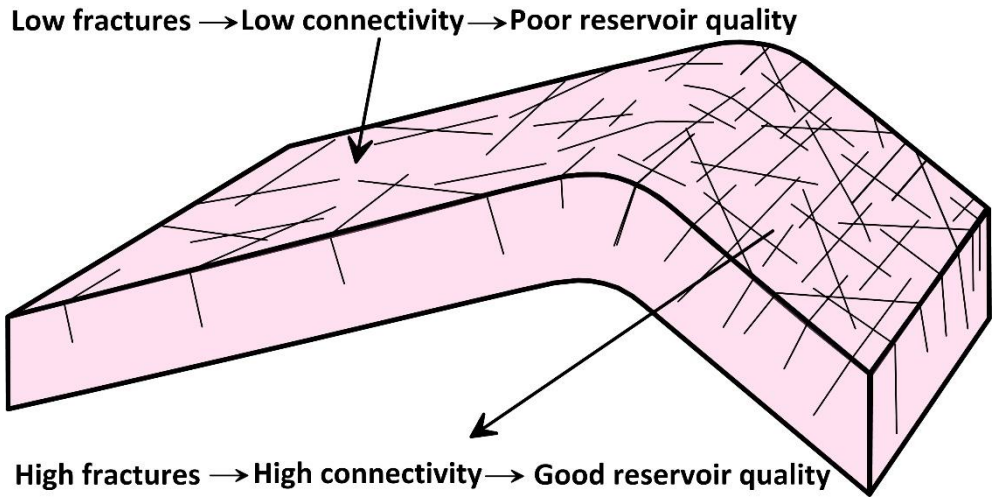

Fig. 3. Naturally fractured characteristics on an anticline (Adopted from Watkins, et al., 2017).

This study proposes an innovative approach to predict lithology in carbonate rocks from the Kometan Formation, Northern Iraq, integrating well log data with geological information. Simultaneously, we investigate the correlation between sequence stratigraphy and reservoir properties in ramp carbonates of the same formation, analyzing both outcrop and subsurface data. Additionally, we explore the relationship between stylolites and microfacies within the formation, aiming to quantify their impact on reservoir characteristics. Furthermore, we demonstrate the capability of conventional well logging tools to identify fractures and detect fracture zones in the Kometan Formation, enhancing understanding of reservoir quality and distribution.

2. Geological Background

The type locality of the Kometan Formation (Upper Turonian to Lower Campanian) is located in the Kometan Village, north-east of the town of Ranya near the city of Sulaimani, the Kurdistan region of Iraq (Fig. 4) (Van Bellen et al., 1959; Dunnington, 2005). The type locality exposes thin-bedded, white to light grey globigerinid–oligosteginid limestone containing locally abundant chert nodules, especially near the base of the section, and occasional glauconite-rich layers. The Kometan Formation was observed in many outcrop sections and the subsurface of the Imbricated Zone, High Folded Zone, and Low Folded Zone of the Zagros Foreland Basin, Kurdistan Region, Iraq; its thickness ranges from 63 to 185 m (Aqrawi et al., 2010). In different parts of the basin, the Kometan Formation rests either conformably or unconformably on the oligosteginid limestone facies of the Balambo Formation and limestones and dolomites of the Dokan, Gulneri, and Qamchuqa Formations of Early Cretaceous to Coniacian ages (Fig. 5) (Buday, 1980; Kaddouri, 1982; Jassim and Goff, 2006; Al-Qayim, 2010). The Kometan Formation is either conformably or unconformably overlain by the Shiranish Formation and Tanjero Formation of Campanian to Maastrichtian age (Buday, 1980; Jassim and Goff, 2006). A distinct, glauconite-rich layer at the base of the Shiranish Formation can be used as a lithostratigraphic marker bed (van Bellen et al., 1959; Dunnington, 2005). Field observations suggest that in places the basal and top boundaries of the Kometan Formation are cut off by post-depositional (early Miocene to Pliocene) faults accompanying the anticlinal structures of the north-western Zagros in the Kurdistan region (cf., László et al., 2012). A variety of fine-grained carbonate lithologies of the Kometan Formation were deposited in shallow marine shelf,

restricted settings (oligosteginid facies), and open marine settings (globigerinid facies) (Buday, 1980; Abawi and Mahmood, 2005; Jassim and Goff, 2006). Towards the west and southwest of Iraq, the globigerinid and oligosteginid facies laterally pass into more argillaceous facies and marls fully corresponding to the oligosteginid biofacies (van Bellen et al., 1959; Dunnington, 2005). The Kometan Formation of the Imbricated, High Folded, and Low Folded Zones passes laterally into bioturbated chalky limestone, shale and marly limestone of the Khasib Formation, lagoonal shale, and carbonate of the Tanuma Formation, and open shelf globigerinid limestone of the Sa'di Formation in the Mesopotamian Zone and the Stable Platform of central and south Iraq (Figs. 4, 5) (Aqrawi, 1996; Al-Qayim, 2010).

3. Methods

The well-log dataset comprises gamma ray, caliper, sonic, density, and neutron logs from nine wells (J-37, BR-1, BH-13, Kz-13, Kz-29, Kz-40, K-216, and K-218, K-243 wells) from the Khabbaz, Kirkuk, Jambur, Bai Hasan, and Barda Rash oil fields (Fig.4), provided by the North Oil Company, Iraq. The Get Data Digitizer 2.2 was used to digitize the analog logs with 0.2 m reading interval.

The gamma-ray log is used as an indicator of formation shaliness, or the volume of shale (Oberto, 1984). The first step in the calculation of the shale volume was the gamma-ray index (I_{GR}), which was calculated using equation (1):

$$I_{GR} = (GR_{log} - GR_{min}) / (GR_{max} - GR_{min}) \quad (1)$$

The gamma-ray index is denoted by I_{GR}, the gamma-ray reading from the log is denoted by GR_{log}, the clean zone gamma-ray reading is denoted by GR_{min}, and the maximum gamma-ray reading from the log is denoted by GR_{max} (shale zone). The following equation was used to determine the shale volumes (Vsh), as proposed by Larionov (Oberto, 1984) (Eq. 2):

$$Vsh = 0.33[2^{2*IGR} - 1.0] \quad (2)$$

Input parameters for multivariate regression including ρb, Δt, and neutron porosity values from digitized logs are used to predict lithology. Multivariate regression combines independent factors to predict dependent values (Mohaghegh et al., 1997). Multivariate linear regression analyses connect several variable predictors (X-variables) to a single response variable (Y-vector). Linear regression between well log response (X-variables) and formation rock lithology (Y-vector) is used in this method. Fig. 6 shows the general methodology: Using rock sample lithology and regression analysis with well logs (ρb, Δt, and neutron) can achieve linear best-fit parameters for lithology prediction. For regression analysis to a continuous lithology log of the examined formation in the same and other wells in the same drilling environment, the coefficient of determination (R^2) between lithology from rock samples and well log readings should be 0.8 or better. This study's multivariate regression used lithology codification and fuzzy logic (Eq. 3).

$$\text{If } X < P \leq Y, \text{ then } S \quad (3)$$

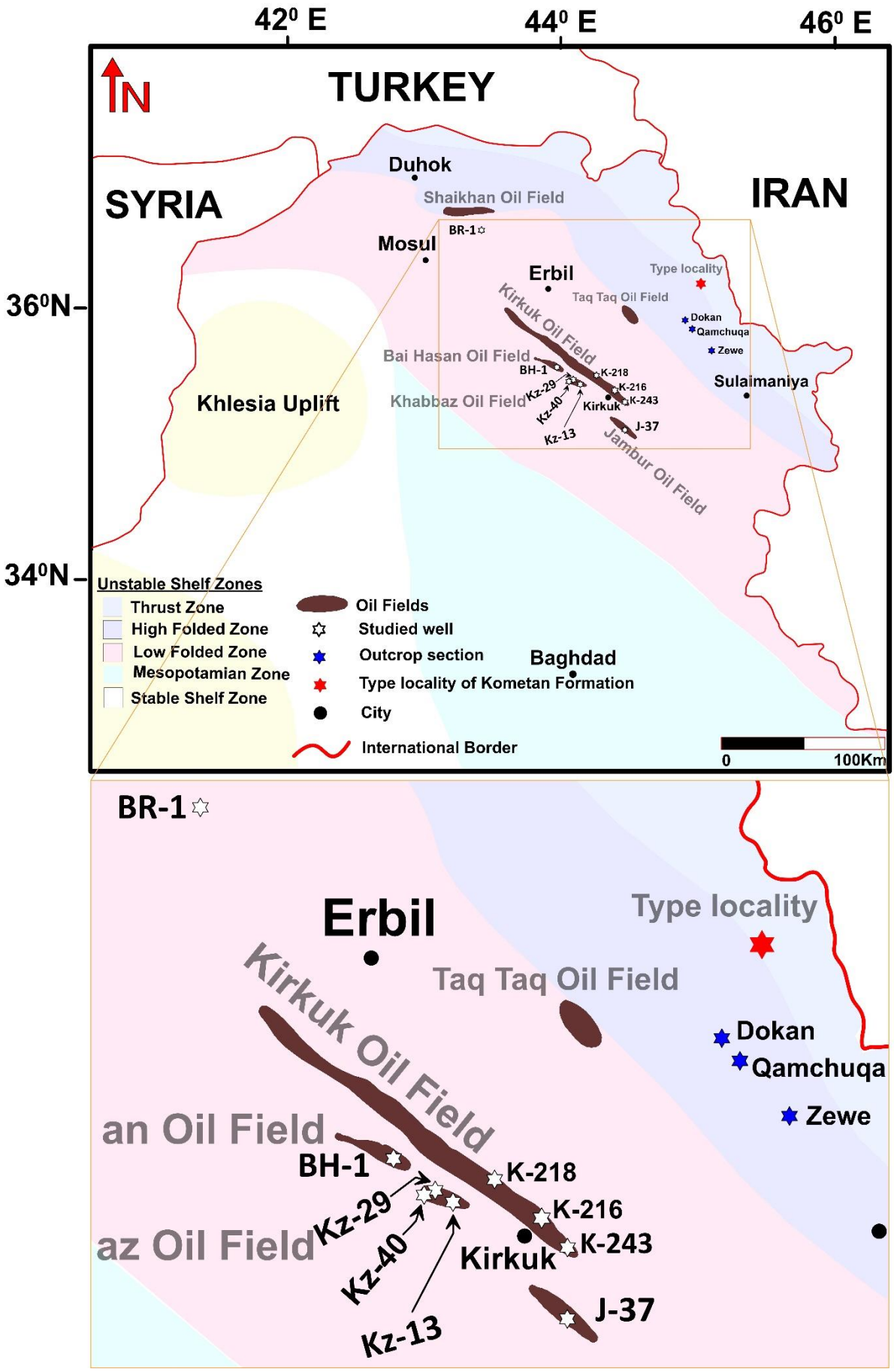

Fig. 4. Location, and tectonic subdivisions of the study area (Adopted from Hussein et al., 2024).

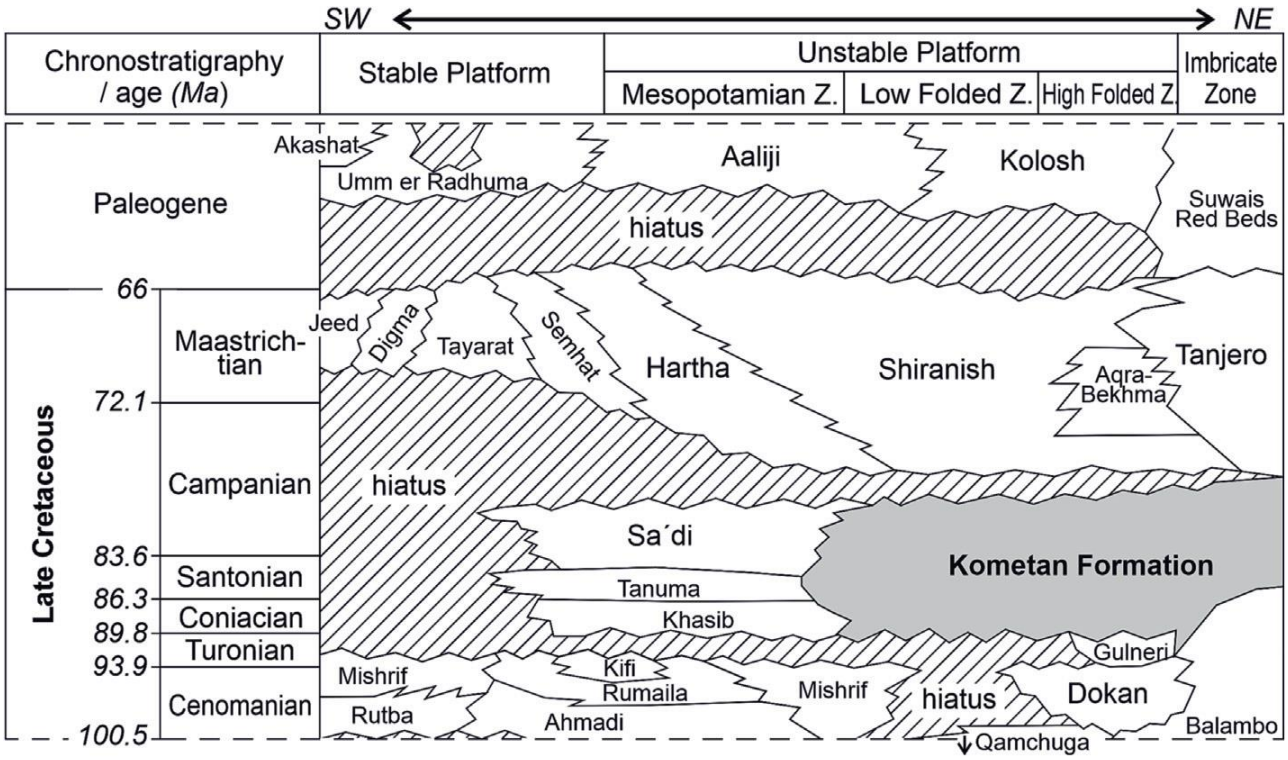

Fig. 5. Chronostratigraphic division of Upper Cretaceous lithostratigraphic units in NE Iraq. (Adopted from Hussein et al., 2024).

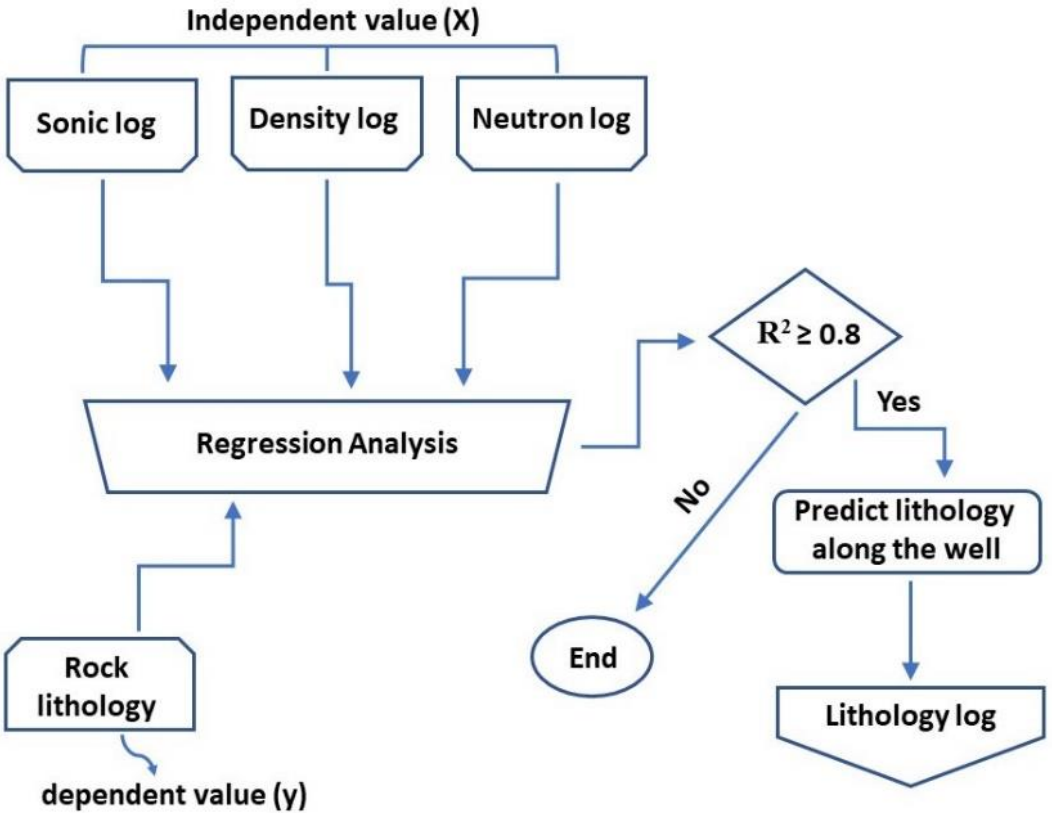

Fig. 6. Proposed quantitative methodology workflow for predicting lithology (Adopted from Hussein et al., 2024).

Porosity cross-plot has been used to identify the fracture zones. Neutron, density, sonic, caliper, and total gamma-ray logs have been used qualitatively to detect fractures. total porosity (neutron-density combination) with sonic porosity can be proposed for the identification of secondary porosity (Eq.4) (Rider, 1999; Lyon, 2010).

$$SPI = \Phi_{total} - \Phi_{sonic} \quad (4)$$

Where:

SPI: Secondary Porosity Index

Φ_{total}: Total Porosity ((Neutron Porosity + Density Porosity) / 2)

Φ_{sonic}: Sonic porosity

Three outcrop sections of the Kometan Formation, Zewe (96 m thick) (35.73535° N, 45.2371° E), Qamchuqa (63 m) (35.897196° N, 45.01338° E), and Dokan (65 m) (35.944634° N, 44.983866° E) (Fig. 4) were sampled and documented using bed-by-bed descriptions of bed thickness, bed geometry, sedimentary structures, and grain size using the approach summarized by Graham (1988). The outcrop sampling was conducted for thin section analysis. A qualitative microfacies analysis following the principles summarized in Scholle and Ulmer-Scholle (2003) and Flügel (2004) was carried out on a total of 50 thin sections using the Dunham classification scheme (Dunham, 1962).

Following Humphrey et al. (2020), the abundance, and various size and morphology parameters of the stylolites and their networks were measured in the field using 1m x 1m sized sampling frames. The framed outcrop sections were marked, photographed, and rectified to maintain a uniform scale and vertical-to-horizontal aspect. To minimize the effects of vegetation and noise from the background, line drawings of all stylolites present were made from each scaled frame picture. The stylolite spacing, amplitudes, wavelengths, junction angles, and types of interaction were measured from the scaled pictures (Fig. 7). Three vertical lines (dashed lines, Fig. 7A) with a lateral offset of 50 cm were drawn in each frame picture perpendicular to the stylolites, to measure the stylolite spacing. The perpendicular spacing values taken from every line were added up for each frame, and the heights between stylolite crossing were documented (Fig. 7B). Thus, the biggest vertical stylolite spacing that can be measured is one meter, but in all frames, the spacing was lower than one meter. The central vertical line in each sampling frame was used to record the stylolite wavelength and amplitude. We recorded every stylolite that crossed the measuring line. The wavelength was measured as a horizontal separation between the nearest two positive peaks located along the measuring line (Fig. 7C), whereas amplitudes were measured as a vertical distance between positive and negative stylolite peaks located nearest to the scanline (Fig. 7D). Selecting the nearest amplitude observations to the measuring line minimized the effects of inclination. The junction angles were calculated between the two intersecting lines (Fig. 7E).

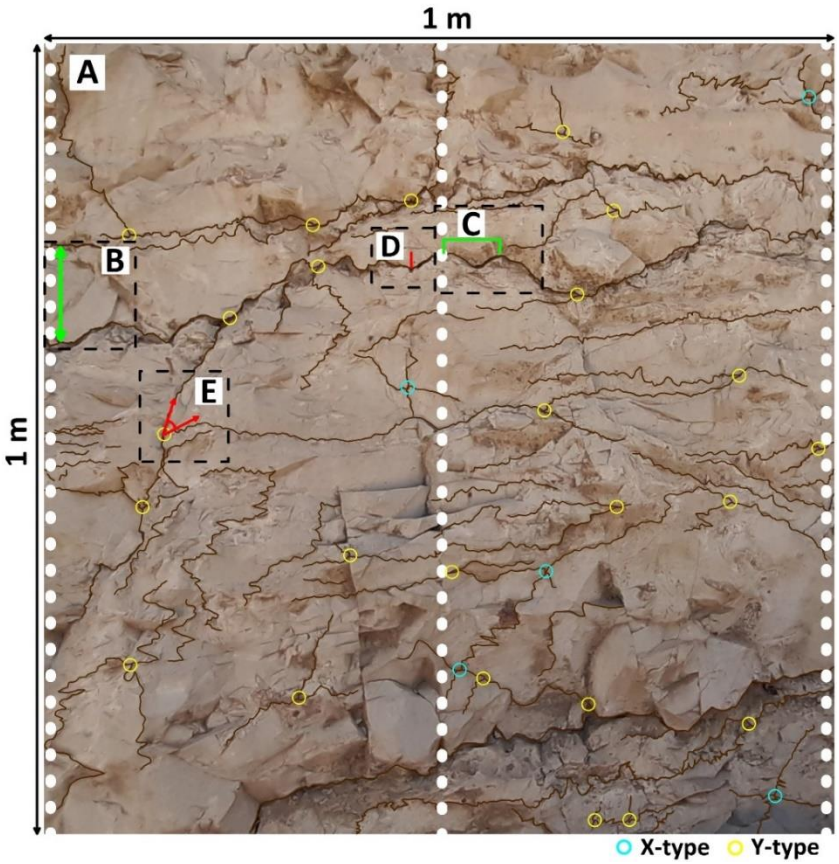

Fig. 7. Example frame size and positions of three scanlines (A) used for recording stylolite spaces (B), wavelength (C) (middle scanline), amplitude (D) (middle scanline), junction angle (E), and labeled image identifying the X-type (Cyan) or Y-type (yellow)of stylolite junction.

Stylolite spacing, wavelength, and amplitude were measured and graphically represented using Past 4.04 software. stylolite data was fitted with log-normal distributions. The Kolmogorov-Smirnov (KS) normality testing and chi-squared tests were employed to determine the goodness of fit (Massey, 1951). The null hypothesis for the KS test was p-value < 0.05. Using stylolite length, junction forms were calculated. The stylolite junction intensity per meter (m) for each frame was calculated (Eq. 5).

$$JI\ (/m) = (Jt / (SLt) \quad (5)$$

where JI (/m) is the junction intensity per meter, Jt is the total amount of junctions in the sample frame, and SLt is the total stylolite length per frame.

Use optical microscope images to identify and measure porosity in thin sections impregnated with blue-dyed epoxy resins. Textural analysis was done with a scanning electron microscope (SEM QUANTA 200 FEI with an EDS detector). The grain area of a thin piece was quantified using ImageJ. Folk and Ward (1957) formulae determined Mean grain size (Mz) and standard deviation or sorting from grain.

Measured element concentrations in 246 powdered rock samples from three outcrop sections and 28 samples from four wells using a Delta Premium EDXRF (Energy Dispersive X-Ray Fluorescence) spectrometer

(Innov-X, U.S.A.) with a large-area silicon-drift detector. The acquisition time was 2 × 120 s at 15 kV and 40 kV accelerating voltages. The samples were pulverized to analytical fineness and stored in Mylar-sealed plastic cells before EDXRF analysis. In each sample, Al, Si, P, S, K, Ca, Ti, Mn, Fe, Ni, Cu, Zn, As, Rb, Sr, Zr, Mo, Pb, and Th concentrations were measured. Calibrated EDXRF concentrations with ICPMS/OES data (Table S1, Appendix 6). We chose 76 geochemically similar limestones, marls, and shales from the Lower Devonian mixed carbonate–siliciclastic ramp system in the Prague Basin, Czechia (Bábek et al., 2021) for calibration. ICP-MS/OES and EDXRF were used, followed by a statistical correlation. Linear or polynomic regression techniques calibrated analysed EDXRF data for ICP-MS/OES. High regression coefficients ($R2 \geq 0.99$) were observed for Si, Al, Fe, Ca, K, Ti, Mn, Zr, Rb, and Zn, somewhat lower for As, Sr, and Pb, and much lower but acceptable for Cu, Ni, and Mo. Not calibrated: sulphur and phosphorus.

An RT-50 shielded laboratory spectrometer (Georadis, s.r.o., Czech Republic) with a 3 x 300" (350 cm^3) NaI (Tl) detector was used to study the gamma-ray spectra of 17 rock samples from the Kz-29 (7) and Kz-40 (10) wells. Based on calibrations utilizing calibration standards provided by the manufacturer, the instrument converted the counts per second from 512 energy windows to K (%), U (ppm), and Th (ppm) concentrations. The declared sensitivity was 0.7 ppm for Th, 0.4 ppm for U, and 0.12% for K. Each sample was ground into a powder, put in a 250 cm^3 plastic container, and measured for 30 minutes.

A Panalytical X'Pert PRO MPD diffractometer with reflection geometry, cobalt tube ($\lambda K\alpha = 0.17903$ nm), Fe filter, and X'Celerator 1-D RTMS detector (Masaryk University Brno, Czechia) was used to analyze the mineralogy of 16 powdered samples from outcrops and well-cuttings. Analytical setup includes step size: 0.033° 2Θ, 160 s per step, angular range: 4–100° 2Θ, and 3702 s total scan duration. Bruker AXS Diffrac + Topas 4 and Panalytical HighScore 4.8 plus processed XRD data. The Rietveld method quantified only crystalline phases in 8 samples.

4. Results

4.1. Lithological Aspect and Shale Content

4.1.1. Outcrop Lithology

In the outcrop sections especially the Qamchuqa and Zewe sections (Fig. 4), the upper boundary of the Kometan Formation is overlain by the marl and marly limestone of the Shiranish Formation, and the lower boundary is defined by the limestone and dolomitic limestone of the Qamchuqa Formation. In outcrop, the lithology of the Kometan Formation is very uniform, corresponding to thin-bedded to medium-bedded, very fine grained, bioturbated limestone and argillaceous limestone that ranges from light grey (lower part) to light brown (upper part) colour. The beds contain poorly identifiable trace fossils. Bed thickness usually ranges from ~15 cm to ~60 cm. The beds are separated by thin marly laminae, very often modified by stylolitization. In all measured sections, the carbonate is highly fractured and contains abundant stylolites which are often very large having up to 4 cm amplitude. The limestones locally contain abundant chert nodules arranged parallel with the bedding planes, which are in places concentrated on the stylolites (Figs. 8, 9).

All samples from the Kometan Formation in the outcrop sections (Zewe, Qamchuqa, and Dokan) (Fig.4) with low concentrations of Al (<1 wt%), Rb, Si, and K correspond to pure carbonates. In outcrop, the Kometan Formation can be roughly subdivided into a lower part, characterized by low K (~0.05 to 0.12 wt%) and Al (~0.1 to 0.4 wt%) concentrations, middle part featuring even little bit lower K (~0 to 0.1 wt%) and Al (~0.1 to 0.4 wt%) concentrations and relatively high Zr/Al ratios, and an upper part with relatively high K (~0.05 to 0.25 wt%) and Al (~0.2 to 0.8 wt%) concentrations and low Zr/Al ratios (Figs. 9, 10). The K, and Al concentrations show well constrained lows and highs, which can be correlated between the Zewe, Qamchuqa, and Dokan sections over the distance of 33 km parallel with the tectonic strike (Fig. 10).

The XRD analyses from 6 samples from the Qamchuqa and Zewe sections (Fig. S1, Appendix 5) show that the limestones contain abundant calcite (up to 96 %), quartz and chert (up to 12 %), clay minerals (illite, illite/smectite and smectite, up to 2 %) and trace amounts of K-feldspars and dolomite.

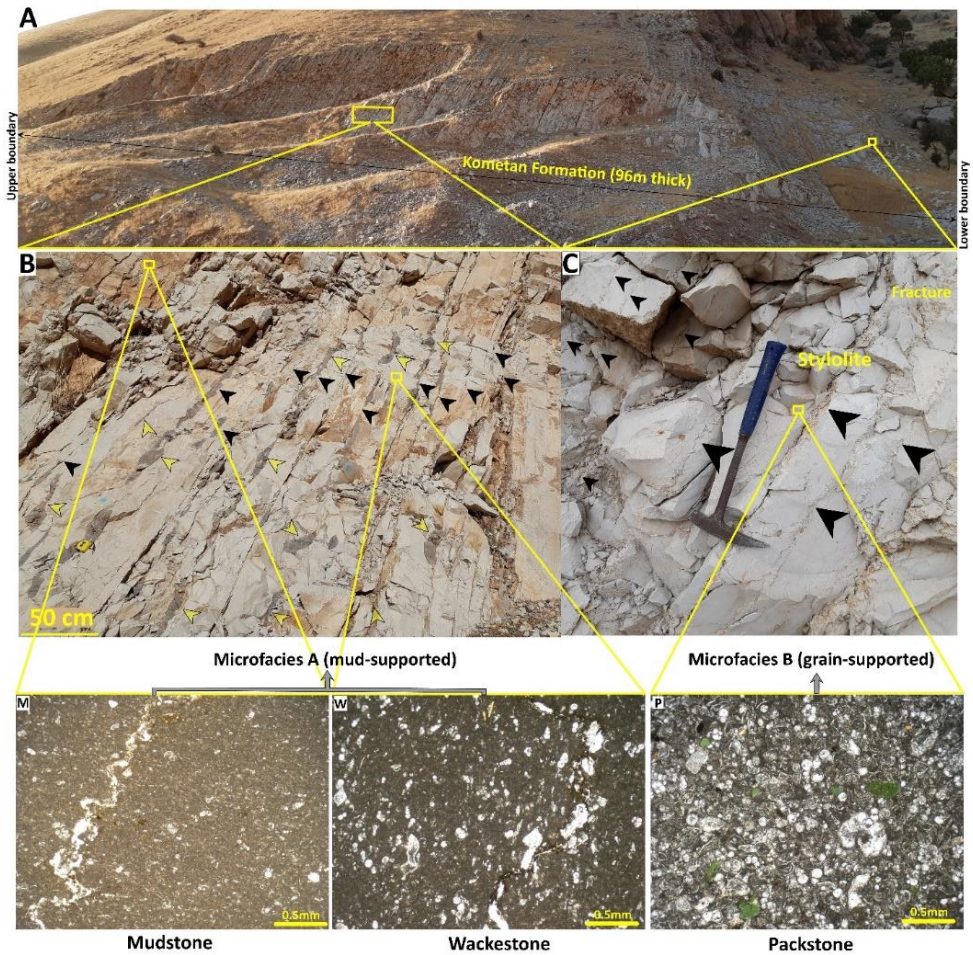

Fig. 8. Field photos of the studied formation in the Zewe section (A) and a close view of bed observations show chert nodules (yellow arrow) and stylolites (black arrow) (B, C). Photomicrographs showing the microfacies: M) planktonic foraminiferal mudstone W) planktonic foraminiferal wackestone, and P) planktonic foraminiferal packstone with glauconite (green particles).

4.1.2. Subsurface Lithology

For subsurface lithology, the description of the available rock samples (well cuttings) from the Kometan Formation could be subdivided into four lithologies: limestone, argillaceous limestone, marly limestone, and marl (Fig. 11). The well log intervals from 2870 to 2885 m in the Kz-29 well (Fig. 11) and 2786 to 2830 m in the Kz-40 well (Fig.4 in Appendix 1) were used as the anchor points (trained samples) in which each lithology was transformed into a code number used in the multivariate regression analysis. The codes ranged from 0.6 to 1.3 (Table 1).

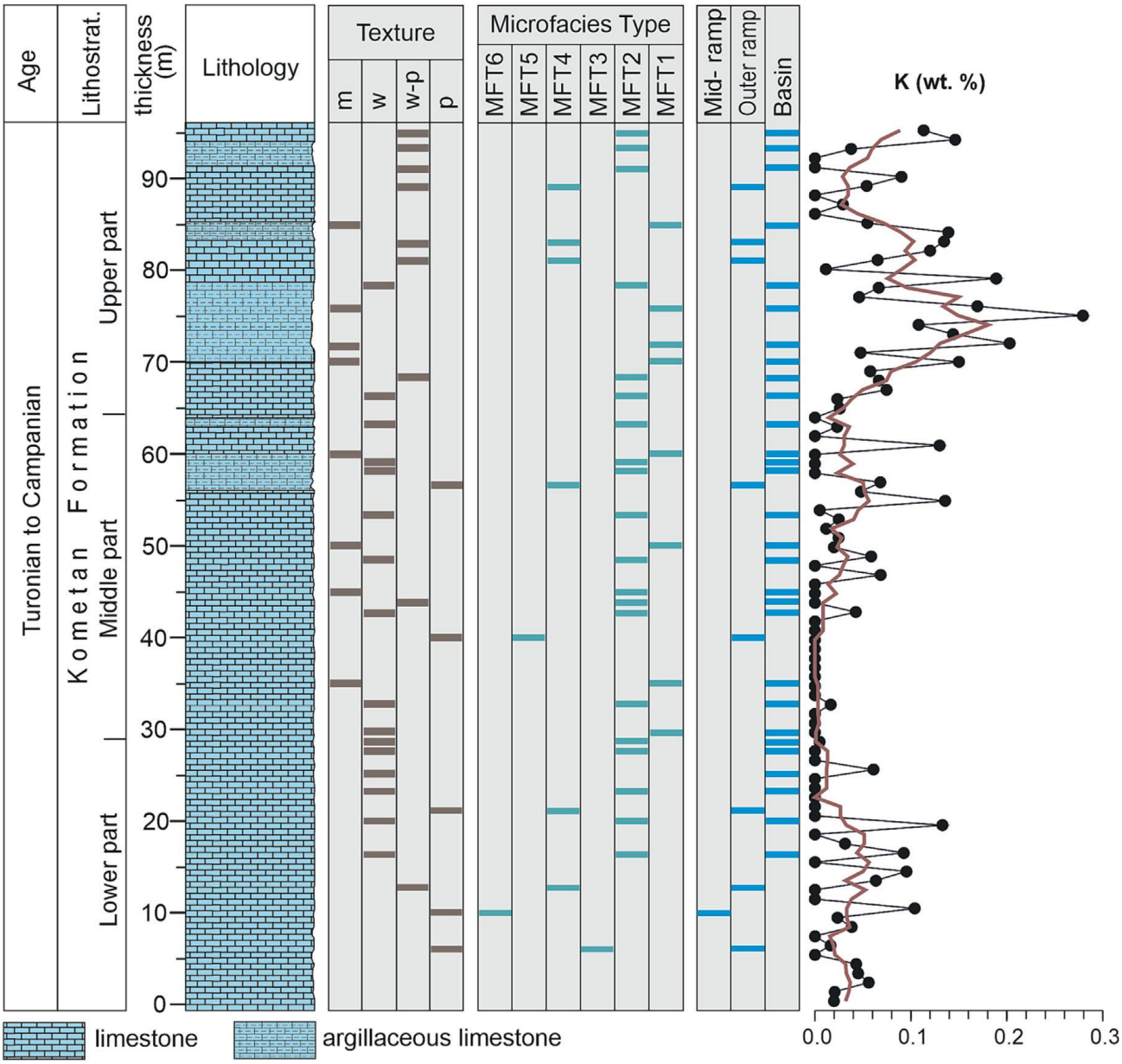

Fig. 9. Stratigraphic log showing lithology, distribution of microfacies, their corresponding depositional settings, and concentration of K (wt%; red line shows the 5-point running mean) in the Kometan Formation at the Zewe section (Adopted from Hussein et al., 2024).

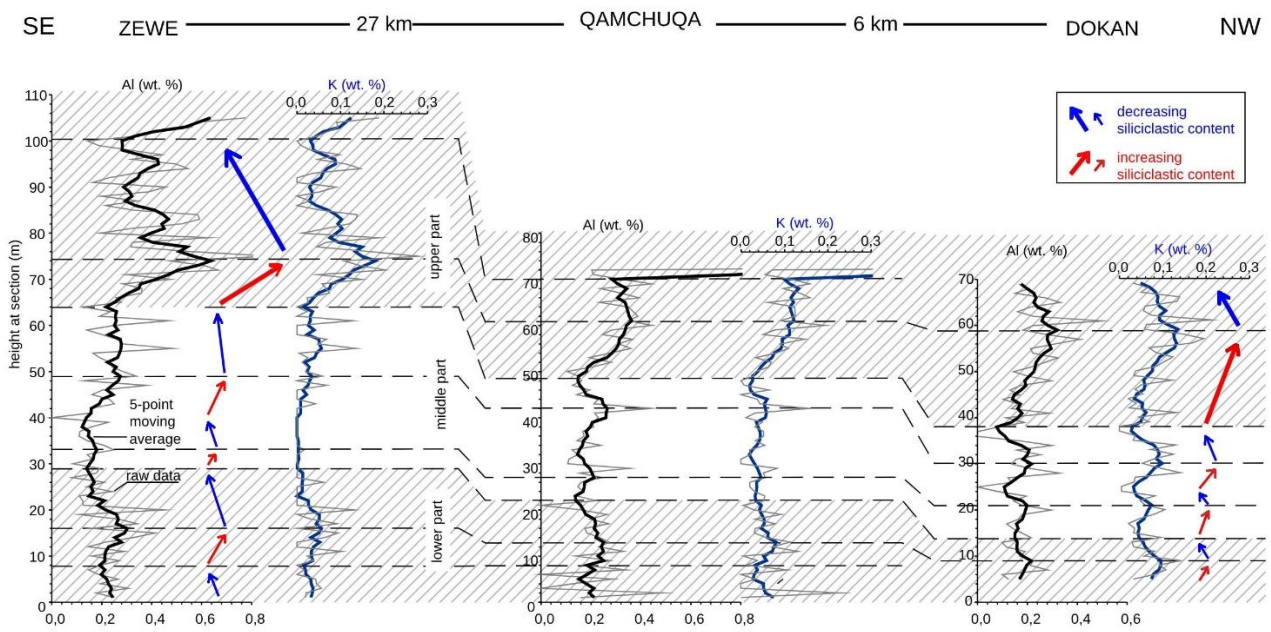

Fig. 10. Geochemical log correlation of the Al (wt%), and K (wt%) logs at the Zewe, Qamchuqa, and Dokan outcrop sections (Adopted from Hussein et al., 2024).

Table 1. Matrix and mineral density values for common types of rocks (Asquith et al., 2004; Derder and Geo, 2016), shale content ranges, and codification for the most common rocks.

Lithology	Density (g/cm^3)	Shale content (%)	Code Number
Anhydrite	2.98	0	1.3
Dolomite	2.87	0-5	1.2
Dolomitic limestone	2.79	0-5	1.1
Limestone	2.71	0-5	1.0
Argillaceous limestone	2.69	15-25	0.9
Marly limestone	2.67	25-35	0.8
Marl	2.66	35-65	0.7
Sandstone	2.65	0-5	0.6

The following equations were derived from the multivariate regressions of bulk density, interval transit time, and neutron porosity log data as independent values to identify the log lithology (dependent value) (Eqs. 6 and 7):

$$\text{Log (Lithology)} = (0.7 + 0.19 * \rho b - 0.0035 * \Delta t + 0.002 * \text{NPHI}) \quad (6)$$

$$\text{Log (Lithology)} = (0.7 + 0.06 * \rho b + 0.0033 * \Delta t - 0.012 * \text{NPHI}) \quad (7)$$

The equations 7 and 8 were generated and applied to the Kz-29 and Kz-40 wells, respectively. The resulting log lithologies varied from limestone to marly limestone in the Kz-29 well (Fig. 11), and from limestone to marl in the Kz-40 well (Fig. 4 in Appendix 1). Statistical correlations were made between the log lithologies and the rock lithologies (cores and cuttings) by using the coefficient of determination (Fig. 5A in Appendix 1),

root mean square error (RMSE), mean absolute error (MAE), and error bar (Fig. 5B in Appendix 1) to show model performance, as well as the error percentage line (Error%) to show the percentages of error between actual and predicted values (Fig.11). A good match was obtained, with the coefficient of determination equalling 0.85 and 0.83 for the Kz-29 and Kz-40 wells, respectively (Fig.5A in Appendix 1). The values for MAE and RMSE for Kz-29 well are 0.00002 and 0.0007, and 0.000021 and 0.0007 for Kz-40, respectively.

The error bar graph (Fig.5 in Appendix 1) shows the average and standard deviation of each of the measured (rock lithology) and predicted (log lithology) values for the Kz-29 well and Kz-40 well. The graph showed that the models are well-performing and can be used to predict the lithology. However, there are some errors presented between the actual and predicted lithology in Fig. 11 (green-filled line). The average errors are 4 % and 8 % in the Kz-29 and Kz-40 wells, respectively.

Based on the average of the error percentage line, equation 7 (Fig.11) provides a more accurate identification of all lithology classes during the performance validation of the multivariate system than Equation 8 (Fig.4 in Appendix 1). Finally, the models were applied to predict the log lithology for the entire thickness of the Kometan Formation in both wells and compared with the observed lithologies (Fig.11).

The shale volumes determined from the gamma-ray log (Fig.11) showed that the studied formation can be divided into three zones: 2802 to 2868 m, with shale volumes ranging from 5.4% to 18% (mean: 8.8%), 2868 to 2920 m, with volumes ranging from 3.7% to 23% (mean: 16%), and 2920 to 2948 m, with volumes from 3.7% to 21.5% (mean: 7.4%) in Kz-29 well. In Kz-40 well, these three intervals corresponded to depths of 2711 to 2792 m, 2792 to 2861 m, and 2862 to 2898 m, with mean shale volume values of 7% (from 4% to 11.4%), 12.6% (3.2% to 22%), and 8% (3.6% to 21.9%), respectively. In both wells, the middle "shaly" part contained more shale than the "clean" upper and lower parts (Fig.11). Gamma rays computed and measured from the available rock samples (Fig.11) validated this. A good correlation between the gamma-ray log and gamma-ray rock was represented by the correlation coefficients equalling 0.70 and 0.82 for wells Kz-29 and Kz-40 wells, respectively (Fig.6 in Appendix 1). The distribution of the elemental proxies shows a relationship with the principal lithologies. The limestone in the Kz-40 well (depth 2711 to 2790 m) has low Al concentrations (1.0 wt.%) and relatively high K/Al (0.4 to 0.6) and Ti/Al (0.08 to 0.12) ratios. On the other hand, marls and argillaceous limestone from the same well have distinctly higher Al concentrations (2.0 to 6.0 wt.%) and lower K/Al (0.2) and Ti/Al (0.06) ratios (Fig. 10B in Appendix 1). The Al concentrations correlated with the shale volumes as determined from the gamma-ray logs, and they could be considered an independent proxy of the shale contents in the Kometan Formation (Fig.11). The concentrations of Al increased in the shaly intervals between 2868–2920 m and 2792–2861 m depths for the Kz-29 (Fig. 12A) and Kz-40 (Fig.10B in Appendix 1) wells, respectively, as demonstrated by the gamma-ray values, which contrasted with those of the overlying and underlying clean units (Fig. 11).

The derived model (Eq. 6) with a coefficient of determination (R^2) higher than 0.8 has been tested to predict the lithology for the Kometan Formation in other wells (Kirkuk 216 (K-216) and Kirkuk 218 (K-218)) (Fig.

4). The lithology estimated by the equation mainly consists of limestone and argillaceous limestone (Fig. 11 in Appendix 1). The thickness of the argillaceous limestone is higher in the K-216 well than in the K-218 well (Fig. 11 in Appendix 1), which is about 25m. The result could be accepted because the Kometan Formation mainly consists of limestone with a small thickness of marly or argillaceous limestone in different locations.

The XRD analyses from 10 subsurface samples (Fig. S1, Appendix 5) show that the rocks are composed of calcite (from 44 to 89 %), illite, illite/smectite and smectite (from 3 to 19 %), kaolinite (from 0 to 22 %), quartz (from 2 to 7 %), K-feldspars (up to 5 %), dolomite (up to 3 %), and minor (<2 %) proportion of siderite, pyrite, hematite, gypsum, anhydrite, baryte and anatase. They show a distinct vertical arrangement: the upper parts of Kometan Formation in Kz- 40 (2710 to 2790 m), Kz-29 (2780 to 2860 m) and K-216 (1440 to 1558 m) are composed of pure limestone and marly limestone; the middle parts in Kz-40 (2810 to 2850 m) and Kz-29 (2880 to 2940 m) are composed of marls, shale and marly limestone, and the lower parts in Kz-40 (2870 to 2888 m) and Kz-29 (2950 m) are composed of marly limestone and pure limestone. The siliciclastic lithologies are fine-grained but any other lithological observations cannot be obtained from the cuttings.

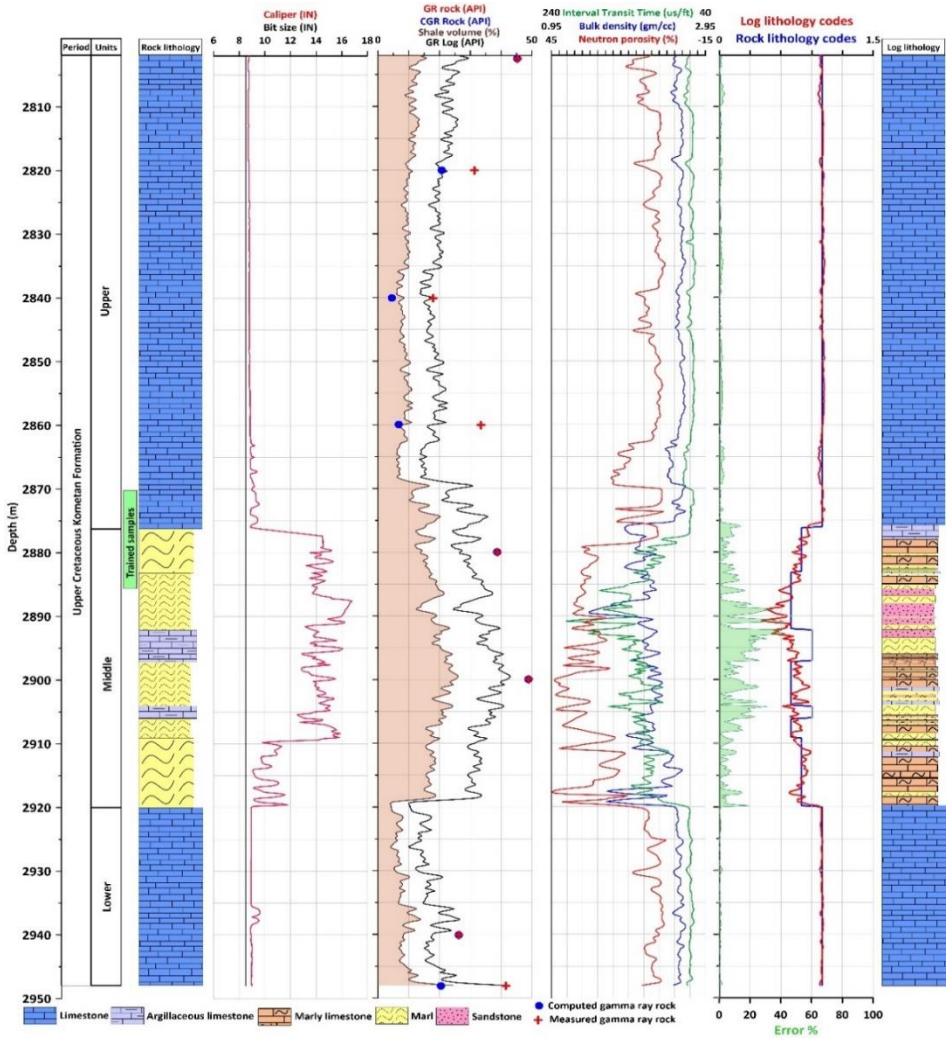

Fig. 11. Log data (caliper, gamma-ray log (GR log), gamma-ray rock (GR rock), computed gamma-ray rock (CGR), sonic (Interval transit time), density (bulk density), and neutron log (neutron porosity)), rock lithology codes (blue line), log lithology codes (red line) computed from multivariate regression, and error percent line (green-filled line) for Kz-29 well (Adopted from Hussein et al., 2024).

The well log data show very similar (correlatable) patterns in both the Kz-29 and Kz-40 wells, but especially the gamma-ray logs can be used for long-distance (>100 km) correlation. The middle, "shaly" interval is well-constrained by blocky patterns at the base and the top, and upwards-increasing and then decreasing GR values in BH-13, Kz-40, Kz-29, Kz-13, and partly K-2018 wells. The middle interval in the K-218, K-216, K-243, and J-37 wells is delimited by a distinct GR peak at the base, which is followed by upwards-decreasing values. In contrast, the lower and upper intervals have lower and more uniform GR values. The correlation results (Fig. 13) show that the middle, shaly interval attains a maximum thickness of ~68 m (Kz40 well) whilst it laterally pinches out to a minimum thickness of ~12 m towards NW (BR-1 well) and to ~15 m towards SE (J-37 well). The gamma-ray values generally decrease consistently with the decreasing thickness of the shaly interval, from maximum values in Kz-40 (~30 to ~70 API) to J-37 wells (~22 to ~35 API, but with a few outliers reaching up to 75 API).

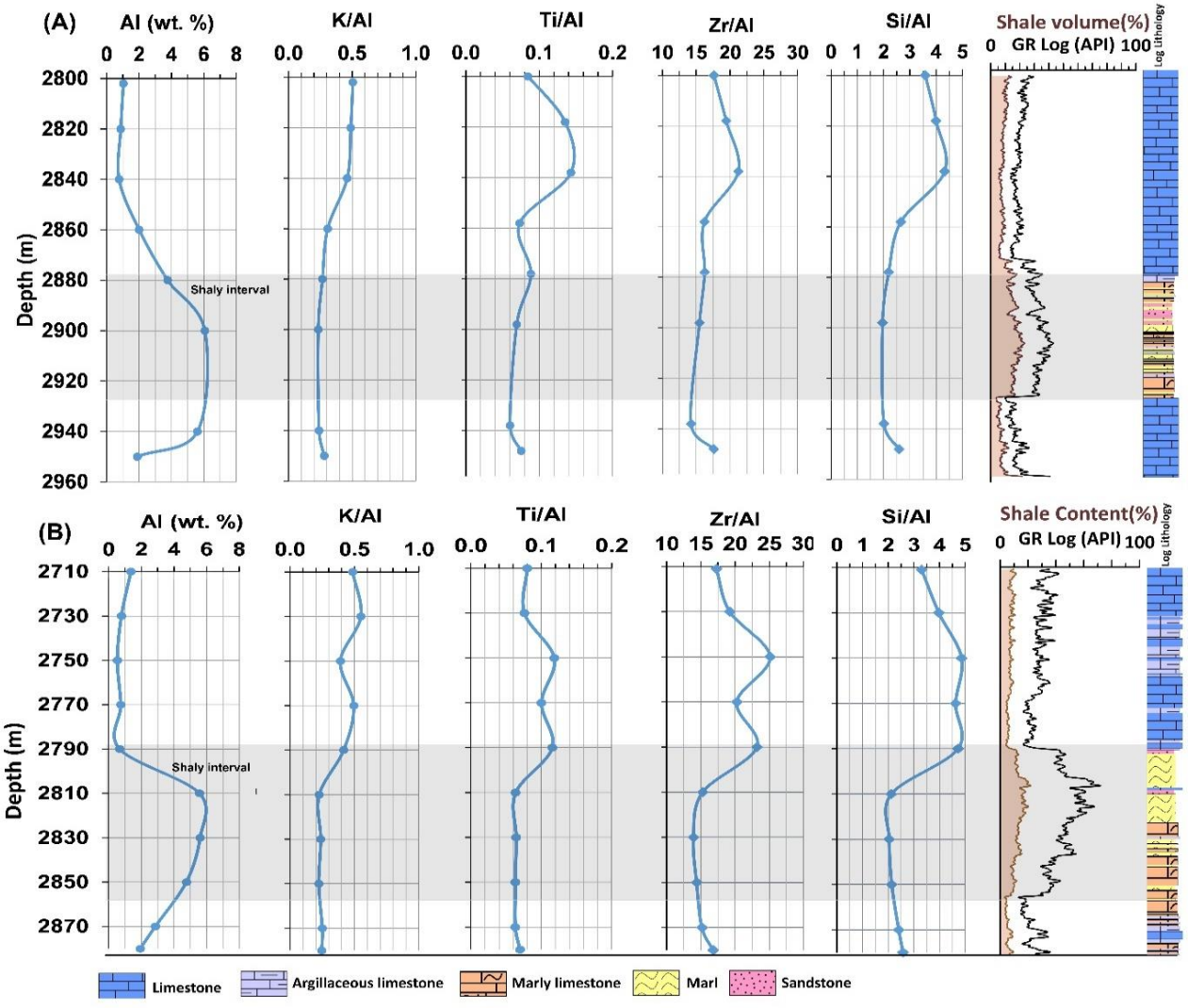

Fig. 12. Vertical distribution of selected elemental proxies and their correlation with selected log data (gamma ray and shale content) in the Kz-29 well (A) and Kz-40 wells (B) (Adopted from Hussein et al., 2024).

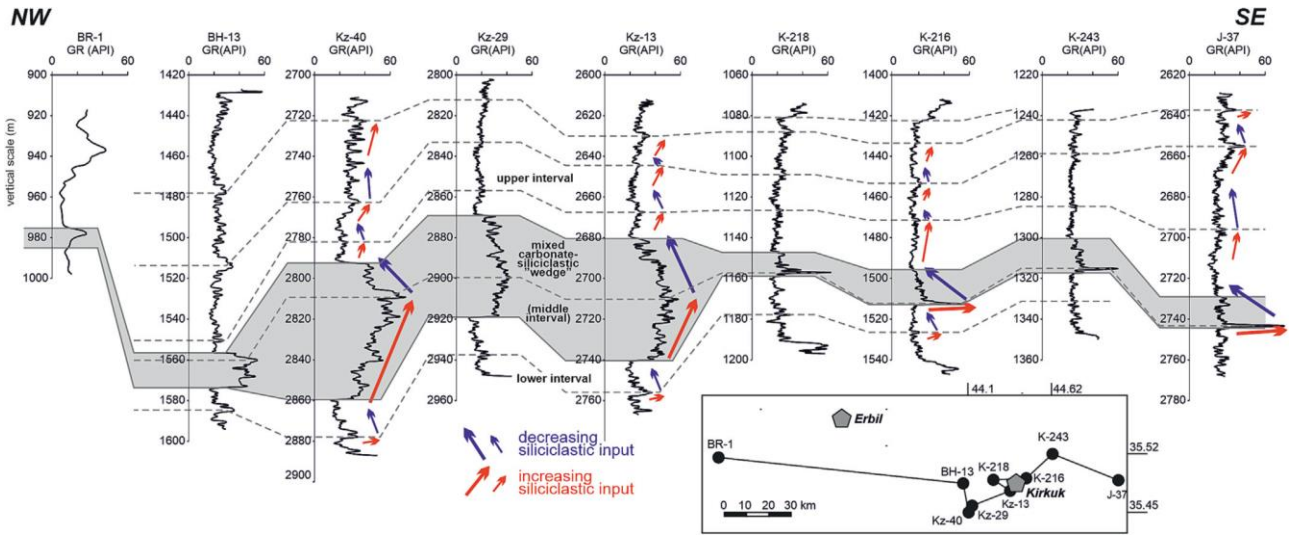

Fig. 13. Well log correlation of the Kometan Formation based on total gamma-ray logs; note the presence of middle, shaly interval (wedge of mixed carbonate–siliciclastic sediment) laterally pinching out (Adopted from Hussein et al., 2024).

4.2. Microfacies Identification

The microfacies analysis is based on thin sections from the Qamchuqa and Zewe sections (Fig. 14). The composition of the Kometan Formation is relatively uniform, but the texture is more variable. Subtle changes in texture and composition of skeletal grains allowed us to classify six microfacies, MFT1–MFT6 (Figs. 9, 14). The MFT1 microfacies is a mudstone including planktonic foraminifers (*Globigerina*, *Heterohelix*, and oligosteginids) and sparse calcispheres (Fig. 14a). The MFT2 microfacies is a wacke-packstone with abundant foraminifers such as *Hedbergella*, *Heterohelix*, and oligosteginids, sparse calcispheres and sponge spicules (Fig. 14b). The MFT3 microfacies is a densely packed, moderately sorted packstone with abundant planktonic foraminifers such as *Globotruncana*, and *Dicarinella*, less abundant *Hedbergella* and *Heterohelix*, sparse calcispheres, fragments of ostracod shells, and relatively large grains of glauconite (Fig. 14c). The MFT4 is a packstone with abundant (35 to 40 %) oligosteginids and less abundant planktonic foraminifers (Fig. 14d). The MFT5 microfacies is a fine-grained, well sorted packstone with oligosteginid planktonic foraminifers, *Hedbergella*, *Heterohelix*, *Globigerina*, and *Globotruncana* (Fig. 14e). The MFT6 microfacies is packstone with benthic foraminifers (e.g., *Textularia*), echinoderm fragments, oligosteginids and sparse ostracods (Fig. 14f).

Analyzing the distribution of these facies, we observe that all six types (MFT1-MFT6) (Fig. 14) are categorized into three main groups: packstone, wackestone, and mudstone. Subsequently, stylolite measurements were conducted for each of these three groups. These groups are further subdivided into Groups A (mud-supported) and B (grain-supported) (Fig. 8B, C), encompassing wackestone and mudstone in group A, while Group B solely comprises packstone. All stylolite analyses are conducted based on these delineated groupings.

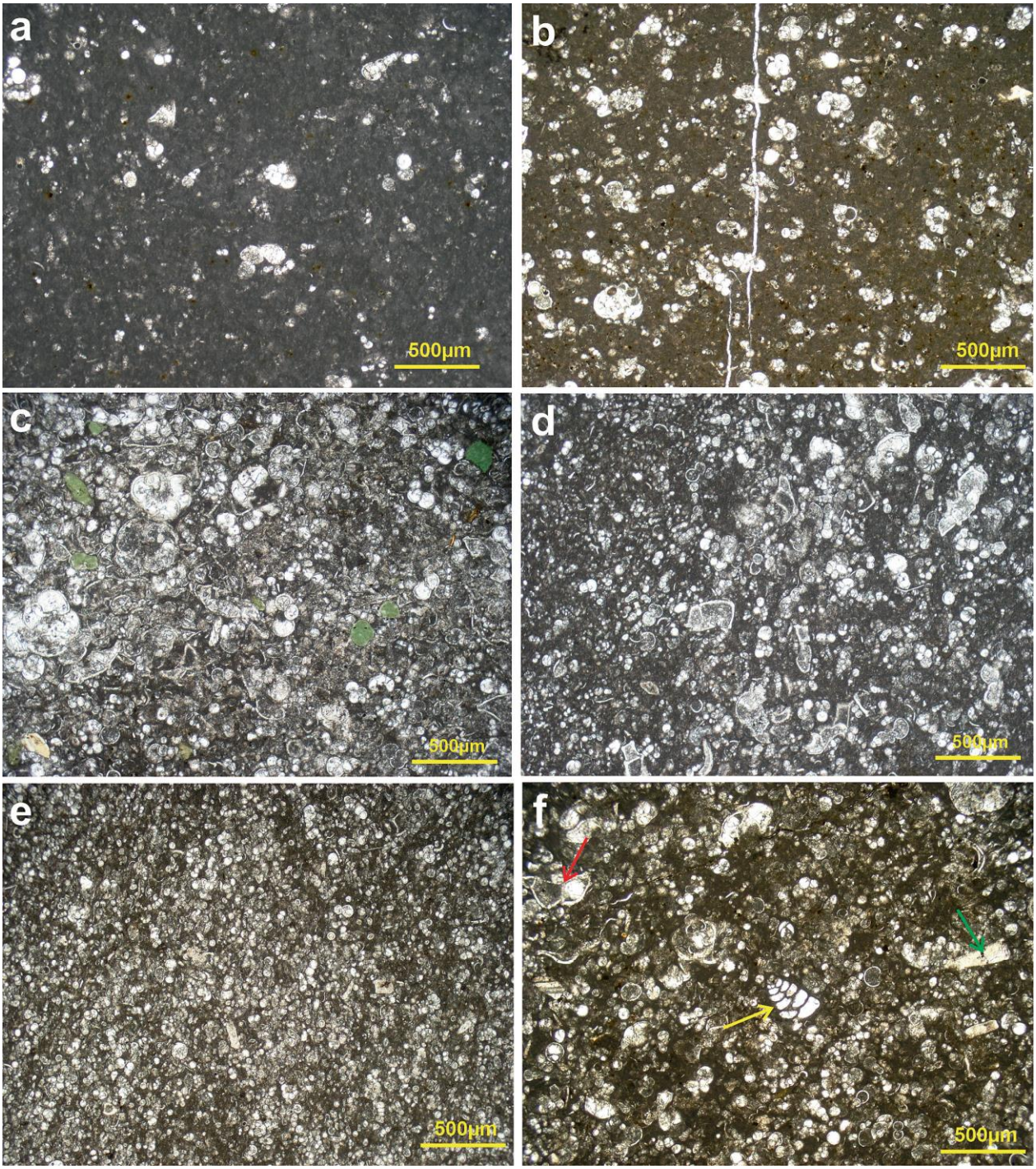

Fig. 14. Photomicrographs of microfacies of the Kometan Formation; a) planktonic foraminiferal mudstone (MFT1); b) *Heterohelix/Hedbergella* wackestone–packstone (MFT2); c) planktonic foraminiferal packstone with glauconite (MFT3); d) oligosteginid packstone (MFT4); e) planktonic foraminiferal wackestone-packstone with oligosteginids (MFT5); f) packstone with benthic foraminifers, echinoderms, and oligosteginids (MFT6), yellow arrow: benthic foraminifer (*Textularia*), green arrow: echinoderm fragments; red arrow: ostracod (Adopted from Hussein et al., 2024)..

4.3. Stylolitization and Pore Networking

4.3.1. Stylolitization

The examined thin sections revealed the presence of lime mudstone, wackestone, and packstone microfacies. They are divided into mud-supported (mudstone and wackestone) (microfacies A) and grain-supported (packstone) (microfacies B) microfacies (Fig. 8). The microfacies, A and B, with relatively uniform allochem composition but different texture, have been identified from petrographic analysis of thin sections from the Qamchuqa and Zewe sections. The microfacies A is a poorly sorted mudstone and wackestone with abundant planktonic foraminifers such as *Hedbergella*, *Heterohelix*, oligosteginid forams, sparse calcispheres, and sponge spicules. The matrix is composed of micrite with silt-sized, unidentifiable calcite fragments (Figs. 8B, 14a, b, e). The microfacies B which is a moderately sorted packstone with numerous planktonic foraminifers including *Globotruncana* and *Dicarinella*, less abundant *Hedbergella* and *Heterohelix*, scarce calcispheres, remnants of ostracod shells, and abundant grains of glauconite (Figs. 8C, 14c, d, f). Both microfacies indicate distal, basinal/pelagic environment, reworked, and sorted by current activity, as evidenced by their lime mudstone/wackestone/packstone texture and the dominance of planktonic foraminifers. The microfacies A volumetrically prevails.

Well-developed stylolites in microfacies A (Fig. 8B) show little weathering. The stylolites in pure carbonate beds are evenly distributed and parallel to the bedding plane. Stylolites are mostly suture and sharp-peak varieties, with many basic wave-like features. The structures' horizontal and vertical connections form intricate anastomosing networks. At junctions, stylolites create Y-type arrangements with occasional X-type configurations. As a result, the stylolite networks exhibit a branching morphology. The maximum thickness of the stylolite seams is 9.5 cm which is filled by clay and chert nodules. The stylolites of microfacies B (Fig. 8C) exhibit comparable outcrop characteristics and formation patterns to those of microfacies A but at a lower frequency and thinner stylolite seams (maximum = 5.4 cm).

The characterization of stylolite populations was initially conducted by measuring stylolite morphology at the outcrop scale, to define the statistical characteristics of stylolites within any facies analyzed. The morphological variables employed for the statistical characterization of stylolites encompassed vertical spacing, amplitude, wavelength, junction type, and junction intensity (Table 2).

The microfacies A has less vertical stylolite spacing than the microfacies B (Fig. 6 in Appendix 4). Specifically, nearly 50% of these spacings are in the range of 0.7 to 7.4 cm, while 40% are in the range of 9.4 to 77.6 cm. Most spacing sizes (60%) between stylolites in this microfacies range between 2.9 and 14.7 cm. The highest spacing frequency of microfacies A in total frequency numbers (683) is equal to 68 (mode = 2.7 cm, 10% of total). In comparison, 50% of the recorded measures in microfacies B show a progressive increase from 0.9 to 9.4 cm. Forty percent of the space ranges from 11.9 to 77.6 cm. Most of the spacings (60%) between stylolites in this microfacies vary from 3.7 to 19 cm. Ten percent of the total measurements are between 9.75 and 12.25 cm, resulting in a maximum frequency of 43 in total frequency numbers of 423 (mode = 3 cm, 6% of total).

The microfacies A exhibits the highest wavelength with a mode equal to 3.31 cm (73 measurements, 30 % of total) (Fig. 6 in Appendix 4). Fifty percent of the measured data ranges from 3.8 to 20 cm. The microfacies B has a shorter wavelength, with approximately half of the recorded values falling within the range of 3.1 to 16.6 cm. The mode is equal to 3.73 cm whereby 22% of the total wavelength (244).

Regarding amplitude, microfacies A shows the largest values (6.17 cm) and the higher mean value (0.66 cm) (Table. 2). The minimum value recorded in this microfacies is 0.2 cm. Contrary to microfacies A, the maximum amplitude recorded in microfacies B is 2.8 cm. The mode value of the amplitude for both microfacies is equal to 0.5 cm (35% of the total measured amplitude (359)) and 0.77 cm respectively (32% of the total measured amplitude (242)).

Table 2. Summary of the statistical properties (mean values) of stylolite networks for microfacies A (mud-supported) and B (grain-supported).

microfacies	Characteristic component	Spacing (cm)	Wavelength (cm)	Amplitude (cm)	Junction intensity (i/m)	Junction angle (°)
A	planktonic foraminiferal mudstone and wackestone	6.92	3.39	0.66	0.73	37.5
B	planktonic foraminiferal packstone with glauconite	8.91	3.09	0.65	0.69	27.5

According to the classification of Koehn et al. (2016), the suture and sharp-peak type, as well as the simple wave-like type stylolites predominate in the Kometan Formation (Fig. 7 in Appendix 4). Stylolites of the suture and sharp-peak type constitute about 55% of the stylolites identified in microfacies A and B. The simple wave-like type stylolites represent about 43% of the stylolites found in microfacies A. Simple wave-like stylolites are found in a slightly higher quantity in microfacies B in contrast to microfacies A, with percentages of 44%. Rectangular layer-type stylolites exhibit the lowest occurrence among various stylolite morphologies, with proportions ranging from 0.5 to 0.1% for microfacies A and B, respectively.

Statistical analysis of stylolite distribution (null hypothesis rejected at p-values < 0.05) indicates that the spacing, amplitude, and wavelength are most accurately represented by a log-normal distribution (Figs. 6, 8 in Appendix 4). The utilization of a log-normal distribution of the stylolite spacing resulted in chi-squared values ranging from 22 to 32, indicating a diminished level of goodness of fit. The KS-test findings with a p-value exceeding 0.05 suggest a stronger level of agreement between the fitted distribution and the stylolite dataset,

indicating a higher degree of goodness of fit. The p-values for both microfacies of spacing measurement for the log-normal distribution are found to be greater than 0.05 (Figs. 6, 8 in Appendix 4).

The records of stylolite wavelength exhibit chi-squared values ranging from 47 to 50 (Fig. 8B in Appendix 4). The chi-squared and p-value exhibit higher values in microfacies A when compared to microfacies B. The p-value associated with the log-normal distribution for microfacies B remains much more than 0.05, suggesting a strong level of agreement between the observed data and the theoretical distribution. The readings of stylolite amplitude exhibit a wider range of chi-squared values (Figs. 6, 8C in Appendix 4), ranging from 63 to 80. Additionally, the results of the KS test display a distribution of p-values above the significance threshold of 0.05, suggesting a satisfactory fit.

X- and Y-type connections make up 10.6% and 89.4% of microfacies A, respectively (Fig. 9A in Appendix 4). About 7% of microfacies B have X-type connections. The junction intensity of microfacies A and B is 0.72 and 0.69 i/m respectively (Fig. 9B in Appendix 4).

4.3.2. Pore Networking

Observations from optical microscopy and SEM of the thin sections (Figs. 15, 16) reveal the primary focus on the stylolite features and associated pore spaces. Stylolites create distinctive intergranular and intragranular pores within the limestone. Intergranular stylolites, visible in thin sections, exhibit linear dissolution seams along grain boundaries, while intragranular stylolites within individual calcite crystals are more prominently visualized in SEM images.

In thin sections embedded in blue resin (Fig. 15), the stylolite features are discernible under transmitted light, providing insights into their morphology in two dimensions. Intergranular pores manifest as dark linear features against the blue background, displaying irregularities and steps along the stylolite surfaces. Intragranular pores within calcite crystals appear as smaller, darker voids within the crystal lattice. In SEM images (Fig. 16), the morphology of these pores is further highlighted, offering a more detailed perspective. Intergranular pores show complex dissolving patterns with uneven surfaces, like irregular shapes and steps. Intragranular pores inside calcite crystals have detailed forms and can be oriented in different directions. Stylolites tend to form preferentially along specific bedding planes or within layers with variations in composition, leading to a non-uniform distribution of intergranular and intragranular pores. The concentration of pores is higher in regions where stylolites are more pronounced, a feature easily discernible in both thin sections (Fig. 15) and SEM images (Fig. 16).

Quantitative analysis involves measuring the pore spaces in both intergranular and intragranular regions. Image analysis software applied to thin sections (Fig. 15) and SEM (Fig. 16) images reveal an average porosity of approximately 8.3% and 12.8% respectively, indicating the percentage of void space within the stylolites. SEM images show an estimation of the size distribution of pores, with pores ranging from 0.008 to 2 millimeters (Fig. 16).

SEM analysis of carbonate rock with stylolites reveals a complex pore network, indicative of localized pressure dissolution (Fig. 16). Residual materials in these pores include illite, kaolinite, montmorillonite, and iron oxide. These secondary minerals suggest intricate alterations during diagenesis, with clay precipitation and potential involvement of oxidation and phosphate mineral formation. This SEM-based exploration offers a nuanced understanding of the dynamic interplay among dissolution, precipitation, and alteration within stylolite seams in carbonate rocks.

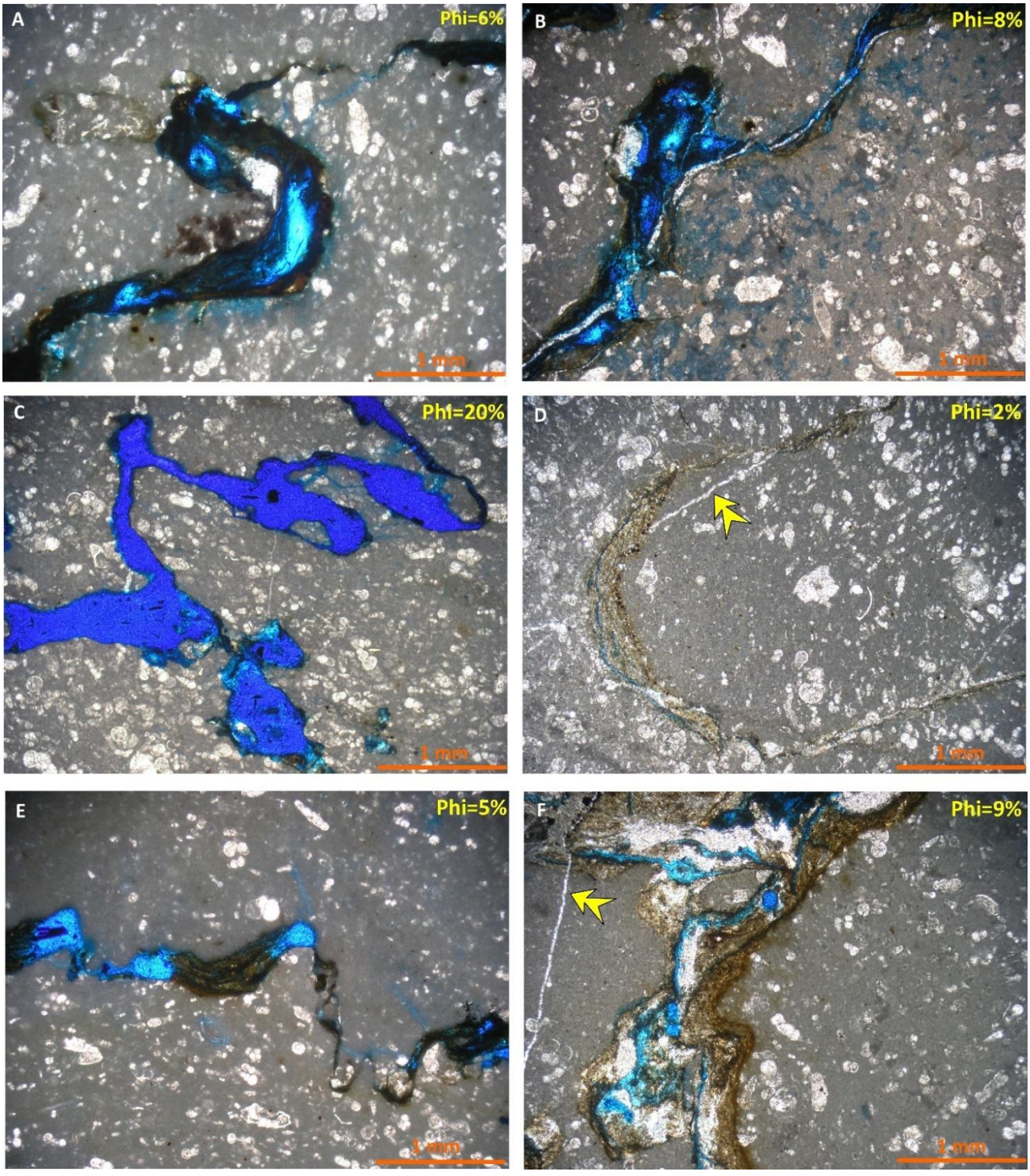

Fig. 15. Microphotograph of the Kometan Formation from the Zewe (A and B), Qamchuqa (C and D), and Dokan (E and F) sections showing pore shapes, sizes, distribution in the rock, relationship to stylolites, and quantification of porosity.

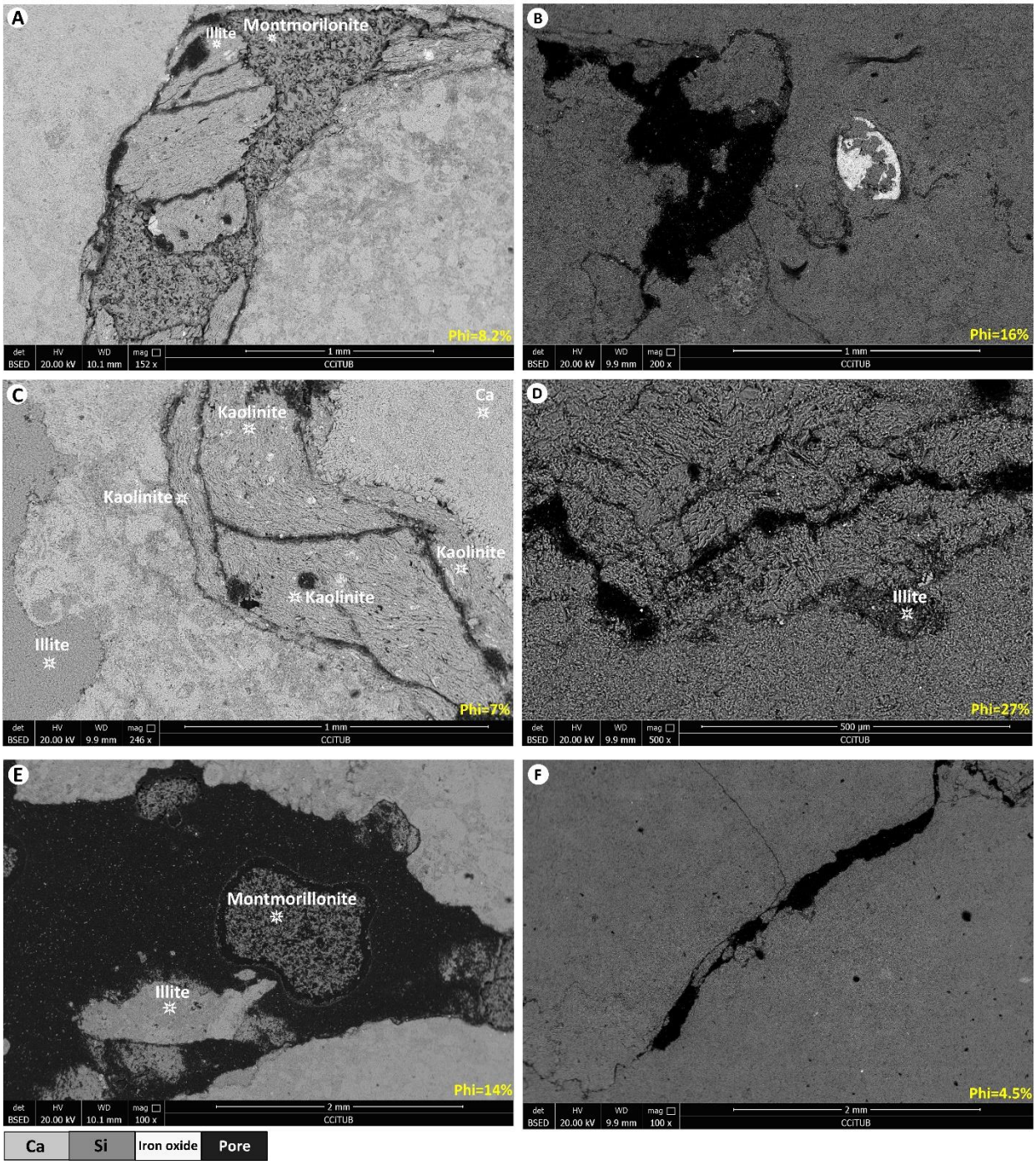

Fig. 16. Microphotograph of scanning electron microscope (SEM) of Qamchuqa (A, C, and E) and Zewe (B, D, and F) sections showing materials in and outside of stylolite seams, dissolved area, and amount of pore spaces (Phi).

The depth distribution of the element concentrations shows that most of the Si enrichment occurs in the Zewe section between 40 and 96 m (Fig. 17). The zone of silica enrichment can be correlated with the upper parts of the Qamchuqa section between 40 and 63 m above the section base, and partly with the top parts of the Dokan section between 45 and 65 m. These increased concentrations of Si partly coincide with increasing Al and decreasing Ca concentrations (Fig. 17). Across the dataset, instances can be found where an increase in Si

concentration corresponds with an increase in total length per cubic meter, suggesting a positive correlation. However, this positive correlation is not universally observed, as there are instances where total length decreases despite higher Si levels. Similarly, while certain cases show a positive correlation between Ca concentration and the total length, others exhibit a decrease in total length despite elevated Ca concentrations (Fig. 17). In addition, the highest amount of stylolite is at depths (9 to 60 m above the section base) where Ca is high, and Si is low.

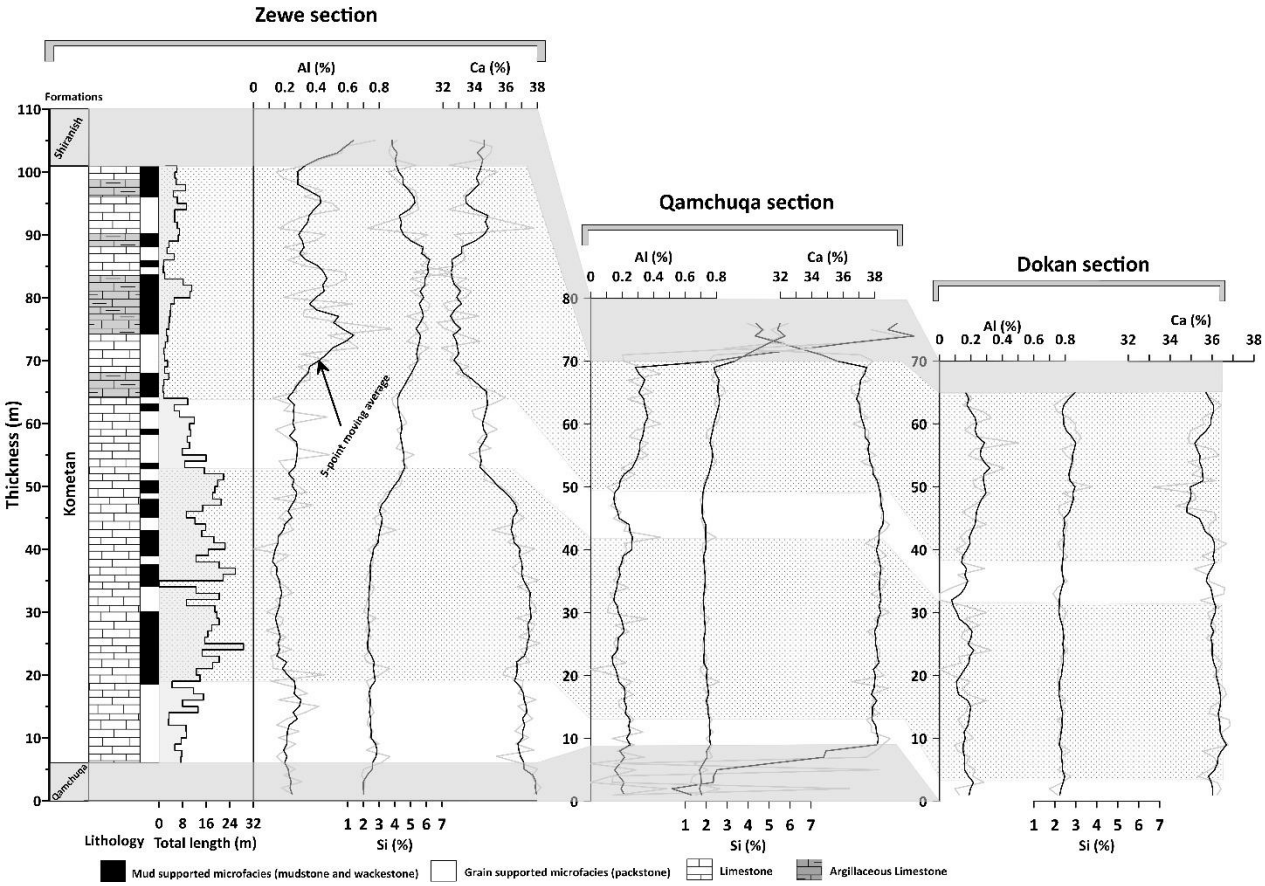

Fig. 17. The total length of stylolite along different microfacies with elemental geochemistry (Al, Ca, and Si) for the studied sections (the lower contact of Kometan Formation in the Dokan section is not exposed).

4.4. Porosity and Fractures

The Fig. 18 demonstrates the porosity structure between total porosity derived from neutron and density on the horizontal (X) axis and sonic porosity on the vertical (Y) axis in the studied wells. The plotted data are equally spread between primary and secondary porosity. There are many points plotted in the secondary zone, which can assume that good secondary porosity is anticipated from the Kometan Formation in the studied wells.

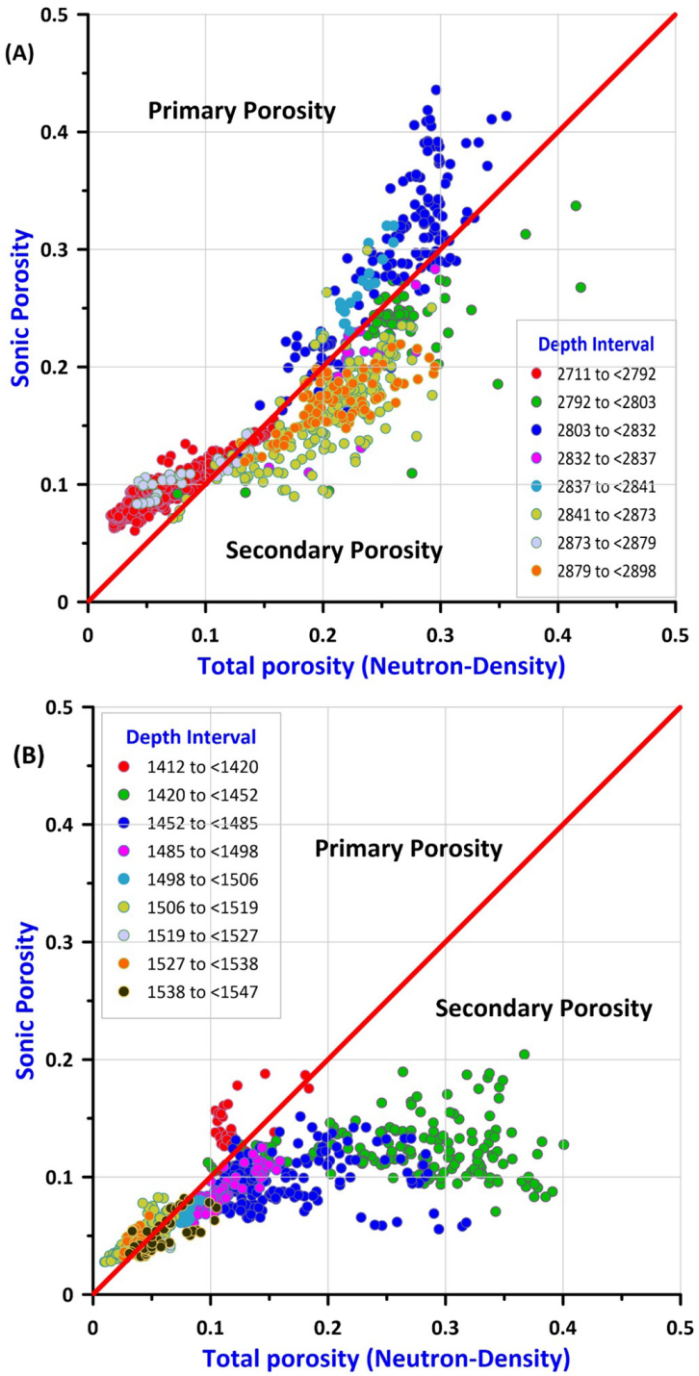

Fig. 18. Secondary porosity is indicated from porosity cross-plots, A in Kz40 and B in K216 wells (Adopted from Hussein, 2022).

The Secondary Porosity Index (SPI) for the inspected interval, reached a maximum value of 17%, and the average is 4% for Kz40 (Fig. 19A), the maximum value is 30%, and the average is 8% for K216 (Fig. 19B). The SPI results in Fig. 19A indicated that four zones are fractured at the specific depths 2792–2803, 2832–2837, 2841–2873, and 2879–2898. In addition, three high and three low fractured zones of K216 are presented in Fig. 19B, in which the high fractured zones are 1420–1452, 1452–1485, and 1485–1498. The porosity cross-plot and SPI methods (Figs. 18A, 19A) do not indicate a fracture zone in 2711–2792 intervals of Kz40, but the caliper log (Fig. 5A in Appendix 3) shows mud cake of this interval which can reveal the presence of permeable

zones and open fractures. Density and neutron log are more affected by mud cake than sonic log, so according to Eq. 1 in Appendix 3, the result of SPI in this interval would be negative (no fracture) (Fig. 19A), and on the cross plot the data plotted on the primary porosity area (Fig. 18A). All other intervals and fracture zones suggested from cross-plot and SPI (Figs. 18, 19) are supported by a caliper log which shows borehole enlargement (Fig. 5A, B in Appendix 3), which can be a good indicator for fractures of competent formation. The behavior of other logs (density, neutron, and sonic) can be applied qualitatively to support the evidence relevant to fractures. Spikes of the sonic log (Fig. 5 in Appendix 3), which indicate the presence of fractures. Spikes for the sonic log are primarily observed in enlarged intervals, but the density spikes also indicate fractures, observed at a depth of 1477, which is not indicated by the neutron log (Fig. 5B in Appendix 3). The enlargement also caused an abrupt increase and decrease in neutron and density log. It is due to the increasing mud thickness in enlarged intervals, and it has been considered during interpretation to identify fractures.

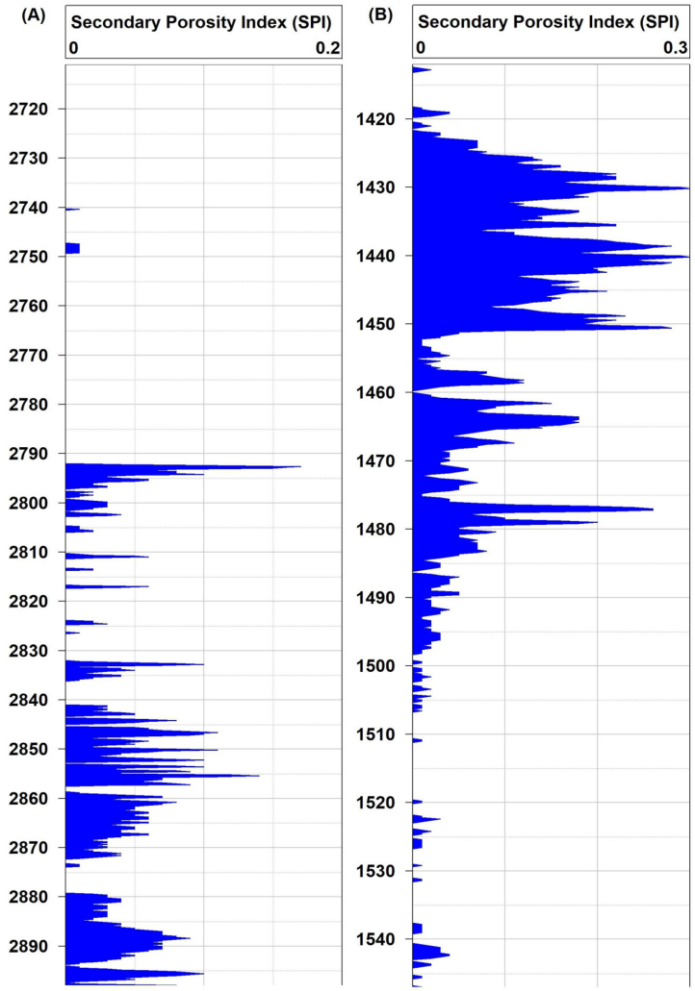

Fig. 19. Secondary Porosity Index (SPI) demonstrating the availability of fractures, A in Kz40 and B in K216 wells (Adopted from Hussein, 2022).

The available gamma-ray log (total gamma-ray) (Fig. 5 in Appendix 3) and spectral gamma-ray from available subsurface rock samples (Fig. 6 in Appendix 3) demonstrate an increment of uranium content against fractures. It can be noticed when the uranium precipitates in the fractures, which the fluid movement may endorse (Rider, 1999). Since the total gamma ray measures combined radioactive elements (uranium, thorium, and potassium)

and the spectral gamma ray log is not available, the shale content from the total gamma ray (Fig. 5 in Appendix 3) can be combined with that from the neutron-density log (Fig. 20) to validate either the gamma ray log reading is due to uranium or other elements (potassium and thorium). In addition, the available spectral gamma ray of rock samples also can be used (Fig. 6 in Appendix 3). The positive difference between gamma ray shale to neutron-density shale (Vsh gamma ray – Vsh neutron-density) may refer to uranium content and, consequently, fractures in the formation. Fig. 20 shows the calculated shale volume from different approaches (gamma ray and neutron-density log) and the differences between them to distinguish fracture zones. The technique was successfully applied especially in K216 (Fig. 20B) which is perfectly comparable with other approaches to fracture identification in this study (Figs. 18B, 19B). However. It couldn't depict the fractures in Kz40 in the 2793–2846 m interval due to the borehole effect which enlarged in this interval. Neutron and density logs are impaired in this interval because the thickness of drilling mud increases, and the tools stay away from the borehole wall. Fresh base mud was used to drill these wells (Kz40 and K216) which is a high hydrogen index, so the value of the neutron log in enlarged interval would be high. The density log value in this interval would be low because the depth of investigation of this log is shallow, so the porosity is overestimated. The computed gamma ray (CGR) also can be used decisively to identify uranium in the formation (Fig. 5 in Appendix 3). Since the total gamma ray (GR) combined uranium, thorium, and potassium and the computed gamma ray (CGR) combined only thorium and potassium, the difference between the total gamma ray to computed gamma ray is equal to uranium content (Fig. 5 in Appendix 3).

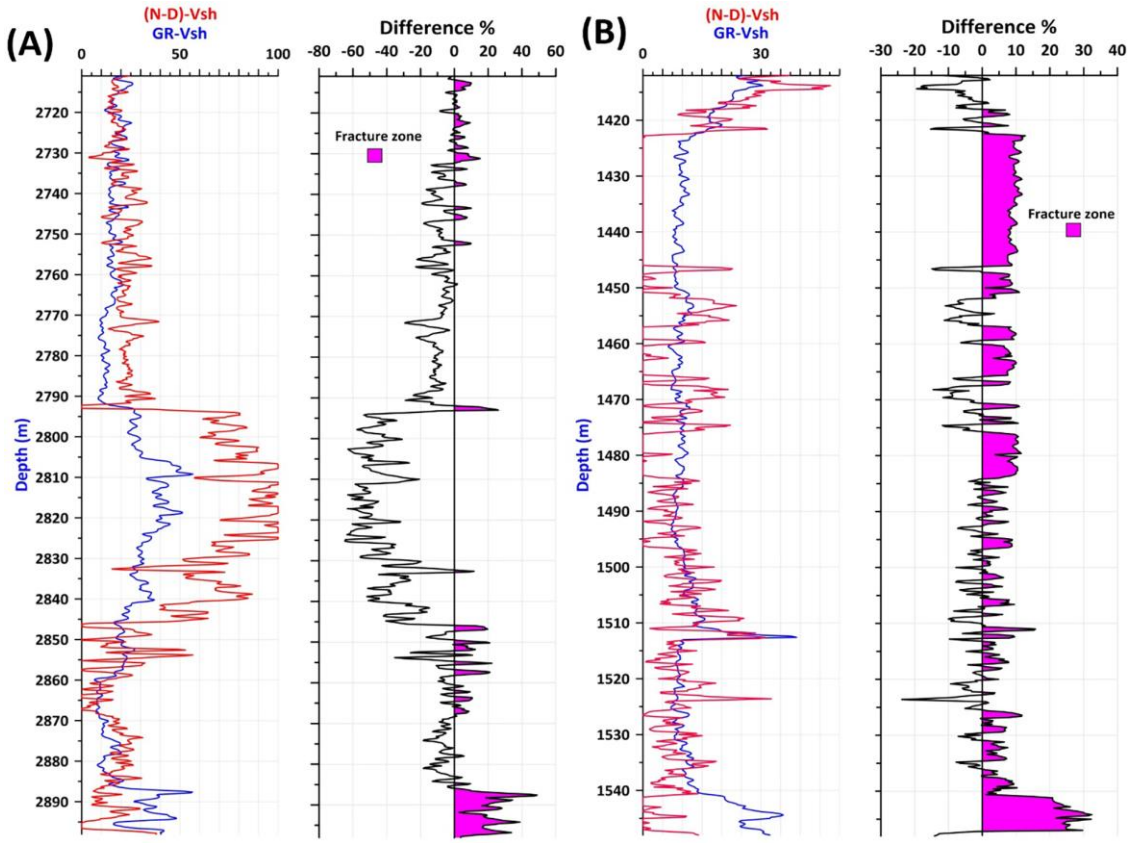

Fig. 20. Shale volume from neutron-density and gamma-ray, and their differences to demonstrate fracture zones in Kz40 (A) and in K216 (B) wells (Adopted from Hussein, 2022).

5. Discussion

5.1. Sequence Stratigraphy and Depositional Environment

5.1.1. Depositional Environment and Sedimentary Trends in Outcrop

The abundance of planktonic foraminifera such as *Hedbergella, Heterohelix, Globigerinoides, Rotallipora, Praeglobotruncana* and *Daicarinella* along with numerous species of *Oligostegina*, and the scarcity of other skeletal/nonskeletal grains suggest relatively a uniform, deep-water depositional environment for the outcrop sections. The similarity of pelagic facies is very high, and the exact separation of the mentioned facies with conventional petrographic methods is difficult. For this reason, the methodology of planktonic foraminifer morphotypes (Keller, 1993) was adopted in this study. The MFT1 microfacies is mainly composed of planktonic foraminifers of the morphotype 3 (Keller, 1993). The abundance of planktonic foraminifers, and abundant micrite indicate deposition in the calm, deep marine environment (Wilson, 1975; Bernaus et al., 2002). This microfacies corresponds to the RMF 5 of Flügel (2004), which belongs to the basinal environment. The MFT2 and MFT3 microfacies containing glauconite also correspond to RMF5 (Flügel, 2004) products of a basinal/pelagic environment, in which glauconite grains and pure carbonate lithology indicate low sedimentation rates, sub-oxic to reducing conditions, and a lack of detrital input (Amorosi, 1995). The grain-supported texture of the MFT4 and especially MFT5 microfacies along with the abundance of planktonic foraminifers, indicates low- to medium-energy water activity, presumably due to bottom currents, in relatively deep marine environments, well below the fair-weather wave base (Scholle and Ulmer-Scholle, 2003; Flügel, 2004). These microfacies are comparable with the open marine facies zones (FZ1, FZ2, FZ3) of Wilson (1975), and the RMF 5 of Flügel (2004), which can be attributed to the outer ramp environment. Due to the predominance of the oligosteginid planktonic foraminifers and other planktonic foraminifers, it can be said that the MFT1 to MFT5 microfacies represent pelagic open marine conditions (Keller et al., 2002). Echinoderm fragments are found in shallow-marine limestones as well as in deep-marine limestone (Flügel, 2004); in addition, ostracod and benthic foraminifera are observed in middle ramp environments (Flügel, 2004). The MFT6 microfacies containing more abundant echinoderms, ostracods, and benthic foraminifers are interpreted as corresponding to the RMF3 microfacies reflecting shallower, middle ramp environments (Flügel, 2004). The general lack of sliding, slumping and resedimented facies such as turbidites indicates predominant basin floor/deep shelf bottom with flat topography with predominant sedimentation from suspension settling, only partly affected by bottom currents. The studied outcrop part of the Kometan Formation was likely deposited in outer ramp rather than in a basin adjacent to carbonate shelf. This is supported by the absence of shelf-derived cortoids, oncoids, and aggregate grains, which are commonly found in age-equivalent carbonates in other parts of the Zagros basin (Ilam Formation; Adabi and Mehmandosti, 2008).

5.1.2. Facies Stacking Patterns

The microfacies stacking patterns are more difficult to interpret. The model of MFT1 to MFT6 microfacies likely represents a gradual transition from open marine/pelagic environments to middle ramp environments but the microfacies do not show distinct vertical trends (Fig. 9). Although, at a first glance, it seems that there

are no relationships between the carbonate geochemistry and microfacies stacking patterns (Fig. 9), the bivariate statistics of the microfacies vs. element geochemistry shows the opposite. When plotted against the microfacies type, the mean Al concentrations show statistically significant (R^2=0.58) decreasing trends from more distal (MFT1) to more proximal (MFT6) microfacies, whilst the Ca concentrations show an opposite, increasing trend (R2 = 0.69) (Fig. 21). This suggests that the slightly more proximal open shelf microfacies are purer carbonate whereas the more distal ones are more argillaceous, exactly the opposite as what we see in the more proximal parts of the basin.

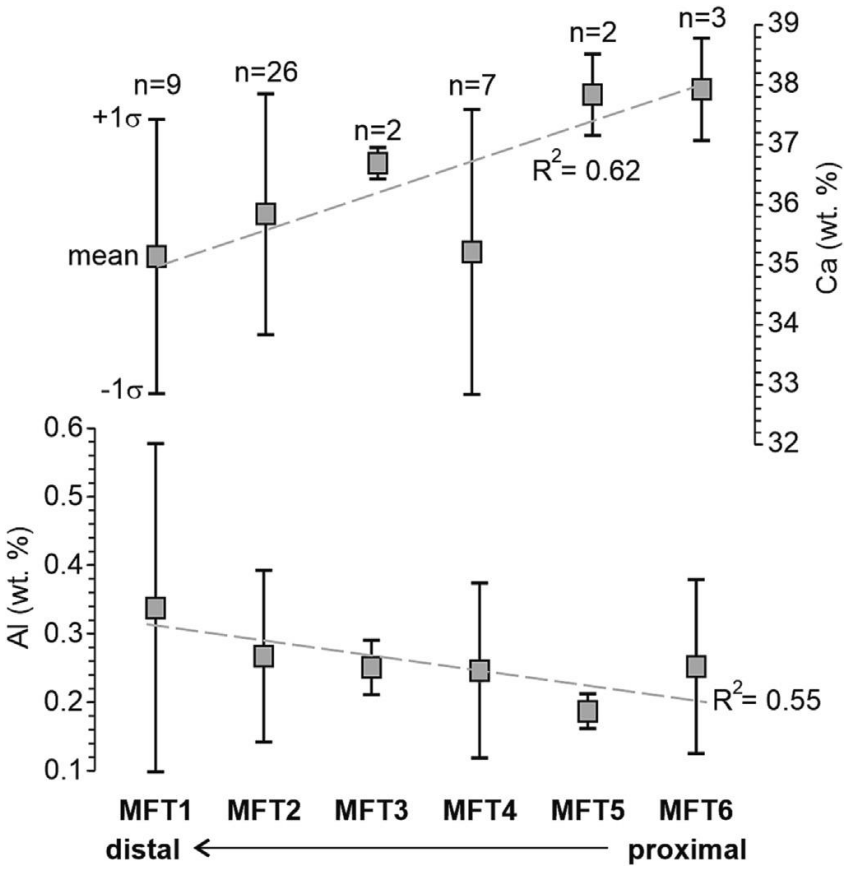

Fig. 21. Trends of decreasing mean Al concentrations and increasing mean Ca concentrations (mean value ± 1 standard deviation) in a microfacies series from MFT1 (open shelf/pelagic environment) to MFT6 (restricted shelf environment) in the Zewe and Qamchuqa sections (total 49 samples) (Adopted from Hussein et al., 2024).

The carbonate production on carbonate ramps can extend well into bathyal and abyssal depths (De Mol et al., 2002; Schlager, 2005). However, in mixed carbonate–siliciclastic depositional systems, the autochthonous carbonate facies (as well as their chemistry and well-log response) are mixed with allochthonous sediment from detrital sources generally located landwards from the carbonate factory. Bábek et al. (2013) described a carbonate ramp profile in Lower Carboniferous of the British Isles showing that from the mid ramp carbonate factory, the CaCO3 contents decrease, and the computed gamma-ray values, based on K and Th concentrations increase both up-dip towards more proximal lagoonal settings, and down-dip towards the deep basin. Trends of increasing gamma-ray values and magnetic susceptibility from a proximal carbonate factory to distal basinal settings have been described from the Devonian mixed carbonate–siliciclastic systems of the Prague Basin,

Czechia, and Eifel Mts., Germany (Mabille et al., 2008; Bábek et al., 2018). Such mixing of biogenic carbonate and detrital siliciclastic sediment, and proximal-to-distal spatial distribution are typical for a hybrid, mixed carbonate–siliciclastic depositional system (Sarg, 1988; Dolan, 1989; Page et al., 2003). Consistently with these examples, the concentrations of Al, K, and Rb (and possibly other elements bound to detrital phyllosilicates) tend to slowly increase basin wards in the distal, outcrop parts of the Kometan Formation (Figs. 21, 22).

5.1.3. Depositional Environment and Sedimentary Trends in Subsurface

The depositional environment of the subsurface parts of the Kometan Formation is more difficult to interpret owing to the lack of lithology and biofacies data. However, published foraminifer data suggest that the Kometan Formation in the Jambur oil field composed of argillaceous limestones and marls corresponds to oligosteginid biofacies deposited in a restricted shelf (Abawi and Mahmood, 2005; Jassim and Goff, 2006). The regional patterns suggest that the open shelf limestone facies of the Kometan Formation of the Zagros foreland basin pass laterally towards W and SW into bioturbated chalky limestone, shale and marly limestone of the Khasib Formation deposited in a restricted shelf, and further into lagoonal shale, and carbonate of the age-equivalent Tanuma Formation (Fig. 5) (Van Bellen et al., 1959; Buday, 1980; Dunnington, 2005; Al-Qayim, 2010). The Kometan Formation in the Jambur, Khabbaz, and Kirkuk oil fields is therefore considered a shallow-water equivalent of the studied outcrop sections.

The average concentrations of Al, Si, K, Ti, Fe, Rb, and Zr in the well samples are 1.8 times to 8.8 times higher than in the outcrops. These elements are associated with the detrital minerals identified from the XRD data: illite, illite/smectite, smectite, kaolinite, quartz, and K-feldspars. In contrast, the concentrations of Ca in subsurface samples are lower than in outcrops (Fig. S1 in Appendix 5; Table S1 in Appendix 6). The mineralogy and geochemistry of the subsurface samples support the interpretation of the Kometan as a mixed carbonate–siliciclastic ramp (Dolan, 1989; Bábek et al., 2013), in which the siliciclastic admixture decreases from more proximal (inner ramp) towards more distal parts (middle ramp). In the same direction, the Ca concentrations tend to increase to attain a maximum in the mid-ramp carbonate factory, and then slowly decrease with reduced carbonate production in the most distal basinal settings as indicated by the geochemical trends in the microfacies (Figs. 21, 22). According to the well-log (especially gamma-ray log) characteristics, the Kometan Formation is subdivided into three distinct intervals in subsurface, the lower clean interval (low GR), the middle shaly interval (high GR) and the upper clean interval (low GR) (Fig.13). We assume that the wedge of mixed carbonate–siliciclastic sediments represented by the middle shaly interval (Fig.13) represents a progradation of more proximal ramp deposits onto the open shelf/pelagic deposits. Thus the upwards increasing gamma-ray trends in the proximal settings (Khabbaz, Kirkuk, Jambur, Bai Hasan, and Barda Rash oil fields) represent progradation (regression) whereas the upwards decreasing ones represent retrogradation (transgression).

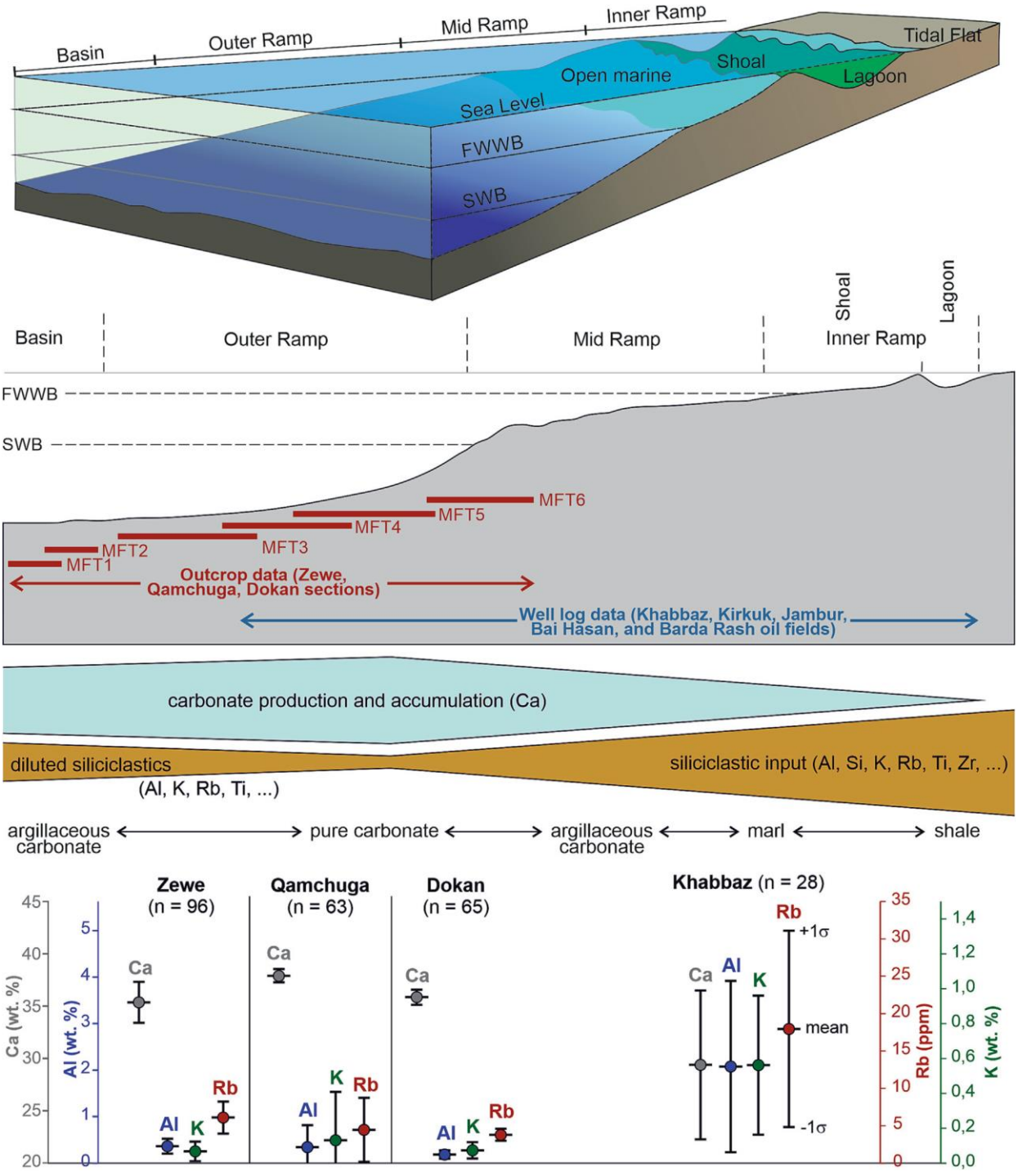

Fig. 22. Depositional model showing the interpreted mixed siliciclastic–carbonate ramp depositional environments of the Kometan Formation, distribution of selected elements (mean± standard deviation of Ca, Al, K, Rb) along the ramp profile, and a schematic distribution of biogenic carbonate (Ca) and detrital elements (Al, Si, K, Rb, Ti, and Zr) along the ramp profile (Adopted from Hussein et al., 2024).

Sequence-stratigraphic interpretation of the Kometan Formation is determined by three factors: (i) the predominance of deep-water sediments in outcrop, with low facies variability that predetermines well log and geochemical data as the only meaningful data source for stratigraphic correlation, (ii) the layer-cake stratigraphic geometry with invisible (or absent) clinoforms as inferred from such correlation, and (iii) lack of lithology data from shallow-water parts of the depositional system. Previous attempts to interpret the sequence stratigraphy of lithologically uniform deep-marine carbonates relied on the presence of specific lithological features such as hardgrounds and bioturbated horizons (Martire, 1992), element geochemistry and outcrop gamma-ray logs (Halgedahl et al., 2009; Ver Straeten et al., 2011; Bábek et al., 2016), and stable isotope geochemistry (Jarvis et al., 2001; Mabrouk et al., 2007). The gamma-ray data supported by facies can be extremely useful in sequence stratigraphic correlations. Using the sequence-stratigraphic model of Hunt and Tucker (1993), Bábek et al. (2013) interpreted the upwards-decreasing computed gamma-ray (CGR) trends, supported by facies analysis, as normal and forced regression during highstand (HST) and falling stage (FSST) systems tracts in the distal carbonate ramp. They conversely interpreted the upwards increasing CGR trends as transgression (TST), the peak CGR values as maximum flooding surfaces (mfs), and the rapid drops in CGR values as basal surfaces of forced regression (bsfr).

Our interpretation of the distal part of the Kometan Formation in outcrop follows similar principles: the peak Al and K concentrations are assumed to represent the overturn from transgression (T) to normal regression (R) i.e., the maximum flooding surface (mfs), whilst the end of regression and passage to transgression (maximum regression surface, mrs) are associated with Al and K concentration minima (Fig. 13 in Appendix 3). In contrast, the well log patterns in the more proximal, subsurface part of the Kometan Formation were primarily controlled by basinwards and landwards shifts of the proximal siliciclastic system onto the more distal ramp carbonates. Consequently, the peak gamma-ray values represent maximum regression surfaces whereas the gamma-ray minima represent maximum flooding surfaces. It is assumed here that the T–R cycles in outcrop were synchronous with the T–R cycles in subsurface. In this rather simplistic model, we use the maxima and minima on the curves as the only reliable correlation points. This approach is close to the "inductive" sequence-stratigraphic concept of Embry and Johannessen (2017) identifying the maximum flooding surfaces as separating underlying, upwards deepening strata from overlying, upwards shallowing ones (and vice versa for maximum regressive surfaces). Using just two easily identifiable surfaces, the T–R sequences of Embry and Johannessen (1993, 2017) consist of just two systems tracts, transgressive (TST) and regressive (RST). Under the conditions defined at the beginning of this section, this model is applicable. The Kometan Formation consists of four T–R sequences, ranging in thickness from ~10 to ~45 m.

5.2. Remarks on Reservoir Quality

The relationship between the wireline log characteristics reveals that the matrix porosity (sonic porosity) decreases with depth, from about 10–20 % at the top to about 5 % at the bottom of the Kometan Formation (Fig. 13A in Appendix 2). However, the reservoir quality is largely given by the fracture porosity, which can be inferred from the residues between the neutron-density (N-D) porosity and sonic porosity. The N-D

porosities reach up to 40 % in the upper interval of the Kometan Formation whilst they drop down to about 5 % in its lower interval (Fig. 13 in Appendix 2). There are four depth segments in the upper interval, in which the N-D minus sonic porosity residues increase. All of them coincide with the passages from transgressive to regressive systems tracts (maximum flooding surface) which corresponds to the pure carbonates. In general, the Zagros foreland oil reservoirs in northern Iraq, including the Kirkuk embayment, the Avanah and Baba Domes, the Bai Hassan field as well as the gas reservoirs in the Jambur oil field all produce from fractured reservoirs of the Kometan Formation (Aqrawi, 1996). Light oils (41 API) are produced from the Kometan Formation, a fractured reservoir in the Taq oil field with estimated recoverable reserves of 700–750 million barrels. When the field is fully established, it is anticipated that it will yield 200,000–250,000 barrels per day (Rashid et al., 2015a, 2015b). Fractures that increase the formation's porosity and permeability are principally responsible for controlling the productivity of carbonate rock in the Kometan Formation (Rashid et al., 2015a, 2015b). In addition, the fractured reservoir quality inferred from well-log data has been supported by rock samples from outcrops (Hussein, 2022). Rheology of the carbonate likely changes with shale content, resulting in higher susceptibility of the pure carbonates to brittle deformation and development of fracture systems, compared to argillaceous carbonates and marls. It is assumed that in mixed carbonate–siliciclastic ramps, the sea-level driven transgressive–regressive, upwards cleaning and dirtying sequences control the post-depositional development of fracture systems and affect the reservoir quality.

In a subsurface geological context, the interplay between shale content and porosity is crucial for understanding the porosity variations at different depths. Fig. 23 illustrates a clear relationship between increasing shale content and decreasing density porosity, especially in crossovers (cyan-filled color) within specific depth intervals. In the Kz-29 well (Fig. 23A), at 2819 meters depth, with a relatively low shale content of 9.8%, the density porosity is 8%. As we descend to 2830 meters, encountering a moderate shale content of 11%, the density porosity decreases to 3.5%. Further, at a depth of 2870 meters, where shale content is higher at 14%, the density porosity diminishes to 2.3%. In the shallower depth of Kz-40 (2711-2747m) (Fig. 23B), characterized by decreasing shale content (e.g., from 20-13%), density porosity values tend to be higher, ranging from 2.4% to 12%. This suggests a more porous and less dense subsurface in these intervals. However, as we progress to greater depths (2762m) where shale content becomes more pronounced (e.g., 13%-20%), there is a consistent decline in density porosity, dropping to the range of 12% to 3%. In the K-216 well (Fig 23C), the range of density porosity spans from a minimum of 0.01% to a maximum of 53%, indicating considerable heterogeneity in reservoir quality. The shale content ranges from 6.5% to 39%. This illustrates a discernible inverse relationship, where an increase in shale content correlates with a reduction in density porosity.

One of the most notable characteristics observed in this study pertains to the capacity of stylolites to improve the porosity and permeability of the formation under investigation. The dissolution of minerals along stylolite planes results in the formation of complex networks of channels and conduits (Figs.15, and 16). These pathways are crucial for the migration of fluids, as they offer paths through rock matrix that would otherwise be impermeable. Within the field of hydrocarbon exploration, stylolites are recognized as significant secondary

migratory paths (Braithwaite, 1988; Peacock et al., 2017; Koehn et al., 2012). They facilitate the transportation of oil and gas, ultimately resulting in their deposition and concentration within reservoir formations. The natural improvement of permeability can have a significant impact on the productivity and economic feasibility of petroleum reservoirs.

In their studies, Koehn et al. (2016) and Humphrey et al. (2019) established a correlation between the morphology of stylolites and their potential effectiveness as fluid flow barriers. They found that stylolites with low roughness tend to exhibit greater continuity, making them more effective barriers compared to stylolites with irregular (rough) profiles. The fluid flow behavior of the material is also influenced by the nature of its filling material (Fig. 16). Stylolites can serve as effective barriers when they are filled with impermeable substances such as clay, organic matter, and/or oxides (Figs. 15, 16) (Mehrabi et al., 2016; Vandeginste and John, 2013). Furthermore, according to Heap et al. (2014), the presence of a stylolite can be deemed effective as a barrier if the material filling it spreads evenly and continuously throughout the seam, and if the mix of insoluble materials is consistent throughout.

5.3. Stylolite and Microfacies Correlation

To effectively analyze the relationship between stylolite types and microfacies, it is crucial to initially define the microfacies criteria that facilitate the assessment of certain lithological and morphological characteristics. These variables have the potential to be integrated with stylolite shape characteristics to construct a matrix of correlations (Fig. 24). This matrix finds potential connections and impacts of lithology and elemental geochemistry on stylolite network geometries. The rock's complexity level, as shown by variations in composition, grain size, and grain size distribution, exhibits clear associations with important stylolite features. In the context of sedimentary facies, it has been shown that mud-supported microfacies with heterogeneous grain sizes exhibit stylolite networks characterized by high amplitudes and wavelengths, accompanied by relatively small vertical spacings. Conversely, microfacies characterized by moderately sorted grain support tend to create stylolites with lower amplitudes and wavelengths and greater vertical spacings.

5.3.1. Mud as Opposed to Grain-Dominated Microfacies.

The identification of micrite and clay minerals has frequently been recognized as a significant factor contributing to heterogeneity and subsequent stylolite roughening (Wanless, 1979; Koehn et al., 2012; Paganoni et al., 2016; Morad et al., 2018). The increased surface area of micrite contributes to the enhanced solubility of the rock. The present work demonstrates that there is a significant correlation between the stylolite amplitudes, which refer to the degree of roughening, and the quantity of micrite. These associations result in greater amplitudes observed in mud-supported facies. Stylolites with greater amplitude and wavelength are found to promote a higher number of junctions, as evidenced by favorable associations with X- and Y-type crossings, as well as reduced vertical separation. It is noteworthy that the correlation matrix reveals contrasting morphological patterns in the development of stylolites within grain-supported facies (Fig. 24). The presence of clay minerals contributes to variability and rise in stylolite amplitude, hence facilitating the initiation and intersection of stylolites (Wanless, 1979; Koehn et al., 2012; Paganoni et al., 2016; Morad et al., 2018). The

process is additionally helped by the feedback loop involving clay minerals and pressure solution, as suggested by Aharonov and Katsman (2009). In this mechanism, the buildup of clay minerals promotes dissolving, leading to the formation of stylolites, which in turn accumulate more clay minerals (Fig. 16).

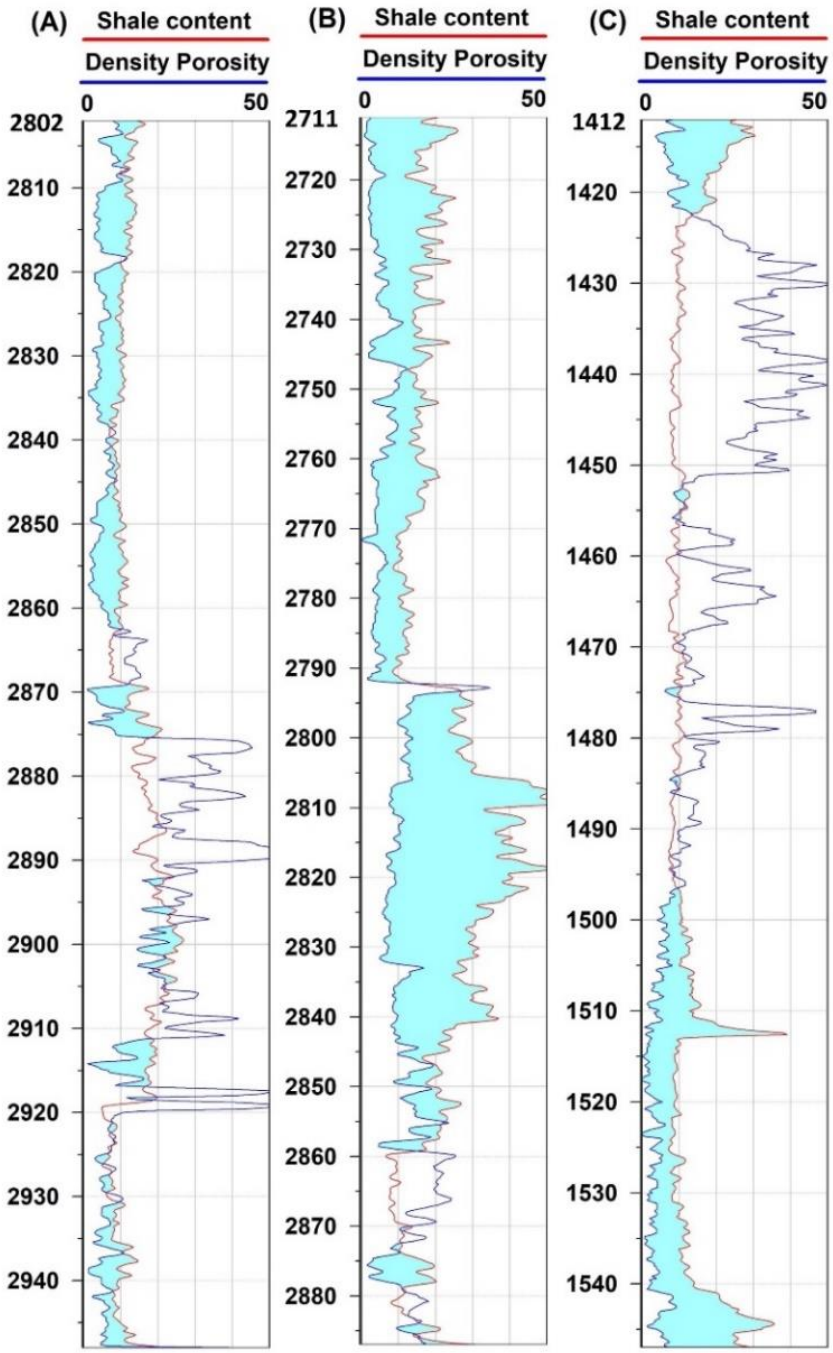

Fig. 23. Density porosity and shale content relationship in percent for wells Kz-29 (A), Kz-40 (B), and K-216 (C). Note the crossover sections (cyan colour) in which the shale contents impact the density porosity (Adopted from Hussein et al., 2024).

5.3.2. Composition and Grain Size Distribution

In addition to the occurrence of micrite and clay minerals, many lithological factors have been seen to contribute to heterogeneity in carbonate host rocks, hence influencing the formation and type of stylolites. The presence of bimodal particle size distribution results in an enhanced suturing process, mostly attributed to

differences in dissolution and resistance to pressure solution (Railsback, 1993; Andrews and Railsback, 1997; Koehn et al., 2012). Stylolites tend to form preferentially in carbonates with a fine-grained texture (Rustichelli et al., 2012). This research has found a negative correlation between grain size and stylolite amplitudes (Fig. 24).

In stylolitized rock, variations in grain size are directly linked to the sorting level. A combination of significant grain size variation and poor sorting leads to increased heterogeneity and, as a result, greater roughness. (Koehn et al., 2012). There is a positive correlation between poorly sorted facies and larger amplitude stylolites (Fig. 24). Stylolites with larger amplitudes tend to exhibit smaller vertical spacings and a greater number of intersections. The occurrence of these situations is influenced by the changes in solubility resulting from variances in particle size and spread. These dissimilarities lead to particle pinning and disparities in solubility rates, which in turn produce favorable situations for the development and roughening of stylolites (Aharonov and Katsman, 2009; Koehn et al., 2016). The process of connection can be facilitated by the phenomenon of stylolite cannibalism', which is induced by enhanced roughening and disintegration resulting from poor sorting, as proposed by Ben-Itzhak et al. (2014). The shape of stylolites is also influenced by the type of particles present in the rock. This is because the composition of these particles results in changes in dissolution, which in turn promotes the formation and binding of stylolites. According to Wanless (1979), magnesium (Mg) is recognized as an impurity that induces fluctuations in dissolution within the rock. Tucker and Wright (1991) demonstrate that the distribution of low- and high-Mg calcite may affect subsequent carbonate dissolution. As an illustration, it is observed that foraminifera generally have a magnesium (Mg) content of up to 25%, whereas other fossils, such as bivalves, display more restricted ranges of 0-5%. The presence of either high or low magnesium (Mg) calcite and dolomite can contribute to variations in dissolution and pressure solution. Other factors that can influence dissolution include the calcite/aragonite content in bioclasts, the presence of non-soluble grains and silica, as well as the dissolution rate of mud (Dewers and Ortleva, 1994) (Fig. 16).

Si and Ca exhibit complex relationships with stylolite length. While Si concentrations vary widely, no clear linear trend with total length emerges (Fig. 17). This scattered distribution shows that the influence of Si is complex and most likely controlled by other factors. Higher Si may sometimes correlate with greater mass loss, but not consistently. Similarly, Ca, despite some concentration variation, lacks a straightforward linear relationship with stylolite length (Fig. 17). Higher Ca values may generally coincide with increased mass loss, but not universally. Figure 17 clearly shows that pure carbonates (high Ca) have a higher total length. However, Ca is affected by the combined effects of Si and Al and other elements. These multifaceted responses emphasize the need for a more comprehensive understanding of factors influencing mass loss. Notably, Ca and Si show opposite correlations with stylolite length (Figs. 17, 24).

According to Wanless (1979), the primary determinant of the jagged or undulose waveform (identical to suture and sharp-peak and wave-like types) of stylolites is the particle size. This waveform is like the suture and sharp-peak, and simple wave-like types found in the stylolite categorization framework. Wanless (1979) argued that undulose waveforms are more likely to form in lithologies with large particles. In their study,

Humphrey et al. (2020) documented a negative association between the prevalence of suture and sharp-peak stylolites, as well as wave-like stylolites, in larger facies characterized by a particle size greater than 2 mm. Notably, the wave-like stylolites were found to predominantly form in smaller facies. The present study examines the link between the abundance of suture and sharp-peak and wave-like type stylolites in mud-supported and grain-supported microfacies, revealing a nearly identical relationship (Fig.7 in Appendix 4).

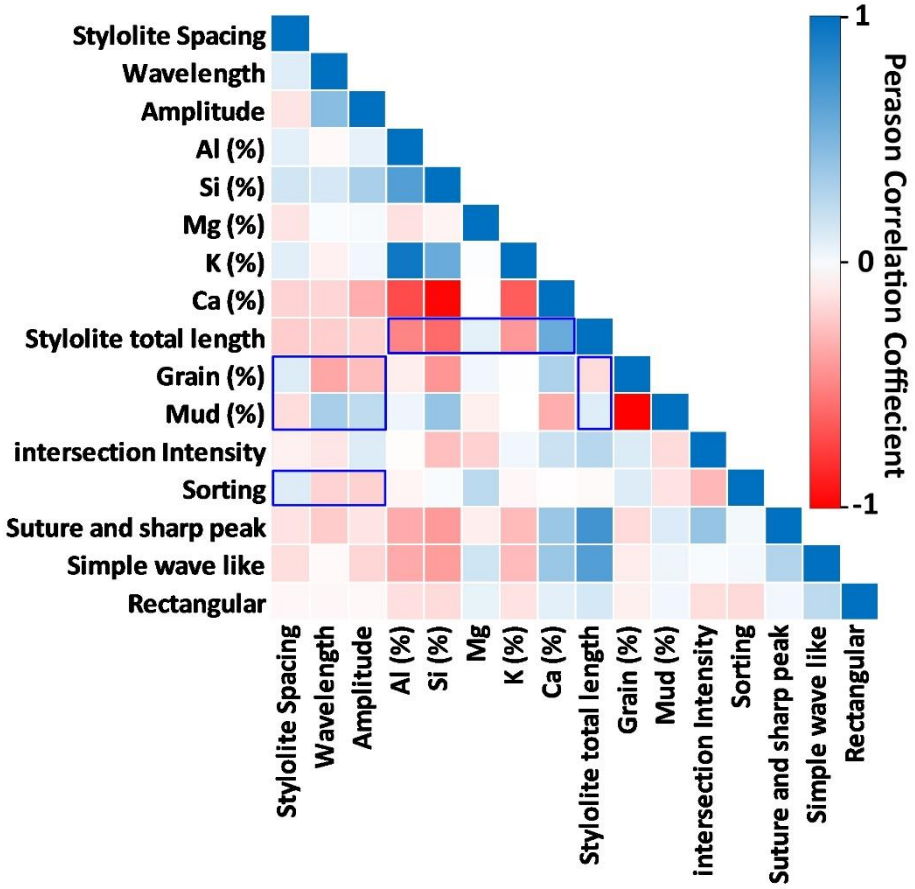

Fig. 24. Evaluation of the Pearson correlation coefficient between studied stylolite morphology and geological factors using a correlation matrix. Blue boxes show the most important connections.

6. Conclusions

The multivariate regression of well log data with fuzzy logic indicates that mixed carbonate-siliciclastic lithologies in reservoir rocks can be identified and quantified from the neutron, sonic, and density logs without a rock sample. All studied wells can employ the model created using the applied approach with the greater coefficient of determination. Calculations from wire-line logging data validated the Kometan Formation's lithologic sequence of limestone, argillaceous limestone, marls, and marly limestone.

In outcrop, the Kometan Formation comprises mudstones to packstones hosting planktonic and benthic foraminifers, divided into six microfacies (MF1 to MF6) found in basinal, outer ramp, and middle ramp environments. Subsurface drilling in northern Iraq reveals limestones, marls, and shales with benthic foraminifers, believed to be inner ramp to middle ramp equivalents of outcropped ramp carbonates. Geochemical logs and gamma-ray patterns exhibit contrasting trends across the formation's lower, middle, and

upper parts. Subsurface gamma-ray maxima in the inner ramp, notably in the middle Kometan Formation, signal maximum regression surfaces (mrs), while gamma-ray minima indicate maximum flooding surfaces (mfs). Conversely, in outcropped outer to middle ramp sections, Al and K log minima in the middle Kometan signify mrs, while Al and K minima denote mfs. These opposing log trends are attributed to shifts in the middle ramp carbonate factory during transgressions and regressions within the mixed carbonate–siliciclastic ramp system.

The Kometan Formation serves as a fractured reservoir, with notable variations in neutron-density and sonic porosity logs suggesting superior reservoir quality in pure carbonates. It's postulated that transgressive–regressive sequences, along with sedimentary cleaning and dirtying, may influence fracture system development and reservoir quality in mixed carbonate–siliciclastic ramps.

High-amplitude stylolites, characterized by tight spacing and extensive connections, are shaped primarily by particle size, grain composition, and sorting levels. They're prevalent in mud-supported facies like mudstone and wackestone. In contrast, less connected stylolites with greater spacing and uniform amplitude are common in grain-supported facies such as packstone. The degree of connection among stylolites, crucial for fluid flow, is dictated by host microfacies attributes. Stylolites significantly enhance rock porosity and permeability, forming intricate networks of channels and conduits through mineral dissolution.

References:

Abawi, T., Mahmood, S., 2005. Biostratigraphy of the Kometan and Gulneri Formations (Upper Cretaceous) in Jambur well No. 46, Northern Iraq. Iraqi Journal of Earth Science 5, 1–8.

Abdelmaksoud, A. and Radwan, A.A., 2022. Integrating 3D seismic interpretation, well log analysis and static modelling for characterizing the Late Miocene reservoir, Ngatoro area, New Zealand. *Geomechanics and Geophysics for Geo-Energy and Geo-Resources*, *8*(2), p.63.

Abdullah, E.A., Abdelmaksoud, A. and Hassan, M.A., 2022. Application of 3D static modelling in reservoir characterization: a case study from the qishn Formation in sharyoof oil field, masila basin, Yemen. *Acta Geologica Sinica-English Edition*, *96*(1), pp.348-368.

Adabi, M.H. and Mehmandosti, E.A., 2008. Microfacies and geochemistry of the Ilam Formation in the Tang-E Rashid area, Izeh, SW Iran. *Journal of Asian Earth Sciences*, *33*(3-4), pp.267-277.

Aharonov, E. and Katsman, R., 2009. Interaction between pressure solution and clays in stylolite development: Insights from modeling. *American Journal of Science*, *309*(7), pp.607-632.

Al-Barzinjy, S.T., 2008. Origin of chert nodules in Kometan Formation from Dokan area, Northeast Iraq. *Iraqi Bulletin of Geology and Mining*, *4*(1), pp.95-104.

Al-Dujaili, A.N., Shabani, M. and AL-Jawad, M.S., 2021. Characterization of flow units, rock and pore types for Mishrif Reservoir in West Qurna oilfield, Southern Iraq by using lithofacies data. *Journal of Petroleum Exploration and Production Technology*, *11*, pp.4005-4018.

Al-Qayim, B., 2010. Sequence stratigraphy and reservoir characteristics of the turonian-coniacian Khasib Formation in central Iraq. *Journal of Petroleum Geology*, *33*(4), pp.387-403.

Alsharhan, A.S. and Sadd, J.L., 2000. Stylolites in Lower Cretaceous carbonate reservoirs, UAE.

Amorosi, A., 1995. Glaucony and sequence stratigraphy; a conceptual framework of distribution in siliciclastic sequences. *Journal of sedimentary research*, *65*(4b), pp.419-425.

Andrews, L.M. and Railsback, L.B., 1997. Controls on stylolite development: morphologic, lithologic, and temporal evidence from bedding-parallel and transverse stylolites from the US Appalachians. *The Journal of Geology*, *105*(1), pp.59-73.

Aqrawi, A.A., 1996. Carbonate-siliciclastic sediments of the upper cretaceous (Khasib, Tanuma and Sa'di formations) of the Mesopotamian basin. *Marine and Petroleum Geology*, *13*(7), pp.781-790.

Aqrawi, A.A., 1996. Carbonate-siliciclastic sediments of the upper cretaceous (Khasib, Tanuma and Sa'di formations) of the Mesopotamian basin. *Marine and Petroleum Geology*, *13*(7), pp.781-790.

Aqrawi, A.A., Goff, J.C., Horbury, A.D. and Sadooni, F.N., 2010. *The petroleum geology of Iraq*. Scientific press.

Asquith, G.B., Krygowski, D. and Gibson, C.R., 2004. *Basic well log analysis* (Vol. 16, pp. 305-371). Tulsa: American Association of Petroleum Geologists.

Bábek, O., Faměra, M., Šimíček, D., Weinerová, H., Hladil, J. and Kalvoda, J., 2018. Sea-level changes vs. organic productivity as controls on Early and Middle Devonian bioevents: Facies-and gamma-ray based sequence-stratigraphic correlation of the Prague Basin, Czech Republic. *Global and Planetary Change*, *160*, pp.75-95.

Bábek, O., Kalvoda, J., Cossey, P., Šimíček, D., Devuyst, F.X. and Hargreaves, S., 2013. Facies and petrophysical signature of the Tournaisian/Viséan (Lower Carboniferous) sea-level cycle in carbonate ramp to basinal settings of the Wales-Brabant massif, British Isles. *Sedimentary Geology*, *284*, pp.197-213.

Bábek, O., Kumpan, T., Kalvoda, J. and Grygar, T.M., 2016. Devonian/Carboniferous boundary glacioeustatic fluctuations in a platform-to-basin direction: A geochemical approach of sequence stratigraphy in pelagic settings. *Sedimentary geology*, *337*, pp.81-99.

Bábek, O., Vodrážková, S., Kumpan, T., Kalvoda, J., Holá, M. and Ackerman, L., 2021. Geochemical record of the subsurface redox gradient in marine red beds: A case study from the Devonian Prague Basin, Czechia. *Sedimentology, 68*(7), pp.3523-3548.

Balaky, S.M., Asaad, I.S. and Al-Juboury, A.I., 2016. Facies analysis and sequence stratigraphy of Kometan Formation (Upper Cretaceous) in the imbricated zone, northeastern Iraq. *Arabian Journal of Geosciences, 9,* pp.1-17.

Baldwin, J.L., Otte, D.N. and Wheatley, C.L., 1989, October. Computer emulation of human mental processes: Application of neural network simulators to problems in well log interpretation. In *SPE Annual Technical Conference and Exhibition?* (pp. SPE-19619). SPE.

Barnett, A.J., Wright, V.P., Chandra, V.S. and Jain, V., 2018. Distinguishing between eogenetic, unconformity-related and mesogenetic dissolution: a case study from the Panna and Mukta fields, offshore Mumbai, India. *Geological Society, London, Special Publications*, *435*(1), pp.67-84.

Baron, M. and Parnell, J., 2007. Relationships between stylolites and cementation in sandstone reservoirs: Examples from the North Sea, UK and East Greenland. *Sedimentary Geology, 194*(1-2), pp.17-35.

Bathurst, R.G., Einsele, G., Ricken, W. and Seilacher, A., 1991. Pressure-dissolution and limestone bedding: the influence of stratified cementation. *Cycles and events in stratigraphy*, pp.450-463.

Baud, P., Rolland, A., Heap, M., Xu, T., Nicolé, M., Ferrand, T., Reuschlé, T., Toussaint, R. and Conil, N., 2016. Impact of stylolites on the mechanical strength of limestone. Tectonophysics, 690, pp.4-20.

Bauerle, G., Bornemann, O., Mauthe, F. and Michalzik, D., 2000. Origin of stylolites in Upper Permian Zechstein anhydrite (Gorleben salt dome, Germany). *Journal of Sedimentary Research, 70*(3), pp.726-737.

Ben-Itzhak, L.L., Aharonov, E., Karcz, Z., Kaduri, M. and Toussaint, R., 2014. Sedimentary stylolite networks and connectivity in limestone: Large-scale field observations and implications for structure evolution. *Journal of Structural Geology, 63*, pp.106-123.

Bergen, D.V. and Carozzi, A.V., 1990. Experimentally-simulated stylolitic porosity in carbonate rocks. *Journal of Petroleum Geology, 13*(2), pp.179-192.

Bernaus, J.M., Arnaud-Vanneau, A. and Caus, E., 2002. Stratigraphic distribution of Valanginian–Early Aptian shallow-water benthic foraminifera and algae, and depositional sequences of a carbonate platform in a tectonically-controlled basin: the Organyà Basin, Pyrenees, Spain. *Cretaceous Research, 23*(1), pp.25-36.

Braithwaite, C.J.R., 1989. Stylolites as open fluid conduits. *Marine and Petroleum Geology, 6*(1), pp.93-96.

Bruna, P.O., Lavenu, A.P., Matonti, C. and Bertotti, G., 2019. Are stylolites fluid-flow efficient features? *Journal of Structural Geology, 125*, pp.270-277.

Buday, T., 1980. *The regional geology of Iraq: stratigraphy and paleogeography* (Vol. 1). State Organization for Minerals, Directorate General for Geological Survey and Mineral Investigations.

Burgess, C.J. and Peter, C.K., 1985, March. Formation, distribution, and prediction of stylolites as permeability barriers in the Thamama Group, Abu Dhabi. In *SPE Middle East Oil and Gas Show and Conference* (pp. SPE-13698). SPE.

Carozzi, A.V. and Bergen, D.V., 1987. Stylolitic porosity in carbonates: a critical factor for deep hydrocarbon production. *Journal of Petroleum Geology*, *10*(3), pp.267-282.

Chandra, V., Wright, P., Barnett, A., Steele, R., Milroy, P., Corbett, P., Geiger, S. and Mangione, A., 2015. Evaluating the impact of a late-burial corrosion model on reservoir permeability and performance in a mature carbonate field using near-wellbore upscaling. *Geological Society, London, Special Publications*, *406*(1), pp.427-445.

Chang, H.C., Kopaska-Merkel, D.C. and Chen, H.C., 2002. Identification of lithofacies using Kohonen self-organizing maps. *Computers & Geosciences*, *28*(2), pp.223-229.

Chang, H.C., Kopaska-Merkel, D.C., Chen, H.C. and Durrans, S.R., 2000. Lithofacies identification using multiple adaptive resonance theory neural networks and group decision expert system. *Computers & Geosciences*, *26*(5), pp.591-601.

Cracknell, M.J. and Reading, A.M., 2014. Geological mapping using remote sensing data: A comparison of five machine learning algorithms, their response to variations in the spatial distribution of training data and the use of explicit spatial information. *Computers & Geosciences*, *63*, pp.22-33.

Cross, T.A., 1988. Controls on coal distribution in transgressive-regressive cycles, Upper Cretaceous, Western Interior, USA.

De Mol, B., Van Rensbergen, P., Pillen, S., Van Herreweghe, K., Van Rooij, D., McDonnell, A., Huvenne, V., Ivanov, M., Swennen, R. and Henriet, J.P., 2002. Large deep-water coral banks in the Porcupine Basin, southwest of Ireland. *Marine Geology*, *188*(1-2), pp.193-231.

Derder, O.M. and Geo, P., 2016. Lithology and mineralogy estimation from matrix density utilizing wireline logs in glauconitic sandstone, Blackfoot area, alberta, Canada. *Can. J. Explor. Geophys*, *41*(1), pp.1-8.

Dewers, T. and Ortoleva, P., 1994. Formation of stylolites, marl/limestone alternations, and dissolution (clay) seams by unstable chemical compaction of argillaceous carbonates. In *Developments in Sedimentology* (Vol. 51, pp. 155-216). Elsevier.

Dolan, J.F., 1989. Eustatic and tectonic controls on deposition of hybrid siliciclastic/carbonate basinal cycles: discussion with examples. *AAPG Bulletin*, *73*(10), pp.1233-1246.

Doveton, J.H., 1994. Applications of Artificial Intelligence in Log Analysis: Chapter 7.

Dunham, R.J., 1962. Classification of carbonate rocks according to depositional textures.

Dunnington, H.V., 2005. Generation, migration, accumulation, and dissipation of oil in Northern Iraq. *GeoArabia*, *10*(2), pp.39-84.

Dutta, P., Singh, S.K., Al-Genai, J., Akhtar, A. and Akbar, M., 2007. A novel approach to fracture characterization utilizing borehole seismic data. In *SPE Middle East Oil and Gas Show and Conference* (pp. SPE-105427). SPE.

Ebner, M., Piazolo, S., Renard, F. and Koehn, D., 2010. Stylolite interfaces and surrounding matrix material: Nature and role of heterogeneities in roughness and microstructural development. *Journal of Structural Geology*, *32*(8), pp.1070-1084.

Ehrenberg, S.N., Eberli, G.P., Keramati, M. and Moallemi, S.A., 2006. Porosity-permeability relationships in interlayered limestone-dolostone reservoirs. *AAPG bulletin*, *90*(1), pp.91-114.

Ehrenberg, S.N., Morad, S., Yaxin, L. and Chen, R., 2016. Stylolites and porosity in a Lower Cretaceous limestone reservoir, onshore Abu Dhabi, UAE. *Journal of Sedimentary Research*, *86*(10), pp.1228-1247.

Elkatatny, S. and Mahmoud, M., 2018. Development of new correlations for the oil formation volume factor in oil reservoirs using artificial intelligent white box technique. Petroleum, 4(2), pp.178-186.

Embry, A.F. and Johannessen, E.P., 1993. T–R sequence stratigraphy, facies analysis and reservoir distribution in the uppermost Triassic–Lower Jurassic succession, western Sverdrup Basin, Arctic Canada. In Norwegian petroleum society special publications (Vol. 2, pp. 121-146). Elsevier.

Embry, A.F. and Johannessen, E.P., 2017. Two approaches to sequence stratigraphy. In Stratigraphy & Timescales (Vol. 2, pp. 85-118). Academic Press.

Finkel, E.A. and Wilkinson, B.H., 1990. Stylolitization as source of cement in Mississippian Salem Limestone, west-central Indiana. *AAPG bulletin*, *74*(2), pp.174-186.

Fletcher, R.C. and Pollard, D.D., 1981. Anticrack model for pressure solution surfaces. *Geology*, *9*(9), pp.419-424.

Flügel, E., 2004. Microfacies of Carbonate Rocks: Analysis, Interpretation, and Application. Springer-Verlag, Berlin Heidelberg (976 pp.).

Folk, R.L. and Ward, W.C., 1957. Brazos River bar [Texas]; a study in the significance of grain size parameters. *Journal of sedimentary research*, *27*(1), pp.3-26.

Gomez-Rivas, E., Martín-Martín, J.D., Bons, P.D., Koehn, D., Griera, A., Travé, A., Llorens, M.G., Humphrey, E. and Neilson, J., 2022. Stylolites and stylolite networks as primary controls on the geometry and distribution of carbonate diagenetic alterations. *Marine and Petroleum Geology*, *136*, p.105444.

Graham, J. and Tucker, M., 1988. Collection and analysis of field data. *Techniques in sedimentology*, pp.5-62.

Gratier, J.P., Muquet, L., Hassani, R. and Renard, F., 2005. Experimental microstylolites in quartz and modeled application to natural stylolitic structures. *Journal of Structural Geology*, *27*(1), pp.89-100.

Groshong Jr, R.H., 1975. Strain, fractures, and pressure solution in natural single-layer folds. *Geological Society of America Bulletin*, *86*(10), pp.1363-1376.

Guiwen, W.A.N.G., Zhongchun, S.U.N., Jianwei, F.U., Xingping, L.U.O., Xianling, Z.H.A.O. and Tuo, P.A.N., 2015. Control factors and logging evaluation method for glutenite reservoir in Mabei area, Junggar Basin. *Xinjiang Petroleum Geology*, *36*(1), p.1.

Haddad, S.N.S. and Amin, M.A., 2007. Mid-Turonian–early Campanian sequence stratigraphy of northeast Iraq. *GeoArabia*, *12*(2), pp.135-176.

Halgedahl, S.L., Jarrard, R.D., Brett, C.E. and Allison, P.A., 2009. Geophysical and geological signatures of relative sea level change in the upper Wheeler Formation, Drum Mountains, West-Central Utah: A perspective into exceptional preservation of fossils. *Palaeogeography, Palaeoclimatology, Palaeoecology*, *277*(1-2), pp.34-56.

Harris, J.R. and Grunsky, E.C., 2015. Predictive lithological mapping of Canada's North using Random Forest classification applied to geophysical and geochemical data. *Computers & geosciences*, *80*, pp.9-25.

Harris, N.B., 2006. Low-porosity haloes at stylolites in the feldspathic Upper Jurassic Ula sandstone, Norwegian North Sea: an integrated petrographic and chemical mass-balance approach. *Journal of Sedimentary Research*, *76*(3), pp.444-459.

Hassan, T.H. and Wada, Y., 1981. Geology and development of Thamama zone 4, Zakum field. *Journal of Petroleum Technology*, *33*(07), pp.1327-1337.

Heap, M., Reuschlé, T., Baud, P., Renard, F. and Iezzi, G., 2018. The permeability of stylolite-bearing limestone. *Journal of structural geology*, *116*, pp.81-93.

Heap, M.J., Baud, P., Reuschlé, T. and Meredith, P.G., 2014. Stylolites in limestones: Barriers to fluid flow? *Geology*, *42*(1), pp.51-54.

Humphrey, E., Gomez-Rivas, E., Koehn, D., Bons, P.D., Neilson, J., Martín-Martín, J.D. and Schoenherr, J., 2019. Stylolite-controlled diagenesis of a mudstone carbonate reservoir: A case study from the Zechstein_2_Carbonate (Central European Basin, NW Germany). *Marine and Petroleum Geology*, *109*, pp.88-107.

Humphrey, E., Gomez-Rivas, E., Neilson, J., Martín-Martín, J.D., Healy, D., Yao, S. and Bons, P.D., 2020. Quantitative analysis of stylolite networks in different platform carbonate facies. *Marine and Petroleum Geology*, *114*, p.104203.

Hussein, H.S., 2022. Carbonate fractures from conventional well log data, Kometan Formation, Northern Iraq case study. *Journal of Applied Geophysics*, *206*, p.104810.

Hussein, H.S., Bábek, O., Mansurbeg, H. and Shahrokhi, S., 2024. Outcrop-to-subsurface correlation and sequence stratigraphy of a mixed carbonate–siliciclastic ramp using element geochemistry and well logging; Upper Cretaceous Kometan Formation, Zagros Foreland, NE Iraq. *Sedimentary Geology*, *459*, p.106547.

Hussein, H.S., Mansurbeg, H. and Bábek, O., 2024. A new approach to predict carbonate lithology from well logs: A case study of the Kometan formation in northern Iraq. Heliyon.

Imamverdiyev, Y. and Sukhostat, L., 2019. Lithological facies classification using deep convolutional neural network. *Journal of Petroleum Science and Engineering*, *174*, pp.216-228.

Jarvis, I.A.N., Murphy, A.M. and Gale, A.S., 2001. Geochemistry of pelagic and hemipelagic carbonates: criteria for identifying systems tracts and sea-level change. *Journal of the Geological Society*, *158*(4), pp.685-696.

Jassim, Z.J., Goff, J.C., 2006. The Geology of Iraq. Dolin, Prague (341 pp.).

Kaddouri, N., 1982. Tel Hajar: A new Cenomanian-lower Turonian stratigraphic unit from north-west Iraq. *Cretaceous Research*, *3*(4), pp.391-395.

Keller, G., 1993. The Cretaceous-Tertiary boundary transition in the Antarctic Ocean and its global implications. *Marine Micropaleontology*, *21*(1-3), pp.1-45.

Keller, G., Adatte, T., Stinnesbeck, W., Luciani, V., Karoui-Yaakoub, N. and Zaghbib-Turki, D., 2002. Paleoecology of the Cretaceous–Tertiary mass extinction in planktonic foraminifera. *Palaeogeography, Palaeoclimatology, Palaeoecology*, *178*(3-4), pp.257-297.

Killeen, P.G., 1997. Borehole geophysics: exploring the third dimension. In *Proceedings of Exploration* (Vol. 97, pp. 31-42).

Koehn, D., Ebner, M., Renard, F., Toussaint, R. and Passchier, C.W., 2012. Modelling of stylolite geometries and stress scaling. *Earth and Planetary Science Letters*, *341*, pp.104-113.

Koehn, D., Renard, F., Toussaint, R. and Passchier, C.W., 2007. Growth of stylolite teeth patterns depending on normal stress and finite compaction. *Earth and Planetary Science Letters*, *257*(3-4), pp.582-595.

Koehn, D., Rood, M.P., Beaudoin, N., Chung, P., Bons, P.D. and Gomez-Rivas, E., 2016. A new stylolite classification scheme to estimate compaction and local permeability variations. *Sedimentary Geology*, *346*, pp.60-71.

Kohonen, T., 1988. Self-organized function of topologically correct feature maps. *Biological Cybernetics*, (43), pp.43-69.

Laongsakul, P., 2010. Characterization of reservoir fractures using conventional geophysical logging (Doctoral dissertation, Prince of Songkla University Faculty of Science (Geophysics)).

László, C., Ágoston, S., Tamás, P., László, K., Salae, A.T. and Athar, A., 2012. Structural evolution of the northwestern Zagros, Kurdistan Region, Iraq: Implications on oil migration. GeoArabia, 17(2), pp.81-116.

Leyon, W.C., 2010. Working Guide to Reservoir Engineering. Elsevier, 129p.

Li, Y. and Anderson-Sprecher, R., 2006. Facies identification from well logs: A comparison of discriminant analysis and naïve Bayes classifier. *Journal of Petroleum Science and Engineering*, *53*(3-4), pp.149-157.

Lind, I., Nykjaer, O., Priisholm, S. and Springer, N., 1994. Permeability of stylolite-bearing chalk. *Journal of Petroleum Technology*, *46*(11), pp.986-993.

Mabille, C., Pas, D., Aretz, M., Boulvain, F., Schröder, S. and Da Silva, A.C., 2008. Deposition within the vicinity of the Mid-Eifelian High: detailed sedimentological study and magnetic susceptibility of a mixed ramp-related system from the Eifelian Lauch and Nohn formations (Devonian; Ohlesberg, Eifel, Germany). *Facies*, *54*, pp.597-612.

Mabrouk, A., Jarvis, I., Belayouni, H., Murphy, A. and Moody, R.T., 2007. Sequence stratigraphy, sea level change and palaeoenvironments via chemostratigraphy: Regional to global correlations. *American Association of Petroleum Geologists Search and Discovery, article*, *40244.*

Mahmood, W., Mohammed, A. and HamaHussein, S., 2020. Predicting mechanical properties and ultimate shear strength of gypsum, limestone and sandstone rocks using Vipulanandan models. *Geomechanics and Geoengineering*, *15*(2), pp.90-106.

Mahmoodi, O., Smith, R.S. and Tinkham, D.K., 2016. Supervised classification of down-hole physical properties measurements using neural network to predict the lithology. *Journal of Applied Geophysics*, *124*, pp.17-26.

Martinez-Torres, L.P., 2002. *Characterization of naturally fractured reservoirs from conventional well logs* (Doctoral dissertation, University of Oklahoma).

Martín-Martín, J.D., Gomez-Rivas, E., Gómez-Gras, D., Travé, A., Ameneiro, R., Koehn, D. and Bons, P.D., 2018. Activation of stylolites as conduits for overpressured fluid flow in dolomitized platform carbonates. *Geological Society, London, Special Publications*, *459*(1), pp.157-176.

Martire, L., 1992. Sequence stratigraphy and condensed pelagic sediments. An example from the Rosso Ammonitico Veronese, northeastern Italy. *Palaeogeography, Palaeoclimatology, Palaeoecology*, *94*(1-4), pp.169-191.

Massey Jr, F.J., 1951. The Kolmogorov-Smirnov test for goodness of fit. *Journal of the American statistical Association*, *46*(253), pp.68-78.

Mehrabi, H., Mansouri, M., Rahimpour-Bonab, H., Tavakoli, V. and Hassanzadeh, M., 2016. Chemical compaction features as potential barriers in the Permian-Triassic reservoirs of Southern Iran. *Journal of Petroleum Science and Engineering*, *145*, pp.95-113.

Mohaghegh, S., Balan, B. and Ameri, S., 1997. Permeability determination from well log data. *SPE formation evaluation*, *12*(03), pp.170-174.

Mohammed, A.S., 2019. Vipulanandan models to predict the mechanical properties, fracture toughness, pulse velocity and ultimate shear strength of shale rocks. *Geotechnical and Geological Engineering*, *37*(2), pp.625-638.

Morad, D., Nader, F.H., Morad, S., Al Darmaki, F. and Hellevang, H., 2018. Impact of stylolitization on fluid flow and diagenesis in foreland basins: evidence from an Upper Jurassic Carbonate gas reservoir, Abu Dhabi, United Arab Emirates. *Journal of Sedimentary Research*, *88*(12), pp.1345-1361.

Morad, S., Ketzer, J.M. and De Ros, L.F., 2000. Spatial and temporal distribution of diagenetic alterations in siliciclastic rocks: implications for mass transfer in sedimentary basins. *Sedimentology*, *47*, pp.95-120.

Morad, S., Ketzer, J.M. and De Ros, L.F., 2013. Linking diagenesis to sequence stratigraphy: an integrated tool for understanding and predicting reservoir quality distribution. *Linking diagenesis to sequence stratigraphy*, pp.1-36.

Neilson, J.E., Oxtoby, N.H., Simmons, M.D., Simpson, I.R. and Fortunatova, N.K., 1998. The relationship between petroleum emplacement and carbonate reservoir quality: examples from Abu Dhabi and the Amu Darya Basin. *Marine and Petroleum Geology*, *15*(1), pp.57-72.

Nelson, R.A., 2001. Geologic Analysis of Naturally Fractured Reservoirs, 2nd edn. Gulf Professional Publishing, Houston, p. 332.

Nenna, F. and Aydin, A., 2011. The formation and growth of pressure solution seams in clastic rocks: A field and analytical study. *Journal of Structural Geology*, *33*(4), pp.633-643.

Nouri-Taleghani, M., Kadkhodaie-llkhchi, A. and Karimi-Khaledi, M., 2015. DETERMINING HYDRAULIC FLOW UNITS USING A HYBRID NEURAL NETWORK AND MULTI-RESOLUTION GRAPH-BASED CLUSTERING METHOD: CASE STUDY FROM SOUTH PARS GASFIELD, IRAN. *Journal of Petroleum Geology*, *38*(2), pp.177-191.

Oberto, S., 1984. Fundamentals of Well-Log Interpretation/the Acquisition of Logging Data. Elsevier Publishers, Amsterdam, 1984, p. 435

Omigie, J.I. and Alaminiokuma, G.I., 2020. Well log sequence stratigraphic analyses for reservoir delineation and hydrocarbon distribution in the eastern part of the central swamp depobelt, Niger Delta. *Journal of Earth Sciences and Geotechnical Engineering*, *10*(5), pp.1-14.

Pabakhsh, M., Ahmadi, K., Riahi, M.A. and Shahri, A.A., 2012. Prediction of PEF and LITH logs using MRGC approach. *Life Science Journal*, *9*(4), pp.974-982.

Paganoni, M., Al Harthi, A., Morad, D., Morad, S., Ceriani, A., Mansurbeg, H., Al Suwaidi, A., Al-Aasm, I.S., Ehrenberg, S.N. and Sirat, M., 2016. Impact of stylolitization on diagenesis of a Lower Cretaceous carbonate reservoir from a giant oilfield, Abu Dhabi, United Arab Emirates. *Sedimentary Geology*, *335*, pp.70-92.

Page, M.C., Dickens, G.R. and Dunbar, G.B., 2003. Tropical view of Quaternary sequence stratigraphy: siliciclastic accumulation on slopes east of the Great Barrier Reef since the Last Glacial Maximum. *Geology*, *31*(11), pp.1013-1016.

Peacock, D.C.P., Korneva, I., Nixon, C.W. and Rotevatn, A., 2017. Changes of scaling relationships in an evolving population: the example of "sedimentary" stylolites. *Journal of Structural Geology*, *96*, pp.118-133.

Posamentier, H.W., Allen, G.P., 1999. Siliciclastic Sequence Stratigraphy: Concepts and Applications. Society for Sedimentary Geology, Tulsa, Oklahoma (193 pp.).

Railsback, L.B., 1993. Lithologic controls on morphology of pressure-dissolution surfaces (stylolites and dissolution seams) in Paleozoic carbonate rocks from the mideastern United States. *Journal of Sedimentary Research*, *63*(3), pp.513-522.

Rashid, F., Glover, P.W.J., Lorinczi, P., Collier, R. and Lawrence, J., 2015a. Porosity and permeability of tight carbonate reservoir rocks in the north of Iraq. *Journal of Petroleum Science and Engineering*, *133*, pp.147-161.

Rashid, F., Glover, P.W.J., Lorinczi, P., Hussein, D. and Lawrence, J.A., 2017. Microstructural controls on reservoir quality in tight oil carbonate reservoir rocks. *Journal of Petroleum Science and Engineering*, *156*, pp.814-826.

Rashid, F., Glover, P.W.J., Lorinczi, P., Hussein, D., Collier, R. and Lawrence, J., 2015. Permeability prediction in tight carbonate rocks using capillary pressure measurements. *Marine and Petroleum Geology*, *68*, pp.536-550.

Rashid, F., Glover, P.W.J., Lorinczi, P., Hussein, D., Collier, R. and Lawrence, J., 2015b. Permeability prediction in tight carbonate rocks using capillary pressure measurements. *Marine and Petroleum Geology*, *68*, pp.536-550.

Read, J.F. and Horbury, A.D., 1993. Eustatic and Tectonic Controls on Porosity Evolution Beneath Sequence-Bounding Unconformities and Parasequence Disconformities on Carbonate Platforms: Chapter 11: DIAGENESIS, SEQUENCE STRATIGRAPHY, AND CHANGES IN RELATIVE SEA LEVEL.

Rider, M.H., 1999. The Geological Interpretation of Well Logs.Whittles Publishing Services (288 pp.).

Ripley, B.D., 2007. *Pattern recognition and neural networks*. Cambridge university press.

Roehl, P.O., Choduette, P.W., 1985. Carbonate Petroleum Reservoirs. Spring-Verlag, New York, p. 622.

Rogers, S.J., Fang, J.H., Karr, C.L. and Stanley, D.A., 1992. Determination of lithology from well logs using a neural network. *AAPG bulletin*, *76*(5), pp.731-739.

Rustichelli, A., Tondi, E., Agosta, F., Cilona, A. and Giorgioni, M., 2012. Development and distribution of bed-parallel compaction bands and pressure solution seams in carbonates (Bolognano Formation, Majella Mountain, Italy). *Journal of Structural Geology*, *37*, pp.181-199.

Sarg, J.F., 1988. carbonate sequence stratigraphy. In: Wigus, C.K. (Ed.), Sea-level Change: An Integrated Approach. Society of Economic Paleontologists and Mineralogists, Special Publicationvol. 42, pp. 155–181.

Schlager, W., 2005. *Carbonate sedimentology and sequence stratigraphy* (No. 8). SEPM Soc for Sed Geology.

Scholle, P.A. and Ulmer-Scholle, D.S., 2003. *A color guide to the petrography of carbonate rocks: grains, textures, porosity, diagenesis, AAPG Memoir 77* (Vol. 77). AAPG.

Schultz, R.A., Fossen, H., 2008. Terminology for structural discontinuities. AAPG (American Association Petroleum Geology) Bull. 92, 15.

Sfidari, E., Kadkhodaie-Ilkhchi, A., Rahimpour-Bbonab, H. and Soltani, B., 2014. A hybrid approach for litho-facies characterization in the framework of sequence stratigraphy: a case study from the South Pars gas field, the Persian Gulf basin. *Journal of Petroleum Science and Engineering*, *121*, pp.87-102.

Simpson, J., 1985. Stylolite-controlled layering in an homogeneous limestone: pseudo-bedding produced by burial diagenesis. Sedimentology, 32(4), pp.495-505.

Stadtműller, M., 2019. Well logging interpretation methodology for carbonate formation fracture system properties determination. *Acta Geophysica*, *67*(6), pp.1933-1943.

Sun, Z., Lin, C., Zhu, P. and Chen, J., 2018. Analysis and modeling of fluvial-reservoir petrophysical heterogeneity based on sealed coring wells and their test data, Guantao Formation, Shengli oilfield. *Journal of Petroleum Science and Engineering*, *162*, pp.785-800.

Taq Taq Operation Company (TTOPCO), 2007. Geological Report.

Thompson, L.B., 2000. Fractured reservoirs: Integration is the key to optimization. *Journal of petroleum technology*, 52(02), pp.52-54.

Tian, Y., Xu, H., Zhang, X.Y., Wang, H.J., Guo, T.C., Zhang, L.J. and Gong, X.L., 2016. Multi-resolution graph-based clustering analysis for lithofacies identification from well log data: Case study of intraplatform bank gas fields, Amu Darya Basin. *Applied Geophysics*, *13*, pp.598-607.

Toussaint, R., Aharonov, E., Koehn, D., Gratier, J.P., Ebner, M., Baud, P., Rolland, A. and Renard, F., 2018. Stylolites: A review. Journal of Structural Geology, 114, pp.163-195.

Tucker, M.E., 1993. Carbonate diagenesis and sequence stratigraphy. *Sedimentology Review/1*, pp.51-72.

Tucker, M.E., Wright, V.P., 1990. Carbonate Sedimentology. Wiley-Blackwell, Oxford (484 pp.).

Van Bellen, R.C., Dunnington, H.V.G.,Wetzel, R., Morton, D.M., 1959. Lexique Stratigraphique international, III, Asie, fasc.10a, Iraq. Centre national de la recherché scientifique, Paris (333 pp.).

Vandeginste, V. and John, C.M., 2013. Diagenetic implications of stylolitization in pelagic carbonates, Canterbury Basin, offshore New Zealand. *Journal of Sedimentary Research*, *83*(3), pp.226-240.

Ver Straeten, C.A., Brett, C.E. and Sageman, B.B., 2011. Mudrock sequence stratigraphy: A multi-proxy (sedimentological, paleobiological and geochemical) approach, Devonian Appalachian Basin. *Palaeogeography, Palaeoclimatology, Palaeoecology*, *304*(1-2), pp.54-73.

Vipulanandan, C. and Mohammed, A., 2018. New Vipulanandan failure model and property correlations for sandstone, shale and limestone rocks. In *IFCEE 2018* (pp. 365-376).

Wang, X., Hou, J., Song, S., Wang, D., Gong, L., Ma, K., Liu, Y., Li, Y. and Yan, L., 2018. Combining pressure-controlled porosimetry and rate-controlled porosimetry to investigate the fractal characteristics of full-range pores in tight oil reservoirs. *Journal of Petroleum Science and Engineering*, *171*, pp.353-361.

Wanless, H.R., 1979. Limestone response to stress; pressure solution and dolomitization. *Journal of Sedimentary Research*, *49*(2), pp.437-462.

Westphal, H., Eberli, G.P., Smith, L.B., Grammer, G.M. and Kislak, J., 2004. Reservoir characterization of the Mississippian Madison formation, Wind river basin, Wyoming. *AAPG bulletin*, *88*(4), pp.405-432.

Watkins, H., Healy, D., Bond, C.E. and Butler, R.W., 2018. Implications of heterogeneous fracture distribution on reservoir quality; an analogue from the Torridon Group sandstone, Moine Thrust Belt, NW Scotland. *Journal of Structural Geology*, *108*, pp.180-197.

Whalen, M.T., Eberli, G.P., Van Buchem, F.S., Mountjoy, E.W. and Homewood, P.W., 2000. Bypass margins, basin-restricted wedges, and platform-to-basin correlation, Upper Devonian, Canadian Rocky Mountains: implications for sequence stratigraphy of carbonate platform systems. *Journal of Sedimentary* Research, 70(4), pp.913-936.

Wilson, J.L., 2012. *Carbonate facies in geologic history*. Springer Science & Business Media.

Wu, P.Y., Jain, V., Kulkarni, M.S. and Abubakar, A., 2018, October. Machine learning-based method for automated well-log processing and interpretation. In *SEG International Exposition and Annual Meeting* (pp. SEG-2018). SEG.

Zhang, C., Zhang, Z., Chen, Y., Xing, Y. and Li, C., 2014. Logging lithology identification of tight sandy conglomerate and its application. *Technology Review*, *32*(25), pp.59-62.

Zhang, J., Liu, S., Li, J., Liu, L., Liu, H. and Sun, Z., 2017. Identification of sedimentary facies with well logs: an indirect approach with multinomial logistic regression and artificial neural network. *Arabian Journal of Geosciences*, *10*, pp.1-9.

Zhang, K., Saeed, A.M., Wang, H., Mi, Z., Qu, J., Jaed, M.A., Wang, Z., Liu, H. and Zhang, Z., 2024. Identification of pore facies for evaluating the reservoir quality: A case study of the Hartha Formation in X Oilfield, Mesopotamian Basin, Iraq. Geological Journal, 59(1), pp.325-339.

Appendices:

Appendix 1: Hussein, H.S., Mansurbeg, H. and Bábek, O., 2024. A new approach to predict carbonate lithology from well logs: A case study of the Kometan formation in northern Iraq. *Heliyon*, *10*(3).

Appendix 2: Hussein, H.S., Bábek, O., Mansurbeg, H. and Shahrokhi, S., 2024. Outcrop-to-subsurface correlation and sequence stratigraphy of a mixed carbonate–siliciclastic ramp using element geochemistry and well logging; Upper Cretaceous Kometan Formation, Zagros Foreland, NE Iraq. *Sedimentary Geology*, *459*, p.106547.

Appendix 3: Hussein, H.S., 2022. Carbonate fractures from conventional well log data, Kometan Formation, Northern Iraq case study. *Journal of Applied Geophysics*, *206*, p.104810.

Appendix 4: Hussein S.H., Bábek, O., Mansurbeg H., Juan Diego Martín-Martín3, Enrique Gomez-Rivas3, Marten-Marten. J.D., Gomez-Rivas, E., 2024 Impact of stylolitization on porosity and permeability of carbonate rocks: the Upper Cretaceous Kometan Formation, Zagros Forland Basin in Iraqi Kurdistan, (**Submitted to Journal of Marine and Petroleum Geology**).

Appendix 5: Fig. S1. X-ray diffractograms with results of quantitative and qualitative phase analyses from the Kometan Formation.
https://ars.els-cdn.com/content/image/1-s2.0-S0037073823002191-mmc1.pdf

Appendix 6: Table S1. Bulk-rock X-ray fluorescence (XRF) concentrations (both raw data and calibrated data) from the Zewe, Qamchuqa and Dokan sections, and calibration equations.
https://ars.els-cdn.com/content/image/1-s2.0-S0037073823002191-mmc2.xlsx

Appendix 7: Table S2. Total gamma-ray logs from Kometan Formation in nine wells from the Khabbaz, Kirkuk, Jambur, Bai Hasan, and Barda Rash oil fields.
https://ars.els-cdn.com/content/image/1-s2.0-S0037073823002191-mmc3.xlsx

Appendix 8: Table S3. Density porosity, neutron porosity, neutron-density porosity and sonic porosity logs from Kometan Formation in K-216 and K-218 wells.
https://ars.els-cdn.com/content/image/1-s2.0-S0037073823002191-mmc4.xlsx

Appendix 9: Table S4. Measured data of stylolite spacing, wavelength, amplitude, junction angle, junction density, and classification of stylolite.

Appendix 1

Heliyon 10 (2024) e25262

Contents lists available at ScienceDirect

Heliyon

journal homepage: www.cell.com/heliyon

Research article

A new approach to predict carbonate lithology from well logs: A case study of the Kometan formation in northern Iraq

Hussein S. Hussein [a,b,*], Howri Mansurbeg [a,c], Ondřej Bábek [a]

[a] Department of Geology, Palacký University, 17. listopadu 12, Olomouc, 77146, Czech Republic
[b] Department of Petroleum Geosciences, Faculty of Science, Soran University, Soran, Erbil, 44002, Iraq
[c] General Directorate of Scientific Research Centre, Salahaddin University, Erbil, Kurdistan Region, Iraq

ARTICLE INFO

Keywords:
Multivariate regression
Lithology prediction
Gamma-ray log
Porosity logs

ABSTRACT

Understanding the spatial variation in lithology is crucial for characterizing reservoirs, as it governs the distribution of petrophysical characteristics. This study focuses on predicting the lithology of carbonate rocks (limestone, argillaceous limestone, marly limestone, and marl) within the Kometan Formation, Khabbaz Oil Field, Northern Iraq, using well logs. Precise lithology prediction was achieved by applying multivariate regression method on neutron, sonic, and density logs. Gamma-ray and elemental concentrations from bulk-rock X-ray fluorescence spectroscopy were employed to identify clay minerals, paleoenvironments, and quantify the shale content. The results indicate that the Kometan Formation predominantly comprises limestone, marl, marly limestone, and argillaceous limestone in the middle section. The middle part exhibits a higher shale content compared to the lower and upper parts. A statistically significant correlation (R^2 = 0.83–0.85) between described and predicted lithology was established. The model with a higher coefficient of determination (0.85) was tested for further predictions in other wells in the Kirkuk Oil Field. This research can be valuable for lithological and petrophysical characterization of carbonate reservoirs and electrofacies analysis, particularly in situations where core data is unavailable.

1. Introduction

The lithology of carbonate successions governs the heterogeneity of petrophysical characteristics such as porosity and permeability. Thus, a precise understanding of the spatial and vertical lithological variations is critical for adequate characterization of the petrophysical and mechanical properties of carbonate reservoirs [1–4]. Lithology parameters largely control the rock density, strength properties of the rock [5–7], and hydraulic fracturing [8]. Visual inspection of core samples and evaluation of well log data facilitate preliminary identification of carbonate lithology. The core description is the simplest way of determining lithology, but it is time-consuming and limited to specific well intervals [1,9–12]. As a result, the study of various well logs is crucial in identifying lithology.

The lithology, petrophysical characteristics, and facies interpretation of subsurface reservoirs were investigated using a variety of well logging approaches [9,13–16]. Conventional techniques of determining lithology from well log data [17,18] and the application of bar graphs and bi-variate statistical analysis [13,19–21] have been extensively employed. These qualitative approaches can benefit

* Corresponding author. Department of Geology, Palacký University, 17. listopadu 12, Olomouc, 77146, Czech Republic.
E-mail address: hussein.hussein01@upol.cz (H.S. Hussein).

https://doi.org/10.1016/j.heliyon.2024.e25262
Received 4 July 2023; Received in revised form 23 January 2024; Accepted 23 January 2024
Available online 1 February 2024

from geologists' knowledge but have disadvantages including high levels of ambiguity, excessive working, poor effectiveness, and potential geologist-introduced artifacts [1,12].

In the last few decades, computational techniques have been utilized to determine the lithology from well log data. The artificial neural network (ANN) has been widely employed as an unpredictable automated estimator in logging-based lithology categorization. Both supervised [22,23] and unsupervised [24–26] ANN, as well as adaptive resonance theory [9,27], have all been used for lithology prediction. The supervised and non-supervised ANN include backpropagation neural networks and Kohonen self-organizing maps. The uses of clustering theory in lithology recognition were studied [14]. The prediction of lithology was also carried out by various studies using clustering techniques [11,28,29]. Several machine-learning techniques including random forest [30,31], support vector machine [32], deep recurrent neural networks [33], and deep convolutional neural networks [34], have recently been used for computerized well log evaluation. Nevertheless, in the approaches mentioned above, the lithology is solely determined by analyzing the readings from multiple logs at the relevant depth, with little regard to the geological features of the combined lithologies. Consequently, the obtained results could disagree with the accepted geologic principles because i) the response properties of log curves of several various lithologies are challenging to differentiate, especially close to the transition surface; and ii) no mathematical solution can adequately integrate data from logs to create the accurate underground lithology pattern [1,10].

This paper provides an innovative approach for predicting carbonate rocks' lithology, employing well logs and rock data from the Kometan Formation (Upper Turonian-Lower Campanian), Khabbaz Oil Field, Northern Iraq. The lithology of rock samples is analyzed using multivariate regression to transform the described lithologies (core and cuttings) into quantitative parameters as dependent values. Finally, the log data (density log, sonic log, and neutron log) as an independent value is used to determine the regression of each applied log to predict lithology. In addition, the gamma-ray log is used to quantify the shale contents and is validated by elemental concentrations from bulk-rock samples measured by X-ray fluorescence. In contrast to many other approaches that solely take log data into account, this approach highlights the importance of geological information and incorporates this information into well log interpretation to increase reliability.

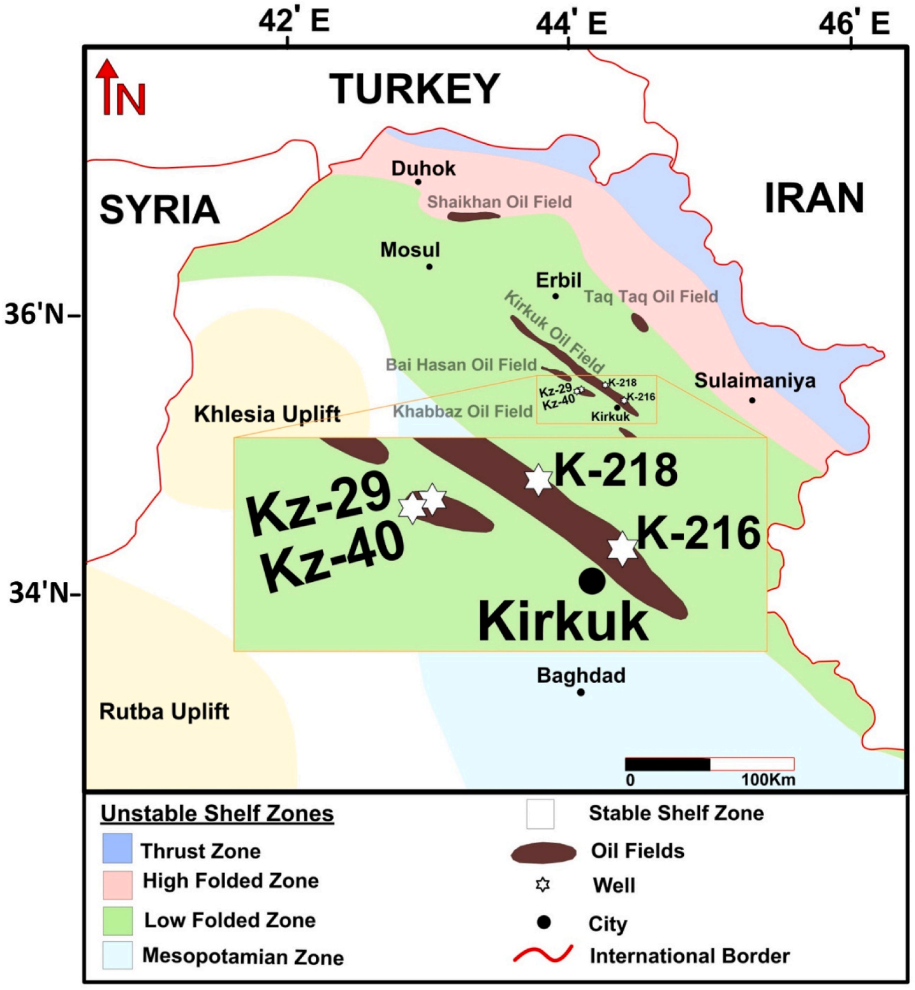

Fig. 1. Map displaying the tectonic divide of Iraq and the locations of the examined wells (Kz-29, Kz-40, K-216, and K-218 wells) [35].

2. Geological setting

The studied oil field is situated in Northern Iraq, approximately 20 km SW of Kirkuk (Fig. 1). The field adjoins the Kirkuk Oil Field, located about 23 km SW of the Baba Dome. The research site is situated in the foothills of the Zagros Foreland Basin in northern Iraq [35]. It is a small asymmetrical subsurface anticline with a NW-SE trending axis. The structure's width and length are about 4 km and 18 km, respectively. Compared to the NE limb, the SW limb is gentler. The first seismic study of the region was carried out by the Iraqi Petroleum Company (I.P.C.) in 1955, and the results showed a subsurface structure that dips towards the NW. In 1971, a second seismic survey verified the structure's existence [36]. The first well (Kz-1) in the area was completed in 1976. A small number of the subsequent wells penetrated Cretaceous carbonate reservoirs, while the majority were drilled into Paleogene carbonate reservoirs.

The Kometan Formation was previously defined at the locality of Kometan Village, which is situated in the High Folded Zone of the Zagros Mountains, Northern Iraq, around 103 km N/NE of Kirkuk [37,38]. Several places, including the Imbricated Zone, the High Folded Zone, and the Low Folded Zone, have seen outcrop and subsurface investigations on the Kometan Formation. It is made up of marls with significant lateral variability and fine-grained pelagic limestone, primarily lime mudstone/wackestone, that ranges in color from white to light grey [39]. Pure limestones laterally transform into marly limestones and marls as they move from E/NE to W/SW [39]. The globigerinid, mixed globigerinid-oligosteginid, and oligosteginid facies make up the Kometan Formation [35,37,38]. According to outcrop measurements, the formation's thickness varies from 36 m at the type locality to 100–120 m in other locations, with an average thickness of about 40–60 m [35]. However, the thickness of the formation is greater in the subsurface sections, typically increasing towards the S/SW. The formation thickness in the Kz-29 and Kz-40 wells is 146 and 185 m, respectively. The thickness in the wells of the K-216 is 135 m and that of the K-218 is 123 m. The Kometan Formation's lower and upper contacts vary. Buday identified the unconformable lower Kometan Formation connections with the underlying Dokan, Upper Qamchuqa, and Gulneri Formations [35], while Kaddouri reported a conformable contact with the Tel Hajar Formation in NW Iraq [40]. Glauconite indicates the unconformability of the upper contact with the Shiranish Formation in some outcrops [37,38]. The glauconitic marl beds have wide aerial distributions in northern Iraq, but they appear between the Qamchuqa and other formations, e.g., Kometan and Bekhme [41]. Alternatively, Buday recorded disconformable or conformable upper contacts in several places [35,42]. According to a statement by the North Oil Company in Iraq, the Kometan Formation is overlain by the Gulneri Formation and the Mushorah Formation in the wells under study.

3. Material and methods

Gamma-ray, density (ρb), sonic (Δt), and neutron logs from the Kz-29, Kz-40, K-216, and K-218 wells, measured with 0.2 m reading intervals, were employed for this investigation. The original analog logs were digitized using the Get Data Digitizer 2.2. The ρb, Δt, and neutron porosity readings from the digitized logs constituted the input parameters for the multivariate regression. Shale volume (Vsh) from the gamma-ray log was used as an independent lithology indicator (Eqs. (1) and (2)). Regression analysis that integrates independent variables to predict dependent values is known as multivariate regression [43]. In multivariate linear regression analyses,

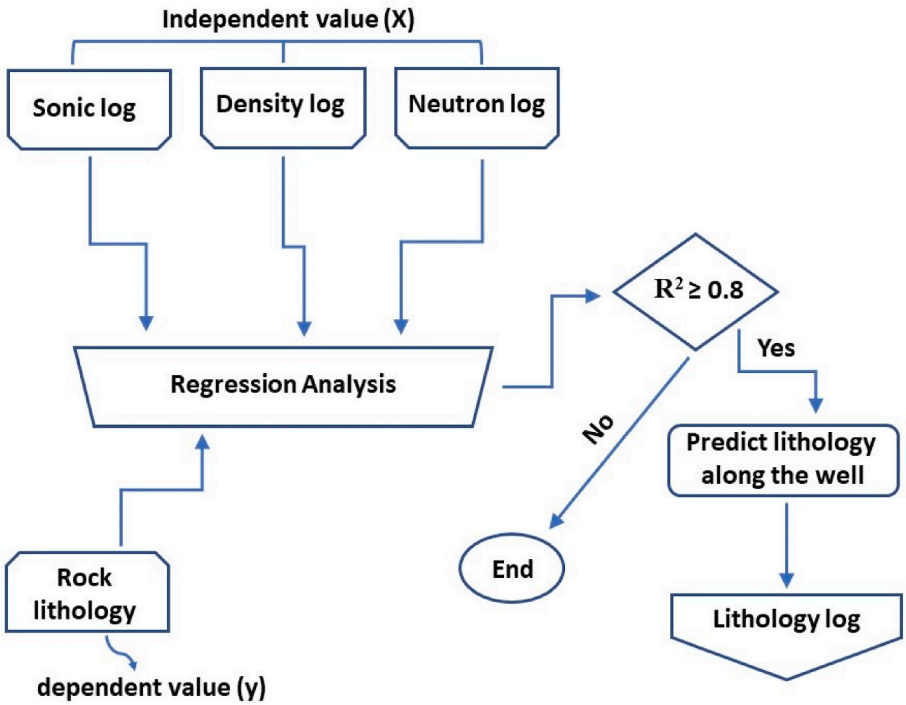

Fig. 2. Proposed quantitative methodology workflow for predicting lithology.

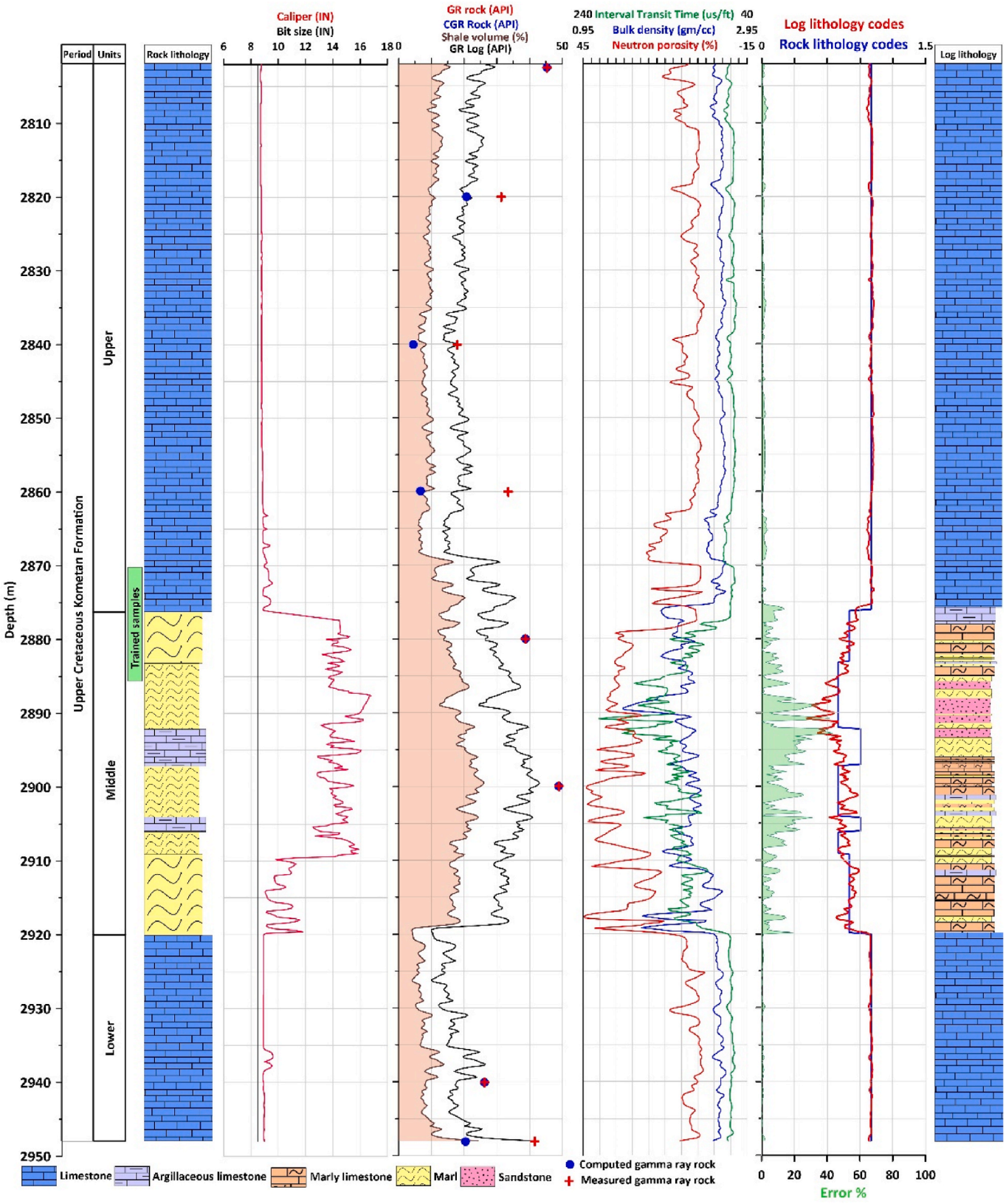

Fig. 3. Log data (caliper, gamma-ray log (GR log), gamma-ray rock (GR rock), computed gamma-ray rock (CGR), sonic (Interval transit time), density (bulk density), and neutron log (neutron porosity)), rock lithology codes (blue line) log lithology codes (red line) computed from multi-variate regression, and error percent line (green-filled line) for Kz-29 well.

more than one variable predictor (X-variables) is correlated using linear regression as close as possible to a single response variable (Y-vector). This method relies on the linear regression between the well log response (X-variables) and rock lithology (Y-vector) in the formation. Fig. 2 depicts the general methodology, which is explained as follows: Using the described lithology from rock samples (the light green rectangle interval in Figs. 3 and 4), different regression analyses can be performed using various well logs (ρb, Δt, and neutron), so the linear best-fit parameters can be obtained and used to predict the lithology. The coefficient of determination (R^2)

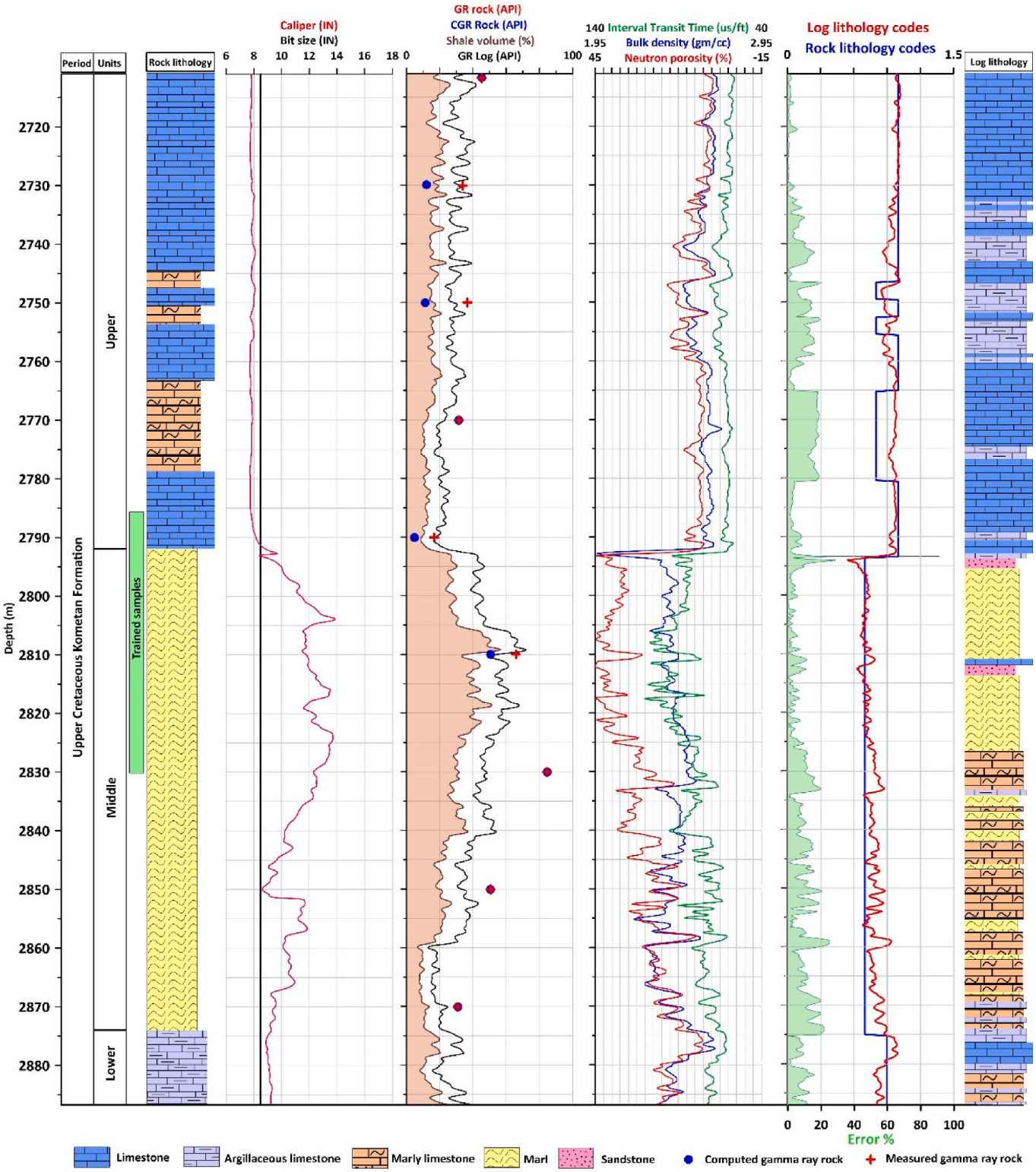

Fig. 4. Log data (caliper, gamma-ray log (GR log), gamma-ray rock (GR rock), computed gamma-ray rock (CGR), sonic (Interval transit time), density (bulk density), and neutron log (neutron porosity)), rock lithology codes (blue line) log lithology codes (red line) computed from multi-variate regression, and error percent line (green-filled line) for Kz-40 well.

between lithology from rock samples and well log readings should be equal to or greater than 0.8 for each regression analysis to a continuous lithology log of the studied formation in the same and other wells considering the same borehole environment.

The main techniques in the multivariate regression established in this study included lithology codification and fuzzy logic. Multivariate regression is a numerical method, and therefore, the descriptive lithologies must be converted to quantitative parameters. For this purpose, a self-generating fuzzy logic system [44] was applied using training data based on the matrix density of the available lithologies (Table 1). The described lithologies, varying from sandstone to anhydrite, were transformed into codes ranging from 0.6 to 1.3 (Table 1).

The "if-then'' function in fuzzy logic involves various formulas for lithology identification. This study used the following formula:

$$\text{If } X < P \leq Y, \text{ then } S \tag{1}$$

where X and Y are the lithology codes (predicted coded lithology, see Table 1), P is the predicted lithology, and S is the name of the lithology (Table 2).

As anchoring points to determine the well lithology, rock samples (cores and cuttings) and thin sections offered by the North Oil Company, Iraq, were employed. The samples were taken along 16 m of thickness in the Kz-29 Well and 44 m in the Kz-40 Well (Figs. 3 and 4, light green rectangle). The log data (density, sonic, and neutron log) were obtained from the same depths as the rock samples. The gamma-ray log was excluded from the multivariate regression and taken as an independent indicator of formation shaliness, or the volume of shale [47]. The first step in the calculation of the shale volume was the gamma-ray index (I_{GR}), which was calculated using Equation (2):

$$I_{GR} = \left(GR_{log} - GR_{min}\right) \; / \; \left(GR_{max} - GR_{min}\right) \tag{2}$$

The gamma-ray index is denoted by I_{GR}, the gamma-ray reading from the log is denoted by GR_{log}, the clean zone gamma-ray reading is denoted by GR_{min}, and the maximum gamma-ray reading from the log is denoted by GR_{max} (shale zone). The following equation was used to determine the shale volumes (Vsh), as proposed by Larionov [47]:

$$Vsh = 0.33\left[2^{2*IGR} - 1.0\right] \tag{3}$$

Traditional well log methods like N-D (Neutron-Density), M-N (Neutron-Density-Sonic), and interval transit time-bulk density cross plots are used to identify lithology [55]. The results from cross plots, correlate with the results from the multivariate regression which could be another advantage of the examined approach in the assessment of the reliability of the most often used lithology cross plots. The following are the definitions of the terms M and N:

$$M = \left[\left(\Delta t_{fl} - \Delta t\right) \; / \; \left(\rho_b - \rho_{fl}\right)\right] * 0.01 \tag{4}$$

$$N = \left(NPHI_{fl} - NPHI\right) \; / \; \left(\rho_b - \rho_{fl}\right) \tag{5}$$

where Δt_{fl} is interval transit time in the fluid in the formation, Δt is interval transit time in the formation (from the log), ρ_b is formation bulk density (from the log), ρ_{fl} is fluid density (generally, 1.0 for fresh mud and 1.1 for saline mud), $NPHI_{fl}$ is neutron porosity of the fluid in the formation (usually 1.0), NPHI is neutron derived porosity (from the log), and the multiplier 0.01 is used to make the M values compatible for easy scaling.

Density porosity is commonly calculated in petrophysics to estimate the pore volume in a rock formation. It is typically determined using a density log and relies on comparing the bulk density of the rock matrix to the density of the formation fluid. The formula for calculating density porosity is as follows:

$$\text{Density porosity} = \left(\rho_{ma} - \rho_b\right) / \left(\rho_{ma} - \rho_{fl}\right) \tag{6}$$

ρ_{ma}**:** The density of the rock matrix.

ρ_b**:** The measured bulk density from the density log.

ρ_{fl}**:** The density of the fluid filling the pore spaces in the rock formation.

Using a Delta Premium EDXRF spectrometer (Innov-X, USA) with a large-area silicon-drift detector, the amounts of 17 elements (Al, Si, K, Ca, Ti, Mn, Fe, V, Ni, Cu, Zn, As, Rb, Sr, Zr, Mo, and Pb) were measured in 27 subsurface rock samples from three wells that went

Table 1
Matrix and mineral density values for common types of rocks [45,46], shale content ranges, and codification for the most common rocks.

Lithology	Density (g/cm^3)	Shale content (%)	Code Number
Anhydrite	2.98	0	1.3
Dolomite	2.87	0–5	1.2
Dolomitic limestone	2.79	0–5	1.1
Limestone	2.71	0–5	1.0
Argillaceous limestone	2.69	15–25	0.9
Marly limestone	2.67	25–35	0.8
Marl	2.66	35–65	0.7
Sandstone	2.65	0–5	0.6

Table 2
Lithology codes are used in the if-then fuzzy lithology system.

Predicted lithology (X < P ≤ Y)	Lithology names (S)
0.95 < P ≤ 1.05	Limestone
0.85 < P ≤ 0.95	Argillaceous limestone
0.75 < P ≤ 0.85	Marly limestone
0.65 < P ≤ 0.75	Marl
0.55 < P ≤ 0.65	Sandstone

into the Kometan Formation. The studies were conducted using two 120-s acquisition times (beam) at accelerating voltages of 15 kV and 40 kV. The materials were crushed and placed in plastic cells that were sealed with Mylar foil before EDXRF analysis. Using sample aliquots from Lower Devonian carbonates and marls of the Prague Basin, Czechia, inductively coupled plasma mass spectrometry/optical emission spectrometry (ICP-MS/OES) data were used to calibrate the amounts of the examined elements [48]. The EDXRF analytical data (dependent variables) were transformed into their equivalent ICP-MS/OES concentrations using linear and polynomic regression equations (independent variables). The regressions had strong coefficients of determination (R2 ranging from 0.85 to 0.99) for all elements, which showed very good consistency in the EDXRF signals. Both phosphorus and sulfur were not calibrated. The amount of shale estimated from the gamma-ray logs was confirmed using the aluminum contents.

An RT-50 shielded laboratory spectrometer (Georadis, s.r.o., Czech Republic) with a 3 × 300" (350 cm^3) NaI (Tl) detector was used to study the gamma-ray spectra of 17 rock samples from the Kz-29 (7) and Kz-40 (10) wells. Based on calibrations utilizing calibration standards provided by the manufacturer, the instrument converted the counts per second from 512 energy windows to K (%), U (ppm), and Th (ppm) concentrations. The declared sensitivity was 0.7 ppm for Th, 0.4 ppm for U, and 0.12 % for K. Each sample was ground into a powder, put in a 250 cm^3 plastic container, and measured for 30 min.

4. Results

4.1. Multivariate regression of log data

The description of the available rock samples (cores and well cuttings) from the Kometan Formation could be subdivided into four lithologies: limestone, argillaceous limestone, marly limestone, and marl (Figs. 3 and 4). The well log intervals from 2870 to 2885 m in the Kz-29 well and 2786–2830 m in the Kz-40 well were used as the anchor points (trained samples) in which each lithology was transformed into a code number used in the multivariate regression analysis (Figs. 3 and 4, green column). The codes ranged from 0.6 to 1.3 (Table 1). The following equations were derived from the multivariate regressions of bulk density, interval transit time, and neutron porosity log data as independent values to identify the log lithology (dependent value) (Eqs. (7) and (8)):

$$\text{Log (Lithology)} = (0.7 + 0.19 * \rho b - 0.0035 * \Delta t + 0.002 * \text{NPHI}) \quad (7)$$

$$\text{Log (Lithology)} = (0.7 + 0.06 * \rho b + 0.0033 * \Delta t - 0.012 * \text{NPHI}) \quad (8)$$

Equations (7) and (8) were generated and applied to the Kz-29 and Kz-40 wells, respectively. The resulting log lithologies varied from limestone to marly limestone in the Kz-29 well (Fig. 3), and from limestone to marl in the Kz-40 well (Fig. 4). Statistical

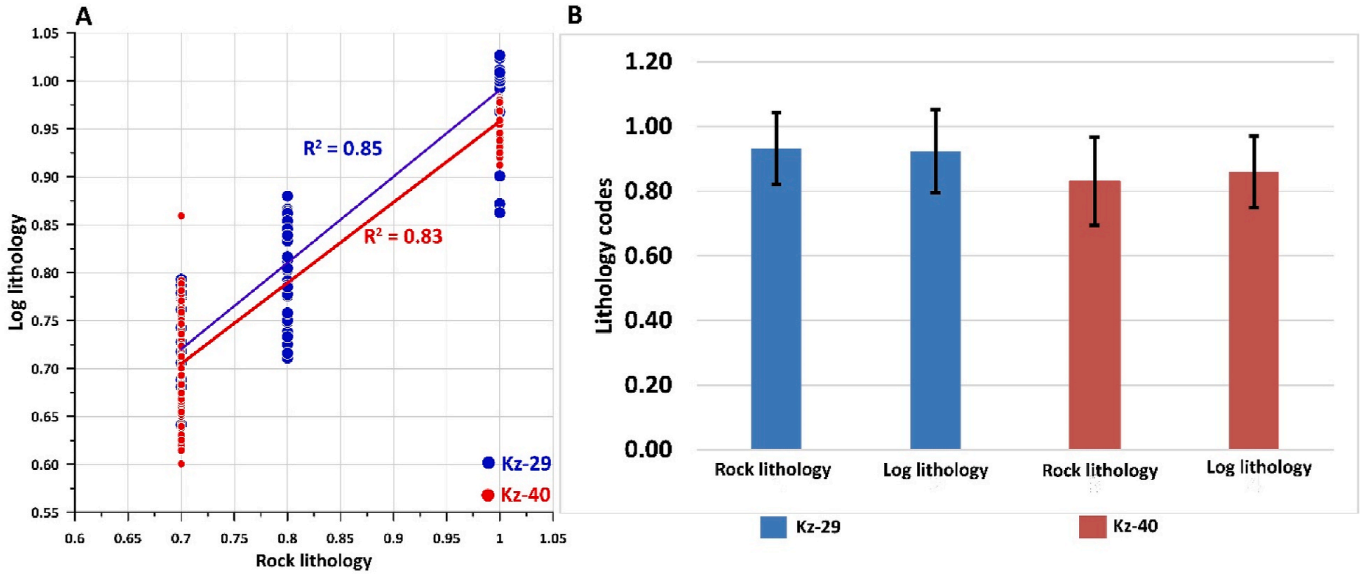

Fig. 5. Bivariate plots (A) and error bar chart (B) of rock lithology codes *vs.* log lithology codes.

correlations were made between the log lithologies and the rock lithologies (cores and cuttings) by using the coefficient of determination (Fig. 5A), root mean square error (RMSE), mean absolute error (MAE), and error bar (Fig. 5B) to show model performance, as well as the error percentage line (Error%) to show the percentages of error between actual and predicted values (Figs. 3 and 4, green-filled lines). A good match was obtained, with the coefficient of determination equalling 0.85 and 0.83 for the Kz-29 and Kz-40 wells, respectively (Fig. 5A). The values for MAE and RMSE for Kz-29 well are 0.00002 and 0.0007, and 0.000021 and 0.0007 for Kz-40, respectively.

Fig. 5B shows the error bar graph, which shows the average and standard deviation of each of the measured (rock lithology) and predicted (log lithology) values for the Kz-29 well and Kz-40 well. The graph showed that the models are well-performing and can be used to predict the lithology. However, there are some errors presented between the actual and predicted lithology in Figs. 3 and 4 (green-filled line). The average errors are 4 % and 8 % in the Kz-29 and Kz-40 wells, respectively.

Based on the average of the error percentage line, Equation (7) (Fig. 3) provides a more accurate identification of all lithology classes during the performance validation of the multivariate system than Equation (8) (Fig. 4). Finally, the models were applied to predict the log lithology for the entire thickness of the Kometan Formation in both wells and compared it with the observed lithologies (Figs. 3 and 4).

4.2. Shale content

The shale volumes determined from the gamma-ray log (Figs. 3 and 4) showed that the studied formation can be divided into three zones: 2802–2868 m, with shale volumes ranging from 5.4 % to 18 % (mean: 8.8 %), 2868–2920 m, with volumes ranging from 3.7 % to 23 % (mean: 16 %), and 2920–2948 m, with volumes from 3.7 % to 21.5 % (mean: 7.4 %) in Kz-29 well. In Kz-40 well, these three intervals corresponded to depths of 2711–2792 m, 2792–2861 m, and 2862–2898 m, with mean shale volume values of 7 % (from 4 % to 11.4 %), 12.6 % (3.2 %–22 %), and 8 % (3.6 %–21.9 %), respectively. In both wells, the middle "shaly" part contained more shale than the "clean" upper and lower parts (Figs. 3 and 4). Gamma rays computed and measured from the available rock samples (Figs. 3 and 4) validated this. A good correlation between the gamma-ray log and gamma-ray rock was represented by the correlation coefficients equalling 0.70 and 0.82 for wells Kz-29 and Kz-40 wells, respectively (Fig. 6).

The concentrations of Th (thorium), U (uranium), and K (potassium) from the spectral gamma-ray data in the Kz-29, Kz-40, and K-216 wells and the interpretations of the mineral carriers of the gamma-ray signal, and the paleoenvironmental conditions are shown in Fig. 7. The Kz-40 well has relatively high average concentrations of Th concentration (4.8 ppm) and concentration of U (2.3 ppm). The average Th/U ratio is high (4 ppm). The average content of K (0.6 %) is low (Fig. 7B). It is inferred here that kaolinite, montmorillonite, chlorite, and heavy Th-bearing minerals are the most common carriers of the gamma-ray signal (Fig. 7A). The Kz-29 well has relatively a moderate average of Th concentration (4.5 ppm) and average U concentration (1.9 ppm). The average ratio of Th/U is low (2.6 ppm). The average potassium content is relatively higher (0.8 %) (Fig. 7B). Montmorillonite is possibly the major mineral carrier of the signal, along with potassium evaporite and Th-bearing heavy minerals (Fig. 7A). K-216 has a low average Th (3.4 ppm) and average U content (1.8 ppm). The average ratio of Th/U is moderate (3.9 ppm). The potassium contents vary but they are often moderate (0.7 %) (Fig. 7B). The most common mineral carrier of the signal is likely montmorillonite, with some potassium evaporite present (Fig. 7A).

To evaluate the sedimentary conditions and variations in Th and U variables along the Kometan Formation at the examined wells

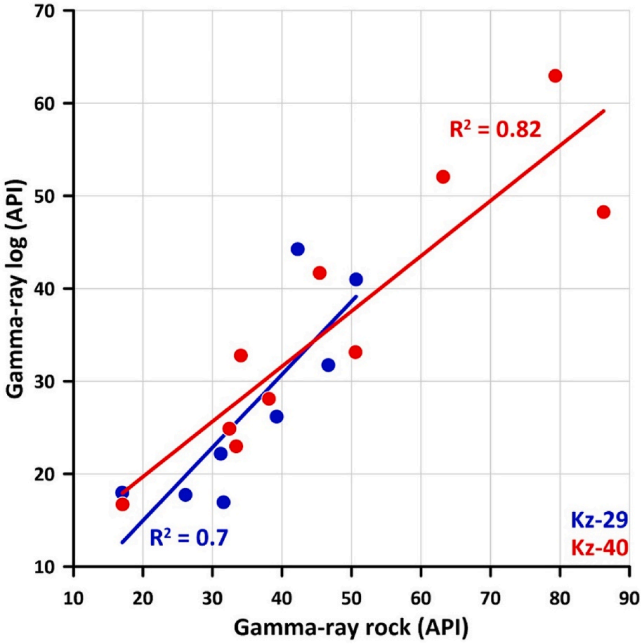

Fig. 6. Correlation between gamma-ray log and measured gamma-ray for Kz-29 and Kz-40 wells.

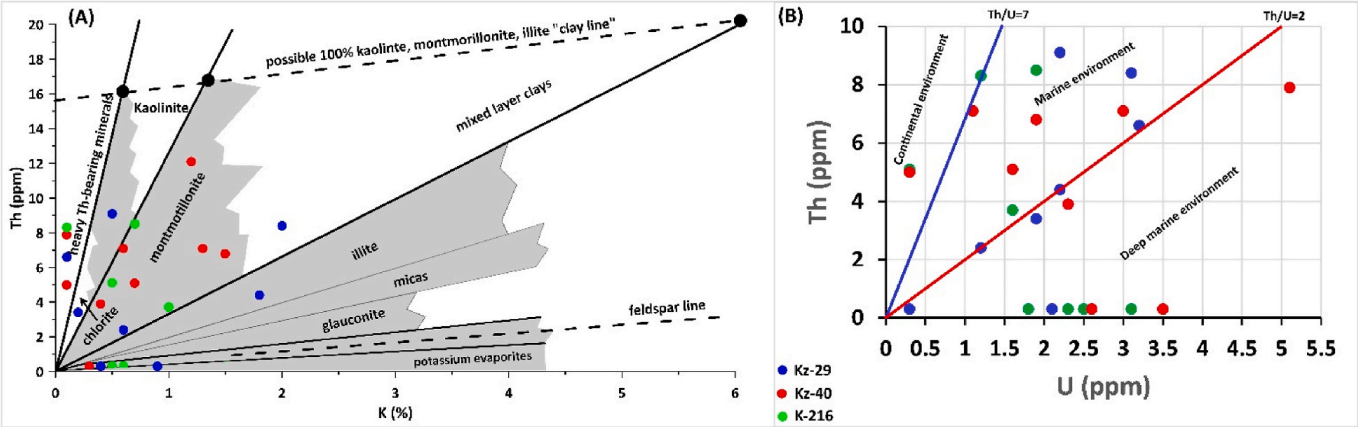

Fig. 7. The Th-K cross plot is used to identify types of clay minerals (**A**) [49] and the Th-U cross plot is used to identify depositional environments (**B**) [53].

(Kz-29, Kz-40, and K-216), It has utilized cross plots depicting the individual Th and U values (Fig. 7B). It employed the threshold values established in Fig. 7B to discern the prevailing environmental conditions. Specifically, a Th/U ratio greater than 7 signifies a continental environment characterized by oxidizing conditions, a Th/U ratio less than 7 suggests marine sedimentation and a Th/U ratio below 2 indicates the presence of marine black shales or phosphorites with reducing conditions.

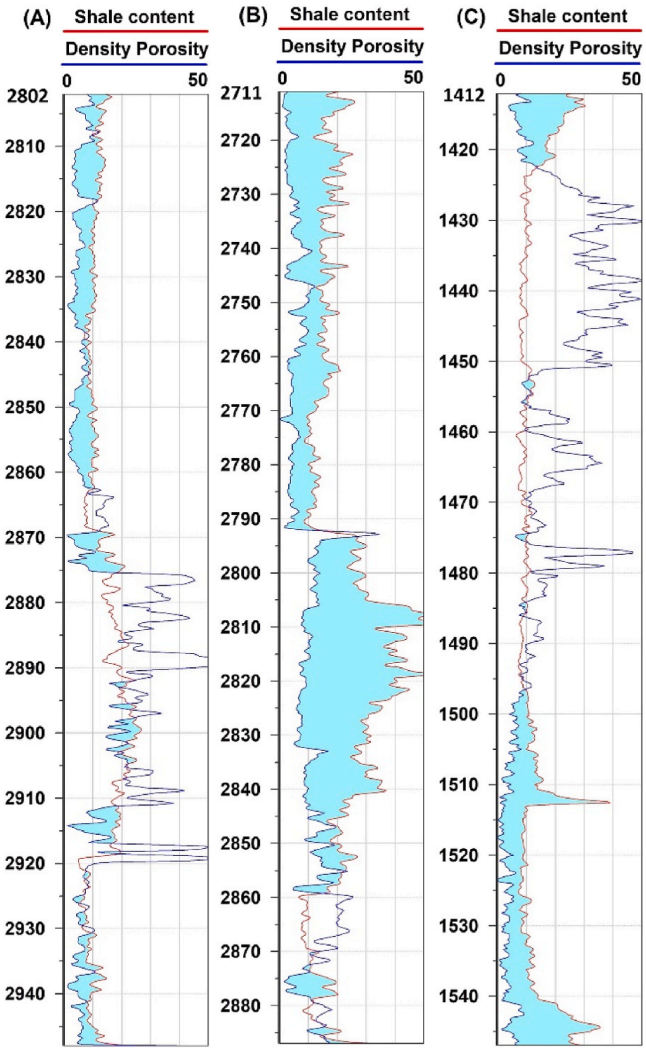

Fig. 8. Density porosity and shale content relationship in percent for wells Kz-29 (A), Kz-40 (B), and K-216 (C). Note the crossover sections (cyan colour) in which the shale contents impact the density porosity.

Table 3
Element concentrations in the studied wells (Kz-29, and Kz-40) of the Kometan Formation.

Well	Depth	Al	Si	P	S	K	Ca	Ti	Mn	Fe	V	Ni	Cu	Zn	As	Rb	Sr	Zr	Mo	Pb
	(m)	wt. %	wt. %	wt. %	wt. %	wt. %	wt. %	wt. %	wt. %	wt. %	ppm	ppm	ppm	ppm	ppm	ppm	ppm	ppm	ppm	ppm
Kz-29	2802	1.03	3.71	1.21	0.11	0.52	34.42	0.09	0.01	0.56	83	28	16	13	4	10	894	18	2	2
Kz-29	2820	0.87	3.48	1.22	0.07	0.42	34.39	0.12	0.01	0.46	351	34	20	16	3	9	880	17	1	3
Kz-29	2840	0.77	3.32	1.20	0.11	0.35	34.30	0.11	0.01	0.46	273	34	21	46	3	9	968	16	1	2
Kz-29	2860	2.00	5.33	1.12	0.13	0.62	30.08	0.15	0.01	1.17	105	30	16	18	4	18	732	33	1	3
Kz-29	2880	3.76	8.27	0.95	0.19	1.00	23.05	0.33	0.03	1.87	859	19	15	27	6	32	494	61	1	5
Kz-29	2900	6.06	11.88	0.70	0.15	1.42	13.78	0.42	0.03	3.92	346	28	30	17	6	45	421	94	2	5
Kz-29	2940	5.60	11.28	0.81	0.14	1.34	17.10	0.34	0.03	3.17	127	31	16	19	6	41	414	80	1	5
Kz-29	2950	1.90	4.91	1.14	0.18	0.53	29.89	0.14	0.01	1.19	95	22	15	24	4	17	440	33	2	3
Kz-40	2710	1.36	4.50	1.16	0.11	0.66	32.23	0.11	0.01	0.61	127	22	21	13	4	14	1201	24	1	3
Kz-40	2730	0.78	3.09	1.20	0.07	0.43	35.21	0.06	0.00	0.34	56	27	17	10	2	7	1378	15	1	3
Kz-40	2750	0.53	2.56	1.22	0.07	0.21	35.78	0.06	0.01	0.30	84	27	12	14	2	6	1380	13	1	3
Kz-40	2770	0.74	3.44	1.21	0.07	0.37	34.20	0.07	0.01	0.41	51	30	23	17	2	9	974	15	1	4
Kz-40	2790	0.67	3.18	1.21	0.07	0.28	34.07	0.08	0.01	0.62	84	28	19	11	3	9	837	16	1	4
Kz-40	2810	5.56	11.79	0.76	0.18	1.26	15.74	0.35	0.03	3.35	114	26	18	23	7	44	468	85	1	7
Kz-40	2830	5.60	11.41	0.78	0.14	1.33	16.19	0.36	0.03	3.62	232	29	23	31	8	42	446	78	1	6
Kz-40	2850	4.76	10.17	0.88	0.14	1.06	19.05	0.30	0.03	2.84	111	35	13	28	6	38	513	68	0	5
Kz-40	2870	2.86	6.89	1.02	0.21	0.71	25.60	0.18	0.02	1.47	47	19	13	27	4	26	452	43	1	4
Kz-40	2888	1.93	4.97	1.16	0.32	0.47	28.65	0.13	0.01	1.61	74	28	22	27	4	16	599	32	1	5

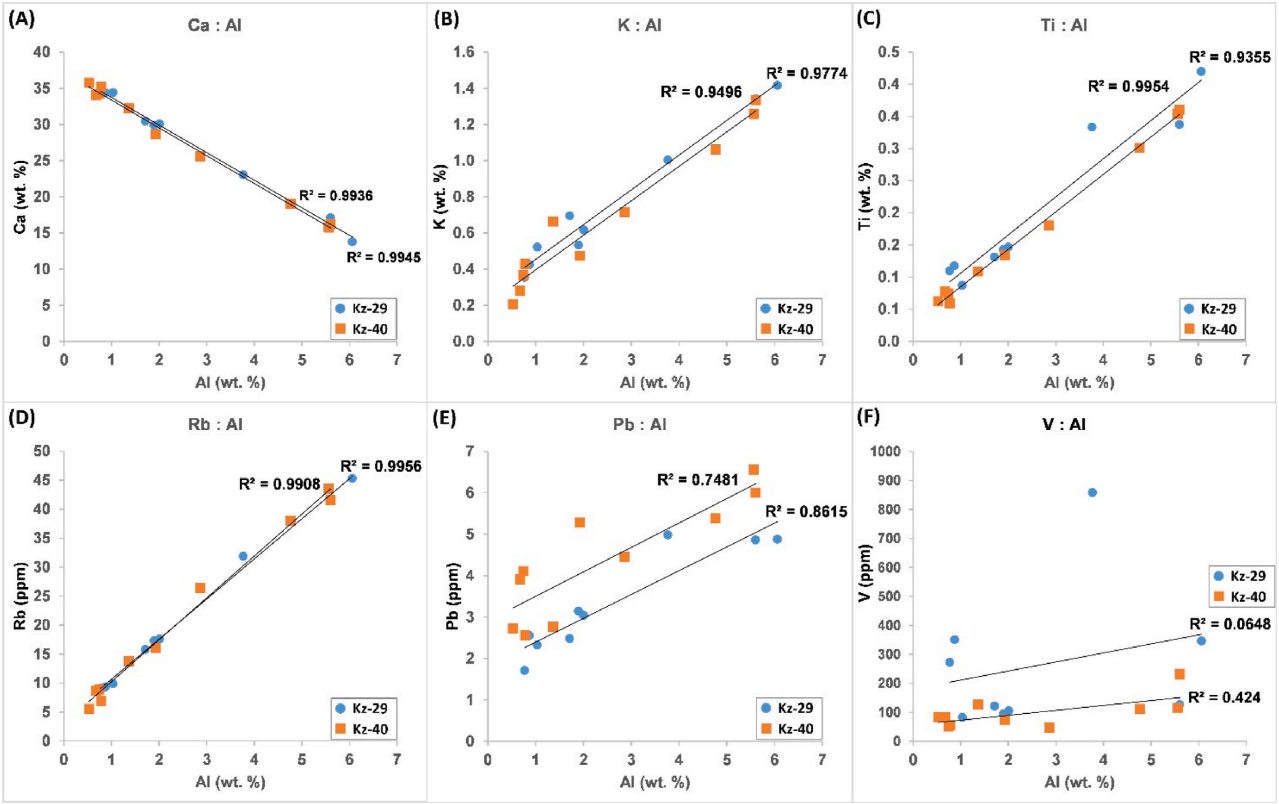

Fig. 9. Bivariate graphs of Ca (A), K (B), Ti (C), Rb (D), Pb (E), and V (F) element concentrations plotted versus Al in powdered rock samples from the Kometan Formation in two wells (Kz-29 and Kz-40). Take note of the almost perfect positive correlation between Rb and Al, the nearly perfect negative correlation between Ca and Al, and the varying quantities of K, Ti, Pb, and V in various wells.

In a subsurface geological context, the interplay between shale content and porosity is crucial for understanding the porosity variations at different depths. Fig. 8 illustrates a clear relationship between increasing shale content and decreasing density porosity, especially in crossovers (cyan-filled color) within specific depth intervals. In the Kz-29 well (Fig. 8A), at 2819 m depth, with a relatively low shale content of 9.8 %, the density porosity is 8 %. As we descend to 2830 m, encountering a moderate shale content of 11 %, the density porosity decreases to 3.5 %. Further, at a depth of 2870 m, where shale content is higher at 14 %, the density porosity diminishes to 2.3 %. In the shallower depth of Kz-40 (2711–2747 m) (Fig. 8B), characterized by decreasing shale content (e.g., from 20 to 13 %), density porosity values tend to be higher, ranging from 2.4 % to 12 %. This suggests a more porous and less dense subsurface in these intervals. However, as we progress to greater depths (2762 m) where shale content becomes more pronounced (e.g., 13 %–20 %), there is a consistent decline in density porosity, dropping to the range of 12 %–3 %. In the K-216 well (Fig. 8C), the range of density porosity spans from a minimum of 0.01 % to a maximum of 53 %, indicating considerable heterogeneity in reservoir quality. The shale content ranges from 6.5 % to 39 %. This illustrates a discernible inverse relationship, where an increase in shale content correlates with a reduction in density porosity.

Table 3 shows the elemental quantities of the Kometan Formation. Elements typically associated with siliciclastic detrital grains such as quartz, feldspars, heavy minerals, and aluminosilicates (K, Ti, Rb, Pb, and V) showed a high positive correlation with Al (R^2 = 0.97, 0.99, 0.99, 0.86, and 0.06 respectively) (Fig. 9B–F). In contrast, Al is negatively correlated with Ca (R^2 = 0.98) (Fig. 9A), which are typically bound to biomineralised phases, calcite, and apatite. Sulfur and other elements such as V, Ni, Cu, Zn, and Mo, which typically bind to authigenic phases, were not correlated with Al (Table 3). The variable concentrations of K, Ti, Pb, and V demonstrate

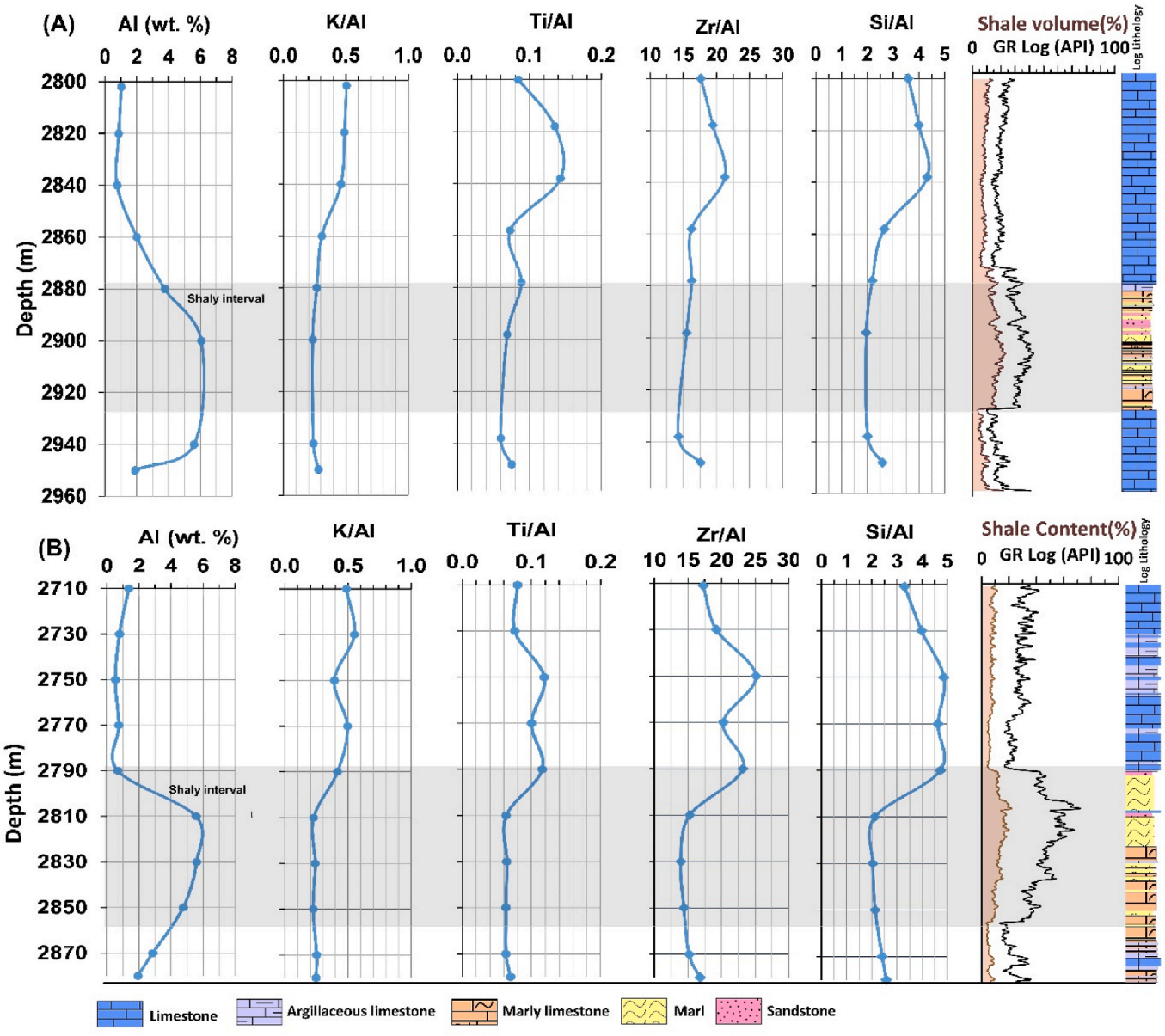

Fig. 10. Vertical distribution of selected elemental proxies and their correlation with selected log data (gamma ray and shale content) in the Kz-29 well (A) and Kz-40 wells (B).

the geochemical variability between the studied wells (Fig. 9).

The distribution of the elemental proxies shows a relationship with the principal lithologies. The limestone in the Kz-40 well (depth 2711–2790 m) has low Al concentrations (1.0 wt%) and relatively high K/Al (0.4–0.6) and Ti/Al (0.08–0.12) ratios. On the other hand, marls and argillaceous limestone from the same well have distinctly higher Al concentrations (2.0–6.0 wt%) and lower K/Al (0.2) and

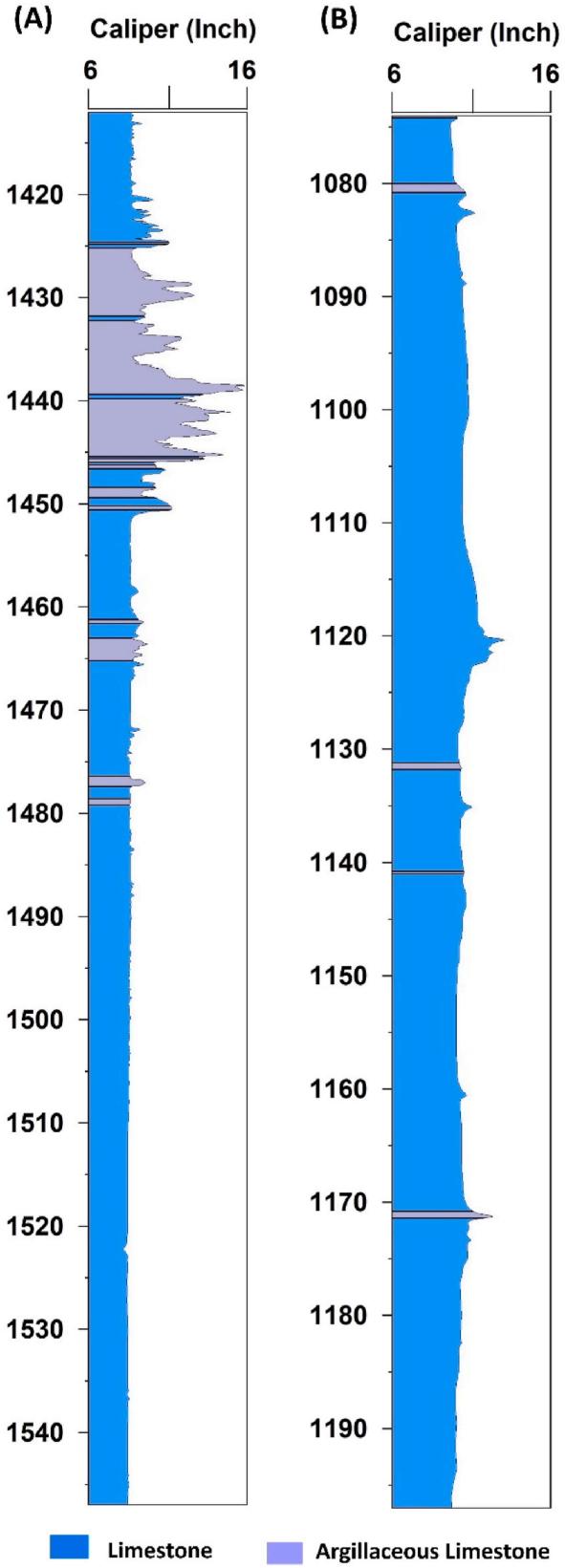

Fig. 11. Profile curve of caliper log filled with the predicted lithology using Equation (7) for the wells of K-216 (A) and K-218 wells (B).

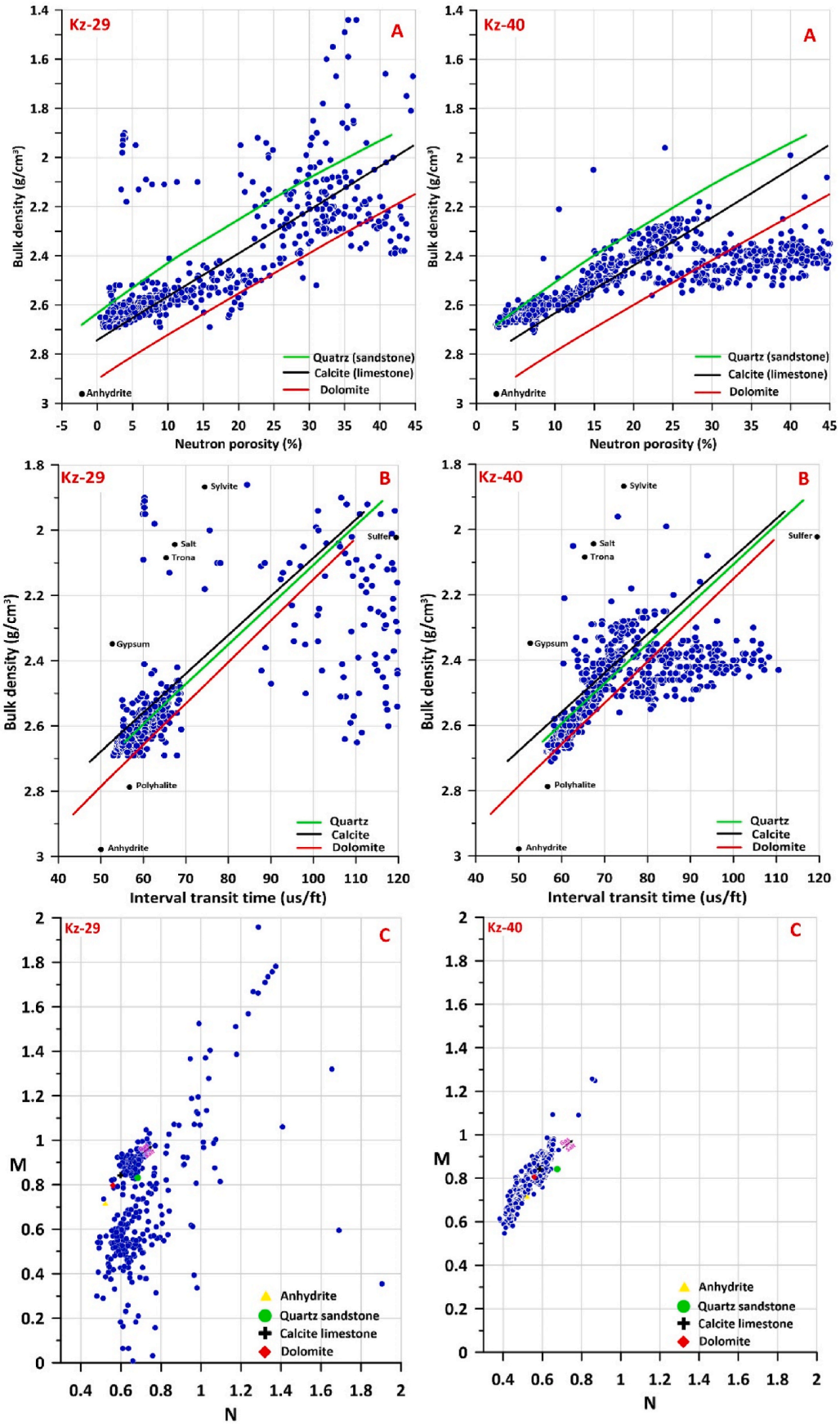

Fig. 12. Lithology identification from N-D (A), interval transit time-bulk density (B), and M-N (C) cross plots for the wells Kz-29 and Kz-40 wells [55].

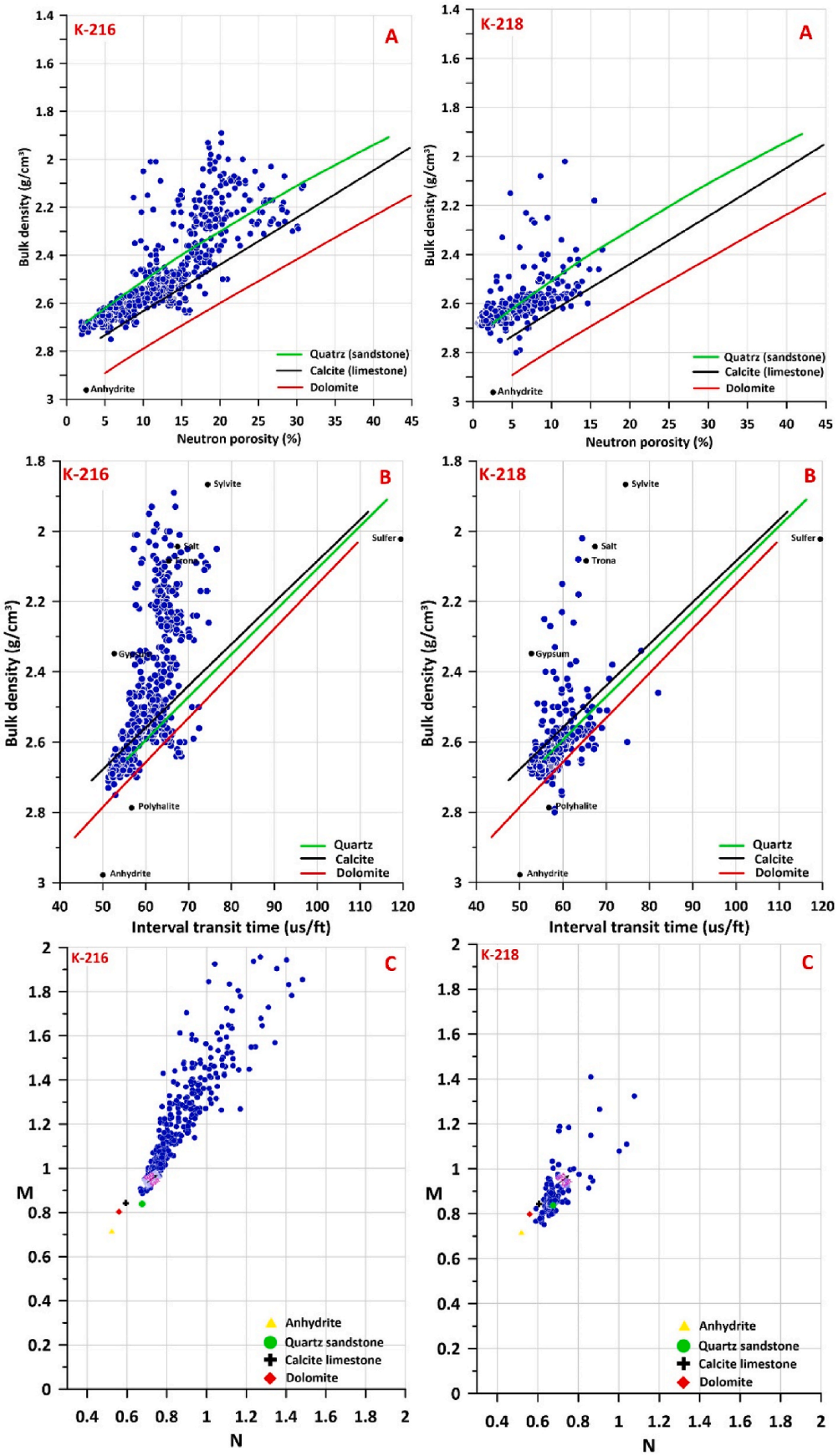

Fig. 13. Lithology identification from N-D (A), interval transit time-bulk density (B), and M-N (C) cross plots for the wells K-216 and K-218 wells [55].

Ti/Al (0.06) ratios (Fig. 10B). The Al concentrations correlated with the shale volumes as determined from the gamma-ray logs, and they could be considered an independent proxy of the shale contents in the Kometan Formation (Figs. 3 and 4). The concentrations of Al increased in the shaly intervals between 2868–2920 m and 2792–2861 m depths for the Kz-29 (Fig. 10A) and Kz-40 (Fig. 10B) wells, respectively, as demonstrated by the gamma-ray values, which contrasted with those of the overlying and underlying clean units (Figs. 3 and 4).

4.3. Lithology identification and prediction

The well log data show that the Kometan Formation can be separated into upper, middle, and lower zones (Figs. 3 and 4). The middle part is more shaly than the lower and upper parts. In selected borehole intervals (2876–2920 m and 2792–2874 m for wells Kz-29 and Kz-40 wells, respectively), the increased shaliness in the middle part is highlighted by the caliper logs, increased gamma-ray values, highly affected neutron log values due to increased drill mud thickness and shale contents, decreased bulk density, and increased interval transit times in the sonic logs (Figs. 3 and 4). In the Kz-29 well, the lower and upper units consist of clean beds, as indicated by the caliper log and the low values of the gamma-ray log. The average values of density (2.61 g/cc) and sonic (59 us/ft) logs indicate that the lower and upper units consisted of porous limestone. The average density and sonic log values in the upper unit of the Kz-40 well are nearly identical to those of Kz-29, indicating the same limestone lithology in both wells. The lower unit in the Kz-40 well has a lower average density (2.4 g/cc), a higher average interval transit time (70 us/ft), and higher gamma-ray log values, representing argillaceous and marly limestone (Figs. 3 and 4).

The derived model (Eq. (7)) with a coefficient of determination (R^2) higher than 0.8 has been tested to predict the lithology for the Kometan Formation in other wells (Kirkuk 216 (K-216) and Kirkuk 218 (K-218)) (Fig. 1). The lithology estimated by the equation mainly consists of limestone and argillaceous limestone (Fig. 11). The thickness of the argillaceous limestone is higher in K-216 well (Fig. 11A) than in K-218 well (Fig. 11B), which is about 25 m. The result could be accepted because the Kometan Formation mainly consists of limestone with a small thickness of marly or argillaceous limestone in different locations.

Figs. 12 and 13 show the neutron-density cross plots (N-D) (Figs. 12A and 13A), interval transit time-bulk density (Figs. 12B and 13B), and neutron-density-sonic cross plots (M-N) (Figs. 12C and 13C), for the Kz-29, Kz-40, K-216, and K-218 wells. In the log analysis, the neutron-density cross plot is used to determine lithology from neutron porosity and bulk density. This plot shows that the lithology of the Kometan Formation is mainly limestone and dolomite with some siliciclastic rocks (Kz-29, and Kz-40 wells) (Fig. 12A), while limestone and siliciclastic rocks are in K-216 and K-218 wells (Fig. 13A). The interval transit time-bulk density cross plot identified lithology from interval transit time and bulk density. It demonstrates that the examined formation's lithology comprises dolomite, sandstone, and limestone throughout the whole well system (Figs. 12B and 13B). It shows that the data is mostly plotted in gypsum and salt areas in the K-216 well (Fig. 13B). The M-N cross plot identifies binary and ternary mineral mixtures using density, neutron, and sonic logs. The identified lithologies are mainly dolomite, limestones, and anhydrite in the Kz-40 well. In the Kz-29 well, limestone is dominant and other data are plotted under the anhydrite region which is considered a shale region (Fig. 12C). The data is mostly plotted in the salt region or toward the gas direction in the K-216 well (Fig. 13C). Limestone admixture with siliciclastic is dominant in the K-218 well and the rest of the data are plotted in the salt or gas region (Fig. 13C). The results shown on the cross plots are highly different from the rock-described lithology relative to predicted lithology.

5. Discussion

The well log lithologies show a good statistical correlation with the rock lithologies, with $R^2 = 0.83$ to 0.85, suggesting that the multivariate regression of log data, combined with fuzzy logic, is a promising tool for identifying and quantifying lithologies from well logs. However, the studied succession is a relatively simple, mixed carbonate-siliciclastic system with variable clay contents in fine-grained carbonates. The presented approach would be more challenging but worth attempting for lithologically complex reservoir systems comprising sandstones, shales, and carbonates with variable grain sizes, porosity, permeability, shale contents, mineral compositions of framework grains, and degrees of cementation.

Approaching the coefficient of determination (R^2) of 1 indicates higher accuracy in the quality of the predictor. In this study, the R^2 value depends on rock descriptions, which are the anchor points and are used to calibrate the regression coefficient of independent variables. Rock description is a qualitative method, so it is possible to diminish the quality of the lithology nomenclature due to the lower efficiency in recognizing mineral compositions relative to the instrumental method. As a result, the predicted lithology (log lithology) could differ from the described lithology (rock lithology). This could also arise if the same formation has different error percentages (Figs. 3 and 4, green-filled lines) from various wells. However, this research considered the higher coefficient of determination ($R^2 = 0.85$) to predict the lithology of the studied formation for different wells. There are three reasons for having different error percentages in this study: i) despite diminishing the effect of the borehole environment by applying the multivariate regression approach to some extent, the Kz-40 well is relatively more impacted than the Kz-29 well (Figs. 3 and 4). ii) the core samples are not standard practice due to the non-availability of the whole interval due to technical and economic reasons. iii) the cutting samples, which are affected by washing, sustained mixing, and contamination during transportation of the drilling mud to the surface are prone to errors in lithological reconstructions. Taking the borehole environment into account we can apply the model where the coefficient of determination is higher than 0.8 (Eq. (7)) to predict the lithology of the Kometan Formation in different wells. This could be the most powerful and cost-effective way to quantify or semi-quantify lithology from well log data (Fig. 11).

The shale volume calculated from the gamma-ray log (Figs. 3 and 4) shows a good match with the rock lithology. The division of the Kometan Formation into three units based on shale contents is consistent with the density (ρb), sonic (Δt), neutron (NPHI) log shapes,

and the computed gamma-ray values calculated from laboratory gamma-ray spectrometry of the rock samples (Figs. 3 and 4). In the middle part of the formation which is composed of marl, marly limestone, and argillaceous limestone, the neutron log increases due to the high hydrogen index in shale; in both free and bound water, the bulk density decreases, and the interval transit time increase, which is consistent with the published log values for limestone and shale [45,49]. Accordingly, the log data indicated limestone-dominated lithologies (clean beds) in the upper and lower parts of the Kometan Formation (Figs. 3 and 4). The total gamma-ray log values are probably influenced by drilling mud, especially at depths ranging from 2880 to 2890 m and 2830–2850 m for the Kz-29 and Kz-40 wells, respectively). The computed gamma-ray and total gamma-ray values from rocks were used to validate the accuracy of the gamma-ray logs (Figs. 3 and 4).

Based on the characteristics observed in the well-log, particularly the gamma-ray log, the Kometan Formation is subdivided into three distinct intervals in the subsurface: the lower clean interval (low gamma-ray), the middle shaly interval (high gamma-ray), and the upper clean interval (low gamma-ray) (Figs. 3 and 4). Our interpretation suggests that the wedge of mixed carbonate–siliciclastic sediments, as indicated by the middle shaly interval, signifies a progradation of deposits from a more proximal onto the open shelf/pelagic deposits. Consequently, the upward increase in gamma-ray trends in proximal settings is indicative of progradation (regression), while the upward decrease signifies retrogradation (transgression) [54].

The Th/U ratios serve as key indicators of redox conditions during sedimentation [53]. In the Kz-29 well, the Th/U ratios range from 0.1 to 7.9, reflecting varying redox states (Fig. 7B). Intervals with higher Th/U ratios suggest more oxidizing conditions, possibly indicative of well-drained environments or periods of increased organic matter decomposition [49]. Conversely, lower ratios may imply more reducing conditions. In Kz-40 well, the wide variation in Th/U ratios (from 0.1 to 16.7) indicates substantial changes in redox conditions during deposition (Fig. 7B). K-216 well displays Th/U ratios ranging from 0.1 to 17.0, suggesting dynamic redox variations during sedimentation (Fig. 7B). These fluctuations in Th/U ratios across all samples imply dynamic shifts in paleoenvironmental conditions, potentially influenced by factors such as sea-level fluctuations, or changes in depositional settings [54]. The integration of this data with additional geological proxies and sedimentary features will provide a more comprehensive understanding of the paleoenvironmental evolution in the region, contributing to a refined interpretation of the geological history in the study area.

The data presented in Fig. 8 reveals a clear relationship between shale content and density porosity in the studied formation. As the shale content increases, there is a noticeable trend of decreasing density porosity. This inverse correlation suggests that the presence of shale has a compaction effect on the porous spaces within the formation, leading to a reduction in density porosity [53]. Shale, being a fine-grained sedimentary rock, tends to fill and occupy pore spaces, limiting the ability of fluids to flow through the formation. Consequently, the density porosity, which is a measure of the void spaces within the rock, diminishes with higher shale content [53]. However, at the interval of 2875–2892 in Kz-29, 2792–2850 in Kz-40, and 1423–1495 in K-216, despite the increase in shale, the porosity is also high, which may be due to fractures in these intervals, which is shown by the caliper log (Fig. 3) and revealed by Hussein [52]. In addition, the effect of shale on the reduction of pores is seen. This information is crucial for understanding the subsurface characteristics of the geological formation, as it provides insights into the permeability and fluid storage capacity of the rock, which are vital considerations in various applications such as hydrocarbon exploration and reservoir engineering [53].

The elemental concentrations (Table 3, Figs. 9 and 10) further support the division of the Kometan Formation into lower, middle, and upper lithological units, as inferred from the rock samples and log data. The concentrations of lithogenic elements such as Al, Si, K, and Fe, and authigenic Ca from depths around 2900–2940 m in the Kz-29 well and 2810–2830 m in the Kz-40 well supported the subdivision of the formation into a middle shaly part and cleaner lower and middle parts. Relatively higher Al, Si, K, and Fe, and lower Ca concentrations in the middle part indicated an increased siliciclastic input and/or decreased primary carbonate production [50,51].

The studied technique (multivariate regression) achieved another benefit, which is the validation of the accuracy of the most widely used lithology cross plots (Figs. 12 and 13). The result of this technique (Figs. 3, 4 and 11), especially Equation (7), which is highly comparative with the rock sample identifications and descriptions, demonstrated that the cross plots are not precise enough to identify complex lithology (Figs. 12 and 13). The accuracy of cross plots is lower, especially in bad borehole conditions (enlargement). The borehole environment had a greater impact on the sonic, density, and neutron log in the enlargement interval than in the gauge interval. The borehole enlargement reduced the actual bulk density, increased the interval transit time, and overestimated neutron porosity. This is due to a higher drilling mud thickness between the log tools and the borehole wall, which affected logs to a mud value. The over and underestimating of measured values from these logs can be seen on the cross plots (Figs. 12 and 13), which resulted in an incorrect interpretation of lithology. This can be noticed by comparing the results of Figs. 3 and 4 with the results of Figs. 12 and 13, respectively. The wells Kz-29, Kz-40 (Figs. 3 and 4), and the K-216 wells (Fig. 11A) are enlarged and washout in the borehole wall, while the K-218 well is in better condition (Fig. 11B), so the cross plots identified a more precise lithology in the K-218 well, especially the N-D cross plot (Fig. 13A).

6. Conclusions

The following conclusions can be derived based on the approach of combining multivariate regression analyses of wireline logs and core data of the Upper Turonian-Lower Campanian carbonate rock of the Kometan Formation:

- In the absence of a rock sample, the multivariate regression of well log data, combined with fuzzy logic, is a promising tool for identifying and quantifying lithologies from neutron log, sonic log, and density log.
- The model built from the applied approach with the higher coefficient of determination can be used for all the studied wells.
- The wire-line logging data obtained was analyzed and computed values confirmed the lithologic sequence of the Kometan Formation, which is limestone, argillaceous limestone, marls, and marly limestone.

- The multivariate regression method is more precise than the lithology cross-plot approach, especially in bad-hole conditions.
- The approach can avoid borehole environments and unwanted effects on well log data due to the calibration process, which relies on rock samples.

Data availability

Data will be made available on request.

CRediT authorship contribution statement

Hussein S. Hussein: Writing – review & editing, Writing – original draft, Visualization, Validation, Supervision, Software, Resources, Project administration, Methodology, Investigation, Funding acquisition, Formal analysis, Data curation, Conceptualization. **Howri Mansurbeg:** Writing – review & editing, Validation, Supervision, Resources, Funding acquisition. **Ondřej Bábek:** Writing – review & editing, Writing – original draft, Validation, Supervision, Data curation.

Declaration of competing interest

The author whose name is listed immediately below certifies that they have no affiliations with or involvement in any organization or entity with any financial interest (such as honoraria; educational grants; participation in speakers' bureaus; membership, employment, consultancies, stock ownership, or other equity interest; and expert testimony or patent-licensing arrangements), or non-financial interest (such as personal or professional relationships, affiliations, knowledge or beliefs) in the subject matter or materials discussed in this manuscript.

Acknowledgements

The North Oil Company, Iraq, and Internal Grant project IGA PrF 2021 013 each contributed a portion of their funding to this study. The Department of Geology at Palacky University and the Fischer Scholarship Program are both gratefully acknowledged by the authors.

References

[1] Y. Li, R. Anderson-Sprecher, Facies identification from well logs: a comparison of discriminant analysis and naive Bayes classifier, J. Pet. Sci. Eng. 53 (3) (2006) 149–157, https://doi.org/10.1016/j.petrol.2006.06.001.
[2] Z.F. Sun, C.Y. Lin, P. Zhu, J. Chen, Analysis and modeling of fluvial-reservoir petrophysical heterogeneity based on sealed coring wells and their test data, Guantao Formation, Shengli oilfield, J. Pet. Sci. Eng. 167 (2018) 785–800, https://doi.org/10.1016/j.petrol.2017.11.006.
[3] X. Wang, J. Hou, S. Song, D. Wang, L. Gong, K. Ma, Y. Liu, Y. Li, L. Yan, Combining pressure-controlled porosimetry and rate-controlled porosimetry to investigate the fractal characteristics of full-range pores in tight oil reservoirs, J. Pet. Sci. Eng. 171 (2018) 353–361, https://doi.org/10.1016/j.petrol.2018.07.050.
[4] A.N. Al-Dujaili, M. Shabani, M.S. AL-Jawad, Characterization of flow units, rock and pore types for Mishrif Reservoir in West Qurna oilfield, Southern Iraq by using lithofacies data, J. Pet. Explor. Prod. Technol. 11 (2021) 4005–4018, https://doi.org/10.1007/s13202-021-01298-9.
[5] C. Vipulanandan, A. Mohammed, New Vipulanandan failure model and property correlations for sandstone, shale, and limestone rocks, in: IFCEE, 2018, pp. 365–376. https://ascelibrary.org/doi/epdf/10.1061/9780784481585.036.
[6] A. Mohammed, Vipulanandan models to predict the mechanical properties, fracture toughness, pulse velocity and ultimate shear strength of shale rocks, Geotech. Geol. Eng. 37 (2019) 625–638, https://doi.org/10.1007/s10706-018-0633-5.
[7] W. Mahmood, A. Mohammed, S.H. Hussein, Predicting mechanical properties and ultimate shear strength of gypsum, limestone and sandstone rocks using Vipulanandan models, Geomechanics Geoengin. 12 (2) (2020) 90–106, https://doi.org/10.1080/17486025.2019.1632494.
[8] C. Vipulanandan, A. Mohammed, Hydraulic Fracturing Fluid Modified with Nanosilica Proppant and Salt Water for Clay Shale Rocks, American Association of Drilling Engineers, Houston, TX, USA, 2015, pp. 1–14. https://www.aade.org/application/files/7515/7261/1266/AADE-15-NTCE-38.pdf.
[9] H.C. Chang, D.C. Kopaska-Merkel, H.Ch Chen, S.R. Durrans, Lithofacies identification using multiple adaptive resonance theory neural networks and group decision expert system, Comput. Geosci. 26 (5) (2000) 591–601, https://doi.org/10.1016/S0098-3004(00)00010-8.
[10] O. Mahmoodi, R.S. Smith, D.K. Tinkham, Supervised classification of down- hole physical properties measurements using neural network to predict the lithology, J. Appl. Geophys. 124 (2016) 17–26, https://doi.org/10.1016/j.jappgeo.2015.11.006.
[11] Y. Tian, H. Xu, X.Y. Zhang, H.J. Wang, T.C. Guo, L.J. Zhang, X. Gong, Multi-resolution graph-based clustering analysis for lithofacies identification from well log data: case study of intraplatform bank gas fields, Amu Darya Basin, Appl. Geophys. 13 (2016) 598–607. https://link.springer.com/article/10.1007/s11770-016-0588-3.
[12] J. Zhang, Sh Liu, J. Li, L. Liu, H. Liu, Zh Sun, Identification of sedimentary facies with logs: an indirect approach with multinomial logistic regression and artificial neural network, Arabian J. Geosci. 10 (2017) 1–9. https://link.springer.com/article/10.1007/s12517-017-3045-6.
[13] P.G. Killeen, Borehole geophysics: exploring the third dimension, in: A. Gubins (Ed.), Exploration 97: Fourth Decennial International Conference on Mineral Exploration, 1997, pp. 31–42. https://www.911metallurgist.com/blog/wp-content/uploads/2015/10/Borehole-Geophysics-Exploring-The-Third-Dimension.pdf.
[14] E. Sfidari, A. Kadkhodaie-Ilkhchi, H. Rahimpour-Bbonab, B. Soltani, A hybrid approach for lithofacies characterization in the framework of sequence stratigraphy: a case study from the South Pars gas field, the Persian Gulf basin, J. Pet. Sci. Eng. 121 (2014) 87–102, https://doi.org/10.1016/j.petrol.2014.06.013.
[15] A. Abdel-maksoud, A.A. Radwan, Integrating 3D seismic interpretation, well log analysis and static modelling for characterizing the Late Miocene reservoir, Ngatoro area, New Zealand, Geomech. Geophys. Geo-Energy Geo-Resour. 8 (2) (2022) 63.
[16] E.A. Abdullah, A. Abdelmaksoud, M.A. Hassan, Application of 3D static modelling in reservoir characterization: a case study from the qishn Formation in sharyoof oil field, masila basin, Yemen, Acta Geologica Sinica-Eng. Ed. 96 (1) (2022) 348–368.
[17] C. Zhang, Z. Zhang, Y. Chen, Y. Xing, C. Li, Logging lithology identification of tight sandy conglomerate and its application, Sci. Technol. Rev. 32 (25) (2014) 59–62, https://doi.org/10.3981/j.issn.1000-7857.2014.25.010.

[18] G. Wang, Z.C. Sun, J.W. Fu, X. Luo, X. Zhoa, T. Pan, Control factors and logging evaluation method for glutenite reservoir in Mabei area, Junggar basin, Xinjing Pet. Geol. 36 (1) (2015) 8–13. https://www.zgxjpg.com/EN/10.7657/XJPG20150102.

[19] G.M. McDowell, A. King, R.E. Lewis, E.A. Clayton, J.A. Grau, In-situ nickel assay by prompt gamma neutron activation wireline logging, in: SEG Annual Meeting. New Orleans, Louisiana, 1998, https://doi.org/10.1190/1.1820589. SEG-1998-0772.

[20] N. Zhao, L. Wang, Y. Tang, J. Qu, X. Luo, L. Sima, Logging identification method for lithology: a case study of Baikouquan formation in wellblock Fengnan, Junggar basin, Xinjing Pet. Geol. 37 (6) (2016) 732–737. https://www.zgxjpg.com/EN/10.7657/XJPG20160618.

[21] M.I. Abdel-Fattah, A.Q. Mahdi, M.A. Theyab, J.D. Pigott, Z.M. Abd-Allah, A.E. Radwan, Lithofacies classification and sequence stratigraphic description as a guide for the prediction and distribution of carbonate reservoir quality: a case study of the Upper Cretaceous Khasib Formation (East Baghdad oilfield, central Iraq), J. Petrol. Sci. Eng. 209 (11) (2022) 109835, https://doi.org/10.1016/j.petrol.2021.109835.

[22] J.L. Baldwin, D.N. Otte, C.L. Whealtley, Computer Emulation of Human Mental Process: Application of Neural Network Simulations to Problems in Well Log Interpretation: Society of Petroleum Engineers SPE Paper 19619, 1989, pp. 481–493, https://doi.org/10.2118/19619-MS.

[23] S.J. Rogers, J.H. Fang, C.L. Karr, D.A. Stanley, Determination of lithology from well logs using a neural network, Am. Assoc. Petrol. Geol. Bull. 76 (5) (1992) 731–739, https://doi.org/10.1306/BDFF88BC-1718-11D7-8645000102C1865D.

[24] T. Kohonen, Self-organized formation of topologically correct feature maps, Biol. Cybern. 43 (1982) 59–69. https://link.springer.com/article/10.1007/BF00337288.

[25] B.D. Ripley, Pattern Recognition and Neural Networks, Cambridge University Press, Cambridge, 1996, p. 403, https://doi.org/10.1017/CBO9780511812651.

[26] H.C. Chang, D.C. Kopaska-Merkel, H.C. Chen, Identification of lithofacies using Kohonen self-organizing maps, Comput. Geosci. 28 (2) (2002) 223–229, https://doi.org/10.1016/S0098-3004(01)00067-X.

[27] J.H. Doveton, Applications of artificial intelligence in log analysis, in: Geologic Log Analysis Using Computer Methods, American Association of Petroleum Geologists, Tulsa, 1994, pp. 151–165, https://doi.org/10.1306/CA2580C7.

[28] M. Pabakhsh, K. Ahmadi, M.A. Riahi, A.A. Shahri, Prediction of PEF and LITH logs using MRGC approach, Life Sci. J. 9 (4) (2012) 974–982. http://www.lifesciencesite.com/lsj/life0904/150_10688life0904_974_982.pdf.

[29] M. Nouri-Taleghani, A. Kadkhodaie-llkhchi, M. Karimi-Khaledi, Determining hydraulic flow units using a hybrid neural network and multi-resolution graph-based clustering method: case study from South Pars Gas field, Iran, J. Petrol. Geol. 38 (2) (2015) 177–191, https://doi.org/10.1111/jpg.12605.

[30] M.J. Cracknell, A.M. Reading, Geological mapping using remote sensing data: a comparison of five machine learning algorithms, their response to variations in the spatial distribution of training data and the use of explicit spatial information, Comput. Geosci. 63 (2014) 22–33, https://doi.org/10.1016/j.cageo.2013.10.008.

[31] J.R. Harris, E.C. Grunsky, Predictive lithological mapping of Canada's North using Random Forest classification applied to geophysical and geochemical data, Comput. Geosci. 80 (2015) 9–25, https://doi.org/10.1016/j.cageo.2015.03.013.

[32] S. Elkatatny, M. Mahmoud, Development of new correlations for the oil formation volume factor in oil reservoirs using artificial ıntelligent white box technique, J. Pet. Sci. Eng. 4 (2) (2018) 178–186, https://doi.org/10.1016/j.petlm.2017.09.009.

[33] P.Y. Wu, V. Jain, M.S. Kulkarni, A. Abubakar, Machine learning-based method for automated well log processing and interpretation, in: SEG International Exposition and 88th Annual Meeting, 2018, https://doi.org/10.1190/segam2018-2996973.1.

[34] Y. Imamverdiyev, L. Sukhostat, Lithological facies classification using deep convolutional neural network, J. Pet. Sci. Eng. 174 (2019) 216–228, https://doi.org/10.1016/j.petrol.2018.11.023.

[35] T. Buday, The Regional Geology of Iraq.V.1.; Stratigraphy and Paleogeography, State Organization for Minerals, Baghdad, 1980, p. 350. https://books.google.cz/books/about/The_Regional_Geology_of_Iraq.html?id=leDUQQAACAAJ&redir_esc=y.

[36] F.M. Qadir, Formation Evaluation of Upper Qamchuqa Reservoir in Khabbaz Oil Field, Northeastern Iraq, Ph.D. Dissertation, Sulaimani University, Sulaimani, Iraq, 2008, p. 192. https://www.amazon.com/Formation-Evaluation-Upper-Qamchuqa-Reservoir/dp/3330967315.

[37] R.C.V. Bellen, H.V. Dunnington, R. Wetzel, D. Morton, Lexique Stratigraphique international, III, Asie, Fasc. 10a, Iraq, Centre national de la recherché scientifique, Paris, 1959, p. 333.

[38] H.V. Dunnington, Generation, migration, accumulation, and dissipation of oil in northern Iraq, in: Habitat of Oil, AAPG Spec. Pub., 1958, pp. 1194–1251. https://www.researchgate.net/publication/284626470_Generation_migration_accumulation_and_dissipation_of_oil_in_Northern_Iraq.

[39] F. Rashid, P.W.J. Glover, P. Lorinczi, R. Collier, J. Lawrence, Porosity and permeability of tight carbonate reservoir rocks in the north of Iraq, J. Petrol. Sci. Eng. 133 (2015) 147–161, https://doi.org/10.1016/j.petrol.2015.05.009.

[40] N. Kaddouri, Tel hajar: a new cenomanian–lower turonian stratigraphic unit from north-west Iraq, cretaceous research, Academic Press Inc., London 3 (4) (1982) 391–395, https://doi.org/10.1016/0195-6671(82)90040-4.

[41] M.S. Nourmohamadi, R.A. Abdula, F. Albeyati, A.O. Sharezwri, E.M. Perot, S.E. Jassim, N.H. Othman, Green glauconitic marl bed as a sequence stratigraphical key for interpretation contact between Qamchuqa and Bekhme formations in Bekhal area, Kurdistan Region, NE Iraq, Bull. Geol. Soc. Malays. 70 (2020) 29–38, https://doi.org/10.7186/bg70202003.

[42] S.Z. Jassim, T. Buday, Late turonian-danian megasequence AP9, chapter 12, in: S.Z. Jassim, J.C. Goff (Eds.), Geology of Iraq, first ed., Prague and Moravian Museum, Brno, Czech Republic, 2006, p. 183–204. https://www.amazon.com/Geology-Iraq-S-Z-Jassim/dp/8070282878.

[43] S. Mohaghegh, B. Balan, S. Ameri, Permeability determination from well log data, SPE Form. Eval. 12 (3) (1997) 170–174, https://doi.org/10.2118/30978-PA.

[44] C.C. Fung, K.W. Wong, P.M. Wong, A self-generating fuzzy rules inference for petrophysical properties prediction, in: Proceedings of the IEEE International Conference on Intelligent Processing System, 1997, https://doi.org/10.1109/ICIPS.1997.672766. Beijing, China.

[45] G. Asquith, D. Krygowski, S. Henderson, N. Hurley, Basic well log analysis, AAPG Methods Explor. 16 (2004), https://doi.org/10.1306/Mth16823.

[46] O.M. Derder, Lithology and mineralogy estimation from matrix density utilizing wireline logs in glauconitic sandstone, Blackfoot area, alberta, Canada, Can. J. Explor. Geophys. 41 (1) (2016) 1–8. https://csegjournal.com/assets/pdfs/2016/2016-06-CJEGLithology_and_Mineralogy_Estimation_from_Matrix_Logs.pdf.

[47] S. Oberto, Fundamentals of Well-Log Interpretation: the Acquisition of Logging Data, Elsevier Publishers, Amsterdam, 1984, p. 435. https://faculty.ksu.edu.sa/sites/default/files/Fundamentals%20of%20Well-Log%20Interpretation%20-%20The%20Acquisition%20of%20Logging%20Data_0.pdf.

[48] O. Bábek, T. Kumpan, M. Calner, D. Šimíček, J. Frýda, M. Holá, L. Ackerman, K. Kolková, Redox geochemistry of the red 'orthoceratite limestone' of Baltoscandia: possible linkage to mid-Ordovician palaeoceanographic changes, Sediment. Geol. 420 (2021) 105934.

[49] M.H. Rider, The Geological Interpretation of Well Logs, second ed., Rider-French Consulting, Sutherland, 2011, p. 280. https://www.amazon.com/Geological-Interpretation-Well-Logs-Rider/dp/0954190688.

[50] O. Bábek, J. Kalvoda, P. Cossey, D. Šimíček, S. Devuyst F-X, Hargreaves, Facies and petrophysical signature of the Tournaisian/Viséan (Lower Carboniferous) sea-level cycle in carbonate ramp to basinal settings of the Wales-Brabant massif, British Isles. Sediment. Geol. (2013) 197–213, https://doi.org/10.1016/j.sedgeo.2012.12.008.

[51] O. Bábek, T. Kumpan, J. Kalvoda, T.M. Grygar, Devonian/Carboniferous boundary glacioeustatic fluctuations in a platform-to-basin direction: a geochemical approach of sequence stratigraphy in pelagic settings, Sediment. Geol. 337 (2016) 81–99, https://doi.org/10.1016/j.sedgeo.2016.03.009.

[52] S.H. Hussein, Carbonate fractures from conventional well log data, Kometan Formation, Northern Iraq case study, J. Appl. Geophys. 206 (2022) 104810, https://doi.org/10.1016/j.jappgeo.2022.104810.

[53] K. Jolanta, D. Lidia, Geological interpretation of spectral gamma ray (SGR) logging in selected boreholes, Nafta Gaz. 72 (2016), https://doi.org/10.18668/NG2016.01.01.

[54] S.H. Hussein, O. Bábek, H. Mansurbeg, S. Shahrokhi, Outcrop-to-subsurface correlation and sequence stratigraphy of a mixed carbonate–siliciclastic ramp using element geochemistry and well logging; Upper Cretaceous Kometan Formation, Zagros Foreland, NE Iraq, Sediment. Geol. 459 (2024) 106547, https://doi.org/10.1016/j.sedgeo.2023.106547.

[55] Schlumberger Limited, Schlumberger Log Interpretation Charts, Schlumberger, 1997. https://www.spec2000.net/downloads/SLB%20Chartbook%201997R.pdf.

Appendix 2

Sedimentary Geology 459 (2024) 106547

Contents lists available at ScienceDirect

Sedimentary Geology

journal homepage: www.elsevier.com/locate/sedgeo

Outcrop-to-subsurface correlation and sequence stratigraphy of a mixed carbonate–siliciclastic ramp using element geochemistry and well logging; Upper Cretaceous Kometan Formation, Zagros Foreland, NE Iraq

Hussein S. Hussein [a], Ondřej Bábek [a,*], Howri Mansurbeg [a,b], Salahadin Shahrokhi [a]

[a] Department of Geology, Palacký University, 17, listopadu 12, Olomouc 77146, Czechia
[b] General Directorate of Scientific Research Centre, Salahaddin University-, Erbil, Kurdistan Region, Iraq

ARTICLE INFO

Article history:
Received 10 August 2023
Received in revised form 2 November 2023
Accepted 11 November 2023
Available online 20 November 2023

Editor: Dr. Massimo Moretti

Keywords:
Sequence stratigraphy
Cretaceous
Carbonate ramp
Well logs
Element geochemistry
Kometan Formation

ABSTRACT

Surface analogues are suitable tools to link reservoir models to real facies but they require a robust outcrop-to-subsurface stratigraphic correlation. In this study, we correlate gamma-ray (GR), and porosity logs from nine wells drilled in the Cretaceous Kometan Formation, a prolific carbonate reservoir of northern Iraq, with geochemical logs from three sections representing surface analogues. The sections were sampled for microfacies, X-ray diffraction mineralogy, and element geochemistry using X-ray fluorescence spectrometry calibrated by ICP-MS data. Six microfacies composed of mudstones to packstones with planktonic, and benthic foraminifers were identified in outcrop, and interpreted as middle ramp, outer ramp, and basin deposits. The microfacies show increasing Al and K, and decreasing Ca concentration trends from the middle ramp to the basin settings. Their subsurface analogues are carbonates, marls and shales with benthic foraminifers, deposited in proximal, inner to middle ramp parts of the Kometan mixed carbonate–siliciclastic ramp system. The K + Al logs are correlated for 33 km, and the subsurface GR logs for over 100 km distance, but both reflect detrital admixture in biogenic carbonate. However, the outcrop- and subsurface log patterns show opposite vertical trends. The subsurface, inner ramp GR maxima in the middle Kometan, correlate with the outcrop K + Al minima jointly reflecting landwards and seawards shifts of the middle ramp carbonate factory during transgressions and regressions, respectively. The maxima and minima are interpreted as maximum regression (mrs) and maximum flooding surfaces (mfs) in the T–R sequence-stratigraphic model. Neutron-density and sonic logs indicate that the best reservoir quality is achieved in fractured pure carbonates, which are controlled by these T–R cycles. The results highlight the importance of elemental geochemistry in stratigraphic correlation of lithologically uniform sequences, and suggest that outcrop geochemistry can be correlated with well logs.

1. Introduction

Outcrop analogues can provide important information for subsurface reservoir modelling. Unlike exploration wells, facies, their stacking patterns, diagenesis, and rock petrophysical properties can be studied directly, and with nearly unlimited sampling in outcrops. However, despite the many benefits that outcrop research offers, the scarcity of quantitative logging techniques in outcrop makes the correlation with the subsurface difficult. Reservoir properties which are typically inferred from well log data are often associated with facies stacking patterns and diagenetic features inherited from sea-level changes during deposition (Westphal et al., 2004; Ehrenberg et al., 2006; Stadtműller, 2019). These features are typically studied in outcrop. Primary and secondary porosity within carbonate rocks has been shown to be associated with transgressive and regressive cycles (Morad et al., 2000; Flügel, 2004). Regression typically involves cementation which fills the larger inter or intra-particle interconnected pores and inhibits the primary porosity (Read and Horbury, 1993; Tucker, 1993; Flügel, 2004). Sea-level fluctuations can also influence diagenesis and the development of secondary porosity (Morad et al., 2012). Near-surface water, hypersaline, brackish, and meteoric depositional settings all have significantly different pore-water chemistry (Hart et al., 1992; Tucker, 1993; Morad, 1998; Morad et al., 2000, 2010). Sea-level changes can alter the chemistry of the pore water in carbonate sediments by altering the chemistry close to the sediment/water contact (Morad et al., 2012). The duration of a diagenetic process and, consequently, the magnitude of diagenetic modifications can be likewise determined by transgressive/regressive cycles. Low rates of sedimentation during transgression cause sediments to be exposed to marine pore water diagenesis for an extended period of

* Corresponding author.
E-mail address: ondrej.babek@upol.cz (O. Bábek).

https://doi.org/10.1016/j.sedgeo.2023.106547
0037-0738/

time, whereas high rates of sedimentation during regression cause widespread meteoric diagenesis (Morad et al., 2012). In addition, the quantity and type of organic matter are impacted by sea level fluctuations (Cross, 1988; Whalen et al., 2000). This in turn affects how the carbonate matrix dissolves, e.g., as a result of biotically produced methane exhalation (Flügel, 2004). Sequence stratigraphy obviously controls primary and secondary diagenetic porosity (Tucker and Wright, 1990; Posamentier and Allen, 1999).

Carbonate rocks of the Upper Cretaceous Kometan Formation, Northern Iraq, represent significant hydrocarbon reservoirs producing gas in the Jambur oil field and oil in the Avanah and Baba Domes of the Kirkuk structure and in the Bai Hassan field (Aqrawi, 1996; Aqrawi et al., 2010). The Kometan Formation is a fractured reservoir that provides light oil (41 API) with estimated recoverable reserves of 700–750 million barrels and production rates reaching up to 200,000–250,000 barrels per day (Rashid et al., 2015a).

Sedimentology, stratigraphy, palaeontology, and the structure of the Kometan Formation have been studied by many authors (Abawi and Mahmood, 2005; Al-Barzinjy, 2007; Haddad and Amin, 2007; Rashid et al., 2015a, 2015b, 2017; Al-Qayim, 2010; Balaky et al., 2016). The Kometan Formation is largely composed of foraminiferal oligostiginid wackestone to grainstone with abundant stylolites, chert nodules, and good secondary porosity. It was deposited in an open marine, low energy, middle to outer ramp depositional setting and partly controlled by the influx of eroded components from shallow-water settings (Haddad and Amin, 2007; Al-Qayim, 2010; Balaky et al., 2016). Al-Barzinjy (2007) showed that the stylolite and chert nodules were produced by deep burial diagenesis. The formation represents a complete third-order sequence separated by type-2 sequence boundaries, which can be divided into transgressive and highstand systems tracts (Haddad and Amin, 2007; Balaky et al., 2016). The porosity, permeability and reservoir quality of the Kometan Formation on surface and in subsurface were studied by Rashid et al. (2015a, 2015b, 2017). Whilst the depositional settings, sequence stratigraphy, and diagenetic history of the Kometan Formation are well-known from outcrop observations, the relationships of these features to its subsurface production potential are unclear.

Applying the sequence stratigraphic technique to reservoir basin analysis is a crucial step in converting the lithology data from well-log data into genetic packages, which are useful to assess subtle stratigraphic reservoirs. It offers a method for the correlation of lithostratigraphy in wells (Omigie and Alaminiokuma, 2020). Application of quantitative methods in reservoir outcrop analogues and correlation with subsurface well logs, however, represents a challenging task. Gamma-ray spectrometry is a useful technique which may link petrophysical properties with facies (Rider, 1999; Šimíček and Bábek, 2015) and open ways for quantitative sequence-stratigraphic interpretations in outcrop research (Bábek et al., 2018). X-ray fluorescence spectroscopy (XRF) of powdered samples is yet another, rapid and inexpensive method which can sensitively pick up changes in lithology and palaeoenvironmental conditions in carbonates, and facilitate quantitative stratigraphic correlation in outcrop (Kumpan et al., 2014; Bábek et al., 2016; Carmichael et al., 2019). Although sediment geochemistry is seldom used in hydrocarbon exploration and production, it is hypothesized here that outcrop geochemistry and subsurface lithology well logs can be mutually correlated and the XRF technique provides a quantitative link between reservoirs and their outcrop analogues.

The aim of this study is to examine the link between the sequence stratigraphy and reservoir properties of ramp carbonates in outcrop and subsurface, using the Kometan Formation reservoir as an example. The outcrop data include three sections sampled with metre-scale sampling density for X-ray fluorescence spectroscopy supplemented by facies and microfacies analysis. The subsurface data include nine wells with gamma-ray, density, neutron, sonic and caliper logs. We will investigate the potential of the dataset for outcrop-to-subsurface correlation and sequence-stratigraphic interpretations.

2. Geological setting

The type locality of the Kometan Formation (upper Turonian to lower Campanian) is located in the Kometan Village, north-east of the town of Ranya near the city of Sulaimani, the Kurdistan region of Iraq (Fig. 1) (Van Bellen et al., 1959; Dunnington, 2005). The type locality exposes thin-bedded, white to light grey globigerinid–oligosteginid limestone containing locally abundant chert nodules, especially near the base of the section, and occasional glauconite-rich layers. The Kometan Formation was observed in many outcrop sections and in the subsurface of the Imbricated Zone, High Folded Zone, and the Low Folded Zone of the Zagros Foreland Basin, Kurdistan Region, Iraq; its thickness ranges from 63 to 185 m (Aqrawi et al., 2010). In different parts of the basin, the Kometan Formation rests either conformably or unconformably on the oligosteginid limestone facies of the Balambo Formation and limestones and dolomites of the Dokan, Gulneri, and Qamchuga Formations of Early Cretaceous to Coniacian ages (Fig. 2) (Buday, 1980; Kaddouri, 1982; Jassim and Goff, 2006; Al-Qayim, 2010). The Kometan Formation is either conformably or unconformably overlain by the Shiranish Formation and Tanjero Formation of Campanian to Maastrichtian age (Buday, 1980; Jassim and Goff, 2006). A distinct, glauconite-rich layer at the base of the Shiranish Formation can be used as a lithostratigraphic marker bed (Dunnington, 1958; van Bellen et al., 1959). Field observations suggest that in places the basal and top boundaries of the Kometan Formation are cut-off by post-depositional (early Miocene to Pliocene) faults accompanying the anticlinal structures of the north-western Zagros in the Kurdistan region (cf., Csontos et al., 2012).

A variety of fine-grained carbonate lithologies of the Kometan Formation were deposited in shallow marine shelf, restricted settings (oligosteginid facies), and open marine settings (globigerinid facies) (Buday, 1980; Abawi and Mahmood, 2005; Jassim and Goff, 2006). Towards the west and southwest of Iraq, the globigerinid and oligosteginid facies laterally pass into more argillaceous facies and marls fully corresponding to the oligosteginid biofacies (Dunnington, 1958, van Bellen et al., 1959). The Kometan Formation of the Imbricated, High Folded, and Low Folded Zones passes laterally into bioturbated chalky limestone, shale and marly limestone of the Khasib Formation, lagoonal shale, and carbonate of the Tanuma Formation, and open shelf globigerinid limestone of the Sa'di Formation in the Mesopotamian Zone and the Stable Platform of central Iraq and south Iraq (Figs. 1, 2) (Aqrawi, 1996; Al-Qayim, 2010).

3. Material and methods

Three outcrop sections of the Kometan Formation, Zewe (96 m thick), Qamchuqa (63 m), and Dokan (65 m) (Fig. 1B) were sampled and documented using bed-by-bed descriptions of bed thickness, bed geometry, sedimentary structures, and grain size using the approach summarized by Graham (1988). The outcrop sampling was conducted for thin section analysis and energy-dispersive X-ray fluorescence (EDXRF). A qualitative microfacies analysis following the principles summarized in Flügel (2004) and Scholle and Ulmer-Scholle (2003) was carried out on a total of 50 thin sections using the Dunham classification scheme (Dunham, 1962).

The well-log dataset comprises gamma ray, caliper, sonic, density, and neutron logs from nine wells from the Khabbaz, Kirkuk, Jambur, Bai Hasan, and Barda Rash oil fields, provided by the North Oil Company, Iraq (Fig. 1A). Because the log data is provided as image files only, the log curves were digitized with 0.2 m reading intervals using GetData digitizer 2.21 to obtain quantitative log readings for further processing. Shale volume was calculated from the gamma-ray logs using Eqs. (1) and (2) adopted from Oberto (1984):

$$IGR = (GR_{log} - GR_{min})/(GR_{max} - GR_{min}) \quad (1)$$

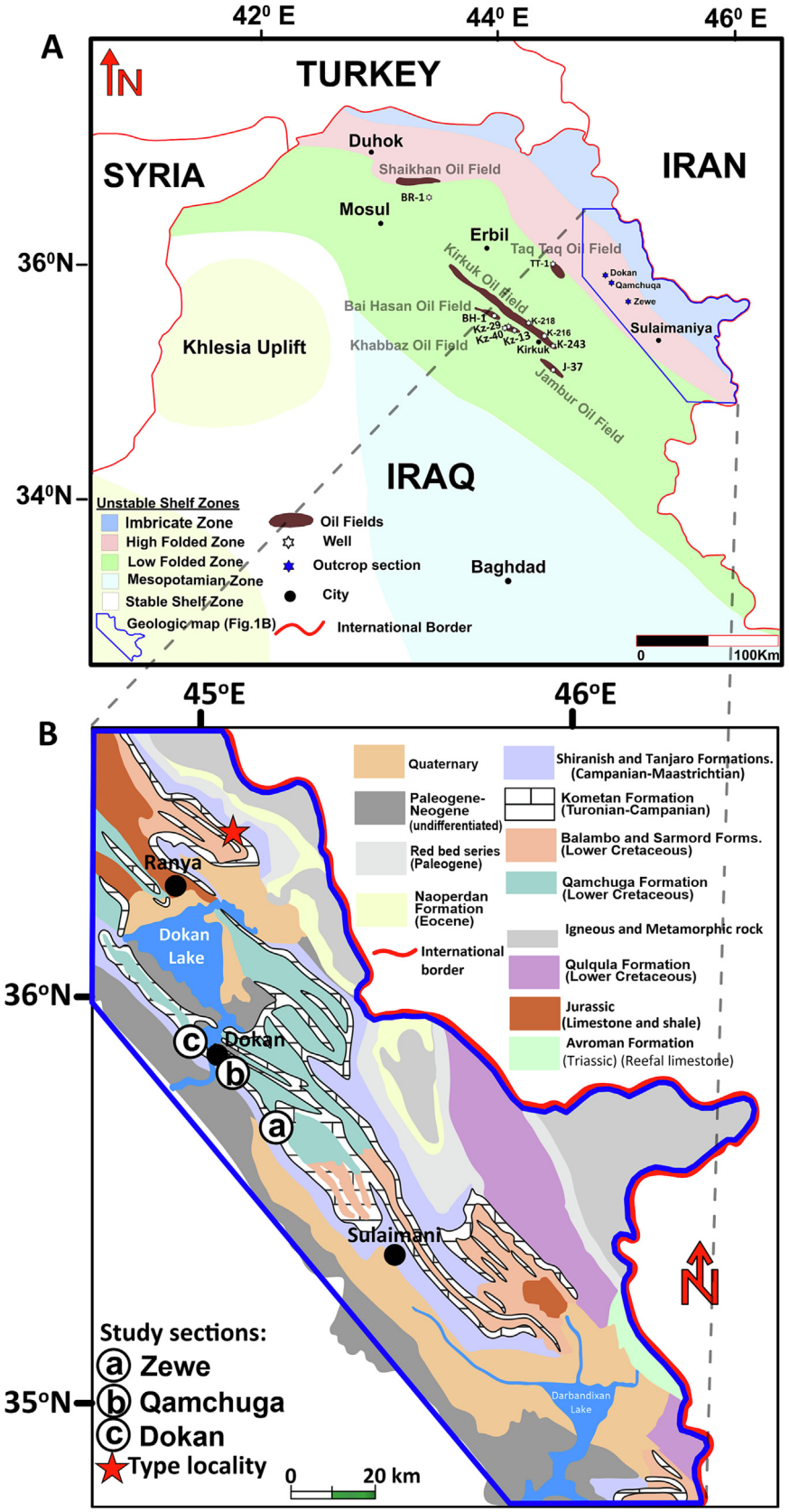

Fig. 1. Location, and tectonic subdivisions of the study area (Buday and Jassim, 1987) (A), and geologic map of the studied area with surface distribution of the Kometan Formation, its type locality, and the studied sections (modified from Sissakian, 2000 and Karim et al., 2011) (B).

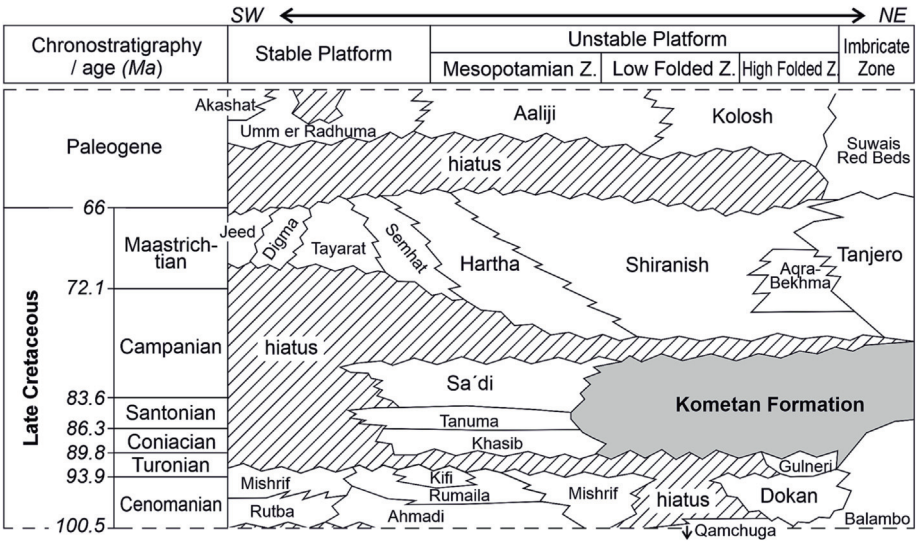

Fig. 2. Chronostratigraphic division of Upper Cretaceous lithostratigraphic units in NE Iraq. (Modified from Al-Qayim (2010).)

$$V_{sh} = 0.33[22{*}IGR - 1.0] \quad (2)$$

where IGR is gamma-ray index, GR_{log} is actual gamma-ray reading from the log, GR_{min} is minimum gamma-ray reading from the log (clean zone), and GR_{max} is maximum gamma-ray reading from the log (shale zone). The neutron, density, and sonic logs were used to determine porosity and lithology.

Using a Delta Premium energy-dispersive X-ray fluorescence (EDXRF) spectrometer (Innov-X, U.S.A.) with a large-area silicon-drift detector, element concentration data were measured from 246 powdered rock samples from three outcrop sections and 28 samples from four wells with 2 × 120 s acquisition time (beam) at 15 kV and 40 kV accelerating voltages. Prior to the EDXRF analysis, the materials were powdered to analytical fineness and stored in plastic cells that were sealed with Mylar foil. Concentrations of nineteen elements including Al, Si, P, S, K, Ca, Ti, Mn, Fe, Ni, Cu, Zn, As, Rb, Sr, Zr, Mo, Pb, and Th were analysed in each sample. ICPMS/OES data were used to calibrate the EDXRF concentrations (Table S1, Supplementary material). For the calibration, we used 76 samples of limestones, marls, and shales from the Lower Devonian mixed carbonate–siliciclastic ramp system of the Prague Basin, Czechia (Bábek et al., 2021), which represent geochemical analogues of the material studied here. They were analysed by both EDXRF and ICP-MS/OES, followed by a statistical correlation. The analytical EDXRF data were transformed into their calibrated ICP-MS/OES equivalents using linear or polynomic regression algorithms. The EDXRF signals were estimated with extremely high regression coefficients (R2 ≥ 0.99) for Si, Al, Fe, Ca, K, Ti, Mn, Zr, Rb, and Zn; they were somewhat lower (R2 ≥ 0.95) for As, Sr, and Pb, and even lower but still acceptable (R2 ≥ 0.85) for Cu, Ni, and Mo. Sulphur and phosphorus were not calibrated.

Mineralogy of 16 powdered samples from the outcrops and well cuttings was analysed by X-ray diffraction (XRD) using a Panalytical X'Pert PRO MPD diffractometer with reflection geometry equipped with a cobalt tube (λKα = 0.17903 nm), Fe filter and X'Celerator 1-D RTMS detector (Masaryk University Brno, Czechia). The analytical settings were: step size: 0.033° 2Θ, time per step: 160 s, angular range: 4–100° 2Θ, and total scan duration: 3702 s. The XRD data was processed using the Panalytical HighScore 4.8 plus and the Bruker AXS Diffrac plus Topas 4 software. A quantitative phase analysis of 8 samples was done by the Rietveld method; only crystalline phases were quantified.

4. Results

4.1. Lithology and microfacies

In the studied sections, the upper boundary of the Kometan Formation is overlain by the marl and marly limestone of the Shiranish Formation, and the lower boundary is defined by the limestone and dolomitic limestone of the Qamchuqa Formation. In outcrop, the lithology of the Kometan Formation is very uniform, corresponding to thin-bedded to medium-bedded, very fine grained, bioturbated limestone and argillaceous limestone that ranges from light grey (lower part) to light brown (upper part) colour. The beds contain poorly identifiable trace fossils. Bed thickness usually ranges from ~15 cm to ~60 cm. The beds are separated by thin marly laminae, very often modified by stylolitization. In all measured sections, the carbonate is highly fractured and contains abundant stylolites which are often very large having up to 4 cm amplitude. The limestones locally contain abundant chert nodules arranged parallel with the bedding planes, which are in places concentrated on the stylolites (Figs. 3, 4, 5).

The XRD analyses from 6 samples from the Qamchuga and Zewe sections (Fig. S1, Supplementary material) show that the limestones contain abundant calcite (up to 96 %), quartz and chert (up to 12 %), clay minerals (illite, illite/smectite and smectite, up to 2 %) and trace amounts of K-feldspars and dolomite.

The microfacies analysis is based on thin sections from the Qamchuqa and Zewe sections (Fig. 6). The composition of the Kometan Formation is relatively uniform, but the texture is more variable. Subtle changes in texture and composition of skeletal grains allowed us to classify six microfacies, MFT1–MFT6 (Figs. 4, 5). The MFT1 microfacies is a mudstone including planktonic foraminifers (*Globigerina*, *Heterohelix*, and oligosteginids) and sparse calcispheres (Fig. 6a). The MFT2 microfacies is a wacke-packstone with abundant foraminifers such as *Hedbergella*, *Heterohelix*, and oligosteginids, sparse calcispheres and sponge spicules (Fig. 6b). The MFT3 microfacies is a densely packed, moderately sorted packstone with abundant planktonic foraminifers such as *Globotruncana*, and *Dicarinella*, less abundant *Hedbergella* and *Heterohelix*, sparse calcispheres, fragments of ostracod shells, and relatively large grains of glauconite (Fig. 6c). The MFT4 is a packstone with abundant (35 to 40 %) oligosteginids and less abundant planktonic foraminifers (Fig. 6d). The MFT5 microfacies is a fine-grained, well-sorted packstone with oligosteginid planktonic foraminifers, *Hedbergella*, *Heterohelix*, *Globigerina*, and *Globotruncana* (Fig. 6e). The MFT6

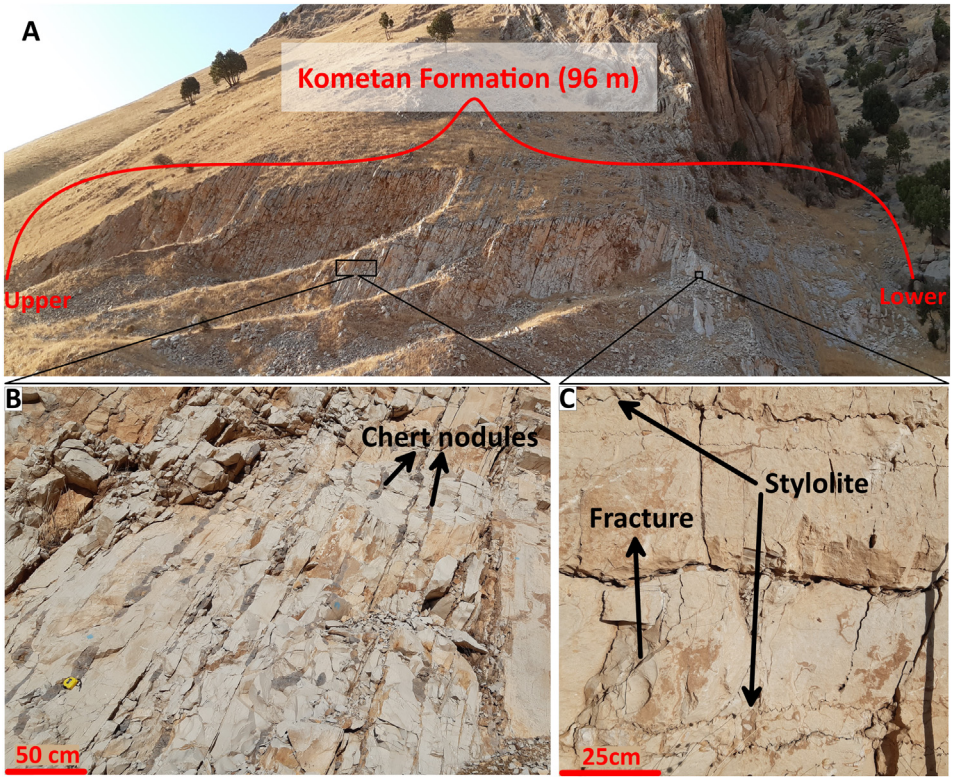

Fig. 3. Field photographs of the Kometan Formation at the Zewe section (A), and close-ups of carbonate lithology (B, C).

microfacies is packstone with benthic foraminifers (e.g., *Textularia*), echinoderm fragments, oligosteginids and sparse ostracods (Fig. 6f).

In well logs, direct lithological observations are scarce and generally based on 28 samples of well cuttings from three wells, Kz-40, Kz-29 and Kz-216. Unfortunately, no cores have been drilled or preserved. The well cuttings are composed of medium grey shales and marls, argillaceous limestones, and pure limestones. The XRD analyses from 10 samples (Fig. S1, Supplementary material) show that the rocks are composed of calcite (from 44 to 89 %), illite, illite/smectite and smectite (from 3 to 19 %), kaolinite (from 0 to 22 %), quartz (from 2 to 7 %), K-feldspars (up to 5 %), dolomite (up to 3 %), and minor (<2 %) proportion of siderite, pyrite, hematite, gypsum, anhydrite, baryte and anatase. They show a distinct vertical arrangement: the upper parts of Kometan Formation in Kz-40 (2710 to 2790 m), Kz-29 (2780 to 2860 m) and K-216 (1440 to 1558 m) are composed of pure limestone and marly limestone; the middle parts in Kz-40 (2810 to 2850 m) and Kz-29 (2880 to 2940 m) are composed of marls, shale and marly limestone, and the lower parts in Kz-40 (2870 to 2888 m) and Kz-29 (2950 m) are composed of marly limestone and pure limestone. The siliciclastic lithologies are fine-grained but any other lithological observations cannot be obtained from the cuttings.

4.2. Well log data

The gamma-ray data for 9 wells are summarized in Table S2 (Supplementary material). The total gamma ray values in the Kz-29 and Kz-40 logs range from ~10 to ~70 API with the corresponding shale volumes ranging from ~3.7 to ~22 % (Fig. 7). The formation can be roughly subdivided into three vertical segments, lower, "clean" part (Kz-29 well, from 2802 to 2868 m) with ~10 to ~28 API, and 8.8 % mean shale volume, middle, shaly part (KZ-29 well, from 2868 to 2920 m) with ~20 to ~42 API, and 16 % mean shale volume, and upper, "clean" part (Kz-29 well, from 2920 to 2948 m) with ~15 to ~30 API, and 7.4 % mean shale volume. Similar vertical patterns have been also observed in the Kz-40 well (Fig. 7). The "clean" parts correspond to pure limestone, argillaceous limestone and marly limestone, whereas the shaly part corresponds to marly limestone, marl and shale. The overlying Mushorah and Shiranish formations show again relatively high and increasing total gamma-ray values (from ~20 to ~75 API) in the Kz-29 and Kz-40 wells. The porosity well logs are shown in Fig. 7 and Table S3 (Supplementary material). The three-fold subdivision, although with some depth deviations, can be observed in the neutron porosity, bulk density, and sonic logs (Fig. 7). The lower and upper "clean", carbonate rich intervals in Kz-29, and the upper "clean" interval in Kz-40 are characterized by relatively low neutron porosities (~5 to ~20 %), high bulk densities (~2.7 to ~2.8 g/cm^3), and low interval transit times (~80 to ~100 μs/ft). The same applies to a layer of pure limestone in the lower "clean" interval in Kz-40 (~2875 m). The middle, "shaly" interval has relatively high neutron porosities (~20 to ~45 %), low bulk densities (~1.5 to ~2.5 g/cm^3), and high interval transit times (~100 to ~220 μs/ft). The lower part in Kz-40 has moderately high neutron porosities, bulk densities and interval transit times.

The well log data show very similar (correlatable) patterns in both the Kz-29 and Kz-40 wells, but especially the gamma-ray logs can be used for long-distance (>100 km) correlation. The middle, "shaly" interval is well-constrained by blocky patterns at the base and the top, and upwards-increasing and then decreasing GR values in BH-13, Kz-40, Kz-29, Kz-13, and partly K-2018 wells. The middle interval in the K-218, K-216, K-243, and J-37 wells is delimited by a distinct GR peak at the base, which is followed by upwards-decreasing values. In contrast, the lower and upper intervals have lower, and more uniform GR values. The correlation results (Fig. 8) show that the middle, shaly interval attains maximum thickness of ~68 m (Kz40 well) whilst it laterally pinches out to a minimum thickness of ~12 m towards NW (BR-1 well) and to ~15 m towards SE (J-37 well). The gamma-ray values generally decrease consistently with the decreasing thickness of the shaly interval, from maximum values in Kz-40 (~30 to ~70 API) to J-37 wells (~22 to ~35 API, but with a few outliers reaching up to 75 API).

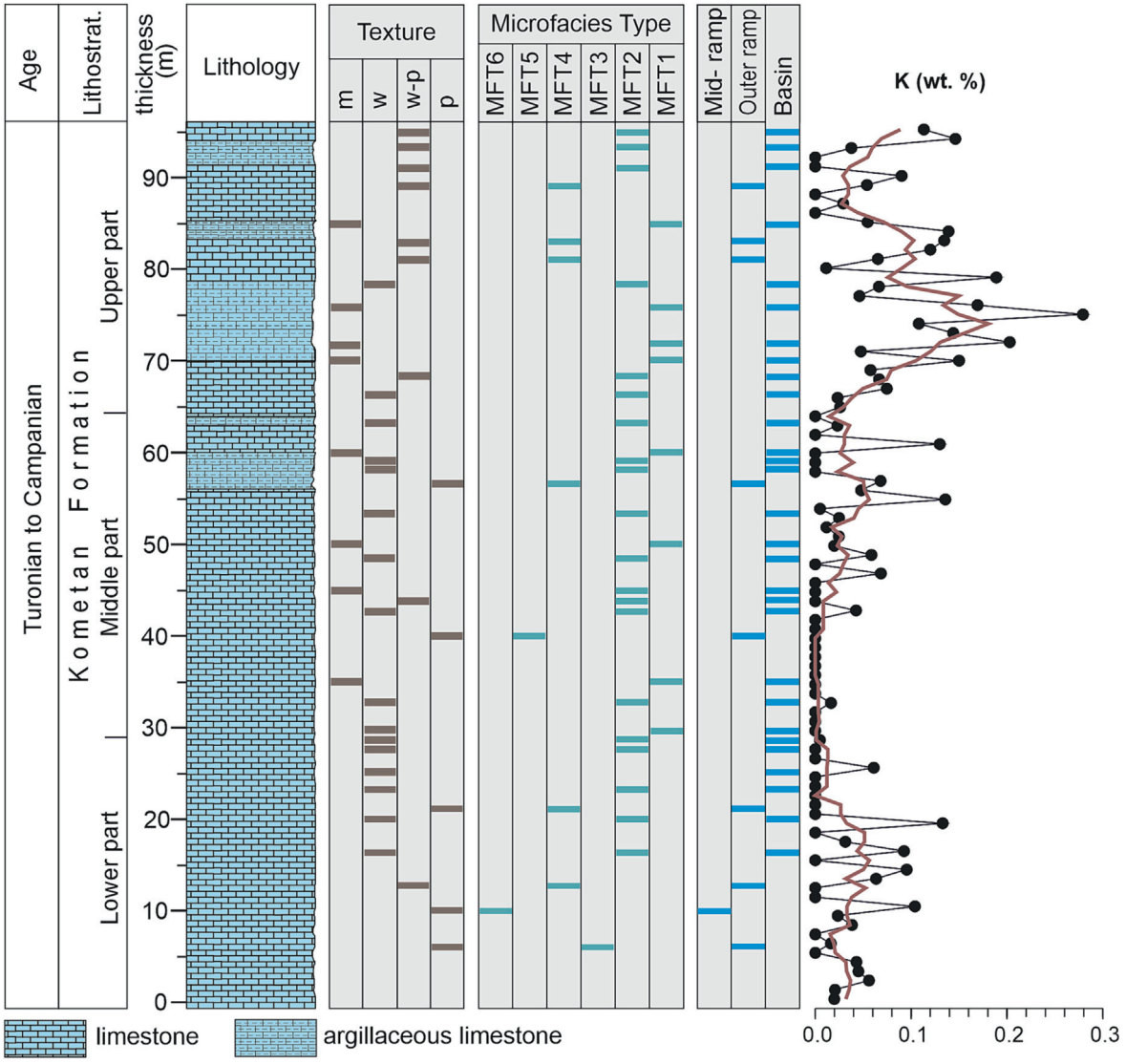

Fig. 4. Stratigraphic log showing lithology, distribution of microfacies, their corresponding depositional settings, and EDXRF concentrations of K (wt%; red line shows the 5-point running mean) in the Kometan Formation at the Zewe section.

4.3. Bulk-rock element concentrations

The bulk-rock element concentrations are shown in Table S1 (Supplementary material). The median values of element concentrations in the outcrop sections are Ca (36.41 wt%), Si (2.43 wt%), P (1.23 wt%), Al (0.21 wt%), Fe (0.08 wt%), K (0.05 wt%), Ti (0.04 wt%), and Mn (0.01 wt%). Trace elements (median values) include Sr (660 ppm), V (30 ppm), Cu (16 ppm), Ni (13 ppm), Zn (10 ppm), Zr (10 ppm), Rb (4 ppm), Pb (2.4 ppm), As (2 ppm) and Mo (1.4 ppm). Element concentrations in the boreholes have higher concentrations of Si (4.1 wt%), Al (1.3 wt%), Fe (0.6 wt %), K (0.4 wt%), Ti (0.1 wt%), Sr (714 ppm), V (127 ppm), Cu (30 ppm), Ni (27 ppm), Zn (20 ppm), Zr (21 ppm), Rb (12 ppm), Pb (3 ppm), and As (3 ppm), and lower concentrations of Ca (32.2 wt%), P (1.2 wt%) and Mo (1.2 ppm).

The elements can be subdivided into several groups according to their covariance in the studied dataset. Aluminium shows very high covariation (R^2) with Fe (0.95), Rb (0.97), and Zr (0.98), and slightly lower but still high covariance with K (0.83), and Ti (0.78) (Fig. 9). All these lithogenic elements, which are typically bound to detrital siliciclastic minerals (phyllosilicates, feldspars, heavy minerals), are negatively correlated with Ca (Al vs. Ca: $R^2 = 0.63$; R2 = 0.98 for the Khabbaz wells) and with P (Al vs. P: $R^2 = 0.6$). This negative correlation is caused by the mixing of the siliciclastic detrital minerals with biogenic/precipitating carbonate minerals containing Ca and P (which are mutually correlated ($R^2 = 0.93$)). Silicon is also positively correlated with Al, but this correlation is weaker ($R^2 = 0.63$) presumably because a part of the Si is bound to cherty limestones and not to detrital aluminosilicates, in particular in the pure carbonates at Zewe and Dokan sections (Fig. 9). The outcrops and the boreholes show uniform elemental composition for some detrital elements, e.g., Zr and Rb, as indicated by their covariance patterns, but they are dissimilar in other elements, e.g., K. The high correlation coefficients between Al and K, but different K/Al ratios in the Qamchuga section and the boreholes indicate different components of the K- and Al-bearing siliciclastic detrital admixture in the carbonates (Fig. 9).

All samples from the Kometan Formation in the outcrop sections (Zewe, Dokan, and Qamchuga) with low concentrations of Al (<1 wt%), Rb, Si, and K correspond to pure carbonates. In outcrop, the Kometan Formation can be roughly subdivided into a lower part, characterized by low K (~0.05 to 0.12 wt%) and Al (~0.1 to 0.4 wt%) concentrations, middle part featuring even little bit lower K (~0 to 0.1 wt%) and Al (~0.1 to 0.4 wt%) concentrations and relatively high Zr/Al ratios, and an upper part with relatively high K (~0.05 to 0.25 wt%) and Al (~0.2 to 0.8 wt%) concentrations and low Zr/Al ratios (Figs. 4, 5, 10). The K,

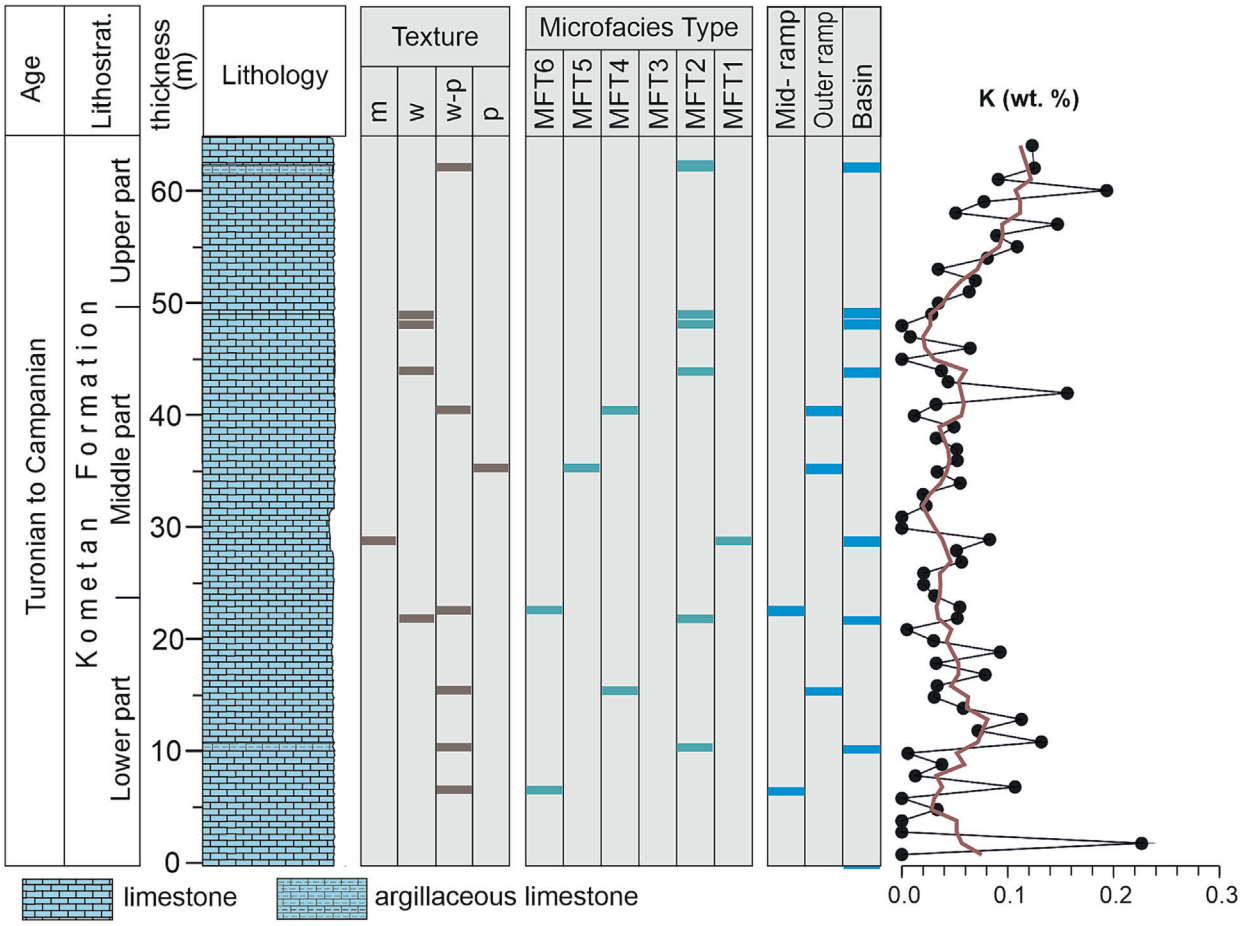

Fig. 5. Stratigraphic log showing lithology, distribution of microfacies, their corresponding depositional settings, and EDXRF concentrations of K (wt%; orange line shows the 5-point running mean) in the Kometan Formation at the Qamchuqa section.

and Al concentrations show well constrained lows and highs, which can be correlated between the Zewe, Qamchuga and Dokan sections over the distance of 33 km parallel with the tectonic strike (Fig. 10).

5. Discussion

5.1. Depositional environment and sedimentary trends in outcrop sections

The abundance of planktonic foraminifera such as *Hedbergella*, *Heterohelix*, *Globigerinoides*, *Rotallipora*, *Praeglobotruncana* and *Daicarinella* along with numerous species of *Oligostegina*, and the scarcity of other skeletal/nonskeletal grains suggest relatively a uniform, deep-water depositional environment for the outcrop sections. The similarity of pelagic facies is very high, and the exact separation of the mentioned facies with conventional petrographic methods is difficult. For this reason, the methodology of planktonic foraminifer morphotypes (Keller, 1993) was adopted in this study. The MFT1 microfacies is mainly composed of planktonic foraminifers of the morphotype 3 (Keller, 1993). The abundance of planktonic foraminifers, and abundant micrite indicate deposition in the calm, deep marine environment (Wilson, 1975; Bernaus et al., 2002). This microfacies corresponds to the RMF 5 of Flügel (2004), which belongs to the basinal environment. The MFT2 and MFT3 microfacies containing glauconite also correspond to RMF5 (Flügel, 2004) — products of a basinal/pelagic environment, in which glauconite grains and pure carbonate lithology indicate low sedimentation rates, sub-oxic to reducing conditions, and a lack of detrital input (Amorosi, 1995). The grain-supported texture of the MFT4 and especially MFT5 microfacies along with the abundance of planktonic foraminifers, indicates low- to medium-energy water activity, presumably due to bottom currents, in relatively deep marine environments, well below the fair-weather wave base (Scholle and Ulmer-Scholle, 2003; Flügel, 2004). These microfacies are comparable with the open marine facies zones (FZ1, FZ2, FZ3) of Wilson (1975), and the RMF 5 of Flügel (2004), which can be attributed to the outer ramp environment. Due to the predominance of the oligosteginid planktonic foraminifers and other planktonic foraminifers, it can be said that the MFT1 to MFT5 microfacies represent pelagic open marine conditions (Keller et al., 2002). Echinoderm fragments are found in shallow-marine limestones as well as in deep-marine limestone (Flügel, 2004); in addition ostracod and benthic foraminifera are observed in middle ramp environments (Flügel, 2004). The MFT6 microfacies containing more abundant echinoderms, ostracods, and benthic foraminifers are interpreted as corresponding to the RMF3 microfacies reflecting shallower, middle ramp environments (Flügel, 2004). The general lack of sliding, slumping and resedimented facies such as turbidites indicates predominant basin floor/deep shelf bottom with flat topography with predominant sedimentation from suspension settling, only partly affected by bottom currents. The studied outcrop part of the Kometan Formation was likely deposited in outer ramp rather than in a basin adjacent to carbonate shelf. This is supported by the absence of shelf-derived cortoids, oncoids, and aggregate grains, which are commonly found in age-equivalent carbonates in other parts of the Zagros basin (Ilam Formation; Adabi and Mehmandosti, 2008).

The microfacies stacking patterns are more difficult to interpret. The model of MFT1 to MFT6 microfacies likely represents a gradual transition from open marine/pelagic environments to middle ramp environments (see the section 5.1) but the microfacies do not show distinct vertical trends (Figs. 4, 5). Although, at a first glance, it seems that there are no

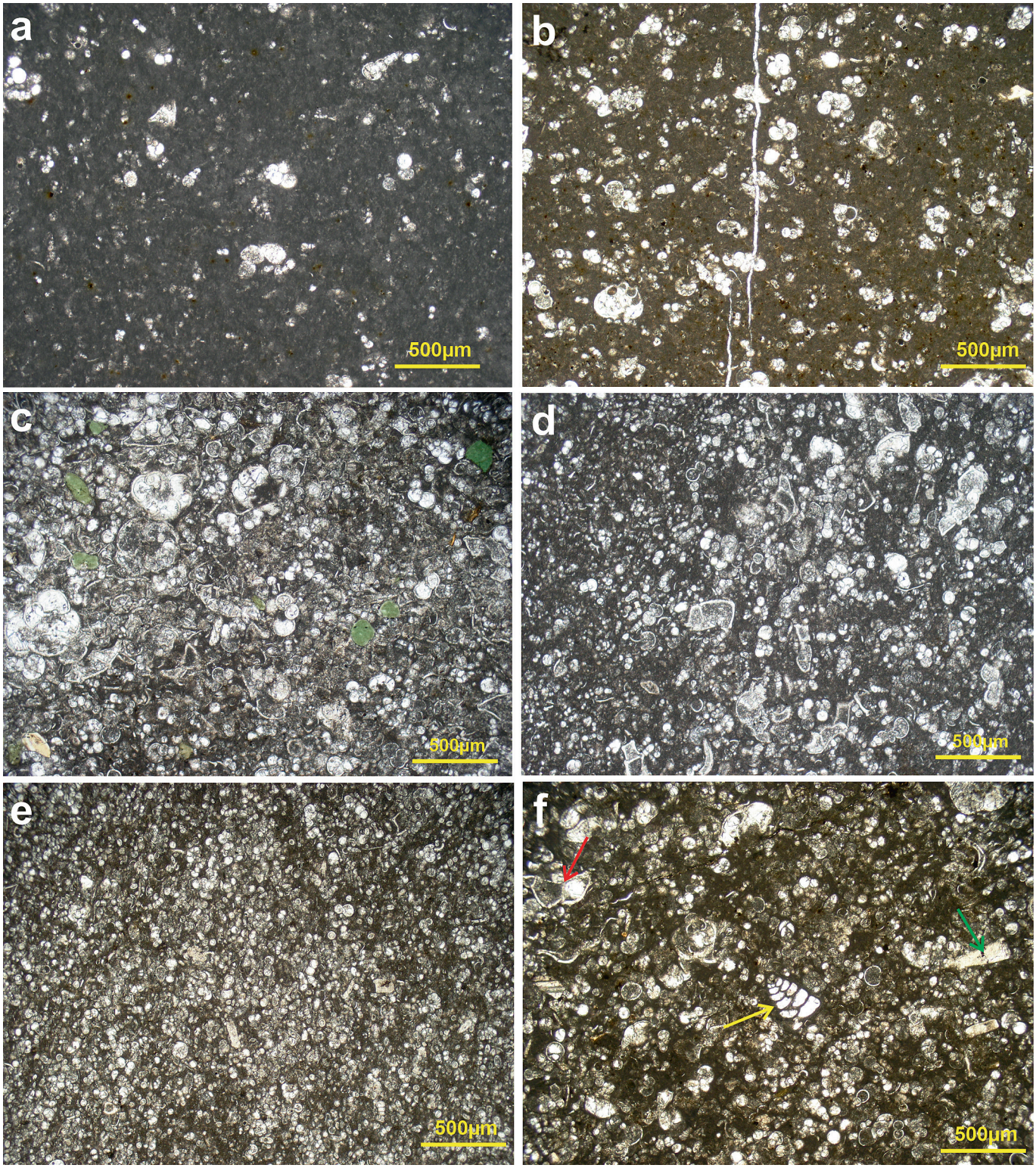

Fig. 6. Photomicrographs of microfacies of the Kometan Formation; a) planktonic foraminiferal mudstone (MFT1); b) *Heterohelix*/*Hedbergella* wackestone–packstone (MFT2); c) planktonic foraminiferal packstone with glauconite (MFT3); d) oligosteginid packstone (MFT4); e) planktonic foraminiferal wacke/packstone with oligosteginids (MFT5); f) packstone with benthic foraminifers, echinoderms, and oligosteginids (MFT6), yellow arrow: benthic foraminifer (*Textularia*), green arrow: echinoderm fragments; red arrow: ostracod.

relationships between the carbonate geochemistry and microfacies stacking patterns (Figs. 4, 5), the bivariate statistics of the microfacies vs. element geochemistry shows the opposite. When plotted against the microfacies type, the mean Al concentrations show statistically significant ($R^2 = 0.58$) decreasing trends from more distal (MFT1) to more proximal (MFT6) microfacies, whilst the Ca concentrations show an opposite, increasing trend ($R^2 = 0.69$) (Fig. 11). This suggests that the slightly more proximal open shelf microfacies are actually more pure carbonate whereas the more distal ones are more argillaceous, exactly the opposite as what we see in the more proximal parts of the basin.

The carbonate production on carbonate ramps can extend well into bathyal and abyssal depths (De Mol et al., 2002; Schlager,

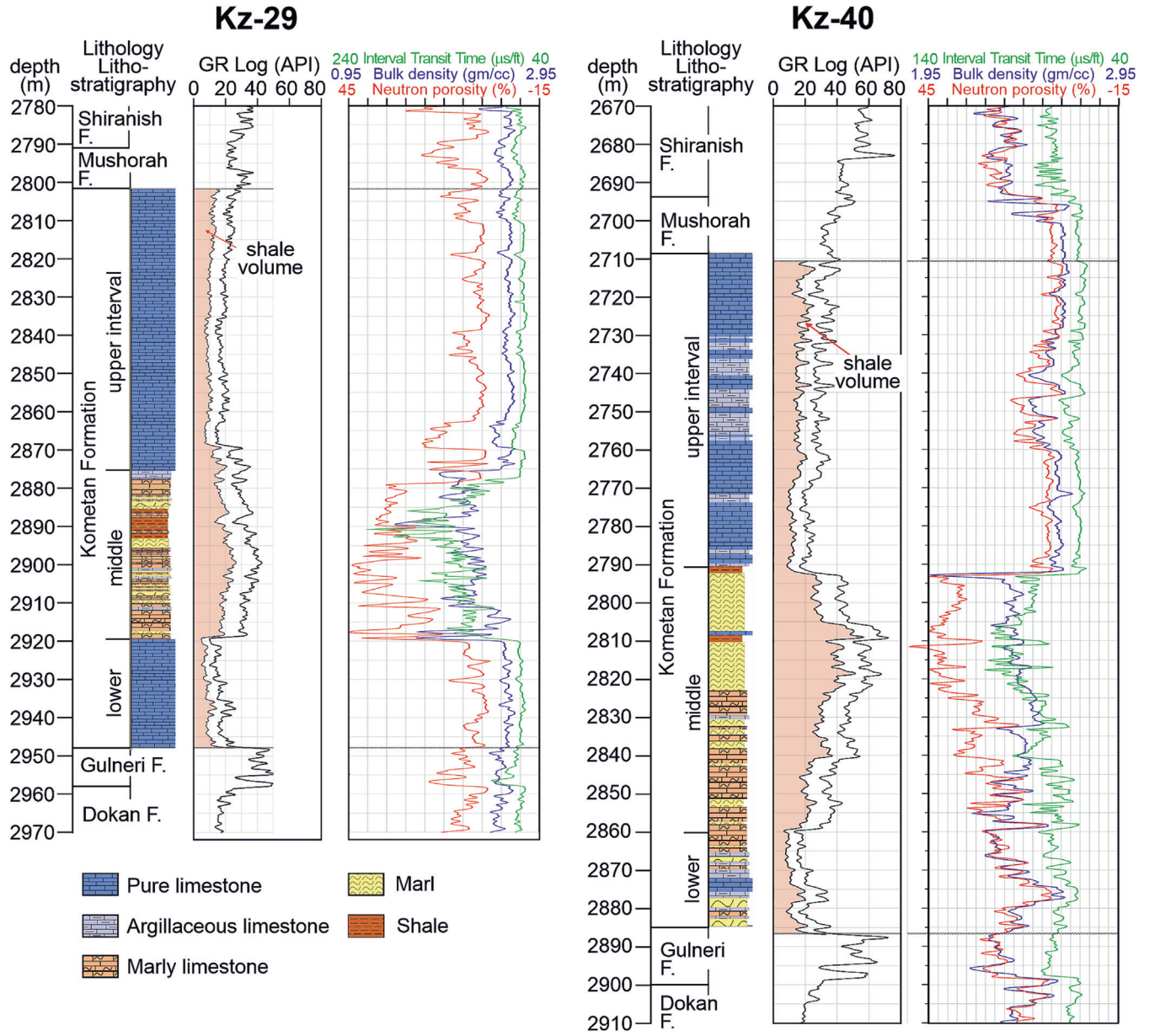

Fig. 7. Lithology and well log patterns (gamma-ray/GR/log, shale volume inferred from the GR log, bulk density, interval transit time, and neutron porosity logs). Note the three intervals with distinct lithology and corresponding log patterns, the lower and upper carbonate dominated intervals, and the middle siliciclastic interval.

2005). However, in mixed carbonate–siliciclastic depositional systems, the autochthonous carbonate facies (as well as their chemistry and well-log response) are mixed with allochthonous sediment from detrital sources generally located landwards from the carbonate factory. Bábek et al. (2013) described a carbonate ramp profile in Lower Carboniferous of the British Isles showing that from the mid ramp carbonate factory, the $CaCO_3$ contents decrease, and the computed gamma-ray values, based on K and Th concentrations increase both up-dip towards more proximal lagoonal settings, and down-dip towards the deep basin. Trends of increasing gamma-ray values and magnetic susceptibility from a proximal carbonate factory to distal basinal settings have been described from the Devonian mixed carbonate–siliciclastic systems of the Prague Basin, Czechia, and Eifel Mts., Germany (Mabille et al., 2008; Bábek et al., 2018). Such mixing of biogenic carbonate and detrital siliciclastic sediment, and proximal-to-distal spatial distribution are typical for a hybrid, mixed carbonate–siliciclastic depositional system (cf., Sarg, 1988; Dolan, 1989; Page et al., 2003). Consistently with these examples, the concentrations of Al, K, and Rb (and possibly other elements bound to detrital phyllosilicates) tend to slowly increase basinwards in the distal, outcrop parts of the Kometan Formation (Figs. 11, 12).

5.2. Depositional environment and sedimentary trends in subsurface

The depositional environment of the subsurface parts of the Kometan Formation is more difficult to interpret owing to the lack of lithology and biofacies data. However, published foraminifer data suggest that the Kometan Formation in the Jambur oil field composed of argillaceous limestones and marls corresponds to oligosteginid biofacies deposited in a restricted shelf (Abawi and Mahmood, 2005; Jassim and Goff, 2006). The regional patterns suggest that the open shelf limestone facies of the Kometan Formation of the Zagros foreland basin pass laterally towards W and SW into bioturbated chalky limestone, shale and marly limestone of the Khasib Formation deposited in a restricted shelf, and further into lagoonal shale, and carbonate of the age-equivalent Tanuma Formation (Fig. 2) (Dunnington, 1958; van

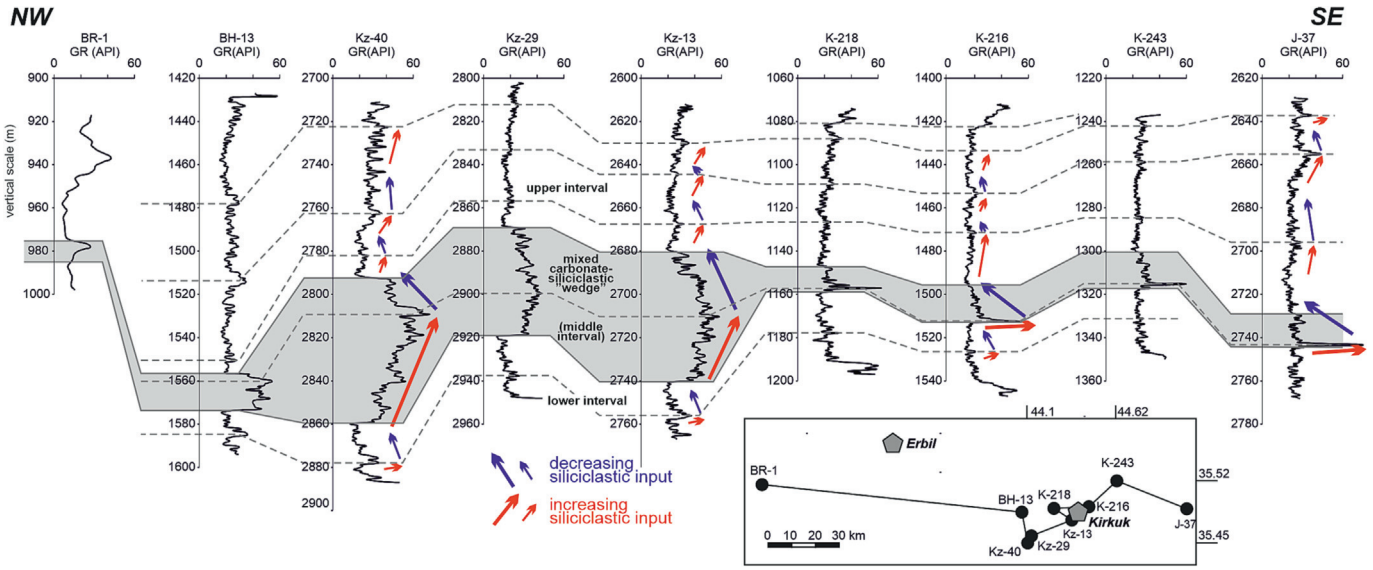

Fig. 8. Well log correlation of the Kometan Formation based on total gamma-ray logs; note the presence of middle, shaly interval (wedge of mixed carbonate–siliciclastic sediment) laterally pinching out.

Bellen et al., 1959; Buday, 1980; Al-Qayim, 2010). The Kometan Formation in the Jambur, Khabbaz, and Kirkuk oil fields is therefore considered a shallow-water equivalent of the studied outcrop sections.

The average concentrations of Al, Si, K, Ti, Fe, Rb, and Zr in the well samples are 1.8 times to 8.8 times higher than in the outcrops. These elements are associated with the detrital minerals identified from the XRD data: illite, illite/smectite, smectite, kaolinite, quartz, and K-feldspars. In contrast, the concentrations of Ca in subsurface samples are lower than in outcrops (Fig. S1, Table S1 Supplementary material). The mineralogy and geochemistry of the subsurface samples support the interpretation of the Kometan as a mixed carbonate–siliciclastic ramp (cf., Dolan, 1989; Bábek et al., 2013), in which the siliciclastic admixture decreases from more proximal (inner ramp) towards more distal parts (middle ramp). In the same direction, the Ca concentrations tend to increase to attain a maximum in the mid-ramp carbonate factory, and then slowly decrease with reduced carbonate production in the most distal basinal settings as indicated by the geochemical trends in the microfacies (Figs. 11, 12). According to the well-log (especially gamma-ray log) characteristics, the Kometan Formation is subdivided into three distinct intervals in subsurface, the lower clean interval (low GR), the middle shaly interval (high GR) and the upper clean interval (low GR) (Figs. 7, 8). We assume that the wedge of mixed carbonate–siliciclastic sediments represented by the middle shaly interval (Fig. 8) represents a progradation of more proximal ramp deposits onto the open shelf/pelagic deposits. Thus the upwards increasing gamma-ray trends in the proximal settings (Khabbaz, Kirkuk, Jambur, Bai Hasan, and Barda Rash oil fields) represent progradation (regression) whereas the upwards decreasing ones represent retrogradation (transgression).

5.3. Well log to outcrop correlation

Both the gamma-ray logs in subsurface and the geochemical logs in outcrop show vertical, upwards increasing and upwards decreasing trends, which are related to the siliciclastic admixture in carbonates. These patterns can be correlated along strike over a distance of about 30 km in outcrop, and for >100 km in subsurface (Figs. 8, 10). The present-day distance from the Khabbaz oil field (more proximal part of the basin) to the outcrop area near Dokan (distal part of the basin) is about 110 km, perpendicular to the tectonic strike. Taking the post-Cretaceous thrust-and-fold deformation into account, the syndepositional distance was presumably higher. The maximum thickness of the Kometan Formation is about 170 m in the more proximal, subsurface areas (Kz-40 well), and 96 m in the more distal outcrop areas (Zewe section). Since the dimensions of the subsurface and outcrop areas, their distance and the thickness of the Kometan Formation are comparable, we assume that it should be possible to correlate them.

In subsurface, the passage from the lower "clean" interval into the "shaly" middle interval corresponds to shallowing upwards — a progradation of the shaly restricted shelf or lagoonal sediments onto more distal carbonate ramp (regression). The passage from the middle to the upper intervals is interpreted as an opposite — transgression of distal pure carbonate onto the shaly restricted shelf/lagoonal deposits. Apart from these two large-scale trends encompassing the entire Kometan Formation, we can observe numerous (up to 5) similar, but minor regressive-to-transgressive intervals, ranging from ~15 to ~40 m in thickness (Fig. 8).

Contrary to the subsurface, in outcrop we observe a general trend of upwards decreasing Al, and K concentrations in the lower part of the Kometan, which is replaced by an upwards increasing trend in the upper part (Fig. 10). These trends split into 4 to 5 minor cycles of decreasing-to-increasing Al + K concentrations, each about 8 m to 35 m thick. The increasing Al, and decreasing Ca concentrations from more proximal to more distal middle- and outer ramp microfacies that we see in outcrop (Fig. 11) indicate that the upwards "cleaning" trend represents progradation of more proximal microfacies (MFT6) onto more distal microfacies (MFT 1, MFT2), whereas the upwards increasing Al + K trends reflect an opposite, transgressive trend.

Correlation of these transgressive–regressive pulses from the subsurface to the outcrop is based on the facies model of the Kometan Formation, and the distribution of biogenic Ca and detrital elements (Al, Rb, K) along the carbonate ramp–shelf profile (Figs. 12, 13). It is hypothesized here that the transgression–regression cycles resulted in down-dip and up-dip shifts of the middle ramp zone of maximum carbonate production. The upwards increasing gamma-ray log patterns are produced by progradation of the lagoonal and inner ramp siliciclastics on the middle ramp carbonates during the regressive phases in up-dip areas. In contrast, upwards increasing Al, and K log shapes are produced due to transgression of basinal argillaceous limestone onto the middle ramp carbonates in down-dip areas (Fig. 13). Independent age data to support this correlation model (e.g., biostratigraphy) are missing, especially in the subsurface.

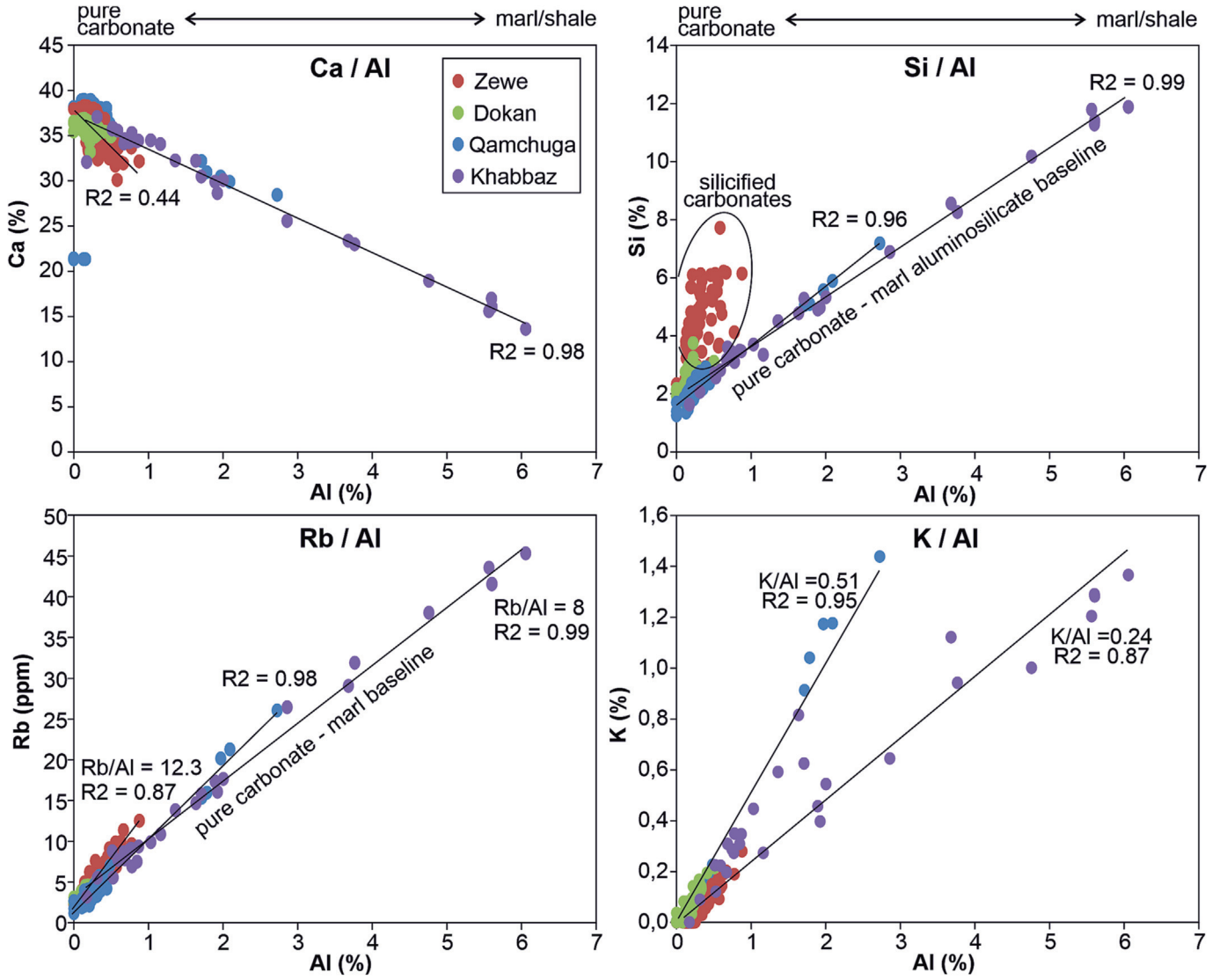

Fig. 9. Bivariate plots of concentrations of major elements representing the carbonate (Ca), and detrital components (Si, Rb, K) against Al from the outcrop sections (Qamchuga, Kometan and Shiranish Formations), and from the Kz-29, Kz-40 and K-216 wells in the Khabbaz oil field. Note the high correlation coefficients between Ca and Al, Si and Al, Rb, and Al, and K and Al in the Qamchuqa, Zewe, Dokan, and Khabbaz field wells, and the contrasting K/Al, Rb/Al ratios in the outcrop data and the Khabbaz field wells.

However, the Kometan Formation is well constrained by its lower and upper boundaries both in the outcrop and in subsurface. The simple three-fold subdivision into the lower, middle and upper intervals suggests that the Kometan Formation features relatively simple, layer-cake stratigraphy, which supports the correctness of the correlation.

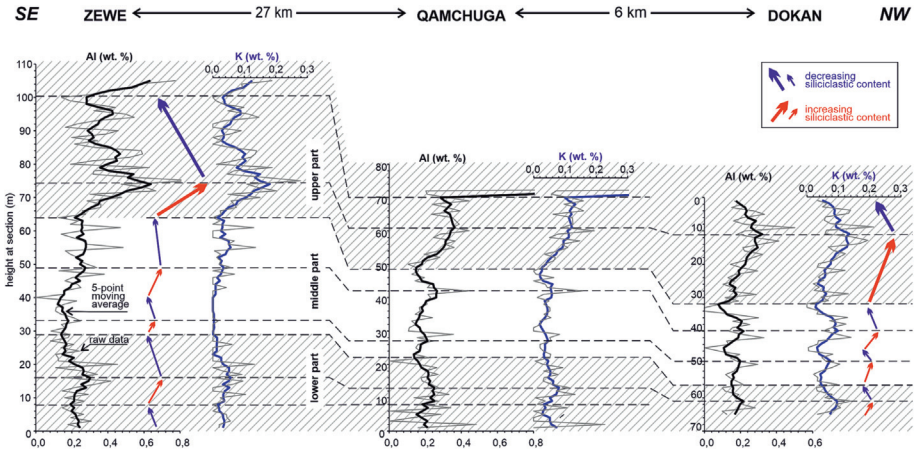

Fig. 10. Geochemical log correlation of the Al (wt%), and K (wt%) logs at the Zewe, Qamchuqa, and Dokan outcrop sections.

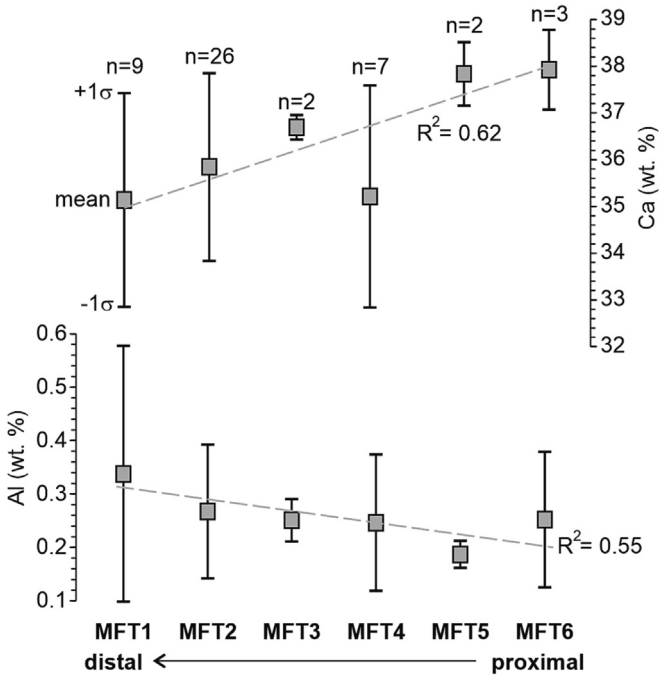

Fig. 11. Trends of decreasing mean Al concentrations and increasing mean Ca concentrations (mean value ± 1 standard deviation) in a microfacies series from MFT1 (open shelf/pelagic environment) to MFT6 (restricted shelf environment) in the Zewe and Qamchuga sections (total 49 samples).

5.4. Sequence-stratigraphic interpretation

Sequence-stratigraphic interpretation of the Kometan Formation is determined by three factors: (i) the predominance of deep-water sediments in outcrop, with low facies variability that predetermines well log and geochemical data as the only meaningful data source for stratigraphic correlation, (ii) the layer-cake stratigraphic geometry with invisible (or absent) clinoforms as inferred from such correlation (see Section 5.2), and (iii) lack of lithology data from shallow-water parts of the depositional system. Previous attempts to interpret the sequence stratigraphy of lithologically uniform deep-marine carbonates relied on the presence of specific lithological features such as hardgrounds and bioturbated horizons (Martire, 1992), element geochemistry and outcrop gamma-ray logs (Halgedahl et al., 2009; Ver Straeten et al., 2011; Bábek et al., 2016), and stable isotope geochemistry (Jarvis et al., 2001; Mabrouk et al., 2007). The gamma-ray data supported by facies can be extremely useful in sequence-stratigraphic correlations. Using the sequence-stratigraphic model of Hunt and Tucker (1992), Bábek et al. (2013) interpreted the upwards-decreasing computed gamma-ray (CGR) trends, supported by facies analysis, as normal and forced regression during highstand (HST) and falling-stage (FSST) systems tracts in the distal carbonate ramp. They conversely interpreted the upwards increasing CGR trends as transgression (TST), the peak CGR values as maximum flooding surfaces (mfs) and the rapid drops in CGR values as basal surfaces of forced regression (bsfr).

Our interpretation of the distal part of the Kometan Formation in outcrop follows similar principles: the peak Al and K concentrations are assumed to represent the overturn from transgression (T) to normal regression (R) i.e., the maximum flooding surface (mfs), whilst the end of regression and passage to transgression (maximum regression surface, mrs) are associated with Al and K concentration minima (Fig. 13). In contrast, the well log patterns in the more proximal, subsurface part of the Kometan Formation were primarily controlled by basinwards and landwards shifts of the proximal siliciclastic system onto the more distal ramp carbonates. Consequently, the peak gamma-ray values represent maximum regression surfaces whereas the gamma-ray minima represent maximum flooding surfaces. It is assumed here that the T–R cycles in outcrop were synchronous with the T–R cycles in subsurface. In this rather simplistic model, we use the maxima and minima on the curves as the only reliable correlation points. This approach is close to the "inductive" sequence-stratigraphic concept of Embry and Johannessen (2017) identifying the maximum flooding surfaces as separating underlying, upwards deepening strata from overlying, upwards shallowing ones (and vice versa for maximum regressive surfaces). Using just two easily identifiable surfaces, the T–R sequences of Embry and Johannessen (1993, 2017) consist of just two systems tracts, transgressive (TST) and regressive (RST). Under the conditions defined at the beginning of this section, this model is applicable. The Kometan Formation consists of four T–R sequences, ranging in thickness from ~10 to ~45 m.

5.5. Remarks on reservoir quality

The relationship between the wireline log characteristics reveals that the matrix porosity (sonic porosity) decreases with depth, from about 10–20 % at the top to about 5 % at the bottom of the Kometan Formation (Kz-216 well, Fig. 13A). However, the reservoir quality is largely given by the fracture porosity, which can be inferred from the residues between the neutron-density (N-D) porosity and sonic porosity. The N-D porosities reach up to 40 % in the upper interval of the Kometan Formation whilst they drop down to about 5 % in its lower interval (Fig. 13). There are four depth segments in the upper interval, in which the N-D *minus* sonic porosity residues increase. All of them coincide with the passages from transgressive to regressive systems tracts (maximum flooding surface) which corresponds to the pure carbonates.

In general, the Zagros foreland oil reservoirs in northern Iraq, including the Kirkuk embayment, the Avanah and Baba Domes, the Bai Hassan field as well as the gas reservoirs in the Jambur oil field all produce from fractured reservoirs of the Kometan Formation (Aqrawi, 1996). Light oils (41 API) are produced from the Kometan Formation, a fractured reservoir in the Taq oil field with estimated recoverable reserves of 700–750 million barrels. When the field is fully established, it is anticipated that it will yield 200,000–250,000 barrels per day (Rashid et al., 2015a, 2015b). Fractures that increased the formation's porosity and permeability are principally responsible for controlling the productivity of carbonate rock in the Kometan Formation (Rashid et al., 2015a, 2015b). In addition, the fractured reservoir quality inferred from well-log data has been supported by rock samples from outcrops (Hussein, 2022).

Rheology of the carbonate likely changes with shale content, resulting in higher susceptibility of the pure carbonates to brittle deformation and development of fracture systems, compared to argillaceous carbonates and marls. It is assumed that in mixed carbonate–siliciclastic ramps, the sea-level driven transgressive–regressive, upwards cleaning and dirtying sequences control the post-depositional development of fracture systems and affect the reservoir quality.

6. Conclusions

Outcrop analogues of the Upper Cretaceous Kometan Formation, a prolific carbonate oil and gas reservoir of northern Iraq, are thin bedded, deep-water carbonates. The formation is composed of mudstones to packstones with planktonic, and benthic foraminifers, subdivided to 6 microfacies, MF1 to MF6, deposited in basinal, outer carbonate ramp and middle ramp, settings. Subsurface parts of the Kometan Formation are drilled in several oil fields in northern Iraq. They are composed of carbonates, marls and shales with benthic foraminifers, which are interpreted as inner ramp to middle ramp equivalents of the ramp carbonates exposed in outcrops.

Concentrations of chemical elements in bulk-rock samples show predictable patterns of increasing Al and K, and decreasing Ca concentrations from more proximal to more distal carbonate ramp microfacies. Vertical distribution in geochemical logs of Al, K, Rb and Si (detrital) concentrations shows correlatable patterns between three outcrops

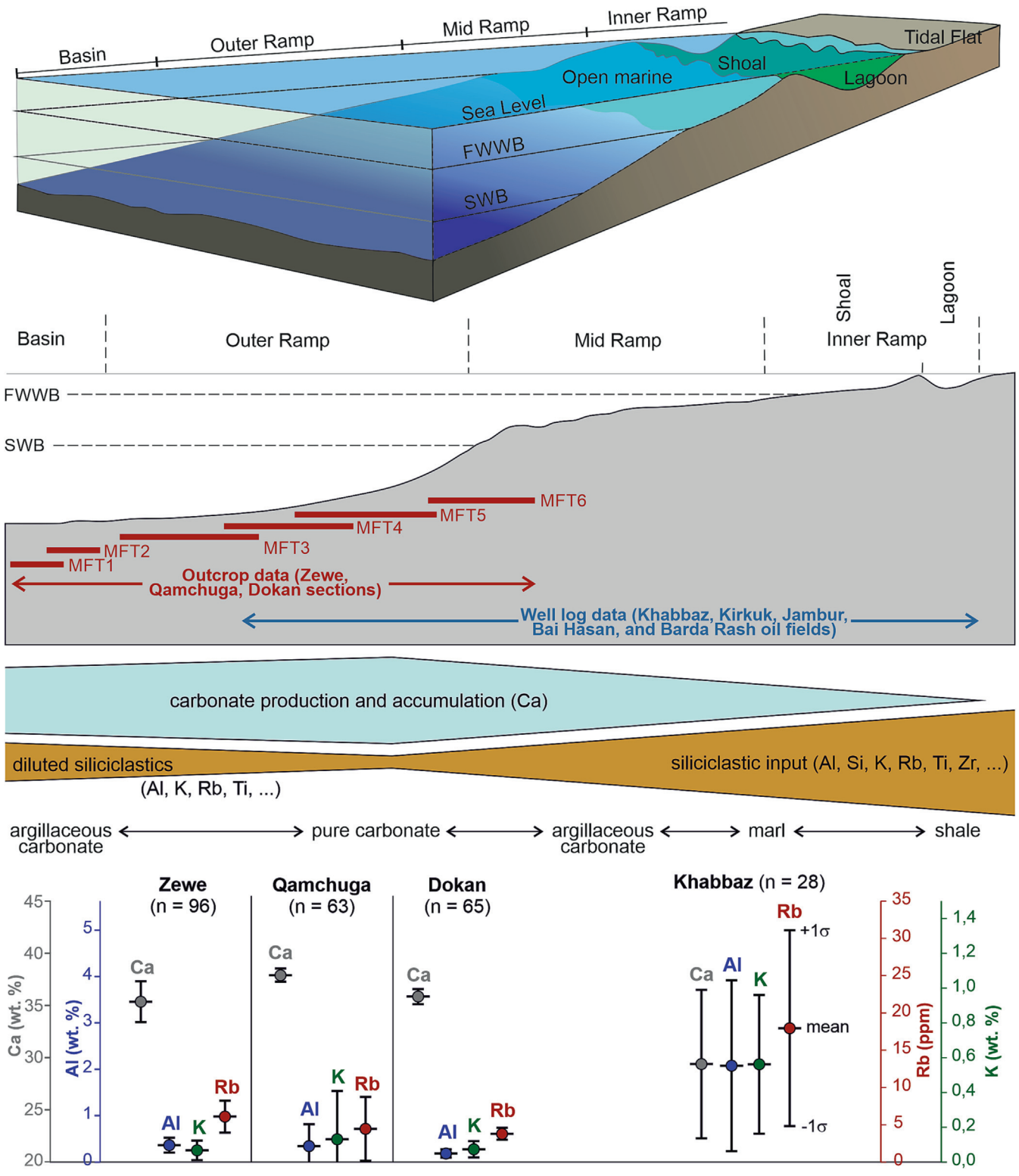

Fig. 12. Depositional model showing the interpreted mixed siliciclastic–carbonate ramp depositional environments of the Kometan Formation, distribution of selected elements (mean ± standard deviation of Ca, Al, K, Rb) along the ramp profile, and a schematic distribution of biogenic carbonate (Ca) and detrital elements (Al, Si, K, Rb, Ti, and Zr) along the ramp profile.

for 33 km distance along strike. Conversely, the inner to middle ramp logs show decreasing gamma-ray values, and shale volumes from more proximal to more distal facies, whilst their log patterns can be correlated for more than a hundred kilometres.

The outcrop geochemical logs and subsurface gamma-ray log patterns show opposite vertical trends across the lower, middle and upper parts of the Kometan Formation. In subsurface, the inner ramp gamma-ray maxima (most prominently in the middle Kometan Formation) indicate maximum regression surfaces (mrs) whilst the GR minima are interpreted as maximum flooding surfaces (mfs). In the outcrop sections representing outer to middle ramp environments, the Al and K log minima (middle Kometan) represent the maximum regression surfaces whereas the Al and K minima represent maximum flooding surfaces. In our interpretation, the opposite log trends were jointly controlled by

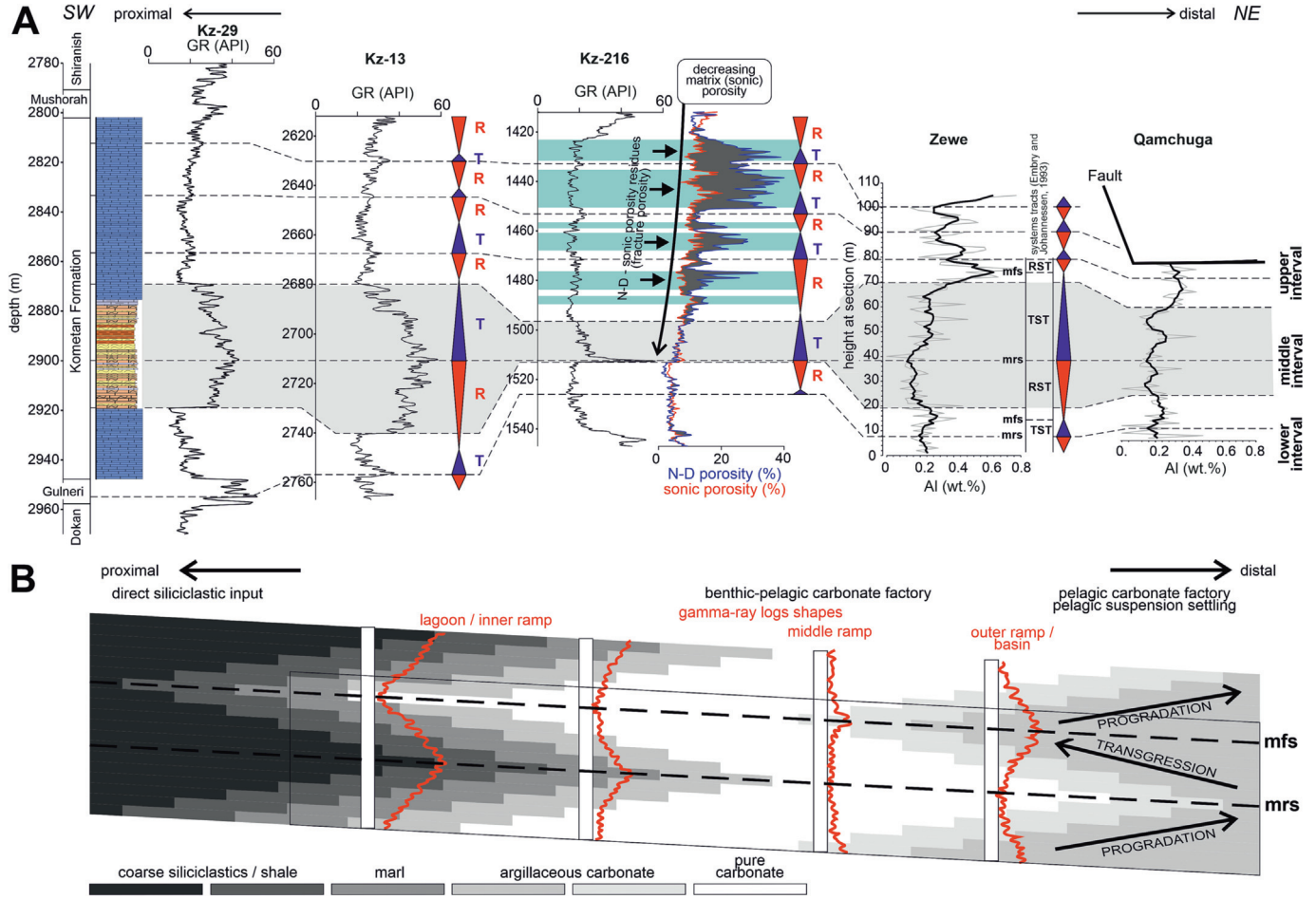

Fig. 13. (A) Subsurface to outcrop correlation of gamma-ray logs and geochemical logs of the Kometan Formation, and (B) simplified schematic model of carbonate–siliciclastic distribution and gamma-ray log shapes along a transgressive–regressive (T–R) cycle in mixed carbonate–siliciclastic ramps based on the Kometan Formation data.

landwards and seawards shifts of the middle ramp carbonate factory within the mixed carbonate–siliciclastic ramp system during transgressions and regressions, respectively.

The Kometan Formation is a fractured reservoir, in which fractures are responsible for reservoir quality. The neutron-density and sonic porosity logs show significant variation across the formation indicating that the best reservoir quality is achieved in pure carbonates. We assume that the transgressive–regressive, upwards cleaning and dirtying sequences might control the development of fracture systems and affect the reservoir quality in mixed carbonate–siliciclastic ramps.

Supplementary data to this article can be found online at https://doi.org/10.1016/j.sedgeo.2023.106547.

Data availability

Data will be made available on request.

Declaration of competing interest

The authors declare that they have no known competing financial interests or personal relationships that could have appeared to influence the work reported in this paper.

Acknowledgements

Hussein Hussein thanks the financial support within the Fischer PhD scholarship programme of Palacký University Olomouc. This research was partly funded from the project 22-15405S of the Czech Science Foundation (GACR). We thank Dalibor Všianský, Masaryk University Brno, for the XRD analyses, and the two journal reviewers, Beatriz Bádenas and Aram Bayet-Goll, and the journal editor Massimo Moretti for insightful comments which helped us to significantly improve the manuscript.

References

Abawi, T., Mahmood, S., 2005. Biostratigraphy of the Kometan and Gulneri Formations (Upper Cretaceous) in Jambur well No. 46, Northern Iraq. Iraqi Journal of Earth Science 5, 1–8.

Adabi, M.H., Mehmandosti, E.A., 2008. Microfacies and geochemistry of the Ilam Formation in the Tang-E Rashid area, Izeh, SW Iran. Journal of Asian Earth Sciences 33, 267–277.

Al-Barzinjy, S., 2007. Origin of Chert Nodules in Kometan Formation from Dokan Area, Northeast Iraq. Iraqi Bulletin of Geology and Mining 4, 95–104.

Al-Qayim, B., 2010. Sequence stratigraphy and reservoir characteristics of the Turonian–Coniacian Khasib Formation in Central Iraq. Journal of Petroleum Geology 33, 387–404.

Amorosi, A., 1995. Glaucony and sequence stratigraphy; a conceptual framework of distribution in siliciclastic sequences. Journal of Sedimentary Research 65, 419–425.

Aqrawi, A.A.M., 1996. The Mesopotamian Basin carbonate–siliciclastic sediments of the Upper Cretaceous (Khasib, Tanuma, and Sa'di Formations). Marine and Petroleum Geology 13, 781–790.

Aqrawi, A.A.M., Horbury, A.D., Goff, J.C., Sadooni, F.N., 2010. The Petroleum Geology of Iraq. Scientific Press Ltd, Beacons field, UK (424 pp.).

Bábek, O., Kalvoda, J., Cossey, P., Šimíček, D., Devuyst, F.-X., Hargreaves, S., 2013. Facies and petrophysical signature of the Tournaisian/Viséan (Lower Carboniferous) sea-level cycle in carbonate ramp to basinal settings of the Wales–Brabant massif, British Isles. Sedimentary Geology 284–285, 197–213.

Bábek, O., Kumpan, T., Kalvoda, J., Matys Grygar, T., 2016. Devonian/Carboniferous boundary glacioeustatic fluctuations in a platform-to-basin direction: a geochemical approach of sequence stratigraphy in pelagic settings. Sedimentary Geology 337, 81–99.

Bábek, O., Faměra, M., Šimíček, D., Weinerová, H., Hladil, J., Kalvoda, J., 2018. Sea-level changes vs. organic productivity as controls on Early and Middle Devonian bioevents:

facies and gamma-ray based sequence-stratigraphic correlation of the Prague Basin, Czech Republic. Global and Planetary Change 160, 75–95.
Bábek, O., Vodrážková, S., Kumpan, T., Kalvoda, J., Holá, M., Ackerman, L., 2021. Geochemical record of the subsurface redox gradient in marine red beds: a case study from the Devonian Prague Basin, Czechia. Sedimentology 68, 3523–3548.
Balaky, S., Asaad, I., Al-Juboury, A., 2016. Facies analysis and sequence stratigraphy of Kometan Formation (Upper Cretaceous) in the imbricated zone, north eastern Iraq. Arabian Journal of Geosciences 9, 1–17. https://doi.org/10.1007/s12517-016-2794-y.
Bernaus, J.M., Arnaud-Vanneau, A., Caus, E., 2002. Stratigraphic distribution of Valanginian–Early Aptian shallow-water benthic foraminifera and algae, and depositional sequences of a carbonate platform in a tectonically-controlled basin: the Organyà Basin, Pyrenees, Spain. Cretaceous Research 23, 25–36.
Buday, T., 1980. The Regional Geology of Iraq. V.L.; Stratigraphy and Paleogeography. S.O.M. Library, Baghdad (350 pp.).
Buday, T., Jassim, S., 1987. The Regional Geology of Iraq: Tectonics, Magmatism, and Metamorphism. In: Kassab, I.I., Abbas, M.J. (Eds.), Geology of Iraq, Geologic Survey, Baghdad 445 p.
Carmichael, S.K., Waters, J., Königshof, P., Suttner, T., Kido, E., 2019. Paleogeography and paleoenvironments of the Late Devonian Kellwasser Event: a review of its sedimentological and geochemical expression. Global and Planetary Change 183, 1–17.
Cross, T.A., 1988. Controls on coal distribution in transgressive-regressive cycles, Upper Cretaceous, Western Interior, U.S.A. In: Wilgus, C.H., Hastings, B.S., Kendall, C.G.S.C., Posamentier, H.W., Ross, C.A., Van Wagoner, J.C. (Eds.), Sea Level Changes – An Integrated Approach. SEPM Special Publication42, pp. 371–380.
Csontos, L., Sasvári, Á., Pocsai, T., Kósa, L., Salae, A.T., Ali, A., 2012. Structural evolution of the northwestern Zagros, Kurdistan Region, Iraq: implications on oil migration. Geo Arabia 17, 81–116.
De Mol, B., Van Resnbergen, P., Pillen, S., Van Herreweghe, K., Van Rooij, D., McDonnell, A., Huvenne, V., Ivanov, M., Swennen, R., 2002. Large deep-water coral banks in the Porcupine Basin, southwest of Ireland. Marine Geology 188, 193–231.
Dolan, J., 1989. Eustatic and tectonic control on deposition of hybrid siliciclastic/carbonate basinal cycles: discussion with examples. American Association of Petroleum Geologists Bulletin 73, 1233–1246.
Dunham, R.J., 1962. Classification of carbonate rocks according to depositional texture. In: Ham, W.E. (Ed.), Classification of Carbonate Rocks. American Association of Petroleum Geologists, Tulsa, pp. 108–121.
Dunnington, H.V., 1958. Generation, Migration, Accumulation and Dissipation of Oil in Northern Iraq. In: Weeks, L.G. (Ed.), Habitite of Oil, Symposium. American Association of Petroleum Geologists, pp. 1194–1251.
Dunnington, H.V., 2005. Generation, migration, accumulation, and dissipation of oil in northern Iraq. Geo Arabia 10, 39–84.
Ehrenberg, S.N., Eberli, G.P., Keramati, M., Moallemi, S.A., 2006. Porosity–permeability relationships in interlayered limestone–dolostone reservoirs: American Association of Petroleum Geologists. Bulletin 90 (1), 91–114.
Embry, A.F., Johannessen, E.P., 1993. T-R sequence stratigraphy, facies analysis and reservoir distribution in the uppermost Triassic-Lower Jurassic succession, western Sverdrup Basin, Arctic Canada. In: Vorren, T., Bergsager, E., Dahl-Stamnes, O.A., Holter, E., Johansen, B., Lie, E., Lund, T.B. (Eds.), Arctic Geology and Petroleum Potential. Norwegian Petroleum Society Special Publications2, pp. 121–146.
Embry, A.F., Johannessen, E.P., 2017. Two approaches to sequence stratigraphy. Stratigraphy & Timescales2 pp. 85–118.
Flügel, E., 2004. Microfacies of Carbonate Rocks: Analysis, Interpretation, and Application. Springer-Verlag, Berlin Heidelberg (976 pp.).
Graham, J., 1988. Collection and analysis of field data. In: Tucker, M.E. (Ed.), Techniques in Sedimentology. Blackwell Scientific Publ., pp. 5–61.
Haddad, S., Amin, M., 2007. Mid-Turonian–early Campanian sequence stratigraphy of northeast Iraq. Geo Arabia 12, 135–176.
Halgedahl, S.L., Jarrard, R.D., Brett, C.E., Allison, P.A., 2009. Geophysical and geological signatures of relative sea level change in the upper Wheeler Formation, Drum Mountains, West-Central Utah: a perspective into exceptional preservation of fossils. Palaeogeography Palaeoclimatology Palaeoecology 277, 34–56.
Hart, B., Longstaffe, F., Plint, A., 1992. Evidence for relative sea level change from isotopic and elemental composition of siderite in the Cardium Formation, Rocky Mountain Foothills. Bulletin of Canadian Petroleum Geology 40, 52–59.
Hunt, D., Tucker, M.E., 1992. Stranded parasequences and the forced regressive wedge systems tract: deposition during base-level fall. Sedimentary Geology 81, 1–9.
Hussein, S.H., 2022. Carbonate fractures from conventional well log data, Kometan Formation, Northern Iraq case study. Applied Geophysics 206, 1–8.
Jarvis, I., Murphy, A.M., Gale, A.S., 2001. Geochemistry of pelagic and hemipelagic carbonates: criteria for identifying systems tracts and sea-level change. Geological Society, London 158, 685–696.
Jassim, Z.J., Goff, J.C., 2006. The Geology of Iraq. Dolin, Prague (341 pp.).
Kaddouri, N., 1982. Tel Hajar: a new Cenomanian–Lower Turonian stratigraphic unit from North west Iraq. Cretaceous Research. Academic Press Inc., London, pp. 391–395.
Karim, K.H., Koyi, H., Baziany, M.M., Hessami, K., 2011. Significance of angular unconformities between Cretaceous and Tertiary strata in the northwestern segment of the Zagros Fold Thrust belt, Kurdistan Region, NE-Iraq. Geological Magazine, Cambridge University Press 148 (6/5), 925–939.
Keller, G., 1993. The Cretaceous–Tertiary boundary transition in the Antarctic Ocean and its global implications. Marine Micropaleontology 21, 1–45.
Keller, G., Adatte, T., Stinnesbeck, W., Luciani, V., Karoui, N., Zaghbib-Turki, D., 2002. Paleoecology of the Cretaceous–Tertiary mass extinction in planktic foraminifera. Palaeogeography Palaeoclimatology Palaeoecology 178, 257–298.
Kumpan, T., Bábek, O., Kalvoda, J., Matys Grygar, T., Frýda, J., 2014. Sea-level and environmental changes around the Devonian–Carboniferous boundary in the Namur–Dinant Basin (S Belgium, NE France): a multi-proxy stratigraphic analysis of carbonate ramp archives and its use in regional and interregional correlations. Sedimentary Geology 311, 43–59.
Mabille, C., Pas, D., Aretz, M., Boulvain, F., Schroder, S., da Silva, A.C., 2008. Deposition within the vicinity of the Mid-Eifelian High: detailed sedimentological study and magnetic susceptibility of a mixed ramp-related system from the Eifelian Lauch and Nohn formations (Devonian; Ohlesberg, Eifel, Germany). Facies 54, 597–612.
Mabrouk, A., Jarvis, I., Belayouni, H., Murphy, A., Moody, R.T.J., 2007. Sequence stratigraphy, sea level change and palaeoenvironments via chemostratigraphy: regional to global correlations. AAPG Search and Discovery Article #40244, 1–12.
Martire, L., 1992. Sequence stratigraphy and condensed pelagic sediments. An example from the Rosso Ammonitico Veronese, northeastern Italy. Palaeogeography Palaeoclimatology Palaeoecology 94, 169–191.
Morad, S., 1998. Carbonate cementation in sandstones: distribution patterns and geochemical evolution. International Association of Sedimentologists Seriesvol. 26, pp. 1–26.
Morad, S., Ketzer, J., De Ros, L.F., 2000. Spatial and temporal distribution of diagenetic alterations in siliciclastic rocks: implications for mass transfer in sedimentary basins. Sedimentology 47, 95–120.
Morad, S., Al-Ramadan, K., Ketzer, J.M., De Ros, L., 2010. The impact of diagenesis on the heterogeneity of sandstone reservoirs: a review of the role of depositional facies and sequence stratigraphy. American Association of Petroleum Geologists Bulletin 94, 1267–1309.
Morad, S., Ketzer, J., DeRos, L., 2012. Linking diagenesis to sequence stratigraphy: an integrated tool for understanding and predicting reservoir quality distribution. International Association Sedimentologists, Special Publicationvol. 45, pp. 1–36.
Oberto, S., 1984. Fundamentals of well-log interpretation. 1. The acquisition of logging data. Developments in Petroleum Sciencevol. 15B. Elsevier, Amsterdam (435 pp.).
Omigie, J.I., Alaminiokuma, G.I., 2020. Well log sequence stratigraphic analyses for reservoir delineation and hydrocarbon distribution in the eastern part of the central swamp depobelt, Niger Delta. Earth Sciences and Geotechnical Engineering 10, 1–14.
Page, M.C., Dickens, G.R., Dunbar, G.B., 2003. Tropical view of Quaternary sequence stratigraphy: siliciclastic accumulation on slopes east of the Great Barrier Reef since the Last Glacial Maximum. Geology 31, 1013–1016.
Posamentier, H.W., Allen, G.P., 1999. Siliciclastic Sequence Stratigraphy: Concepts and Applications. Society for Sedimentary Geology, Tulsa, Oklahoma (193 pp.).
Rashid, F., Glover, P.W.J., Lorinczi, P., Collier, R., Lawrence, J., 2015a. Porosity and permeability of tight carbonate reservoir rocks in the north of Iraq. Petroleum Science and Engineering 133, 147–161.
Rashid, F., Glover, P., Lorinczi, P., Hussein, D., Collier, R., 2015b. Permeability prediction in tight carbonate rocks using capillary pressure measurements. Marine and Petroleum Geology 68, 536–550.
Rashid, F., Glover, P., Lorinczi, P., Hussein, D., Lawrence, J., 2017. Microstructural controls on reservoir quality in tight oil carbonate reservoir rocks. Petroleum Science and Engineering 156, 814–826.
Read, J., Horbury, A.D., 1993. Eustatic and tectonic controls on porosity evolution beneath sequence bounding unconformities and parasequence disconformities on carbonate Platforms. In: Horbury, A., Robinson, A.G. (Eds.), Diagenesis and Basin Development. AAPG, Tulsa, pp. 155–197.
Rider, M.H., 1999. The Geological Interpretation of Well Logs. Whittles Publishing Services (288 pp.).
Sarg, J.F., 1988. carbonate sequence stratigraphy. In: Wigus, C.K. (Ed.), Sea-level Change: An Integrated Approach. Society of Economic Paleontologists and Mineralogists, Special Publicationvol. 42, pp. 155–181.
Schlager, W., 2005. Carbonate sedimentology and sequence stratigraphy. SEPM Society for Sedimentary Geology, Concepts in Sedimentology and Paleontologyvol. 8 Tulsa, (200 pp.).
Scholle, P.A., Ulmer-Scholle, D.S., 2003. A color guide to the petrography of carbonate rocks: grains, textures, porosity, diagenesis. American Association of Petroleum Geologists Memoir. 77 (Tulsa, 474 pp.).
Šimíček, D., Bábek, O., 2015. Spectral gamma-ray logging of the Grès d'Annot, SE France: an outcrop analogue to geophysical facies mapping and well-log correlation of sand-rich turbidite reservoirs. Marine and Petroleum Geology 60, 1–17.
Sissakian, V.K., 2000. Geological Map of Iraq. Sheets No.1, Scale 1: 1000 000, State Establishment of Geological Survey and Mining. GEOSURV, Baghdad, Iraq.
Stadtmůller, M., 2019. Well logging interpretation methodology for carbonate formation fracture system properties determination. Acta Geophysica 67, 1933–1943.
Tucker, M.E., 1993. Carbonate diagenesis and sequence stratigraphy. In: Wright, P.V. (Ed.), Sedimentology Review/1. Blackwell Scientific Publications, Oxford, pp. 51–72.
Tucker, M.E., Wright, V.P., 1990. Carbonate Sedimentology. Wiley-Blackwell, Oxford (484 pp.).
Van Bellen, R.C., Dunnington, H.V.G., Wetzel, R., Morton, D.M., 1959. Lexique Stratigraphique international, III, Asie, fasc.10a, Iraq. Centre national de la recherché scientifique, Paris (333 pp.).
Ver Straeten, C.A., Brett, C.E., Sageman, B.B., 2011. Mudrock sequence stratigraphy: a multi-proxy (sedimentological, paleobiological and geochemical) approach, Devonian Appalachian Basin. Palaeogeography Palaeoclimatology Palaeoecology 304, 54–73.
Westphal, H., Eberli, G.P., Smith, L.B., Grammer, G.M., Kislak, J., 2004. Reservoir characterization of the Mississippian Madison Formation, Wind River basin, Wyoming. American Association of Petroleum Geologists Bulletin 88 (4), 405–432.
Whalen, M.T., Eberli, G.P., Van Buchem, F.S., Mountjoy, E.W., Homewood, P.W., 2000. Bypass margins, basin-restricted wedges, and platform-to-basin correlation, Upper Devonian, Canadian Rocky Mountains: implications for sequence stratigraphy of carbonate platform systems. Journal of Sedimentary Research 70, 913–936.
Wilson, J.L., 1975. The Lower Carboniferous Waulsortian facies. Carbonate Facies in Geologic History. Springer, Berlin, pp. 148–168.

Appendix 3

Journal of Applied Geophysics 206 (2022) 104810

Contents lists available at ScienceDirect

Journal of Applied Geophysics

journal homepage: www.elsevier.com/locate/jappgeo

Carbonate fractures from conventional well log data, Kometan Formation, Northern Iraq case study

Hussein S. Hussein [a,b,*]

[a] Department of Geology, Palacký University, 17. listopadu 12, Olomouc 77146, Czech Republic
[b] Department of Petroleum Geosciences, Soran University, Soran, Erbil 44002, Iraq

ARTICLE INFO

Keywords:
Fractures
Conventional well logging
Kometan Formation

ABSTRACT

The Borehole Acoustic Televiewer, Formation Micro scanner (FMS), Formation Micro-Imager (FMI), and Electric Micro Imaging (EMI) are the most qualified approaches to fracture identification. Still, they are more expensive and only give images at specific intervals. Conventional well log tools can be identified without interval limitations. This study aimed to demonstrate the ability of the Conventional well logging tools to identify fractures in the Upper Cretaceous Kometan Formation in the Northern part of Iraq. The study area is located at latitudes 3,922,836.34 N to 3,930,557 N and longitudes 448,350.78E to 417772E for the well of Kirkuk 216 (K216) and Khabbaz 40 (Kz40), respectively. Quantitative interpretations like secondary porosity index and qualitative are the total porosity-sonic porosity cross-plot, caliper log, total gamma-ray log, and porosity logs (neutron, sonic, and density log) have been used to identify fractures in the studied formation. Some subsurface rock samples (spectral gamma ray) and outcrop observations were also used to validate well log data results. Good secondary porosity (fractures) has been Identified from the Secondary Porosity Index (SPI), which is reached a maximum value of 17%, and the average is 4% for Kz40. The maximum value is 30%, and the average is 8% for K216. Based on the qualitative interpretations of the available log data, which were validated by subsurface rock samples and observed outcrop sections of the studied formation, it has been concluded that the reservoir quality of the Kometan formation was enhanced due to high fractures in the studied wells.

1. Introduction

The complexity and heterogeneity of carbonate rocks due to different depositional textures and diagenetic impact over a large scale of Northern Iraq's geology makes evaluating reservoir quality remarkably challenging since fractures are common in carbonate reservoirs. The complexity and heterogeneity of carbonate rocks primarily result from naturally fractured properties. These fractures have an essential impact on reservoir quality, which enhances the movability of fluids and production (Roehl and Choduette, 1985).

1.1. Fracture identification

Fractures can be identified directly from core samples and indirectly from seismic sections, well log data, well tests, and drilling mud losses (Thompson, 2000; Nelson, 2001; Martinez-Torres, 2002; Dutta et al., 2007). The Borehole Acoustic Televiewer, Formation Micro scanner (FMS), Formation Micro-Imager (FMI), and Electric Micro Imaging (EMI) are the most qualified approaches to fracture identification, but they are more expensive and only give images at specific intervals. On the other hand, the Conventional well log tools can be evaluated without limitations. In addition, open and fluid-filled fractures are also sensitive to the conventional logging approaches (Laongsakul and Durrast, 2011). The recognition of fracture networks is critical for carbonate reservoirs, especially in low pores and permeability carbonates, because permeability would enhance by fractures.

1.2. Carbonate of Kometan Formation

The Kometan Formation is a fractured reservoir that produces commercial oil in some oil fields in the north of Iraq (Aqrawi, 1996). In Kirkuk embayment, the Kometan Formation is productive in the oil reservoirs at the Avanah and Baba Domes of the Kirkuk structure and the Bai Hassan field and produces gas in the Jambur oil field (Aqrawi et al., 2010). The Kometan Formation is a fractured reservoir in the Taq Taq oil field and produces light oils (41 API) with estimated recoverable

* Corresponding author at: Department of Geology, Palacký University, Tř. Svobody 26, 77146 Olomouc, Czech Republic.
E-mail address: hussein.hussein01@upol.cz.

https://doi.org/10.1016/j.jappgeo.2022.104810
Received 19 April 2022; Received in revised form 27 June 2022; Accepted 7 September 2022
Available online 11 September 2022
0926-9851/

Fig. 1. Location map and tectonic subdivision for the study area and well locations.

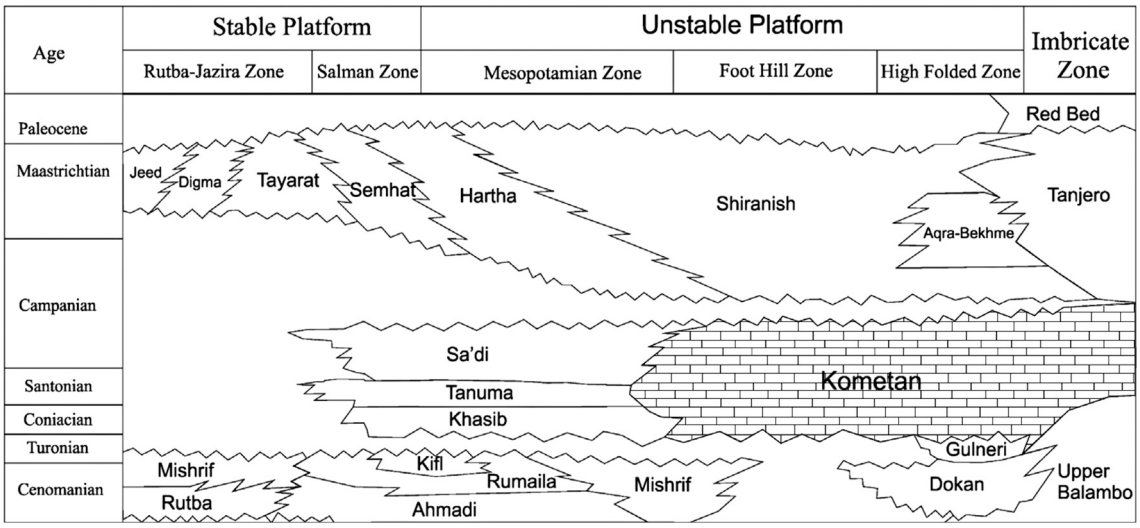

Fig. 2. Chronostratigraphic division of Cretaceous rock in Iraq (Al-Qayim, 2010)

reserves of 700–750 million barrels. It has been predicted that the field will produce 200,000–250,000 barrels per day when it is fully developed (Taq Taq Operation Company (TTOPCO), 2007 in Rashid et al., 2015). The productivity of carbonate rock in the Kometan Formation is mainly controlled by fractures which enhanced the Formation's porosity and permeability (Rashid et al., 2015).

The objectives of this study are to demonstrate the ability of Conventional well logging tools to identify fractures and the detection of fracture zones in the Upper Cretaceous Kometan Formation in the Northern part of Iraq.

2. Geological setting

2.1. Study area

The Khabbaz Oil Field (Kz) is located about 20 km southwest of Kirkuk city between the Jambour and Bai Hassan oil fields, northern Iraq (Fig. 1). The field extends alongside Kirkuk Oil Field about 23 km southwest of the Baba Dome. The Folded Zone of Unstable Shelf is located in the Foot Hill Zone (Buday and Jasim, 1986). It represents a small subsurface asymmetrical anticline with an NW-to-SE trending axis. The length and width of the structure are about 18 km and 4 km, respectively. The southwest limb is gentler than the northeast.

In 1955, the Iraqi Petroleum Company (I.P.C) explored the first seismic of the area, which indicated a subsurface structure plunging to NW. Another seismic investigation confirmed the presence of the structure in 1971 (Qadir, 2008). The first well (Kz-1) in the field was drilled in 1976. Most of the wells drilled later reached Tertiary reservoirs, and some of them penetrated Cretaceous reservoirs.

In the subsurface, the Kirkuk Oil field is an anticlinal structure trending northwest to the southeast, 100 km long and 4 km wide at the original oil/water contact level in the Tertiary Reservoir. Structurally, it is composed of three domes, referred to, from south-east to north-west, as Baba, Avanah, and Khurmala, separated by saddles, namely Amshe

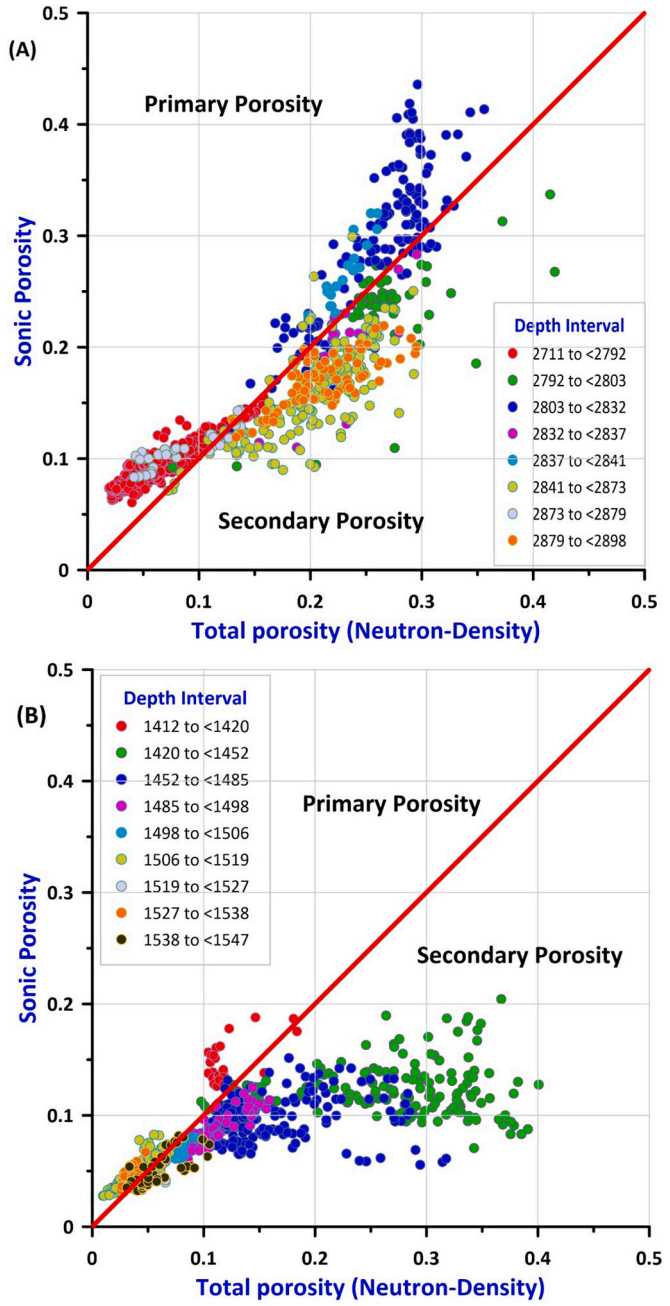

Fig. 3. Secondary porosity indicated from porosity cross-plots, A in Kz40 and B in K216 wells.

and Dibega (Dunnington, 2005). However, it is a simple folded structure at the surface due to the Miocene salt flowage of the Lower Fars Formation. Kirkuk field includes three pay zones. The Kirkuk Tertiary Reservoir first, the second, and third pay in the Upper and Middle Cretaceous (Dunnington, 2005). The study area is located at latitudes 3,922,836.34 N to 3,930,557 N and longitudes 448,350.78E to 417772E for the well of Kirkuk 216 (K216) and Khabbaz 40 (Kz40), respectively (Fig. 1).

2.2. Study formation

This study focuses on the Kometan Formation of the Late Cretaceous (Turonian to Campanian) age. Carbonate rocks of the Kometan Formation were first defined at Kometan village (Dunnington, 1958; Van Bellen et al., 1959), located north-east of the town of Rania, about 103 km NNE of Kirkuk, located in the High Folded Zone of the Zagros Mountains, northern Iraq. The Kometan Formation has been studied in various locations such as Imbricated Zone, High Folded Zone, Low Folded Zone, and outcrop and sub-surface sections. The Kometan Formation consists of white weathered, light grey limestone (Fig. 2).

The lower contact of the Shiranish Formation is unconformable with the Kometan Formation, which is the presence of glauconitic at the lower contact of the Shiranish Formation can be used as a marker bed (Van Bellen et al., 1959; Dunnington, 1958). The lithology of the studied formation varies from other outcrops and in the subsurface of Low Folded Zone, which changes to marly into the west and southwest of Iraq (Van Bellen et al., 1959; Dunnington, 1958), and laterally, the biofacies vary from a composite of globigerinal limestone and oligosteginal intercalation to oligosteginal facies (Buday, 1980).

In outcrop, it has a variable thickness ranging from about 36 m at the type locality to about 100–120 m in other areas, with an average of about 40 to 60 m (Buday, 1980), while in the subsurface, its thickness is even higher. In Kz40 and K216 wells, the thickness of the formation is 187 and 135 m, respectively. Buday (1980) demonstrated that the lower contacts of the Kometan Formation are unconformable with the Dokan Formation, Upper Qamchuqa, and Gulneri Formations, while Kaddouri (1982) has stated that it is conformable contact between the base of the Kometan Formation and Tel Hajar Formation. The contact is infrequently present as conformable or as a disconformity (Jassim and Goff, 2006).

The final report of the North Oil Company stated that in the Kz40 wells, The Mushorah Formation overlies, and the Guarneri Formation underlies the Kometan Formation. It consists of limestone, argillaceous limestone, marl, and marly limestone.

3. Methodology

3.1. Conventional well log data

Estimation of Porosity structure is critical in studying the identification of fracture units in the formation. A porosity cross-plot has been used to identify the fracture zones in the Kometan Formation. Neutron, Density, Sonic, Caliper, and Total Gamma-ray logs have been collected for two wells in the study area from two different oil fields (Kz40 and K216). The interval of Kz40 is 187 m thick, starting from 2711 to 2898 m. The thickness of the study formation is 135 m in K216, which is from 1412 to 1547 m. Some rock samples are available for the studied wells and used to measure spectral gamma-ray. They validate the shale volume from the Total gamma-ray log and recognize fractures.

Logging tools are designed to respond to different characteristics of the wellbore environment, so fracture identification cannot rely on a single log technique but must be taken several tools together to understand fracture systems. Accordingly, all available logging tools have contributed to identifying fractures. More information on the fundamental approaches to fracture identification can be found in (Serra, 1986, 1988, Rider, 2002, Ellis, 1987, Ellis and Singer, 2008). The following is a sequence of concise explanations on the application manner of conventional logging tools to identify fracture sections.

Fractures can be identified from density and neutron logs, in which the density log demonstrates high porosity spikes while the neutron log is not. Mud cake and borehole rugosity affect the measurements because the depth investigation of the density log is shallow. The neutron log is usually decentralized to diminish the borehole effect. The neutron log is not appropriate to identify fractures as a single tool, but it can be compared with other logs to indicate the perspective of fractures. Recently, neutron and density log combination to detect fractures is the most common log run. Since the sonic tool only measures the matrix porosity, so the comparison of total porosity (neutron-density combination) with sonic porosity can be proposed for the identification of secondary porosity (Eq. (1)) (Rider, 2002; Leyon, 2010).

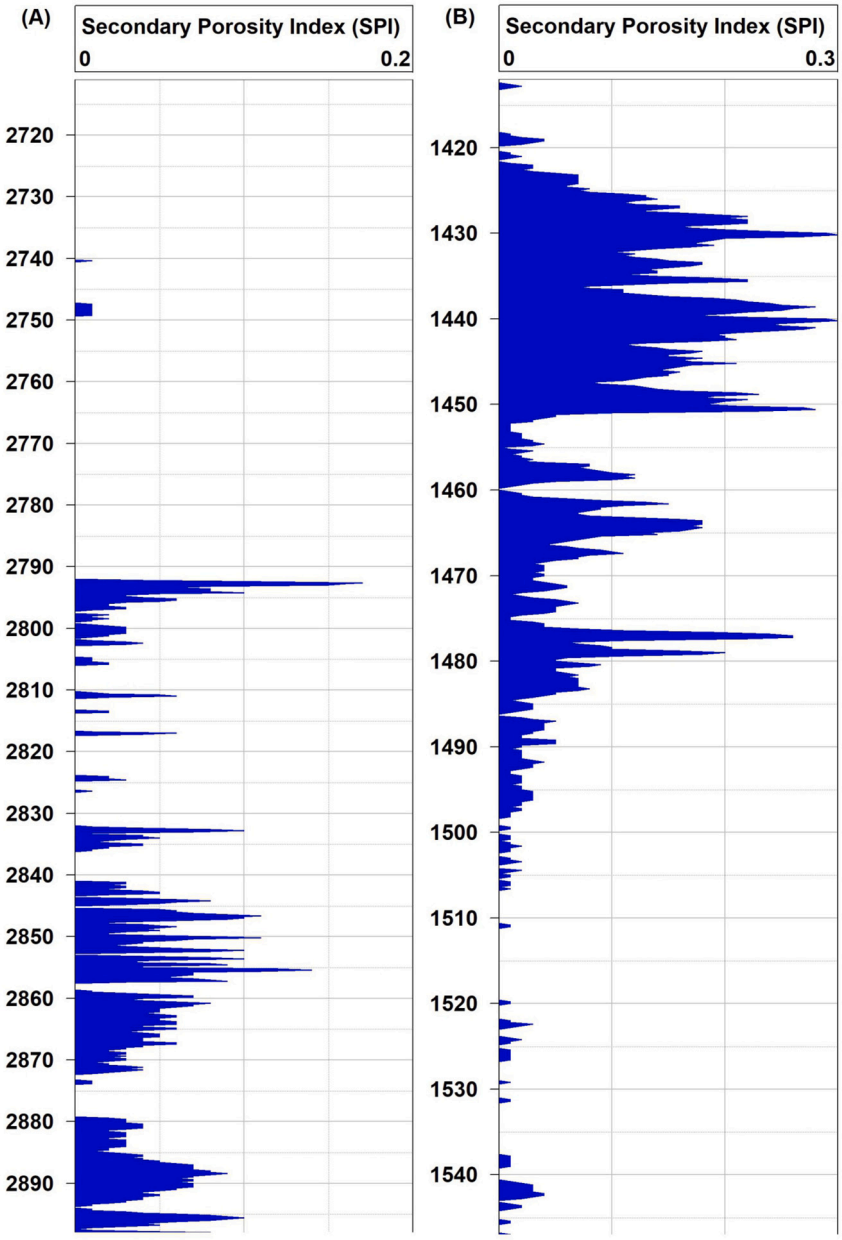

Fig. 4. Secondary porosity Index (SPI) demonstrating the availability for fractures, A in Kz40 and B in K216 wells.

$$SPI = \Phi_{total} - \Phi_{sonic} \quad (1)$$

Where:

SPI: Secondary Porosity Index.

Φ_{total}: Total Porosity ((Neutron Porosity + Density Porosity) / 2).

Φ_{sonic}: Sonic porosity.

Sound pulses reflect at the fracture face, and its amplitude would diminish, creating cycle skipping based on the first arrival of the compressional transit time curve. Sound pulses on the sonic log pass only through the matrix, which is the fastest way and avoids fractures to record matrix porosity.

In massive formations, borehole enlargement is associated with fractures. The design of the caliper log is not allowed to detect of minor fractures and abrupt changes. Mudcake, good permeability, and desirable fracture indicator can be observed on the caliper log. The presence of mud cake and the low porosity value of the formation mainly indicate fractures. It must be accountable for the borehole enlargement and washout because they are not always indicating fractures, especially if shale, salt, and unconsolidated formations are present, and other log characteristics can distinguish them.

3.2. Measured spectral gamma-ray from rock samples

For the same purpose (validation), some shale and fracture sections have been taken from an outcrop for the studied formation. Spectral gamma-ray have measured for ten and eight rock samples for well Kz40 and K216 respectively. It has been done in the laboratory (lab GRS) across the spectrum of facies using an RT-50 shielded laboratory spectrometer (Georadis, s.r.o., Czech Republic) with $3 \times 300''$ (350 cm^3) NaI (Tl) detector. The device transforms the count per second from 512 energy windows to concentrations of the K (%), U (ppm), and Th (ppm) based on calibrations using calibration standards provided by the manufacturer. The declared sensitivity is 0.7 ppm for Th, 0.4 ppm for U, and 0.12% for K. Each sample was milled into powder, placed within a 250 cm^3 plastic container, and measured for 30 min.

The potassium and thorium in the gamma-ray log are associated with

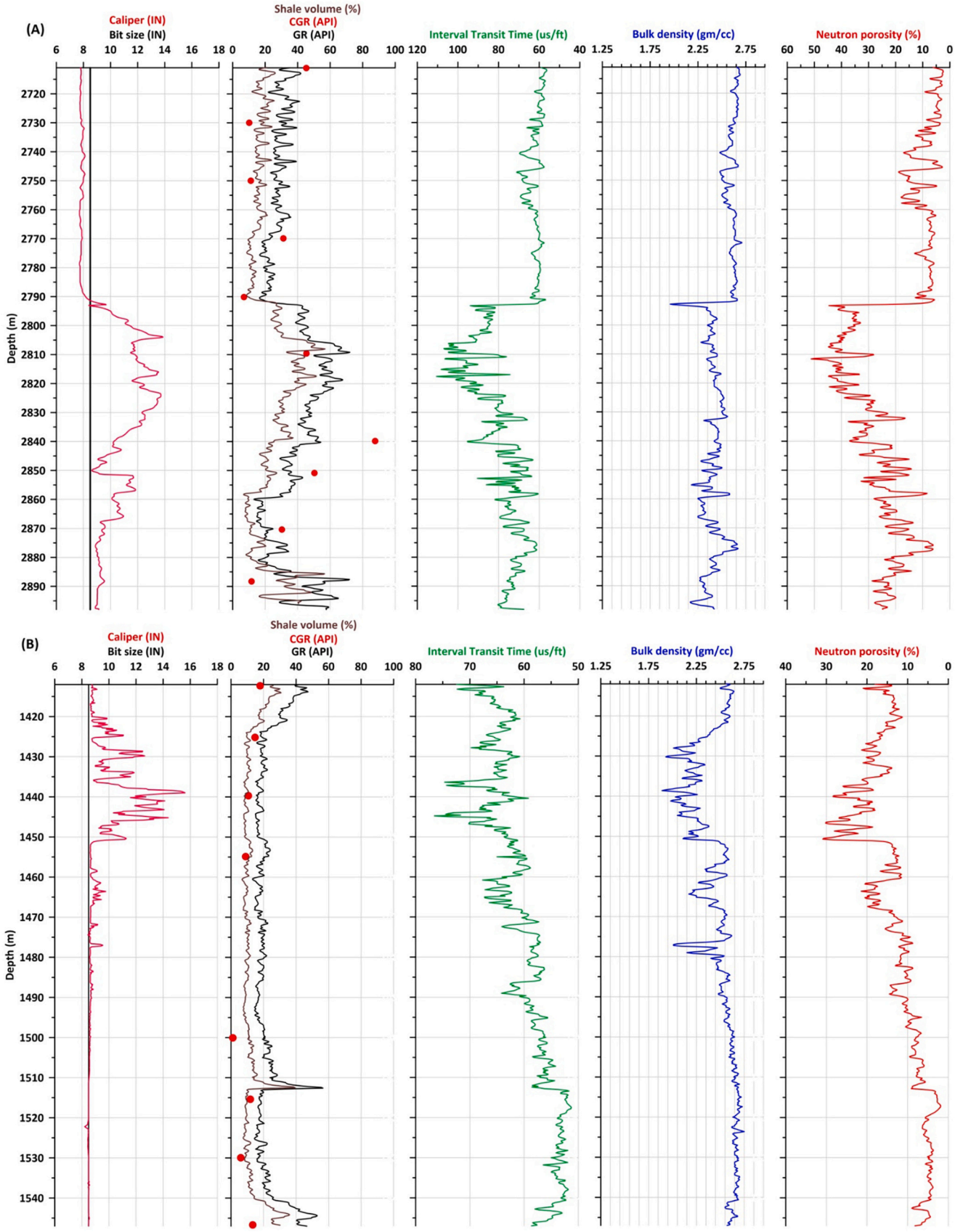

Fig. 5. Log curves for caliper, sonic, density, neutron, total (GR), shale volume calculated from total gamma ray and contributed (CGR) gamma ray, A in Kz40 and B in K216 wells.

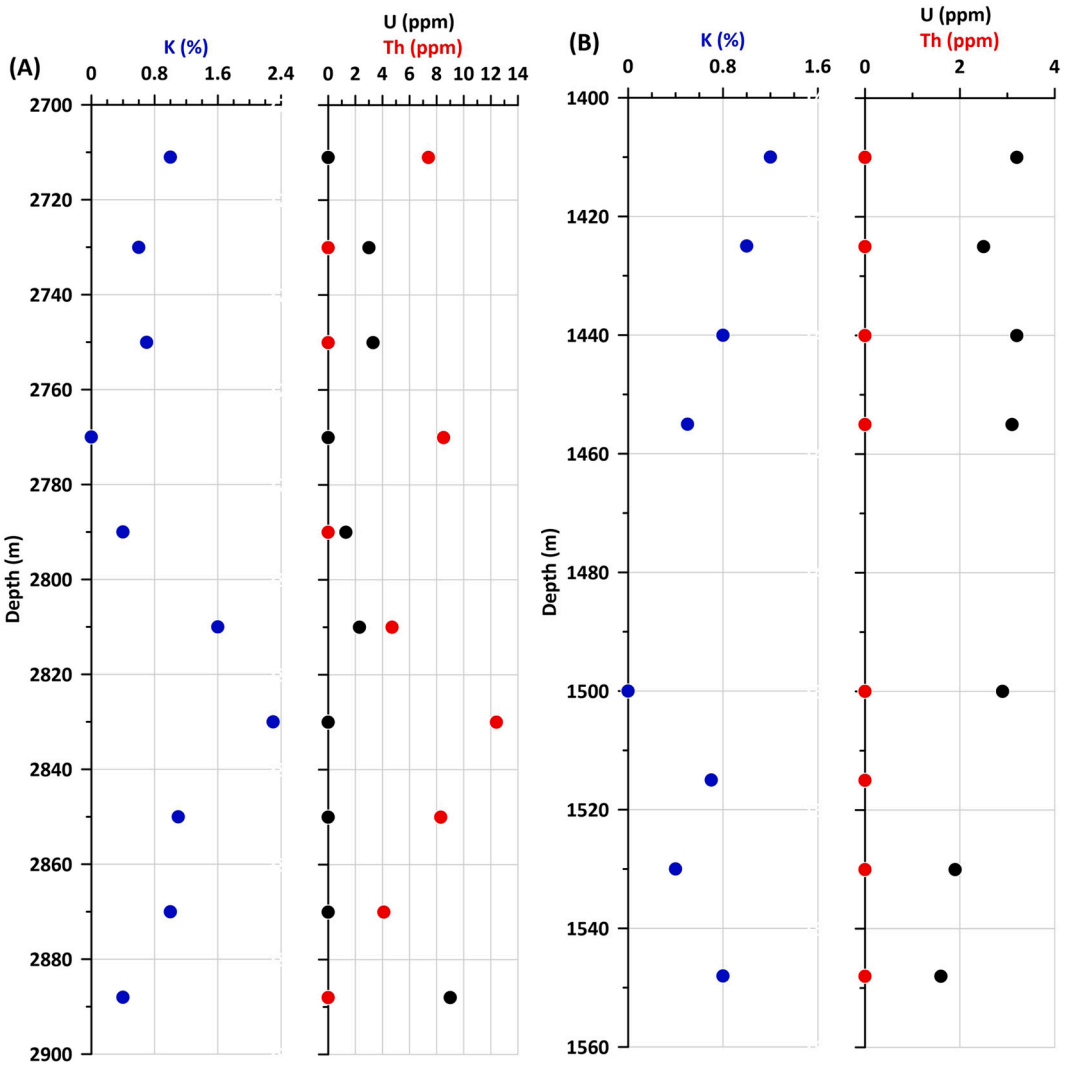

Fig. 6. Individual elements (uranium, thorium, and potassium) of spectral gamma ray for available well rock samples, A in Kz40 and B in K216 wells.

shale in the formation, and uranium salts are dissolved in fluids, so zones of high uranium concentration are associated with fracturing zones and can indicate fluid migration. Using the gamma-ray log as a single tool and uranium content to identify fractures is impossible. In some cases, there is porosity that contains uranium without fractures or may fracture with no uranium. If the uranium element is not available, the comparison between calculated shale volume from the total gamma-ray and shale content from the neutron-density log would be helpful because it can be suspected uranium in fractures when shales from the total gamma-ray are higher than that from the neutron-density log. Techlog 2015.3 has been used for shale volume calculation for both approaches (gamma ray and neutron-density log).

4. Result and discussion

4.1. Fractures from porosity logs

Fig. 3 demonstrates the porosity structure between total porosity derived from neutron and density on the horizontal (X) axis and sonic porosity on the vertical (Y) axis in the studied wells. The plotted data are equally spread between primary and secondary porosity. There are many points plotted in the secondary zone, which can assume that good secondary porosity is anticipated from the Kometan Formation in the studied wells.

The Secondary Porosity Index (SPI) for the inspected interval, reached a maximum value of 17%, and the average is 4% for Kz40 (Fig. 4A), the maximum value is 30%, and the average is 8% for K216 (Fig. 4B). The SPI results in Fig. 4A indicated that four zones are fractured at the specific depths 2792–2803, 2832–2837, 2841–2873, and 2879–2898. In addition, three high and three low fractured zones of K216 are presented in Fig. 4B, in which the high fractured zones are 1420–1452, 1452–1485, and 1485–1498.

The porosity cross-plot and SPI methods have (Figs. 3A and 4B) not indicated a fracture zone in 2711–2792 intervals of Kz40, but the caliper log (Fig. 5A) shows mud cake of this interval which can reveal the presence of permeable zones and open fractures. Density and neutron log are more affected by mudcake than sonic log, so according to Eq. (1), the result of SPI in this interval would be negative (no fracture) (Fig. 4A) and on the cross plot the data plotted on the primary porosity area (Fig. 3A). All other intervals and fracture zones suggested from cross-plot and SPI (Figs. 3 and 4) are supported by a caliper log which shows borehole enlargement (Fig. 5A and B), which can be a good indicator for fractures of competent formation (Fig. 2).

The behavior of other logs (density, neutron, and sonic) can be applied qualitatively to support the evidence relevant to fractures. Figs. 5 show spikes of the sonic log, which indicate the presence of fractures. Spikes for sonic log are primarily observed in enlarged intervals, but the density spikes also indicate fractures, observed at a depth

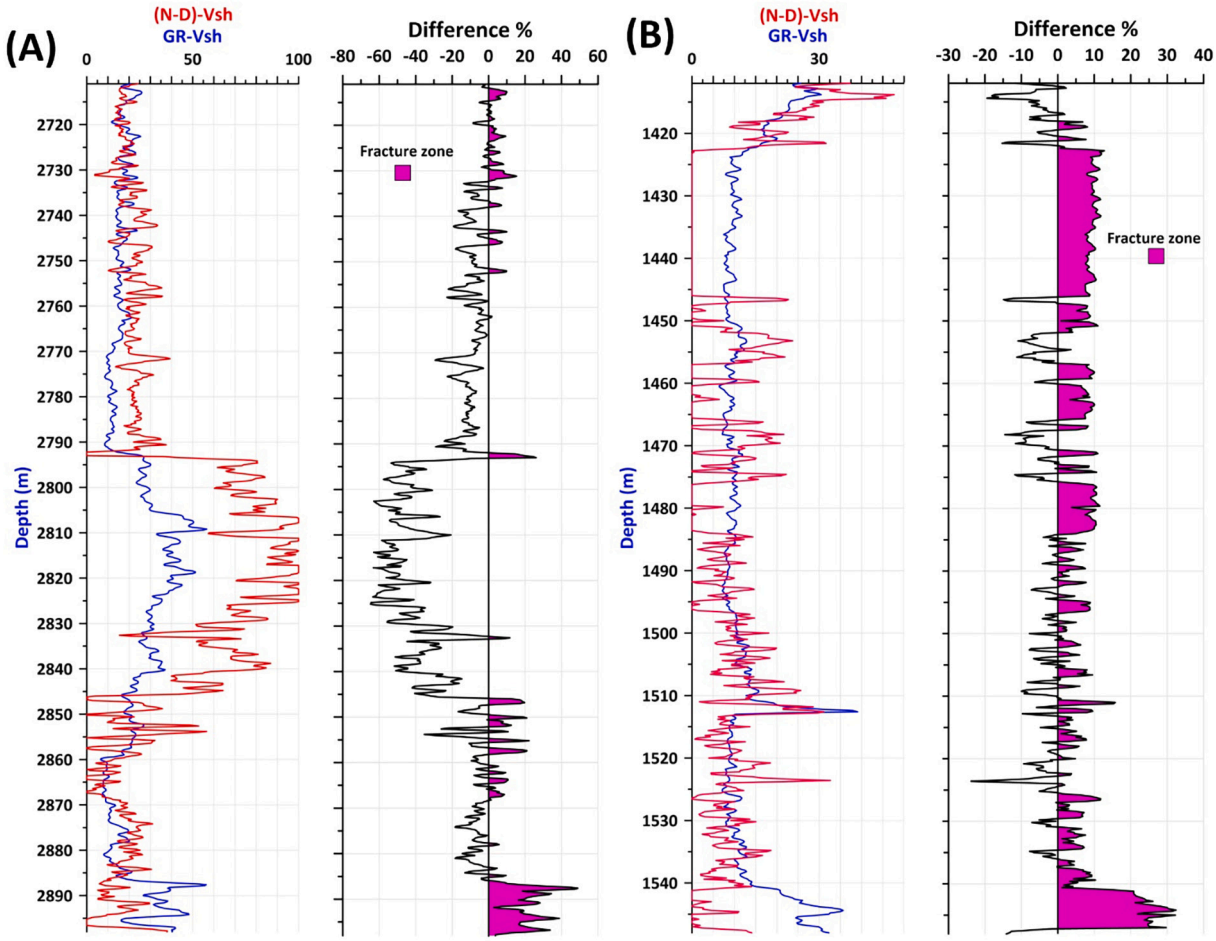

Fig. 7. Shale volume from neutron-density and gamma-ray, and their differences to demonstrate fracture zones A in Kz40 and B in K216 wells.

Fig. 8. Outcrop section of Kometan Formation in Zewe area.

of 1477, which is not indicated by neutron log (Fig. 5B). The enlargement also caused an abrupt increase and decrease in neutron and density log. It is due to the increasing mud thickness in enlarged intervals, and it has been considered during interpretation to identify fractures.

4.2. Fractures from relationship between total gamma-ray log and spectral gamma-ray rock

The available gamma-ray log (total gamma-ray) (Fig. 5) and spectral gamma-ray from available subsurface rock samples (Fig. 6) demonstrate an increment of uranium content against fractures. It can be noticed when the uranium precipitates in the fractures, which the fluid movement may endorse.

Since the total gamma ray measures combined radioactive elements (uranium, thorium, and potassium) and the spectral gamma ray log is not available, it can be combined the shale content from the total gamma ray (Fig. 5) with that from the neutron-density log (Fig. 7) to validate either the gamma ray log reading is due to uranium or other elements (Potassium and thorium). In addition, the available spectral gamma ray of rock samples also can be used (Fig. 6).

The positive difference between gamma ray shale to neutron-density shale (Vsh gamma ray – Vsh neutron-density) may refer to uranium content, consequently fractures in the formation. Fig. 7 shows the calculated shale volume from different approaches (gamma ray and neutron-density log) and the differences between them to distinguish fracture zones. The technique was successfully applied especially in K216 (Fig. 7 B) which is perfectly comparable with other approaches to fracture identification in this study (Figs. 3B, 4B). However. It couldn't depict the fractures in Kz40 in the 2793–2846 interval due to the borehole effect which enlarged in this interval. Neutron and density log are impaired in this interval because the thickness of drilling mud increases and the tools stay away from the borehole wall. Fresh base mud was used to drill these wells (Kz40 and K216) which is high hydrogen index, so the value of the neutron log in enlarged interval would be high. The density log value in this interval would be low because the depth of investigation of this log is shallow, so the porosity is overestimated. The computed gamma ray (CGR) also can be used decisively to identify uranium in the formation (Fig. 5). since the total gamma ray (GR)

combined uranium, thorium, and potassium and the computed gamma ray (CGR) combined only thorium and potassium, so the difference between the total gamma ray to computed gamma ray is equal to uranium content (Fig. 5).

4.3. Fractures in outcrop section

Fig. 8 is an outcrop section of the Kometan Formation in the Zewe area (Fig. 1), which shows fractures, stylolites, and the shale distributions in the studied formation. It has been indicated that the shale is mainly distributed as dispersed, and a few thin laminated shales were also observed. The exposed rock of the Kometan Formation verified that the porosity and permeability are enhanced by fractures.

5. Conclusions

- Good secondary porosity (fractures) has been Identified from the Secondary Porosity Index (SPI), which is quantified from total porosity (Neutron and Density) and Sonic porosity and validated by qualitative interpretations of other logs.
- The porosity of the Kometan formation is primarily secondary, especially fractures.
- Based on the qualitative interpretations of the available log data, which were validated by subsurface rock samples and observed outcrop sections of the studied formation, it has been concluded that the reservoir quality of the Kometan formation was enhanced due to high fractures in the studied wells.
- Conventional well log data can be an excellent alternative to detect fractures instead of high-cost laboratory measurements when different logging tools are used with precise interpretation and accounting for each log deflection's behavior against each other.

CRediT authorship contribution statement

Hussein S. Hussein: Conceptualization, Methodology, Software, Formal analysis, Investigation, Writing – original draft, Writing – review & editing, Visualization, Supervision, Project administration.

Declaration of Competing Interest

None.

References

Al-Qayim, B., 2010. Sequence stratigraphy and reservoir characteristics of the Turonian–Conacian Khasib Formationin Central Iraq. J. Petrol. Geol. 33 (4), 387–404.

Aqrawi, A.A.M., 1996. Carbonate–siliciclastic sediments of the Upper cretaceous (Khasib, Tanumaand Sa'di Formations) of the Mesopotamian Basin. Mar. Pet. Geol. 13, 781–790.

Aqrawi, A.A.M., Horbury, A.D., Goff, J.C., Sadooni, F.N., 2010. The Petroleum Geology of Iraq. Scientific Press Ltd, Beacons field, UK, 424 p. https://www.researchgate.net/publication/261250626_The_Petroleum_Geology_of_Iraq.

Buday, T., 1980. The Regional Geology of Iraq, vol. I. Stratigraphy and Paleogeography. S.O.M, Library, Baghdad, p. 350.

Buday, T., Jasim, Z., 1986. The Regional Geology of Iraq, vols. II. GEOSURV-Iraq, printed at Dar Al-Kutib Publishing house. University of Mosul, Iraq, 352 p.

Dunnington, H.V., 1958. Generation, Migration, Accumulation, and Dissipation of Oil in Northern Iraq. In: Weeks, L.G. (Ed.), Habitate of Oil, a Symposium. Association of Petroleum Geologists, Tulsa, pp. 1194–1251. https://pubs.geoscienceworld.org/aapg/books/book/1490/chapter/107178783/Generation-Migration-Accumulation-and-Dissipation.

Dunnington, H.V., 2005. Generation, migration, accumulation, and dissipation of oil in Northern Iraq. J. GeoArabia 10, 39–84. https://doi.org/10.2113/geoarabia100239.

Dutta, P., Singh, S.K., Al-Genai, J., Akhtar, A., Akbar, M., 2007. A novel approach to fracture characterization utilizing borehole seismic data. In: 15th SPE Middle East Oil & Gas Show and Conference, Bahrain. https://doi.org/10.2118/105427-MS. Paper SPE-105427-MS.

Ellis, D.V., 1987. Well Logging for Earth Scientists. Elsevier, New York, p. 532. https://www.amazon.com/Logging-Earth-Scientists-Darwin-Ellis/dp/0135005620.

Ellis, D.V., Singer, J.M., 2008. Well Logging for Earth Scientists, 2nd edn. Springer, Berlin. https://www.academia.edu/10053517/Well_Logging_for_Earth_Scientists.

Jassim, S.Z., Goff, J.C., 2006. Geology of Iraq, 1st edition. Published by Dolin, Prague and Moravian Museum, Brno, Printed in the Czech Republic. 348 p.

Kaddouri, N., 1982. Tel Hajar: A new Cenomanian–Lower Turonian Stratigraphic Unit from North-west Iraq, Cretaceous Research. Academic Press Inc., London, pp. 391–395.

Laongsakul, P., Durrast, H., 2011. Characterization of reservoir fractures using conventional geophysical logging. Songklanakarin J. Sci. Technol. 33, 237–246.

Leyon, W.C., 2010. Working Guide to Reservoir Engineering. Elsevier, 129p.

Martinez-Torres, L.P., 2002. Characterization of Naturally Fractured Reservoirs from Conventional Well Logs. M.Sc. Thesis. University of Oklahoma, USA.

Nelson, R.A., 2001. Geologic Analysis of Naturally Fractured Reservoirs, 2nd edn. Gulf Professional Publishing, Houston, p. 332.

Qadir, F.M., 2008. Formation Evaluation of Upper Qamchuqa Reservoir in Khabbaz Oil Field, Northeastern Iraq. Ph.D. dissertation. Sulaimani University, Iraq.

Rashid, F., Glover, P.W.J., Lorinczi, P., Collier, R., Lawrence, J., 2015. Porosity and permeability of tight carbonate reservoir rocks in the north of Iraq. J. Pet. Sci. Eng. 133, 147–161.

Rider, M., 2002. The Geological Interpretation of Well Logs, Second edition. Rider French Consulting Ltd, Aberdeen, and Sutherland. (280 P).

Roehl, P.O., Choduette, P.W., 1985. Carbonate Petroleum Reservoirs. Spring-Verlag, New York, p. 622.

Serra, O., 1986. Advanced Interpretation of Wireline Logs. Schlumberger copyright, p. 295.

Serra, O., 1988. Fundamental of well-log interpretation. In: Developments in Petroleum Science. Elsevier Science Publishers, Amsterdam.

Taq Taq Operation Company (TTOPCO), 2007. Geological Report.

Thompson, L.B., 2000. Fractured reservoirs: integration is the key to optimization. Dist. Author Ser SPE 56010, 52–54.

Van Bellen, R.C., Dunnington, H.V.G., Wetzel, R., Morton, D.M., 1959. Lexique Stratigraphique international, III, Asie, fasc. 10a, Iraq. Centre national de la recherché scientifique, Paris, p. 333.

Appendix 4

Marine and Petroleum Geology

Impact of stylolitization on porosity and permeability of carbonate rocks: the Upper Cretaceous Kometan Formation, Zagros Foreland Basin in Iraqi Kurdistan

--Manuscript Draft--

Manuscript Number:	
Article Type:	Full Length Article
Keywords:	Keywords: Stylolite, fluid conduit, fluid barrier, Kometan Formation, silica
Corresponding Author:	Howri Mansurbeg Univerzita Palackého v Olomouci CZECH REPUBLIC
First Author:	Hussein S Hussein
Order of Authors:	Hussein S Hussein
	Ondřej Bábek
	Howri Mansurbeg
	Juan Diego Martín-Martín
	Enrique Gomez-Rivas
Abstract:	Stylolites are relatively prevalent diagenetic features in carbonate rocks, play a significant role in either enhancing or inhibiting the flow of fluids within reservoirs. Recently, there has been a growing interest in understanding how lithological variability of the host rock, diagenetic fluid flow, and oil emplacement may affect the formation, distribution, and size of stylolites. This study investigates the relationship between stylolite systems, elemental geochemistry, and microfacies in the Upper Cretaceous carbonates of the Kometan Formation in Northern Iraq to contribute to this discourse. Stylolites, formed through pressure solution, exhibit diverse morphologies across mud-dominated and grain-dominated facies in shallow to moderately deep marine settings. Statistical analyses focus on parameters such as stylolite spacing, wavelength, amplitude, intersection morphology, and connectivity to discern stylolite networks. Grain size, grain size distribution, and composition play pivotal roles in shaping the development of interconnected stylolite networks. In facies primarily composed of grain-supported packstone with moderate sorting, where grains are dispersed within a finer matrix, predominant stylolites typically exhibit weak connectivity and considerable vertical spacing. Conversely, mud-supported facies, marked by poor sorting and heterogeneity, display well-developed intersection stylolite networks. Stylolites in mud-supported facies demonstrate closer spacing, heightened amplitudes, and intensified junctions, with prevalent morphologies of the suture and sharp-peak varieties. Notably, this study unveils that stylolite significantly enhances porosity and permeability in the studied formation. Dissolution of minerals along stylolite seams forms intricate networks of channels and conduits.
Suggested Reviewers:	Rudy Swennen KU Leuven rudy.swennen@kuleuven.be
	Hossain Rahimpour-Bonab Tehran University rahimpor@ut.ac.ir
	Stephen Ehrenberg retired 111sne@gmail.com
	Robert Goldstein University of Kansas gold@ku.edu

Impact of stylolitization on porosity and permeability of carbonate rocks: the Upper Cretaceou Kometan Formation, Zagros Forland Basin in Iraqi Kurdistan

Hussein S. Hussein[1], Ondřej Bábek[1], Howri Mansurbeg[1,2]*, Juan Diego Martín-Martín[3], Enrique Gomez-Rivas[3],

[1] Department of Geology, Palacký University, 17. listopadu 12, Olomouc 77146, Czechia

[2] General Directorate of Scientific Research Center, Salahaddin University, Erbil 44002, Iraq

[3] Departament de Mineralogia, Petrologia i Geologia Aplicada, Facultat de Ciències de la Terra, Universitat de Barcelona (UB), Martí i Franquès s/n, 08028 Barcelona, Spain

* Corresponding author: E-mail: howri.mansurbeg@upol.cz

Abstract

Stylolites are relatively prevalent diagenetic features in carbonate rocks, play a significant role in either enhancing or inhibiting the flow of fluids within reservoirs. Recently, there has been a growing interest in understanding how lithological variability of the host rock, diagenetic fluid flow, and oil emplacement may affect the formation, distribution, and size of stylolites. This study investigates the relationship between stylolite systems, elemental geochemistry, and microfacies in the Upper Cretaceous carbonates of the Kometan Formation in Northern Iraq to contribute to this discourse. Stylolites, formed through pressure solution, exhibit diverse morphologies across mud-dominated and grain-dominated facies in shallow to moderately deep marine settings. Statistical analyses focus on parameters such as stylolite spacing, wavelength, amplitude, intersection morphology, and connectivity to discern stylolite networks. Grain size, grain size distribution, and composition play pivotal roles in shaping the development of interconnected stylolite networks. In facies primarily composed of grain-supported packstone with moderate sorting, where grains are dispersed within a finer matrix, predominant stylolites typically exhibit weak connectivity and considerable vertical spacing. Conversely, mud-supported facies, marked by poor sorting and heterogeneity, display well-developed intersection stylolite networks. Stylolites in mud-supported facies demonstrate closer spacing, heightened amplitudes, and intensified junctions, with prevalent morphologies of the suture and sharp-peak varieties. Notably, this study unveils that stylolite significantly enhances porosity and permeability in the studied formation. Dissolution of minerals along stylolite seams forms intricate networks of channels and conduits.

Keywords: Stylolite, fluid conduit, fluid barrier, Kometan Formation, silica

1. Introduction

The heterogeneity of depositional rock textures and post-depositional diagenetic overprints make reservoir properties of carbonate rocks difficult to predict in the subsurface. Carbonate textures and their petrophysical properties typically vary through space vertically, laterally, and through time following diagenetic pathways. Therefore, assessing reservoir quality, in particular carbonate permeability, presents significant challenges (Ehrenberg and Nadeau, 2005; Ehrenberg, 2006; Lucia and Jennings, 2003; Harris, 2010; Palermo et al., 2010; Ronchi et al., 2010; Rashid et al., 2015).

Stylolites are distinct and very common diagenetic products in carbonate rocks, which can be otherwise lithologically uniform (Bathurst, 1991). Stylolites are thin, undulating tooth-like surfaces that form by pressure-solution. Sometimes they collect concentrated insoluble residue while they grow parallel to bedding planes. Stylolites may exaggerate the original bedding planes defined by changes in lithology or even form new, so-called pseudo-bedding surfaces, which do not coincide with the original bedding and separate units of the same lithology (Simpson, 1985). Stylolite orientation is related to targeted contractional strain (Fletcher and Pollard, 1981; Schultz and Fossen, 2008). Stylolite peaks are parallel to the largest principal stress (σ_1) (Groshong, 1975). However, the plane of a stylolite may be tilted concerning the direction of movement, as seen in slickolites (Gratier et al., 2005). Sedimentary stylolites, also called diagenetic stylolites, usually form in sedimentary basins parallel to bedding and perpendicular to burial stress due to the weight of the overburden. By contrast, tectonic stylolites form due to tectonic stress (Toussaint, et al., 2018). Stylolites nucleate and grow through a pressure-dissolution process that begins on a sub-micron scale (grain and/or crystal interfaces). The process involves both the chemical dissolution of the rock-forming minerals and localized physical stress-induced compaction of grains along an interface that is filled with fluid (Ebner et al., 2009; Vandeginste and John, 2013). The mineralogical heterogeneity of the rock, at least in part, controls this process because it supplies the necessary solubility contrast to initiate the stylolite surface generation. At first glance, the proto-stylolite plane is a sharp surface that will roughen on localized, less-soluble heterogeneous material (Koehn et al., 2012).

The stylolite morphology and orientation can be utilized to determine the orientation, distribution, and magnitude of compressive stress in a region at a given time (Koehn et al., 2012). The morphological parameters defining a stylolite comprise amplitude, wavelength, spacing, and connectivity, while their combination results in a wide range of stylolite network architectures (Vandeginste and John, 2013; Ben-Itzhak et al., 2014; Humphrey et al., 2020). Several studies demonstrated that stylolites can control fluid flow and petrophysical parameters in various ways

(Paganoni et al., 2016; Martín-Martín et al., 2018; Heap et al., 2018; Toussaint et al., 2018; Bruna et al., 2019; Humphrey et al., 2019; Gomez-Rivas et al., 2022). Field and laboratory observations led some authors to conclude that stylolites and stylolites networks can operate as barriers to fluid flow (Burgess and Peter, 1985; Finkel and Wilkinson, 1990; Alsharhan and Sadd, 2000; Martín-Martín et al., 2018; Gomez-Rivas et al., 2022). However, it has also been proposed that stylolites can act as conduits that increase permeability parallel with their planes, as seen in various carbonate reservoirs, outcrops (e.g., Carozzi and Bergen 1987; Bergen and Carozzi, 1990; Lind et al., 1994; Harris, 2006; Chandra et al., 2015; Barnett et al., 2018; Paganoni et al., 2016; Martín-Martín et al., 2018; Morad et al., 2018; Gomez-Rivas et al., 2022), and laboratory permeability tests (Heap et al., 2014, 2018; Rustichelli et al., 2015). Preferential dissolution along existing stylolite planes has been linked to the development of localized porosity surrounding the stylolites (Bergen and Carozzi, 1990) and an increase in the average diameter of pore throats (Baud et al., 2016).

Despite the impact of stylolites in fluid flow on a local scale has been the subject of several studies, less attention has been paid to understanding how depositional facies and carbonate rock components affect the morphology, type, and growth of stylolites. In addition, there has been an increasing interest in how the variability of the host rock properties affects the form, distribution, and size of stylolites (Toussaint et al., 2018; Morad et al., 2018; Humphrey et al., 2020). In this regrd, Koehn et al. (2016) emphasized the significance of the interaction between various lithological controls that affect stylolite formation.

In addition to depositional facies, the influence of hydrocarbons on the formation and evolution of stylolites is not totally understood. In this regard, petroleum emplacement can prevent stylolitization (e.g., Neilson et al., 1998; Morad et al., 2018). However, hydrocarbon-bearing limestones frequently include widespread lateral stylolite networks that can compartmentalize reservoirs and cause changes in fluid migration (Hassan and Wada, 1981; Ehrenberg et al., 2016). Heap et al. (2014) revealed that the discontinuous nature of stylolites can influence petrophysical properties locally. These authors further determined that stylolites may introduce permeability heterogeneities, which can enhance permeability along their surfaces. This was also observed by Humphrey et al. (2019) in a subsurface gas reservoir.

Stylolite studies have predominantly been carried out in carbonate rocks (Koehn et al., 2007; Ebner et al., 2010; Paganoni et al., 2016; Martín-Martín et al., 2018; Heap et al., 2018; Toussaint et al., 2018; Bruna et al., 2019; Humphrey et al., 2020; Gomez-Rivas et al., 2022). However, stylolites sandstones (Baron and Parnell, 2007; Nenna and Aydin, 2011) and evaporites (Bauerle et al., 2000) have been also reported. Despite these studies, it remains a notable gap in the understanding of stylolite formation in mixed carbonate–siliciclastic facies. Such compositions are very common in carbonate reservoirs,

where silica enrichment often stems from the accumulation and diagenesis of siliceous organisms, including diatoms, radiolarians, and sponge spicules.

The aim of this research is to explore the relationship between stylolites and carbonate microfacies within the Upper Cretaceous Kometan Formation (Zagros Foreland Basin, Iraq) (Fig. 1). The Kometan Formation contains well-developed stylolites and forms an important oil reservoir in the region. Specifically, the objectives of this paper are: 1) to characterize the lithological parameters of the Kometan carbonates, including particle size, sorting, composition, and diagenetic features, 2) to characterize the bulk-rock element geochemistry of the Kometan carbonates, 3) to characterize and quantify their morphological parameters of the stylolites and their networks (spacing, wavelength, amplitude, junction intensity, and connecting angle), 4) to assess the influence of lithology and elemental geochemistry on the formation and morphology of stylolites and stylolite network using quantitative statistical analyses, and 5) to explore the role of clay content and micrite influence on stylolite characteristics and their impact on reservoir porosity and permeability.

2. Geological setting

The study area is located northwest of Sulaimani City, within the high fold of the Zagros Foreland Basin in the Kurdistan region of Iraq (Fig. 1). The stratigraphy of the Kurdistan region of Iraq varies due to a combination of thrusting events, isolated depocenters, and erosion. A representative stratigraphic sequence for the study area is shown in Fig. 2. Following the Hercynian Orogeny, the region's topography influenced the deposition of extensive upper Paleozoic strata (Martin, 2001). Spanning the Permian to Jurassic, Kurdistan witnessed a rift phase, heralding the birth of the Neo-Tethys Ocean (Muttoni et al., 2009). The Chia Zairi formation of the Upper Permian delineates the genesis of the Neo-Tethys Ocean and the subsequent marine sedimentary deposition (Fig. 2) (Sharland et al., 2001).

Continuing through the Triassic, carbonate deposition, evident in formations like the dolomitized Geli Khana and the Kurre Chine, persisted (Szabo and Kheradpir, 1978; Alavi, 2004; Sadooni and Alsharhan, 2004; Bordenave, 2008). The latter encountered evaporitic deposits during the 'Saharan Salinity Crisis. The Baluti Formation, marking the Triassic's culmination, embodies clastics interspersed with limestones and dolomites sourced from the Rutbah High in western Iraq (Martin, 2001). Shifting into the Jurassic, the overlying Butmah Formation is characterized by marine carbonates interspersed with evaporitic sequences from the Gotnia Basin. Subsequent units, including the Adaiyah and Mus formations, maintained this sedimentary regimen (English et al., 2015).

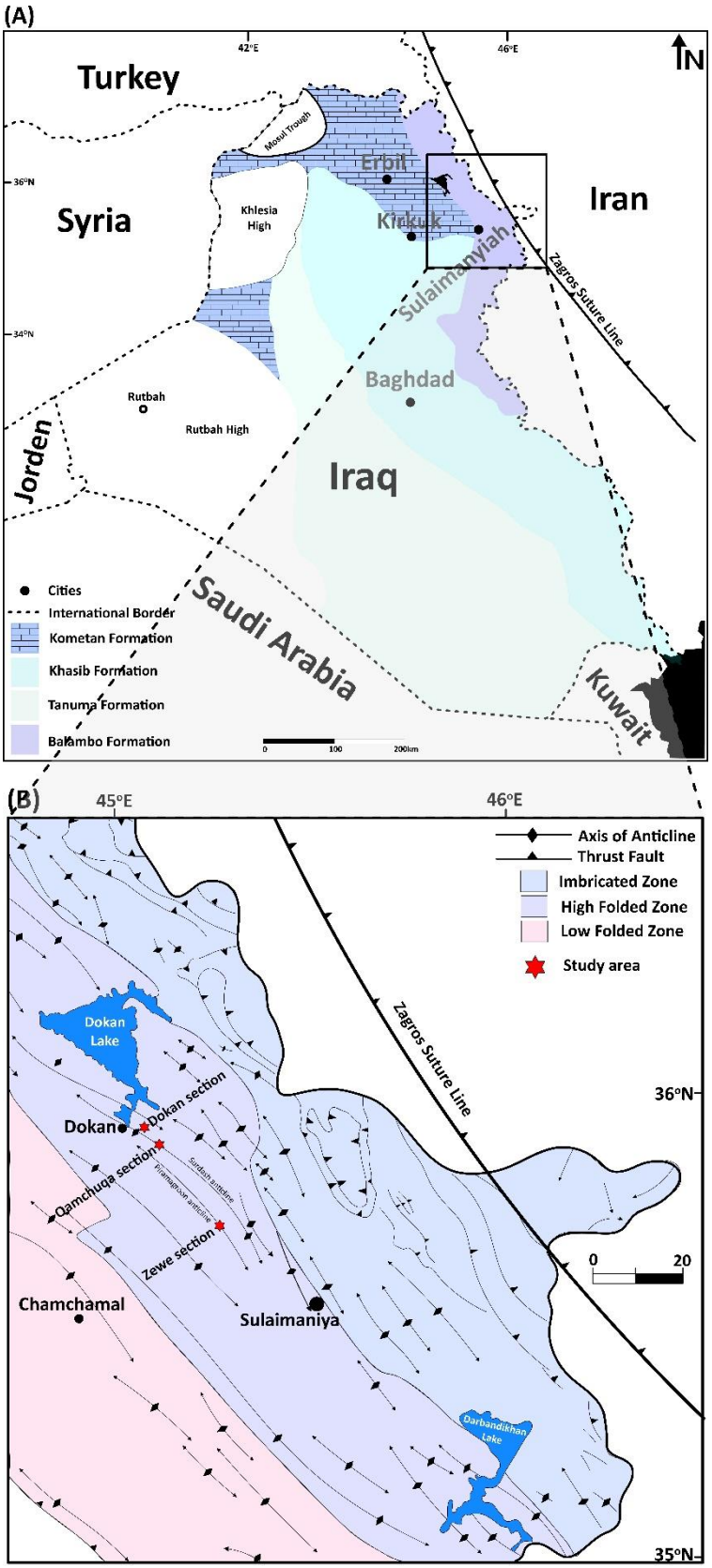

Fig. 1. A) Map showing the location of the study is in north Iraq. B) Close view of A (black rectangle) showing the structure and tectonic subdivisions of the study area and the location of the studied sections (Modified from Al-Hmadani, 1986, Aqrawi et al., 2010).

The Late Jurassic is characterized by the evaporites of the Barsarin formation. The Late Jurassic and Early Cretaceous transitions brought fluctuating sea levels (Aqrawi et al., 2010). This dynamic saw the development of the Chia Gara formation's shale and carbonate facies in the focal region. Ensuing units, like the Garagu and Sarmord Formations, echoed the Gotnia Basin's waning influence (Aqrawi et al., 2010).

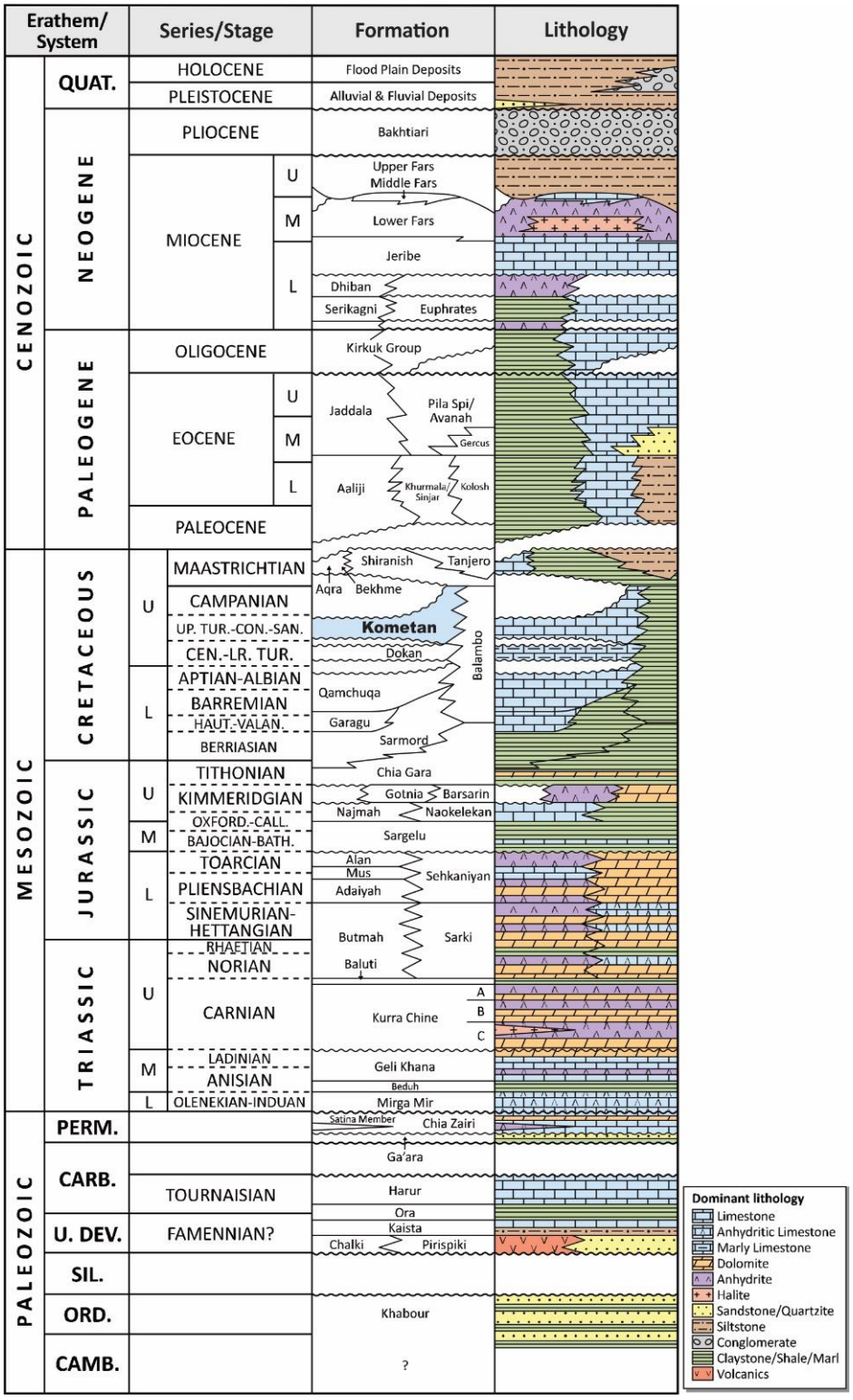

Fig. 2. Chronostratigraphy of major lithostratigraphic units in the Kurdistan region of Iraq (English, et al., 2015).

The Early Cretaceous (Albian) Kometan Formation is notable for its hydrocarbon potential and intricate stratigraphy (Aqrawi et al., 2010). The Kometan Formation is widespread throughout northern Iraq (Figs. 1, 3) and was deposited during the later stages of the Turonian transgression (Fig.2). This formation is made of carbonate and shale cycles resulting from variable sea level and sediment influx (Hussein, et al, 2024; Hussein, et al, 2023). These layers hint at periodic marine transgressions and regressions intricately linked to tectonic activities, notably the nascent Arabia-Eurasia plate collision (English et al., 2015). Thus, the formation provides crucial insights into the sedimentary processes and overarching tectonic dynamics of the Turonian.

The thickness of the Kometan Formation in the type locality is 36 meters but reaches up to 185 meters in the subsurface. The thickness of the Kometan Formation in the studied sections is 96 m, 63 m, and 65 m for the Zewe section, Qamchuqa section, and Dokan section respectively. The formation is composed of light grey to cream-colored, fine-grained limestones (lime mudstones and wackestone/packstones) and dolomitic limestones with abundant planktonic foraminifera. Its deposition correlates chronologically with the latter phases of the Turonian transgression (Haddad and Amin, 2007). Within the confines of the Zagros Foreland Basin, the depositional facies of the Kometan Formation vary from shallow shelf, restricted (oligostenginal facies) to open marine environment (Globigerinia facies). Notably, the oligostenginal facies formed in semi-isolated basins, experiencing periodic episodes of hypersalinity (Jassim and Goff, 2009). The formation is oil-bearing in both the Taq Taq and Miran West-1 fields. In contrast, the Demir Dagh-1 well has shown the formation to be water-bearing. The Kometan Formation predominantly relies on fractured porosity for production, with limitations imposed by the fine-grained facies and a non-interconnected porosity framework that hinders matrix porosity contributions (Rashid et al., 2015).

Tertiary period stratigraphy is characterized by deep marine sediments that form abundant carbonate reservoirs (Fig. 1). This stratigraphic record is marked by repeated depositional cycles, commencing with the regressive episodes of the early Miocene and extending into the clastic-rich Upper Fars and Bakhtiari formations. Throughout this epoch, the ongoing impact of tectonic collisions and the northeastward rise of the Zagros Foreland Basin (Jassim and Goff, 2009) played a prominent role.

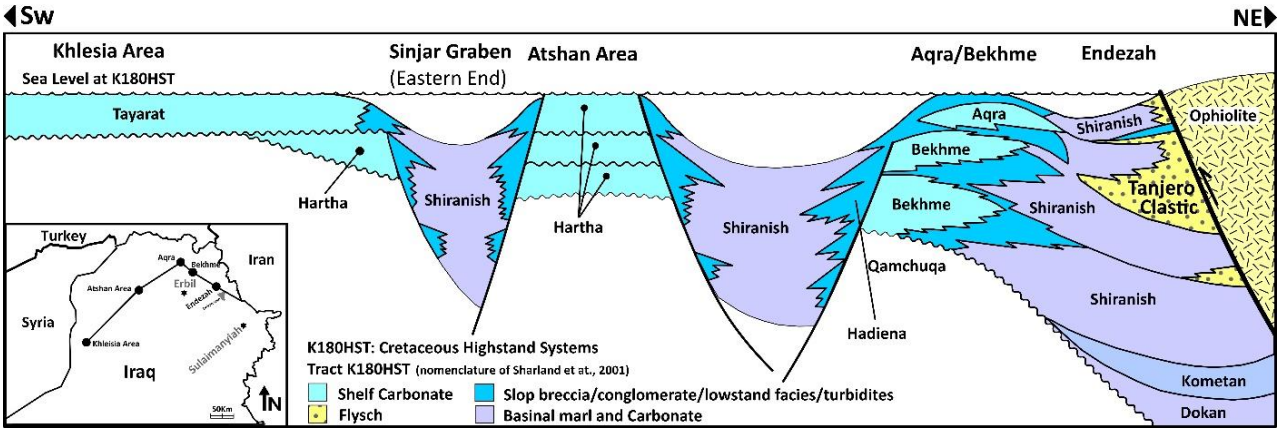

Fig. 3. Schematic Upper Cretaceous (Campanian–Maastrichtian) stratigraphic cross section across northern Iraq illustrating segmentation of the margin into a series of structural highs and lows, and the relative thicknesses of each of the stratigraphic units (modified from Aqrawi et al., 2010; English et al., 2015).

3. Methods

The Kometan Formation was studied and sampled in three outcrop sections called Zewe (35°44'7.171"N, 45°14'13.930"E), Qamchuqa (35°53'49.472"N, 45°0'48.324"E), and Dokan (35°56'37.197"N, 44°58'45.385"E) (Fig. 1). The sections were studied bed-by-bed including, bed thickness, bed geometry, sedimentary structures, texture, composition, diagenetic structures (cherts), and grain size using the routine field approach. Rock texture and microfacies were studied in 50 samples using the approach described by Dunham (1962), Scholle and Ulmer-Scholle (2003), and Flügel (2004).

Following Humphrey et al. (2020), the abundance, size, and morphological parameters of the stylolites and stylolite networks were measured in the field using 1m x 1m sized sampling frames to minimize the impact of vertical lithological variations, the objects were positioned closely alongside the stratigraphic beds. The framed outcrop sections were marked, photographed, and rectified to maintain a uniform scale and vertical-to-horizontal aspect. To minimize the effects of vegetation and noise from the background, line drawings of all stylolites present were made from each scaled frame picture. The stylolite spacing, amplitude, wavelength, intersection angle, and type of intersection were measured from the scaled pictures (Fig. 4). Three vertical lines (dashed lines, Fig. 4A) with a lateral offset of 50 cm were drawn in each frame picture perpendicular to the stylolites, to measure the stylolite spacing. The perpendicular spacing values taken from every line were added up for each frame, and the heights between stylolite crossing were documented (Fig. 4B). Thus, the longest vertical stylolite spacing that can be measured is one meter, but in all frames, the spacing was lower than one meter. The central vertical line in each sampling frame was used to record the stylolite wavelength and

amplitude. We recorded every stylolite that crossed the measuring line. The wavelength was measured as the horizontal separation between the nearest two positive peaks located along the measuring line (Fig. 4C), whereas amplitudes were measured as a vertical distance between positive and negative stylolite peaks located nearest to the scanline (Fig. 4D). Selecting the nearest amplitude observations to the measuring line minimized the effects of inclination.

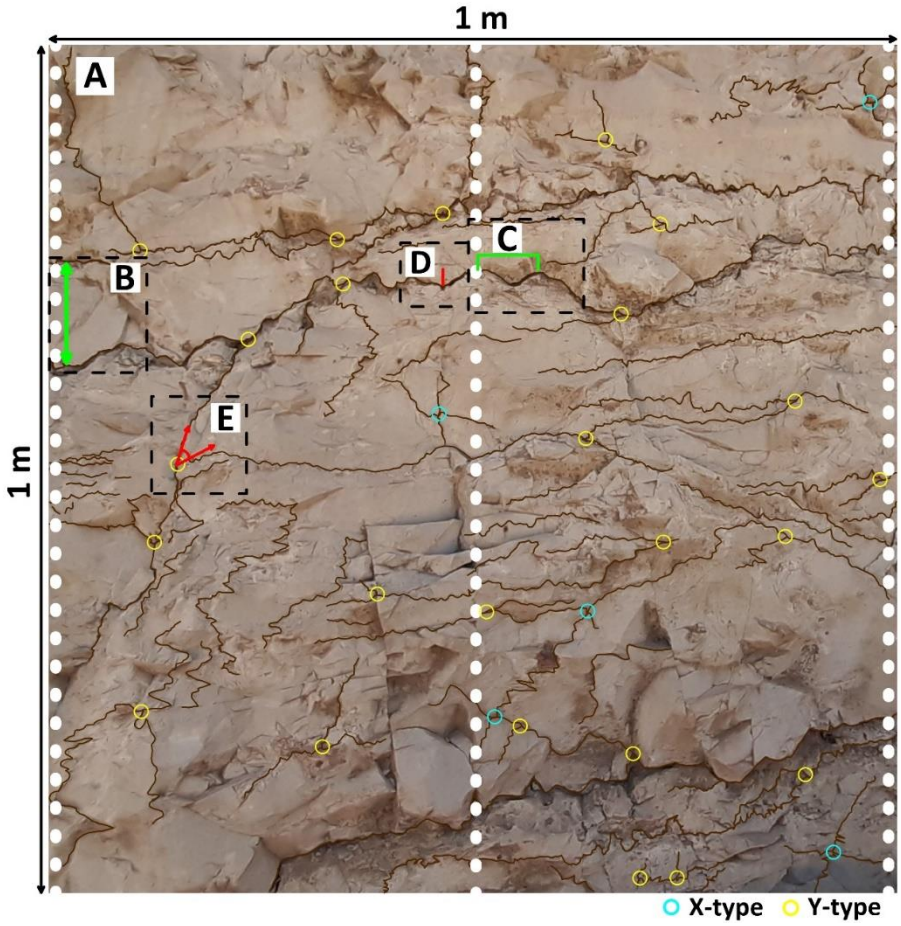

Fig. 4. Example frame size and positions of three scanlines (A) used for recording stylolite spaces (B), wavelength (C) (middle scanline), amplitude (D) (middle scanline), junction angle (E), and labeled image identifying the X-type (Cyan) or Y-type (yellow)of stylolite junction.

Univariate statistics of the stylolite spacing, wavelength, and amplitude were calculated and graphically represented using Past 4.04 software. Log-normal statistical distributions were used to fit the stylolite data. The distributions of individual parameters were matched, and the Kolmogorov-Smirnov (KS) normality testing and chi-squared tests were used to assess the goodness of fit (Massey, 1951) with higher chi-squared results suggesting a better match between the distributions. For the KS test, a null hypothesis was chosen at the p-value lower than 0.05. The quantity of different junction forms was calculated based on the stylolite length. The techniques of Manzocchi (2002) and Sanderson et al. (2015) were utilized to determine fracture network connections, leading to the classification of

junctions as X or Y (Fig. 4). By dividing the total number of junctions by the overall stylolite length per frame, the number of junctions per facies was determined. Consequently, the ratio of stylolite junction intensity per meter (m) for each frame was obtained. This was then averaged to derive a ratio for each microfacies (Eq. 1):

$$JI\ (/m) = (Jt\ /\ (SLt) \quad (1)$$

where JI (/m) is the junction intensity per meter, Jt is the total amount of junctions in the sample frame, and SLt is the total stylolite length per frame. Since the sampling frame's dimensions have an impact on the total length of the stylolite samples, the SLt is not a good indicator of the horizontal length of stylolite networks, but it can be used to normalize junction intensities for each sampling frame for comparing junction intensities across microfacies. We used the classification of Koehn et al. (2016) for stylolite types. This scheme classifies stylolites in four types: rectangular layer, seismogram pinning, suture, sharp-peak, and wave-like type. The proportional frequencies of stylolite types per microfacies were calculated by adding the number of stylolite types recorded for each frame.

Pores were identified, and porosity estimated, from thin sections impregnated with blue-dyed epoxy resins using the image analysis approach of optical microscopy images (Grove and Jerram, 2011; Haines et al., 2015). A Scanning Electron Microscope (SEM) QUANTA 200 FEI equipped with an EDS detector was utilized for detailed textural analysis. Backscatter Electron (BSE) SEM images facilitated porosity estimation through greyscale image analysis (Haines et al., 2015). The ImageJ software was utilized to quantify grain area within a specified region of interest in thin sections. Mean grain size (M_z) and standard deviation or sorting (s_i) were calculated from the grain using the equations of Folk and Ward (1957).

Bulk rock samples (n = 227) from the Dokan, Zewe, and Qamchuqa sections were pulverized to analytical fineness and analyzed by energy-dispersive X-ray fluorescence (EDXRF) spectrometry. Concentrations of 19 elements (Al, Si, P, S, K, Ca, Ti, Mn, Fe, Ni, Cu, Zn, As, Rb, Sr, Zr, Mg, Pb, and Th) were determined using Delta Premium EDXRF spectrometer (Innov-X, USA) with a large-area Si-drift detector operating with 2 x 120 second acquisition time at 15 kV and 40 kV beam voltage, respectively. Before the EDXRF analysis, the pulverized samples were enclosed in plastic containers sealed with Mylar foil. The EDXRF concentrations of the studied elements were calibrated using analytical results from EDXRF and optical emission- and mass-spectrometry with inductively coupled plasma (ICP-OES/MS) of 76 sample aliquots of Lower Devonian carbonates and marls of the Prague Basin, Czechia, which represent close lithological analogues of the Kometan Formation (Bábek et al., 2021). The EDXRF data from the Kometan were converted into equivalent concentrations for ICP-

MS/OES using linear and polynomial regression equations from the Prague basin data set. The regression analyses yielded high coefficients of determination (R^2) ranging from 0.85 to 0.99 for all elements, indicating a high level of analytical precision of the EDXRF technique.

4. Results

4.1. Microfacies

Within the studied sections, the limestone and dolomitic limestone of the Qamchuqa Formation define the lower boundary, while the marl and marly limestone of the Shiranish Formation cover the upper boundary of the Kometan Formation. The Kometan Formation exhibits a highly consistent lithology in outcrop, with argillaceous limestone and thin- to medium-bedded, fine-grained, bioturbated limestone ranging in color from light grey (lower part) to light brown (upper part). Typically, beds are between 15 and 60 cm thick. The thin marly laminae that divide the beds are frequently altered by stylolitization. The carbonate is severely fractured and contains a large number of stylolites. Locally, the limestones include numerous chert nodules distributed parallel to the bedding planes, some of which are concentrated on the stylolites (Fig. 5).

The examined thin sections reveal the presence of lime mudstone, wackestone, and packstone microfacies. They are divided into mud-supported (mudstone and wackestone) (microfacies A) and grain-supported (packstone) (microfacies B) microfacies (Fig. 5). The microfacies A and B show relatively uniform allochem composition appear in the Qamchuqa and Zewe sections. The microfacies A correspond to poorly sorted wackestones with abundant planktonic foraminifers such as *Hedbergella*, *Heterohelix*, oligosteginid foraminifera, sparse calcispheres, and sponge spicules. The matrix is composed of micrite together with silt-sized, unidentifiable calcite fragments (Fig. 5). The microfacies B correspond to moderately sorted packstones with numerous planktonic foraminifera including *Globotruncana* and *Dicarinella*, less abundant *Hedbergella* and *Heterohelix*, scarce calcispheres, remnants of ostracod shells, and abundant grains of glauconite (Fig. 5). Both microfacies indicate distal, basinal/pelagic environment, reworked, and sorted by current activity, as evidenced by its lime mudstone/wackestone/packstone texture and the dominance of planktonic foraminifers. The microfacies A volumetrically prevails.

4.2. Stylolite morphology and distribution

Well-developed stylolites in microfacies A show little weathering (Fig. 5B). The stylolites in pure carbonate beds are evenly distributed and parallel to the bedding plane. Stylolites are mostly of the suture and sharp-peak type with many basic wave-like features. The horizontal and vertical

connections of stylolites with others form intricate anastomosing networks. At junctions, stylolites create Y-type arrangements with occasional X-type configurations. As a result, the stylolite networks exhibit a branching morphology. The maximum thickness of the stylolite seams is 9.5 cm and appear frequently filled by clay and chert nodules. The stylolites of microfacies B (Fig. 5C) exhibit comparable outcrop characteristics and formation patterns to those of microfacies A but at a lower frequency and thinner stylolite seams (maximum = 5.4 cm).

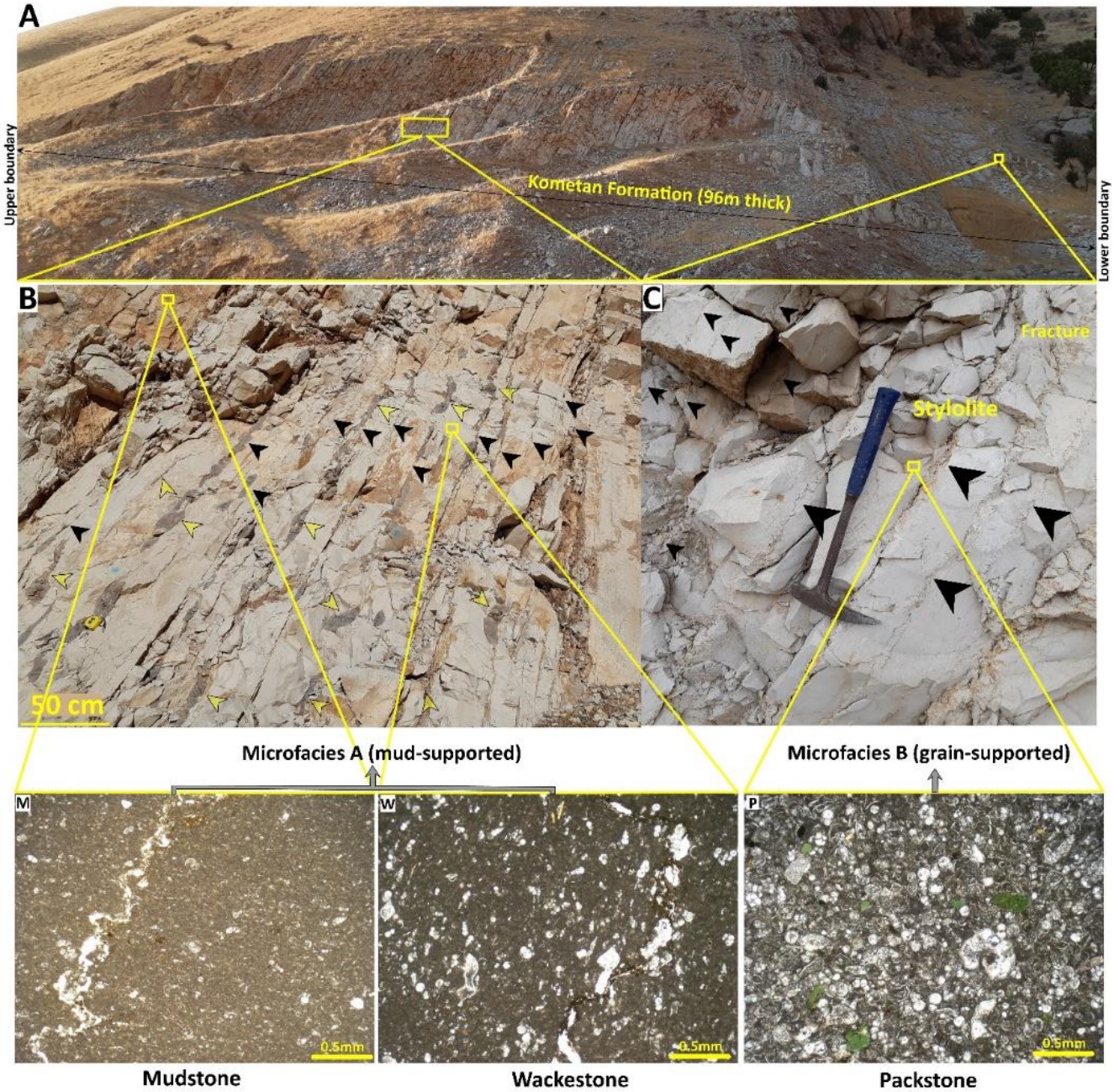

Fig. 5. Field photos of the studied formation in the Zewe section (A) and a Close view of bed observations show chert nodules (yellow arrow) and stylolites (black arrow) (B, C). Photomicrographs showing the microfacies: M) planktonic foraminiferal mudstone W) planktonic foraminiferal wackestone, and P) planktonic foraminiferal packstone with glauconite (green particles).

337 **Table 1.** Summary of the statistical properties (mean values) of stylolite networks for microfacies A (mud-
338 supported) and B (grain-supported).

microfacies	Characteristic component	Spacing (cm)	Wavelength (cm)	Amplitude (cm)	Junction intensity (i/m)	Junction angle (°)
A	planktonic foraminiferal mudstone and wackestone	6.92	3.39	0.66	0.73	37.5
B	planktonic foraminiferal packstone with glauconite	8.91	3.09	0.65	0.69	27.5

339

340 The characterization of stylolite populations was initially conducted by measuring stylolite
341 morphology at the outcrop scale to define the statistical characteristics of stylolites within any facies
342 analyzed. The morphological parameters employed for the statistical characterization of stylolites
343 encompassed vertical spacing, amplitude, wavelength, junction type, and junction intensity (Table 1).
344 Microfacies A has lower vertical stylolite spacing than microfacies B (Fig. 6). Specifically, nearly
345 50% of the A spacings are in the range of 0.7 to 7.4 cm, while 40% are in the range of 9.4 to 77.6 cm.
346 Most spacing values (60%) in this microfacies range between 2.9 and 14.7 cm. The highest spacing
347 frequency of microfacies A in total frequency numbers (683) equals 68 (mode = 2.7 cm, 10% of total).
348 In comparison, 50% of the recorded measures in microfacies B show a progressive increase from 0.9
349 to 9.4 cm. 40% of the space ranges from 11.9 to 77.6 cm. Most of the spacings (60%) between stylolites
350 in this microfacies vary from 3.7 to 19 cm. Ten percent of the total measurements are between 9.75
351 and 12.25 cm, resulting in a maximum frequency of 43 in total frequency numbers of 423 (mode = 3
352 cm, 6% of total).
353 The microfacies A exhibits wavelength with a mode equal to 3.31 cm (73 measurements, 30 % of
354 total) (Fig. 6). Fifty percent of the measured data ranges from 3.8 to 20 cm. The microfacies B has
355 shorter wavelength compared to A, with approximately half of the recorded values falling within the
356 3.1 to 16.6 cm range. The mode equals 3.73 cm, constituting 22% of the total wavelength (244).

Regarding amplitude, microfacies A shows the largest values (6.17 cm) and the higher mean value (0.66 cm) (Table. 1, Fig. 6). The minimum value recorded in this microfacies is 0.2 cm. Contrary to microfacies A, the maximum amplitude recorded in microfacies B is 2.8 cm. The mode value of the amplitude for both microfacies is equal to 0.5 cm (35% of the total measured amplitude (359)) and 0.77 cm, respectively (32% of the total measured amplitude (242)).

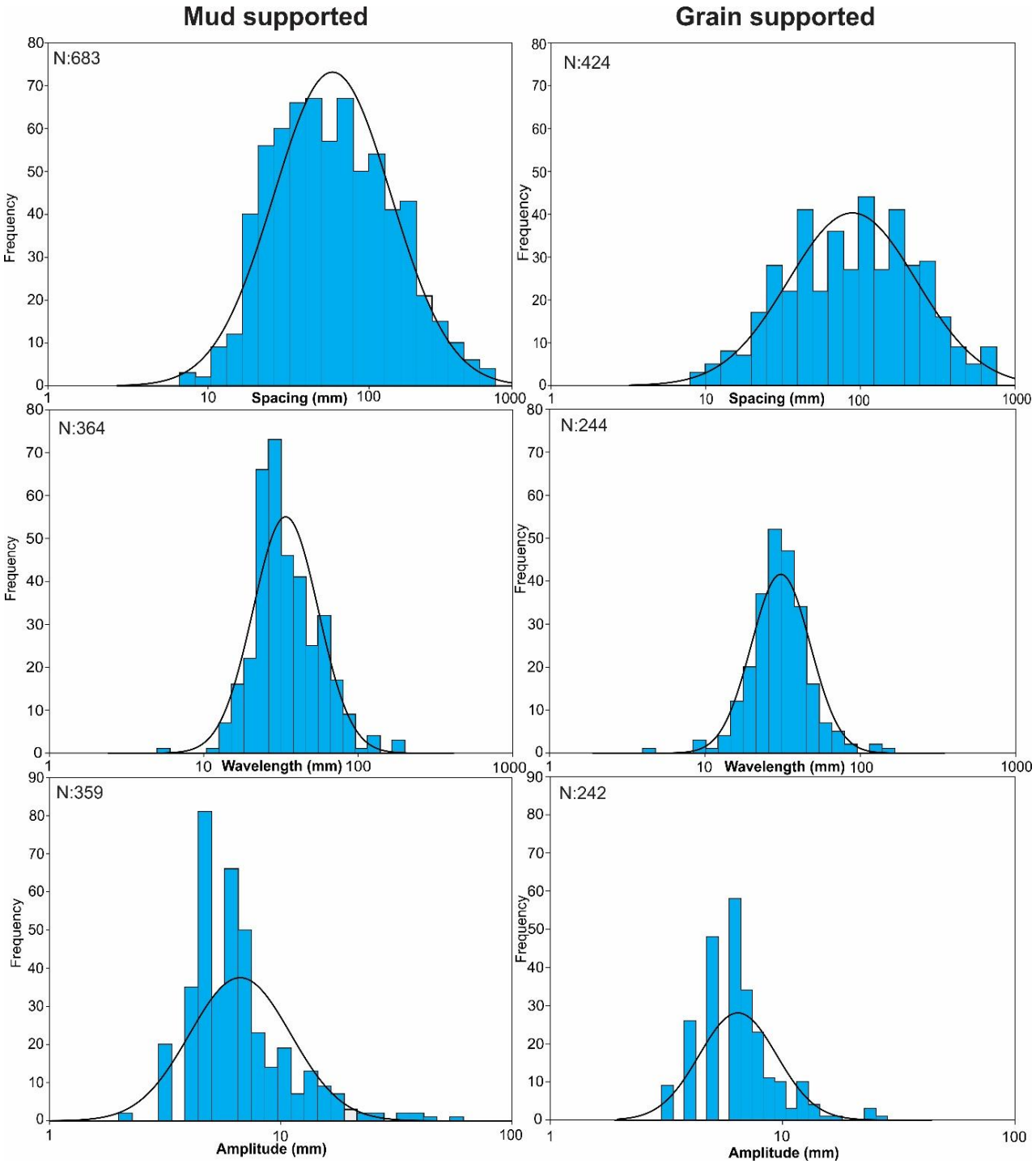

Fig. 6. Histograms showing the log-normal distribution of stylolite spaces, amplitude, and wavelength observations for microfacies A (mud-supported) and B (grain-supported).

According to the classification of Koehn et al. (2016), the suture and sharp-peak type, as well as the simple wave-like type stylolites, predominate in the Kometan Formation (Fig. 7). Stylolites of the suture and sharp-peak type constitute about 55% of the stylolites identified in microfacies A and B. Simple wave-like type stylolites represent about 43% and 44% of the stylolites found in microfacies A and B, respectively. Rectangular layer-type stylolites exhibit the lowest occurrence among various stylolite morphologies, with proportions ranging from 0.5 to 0.1% for microfacies A and B, respectively.

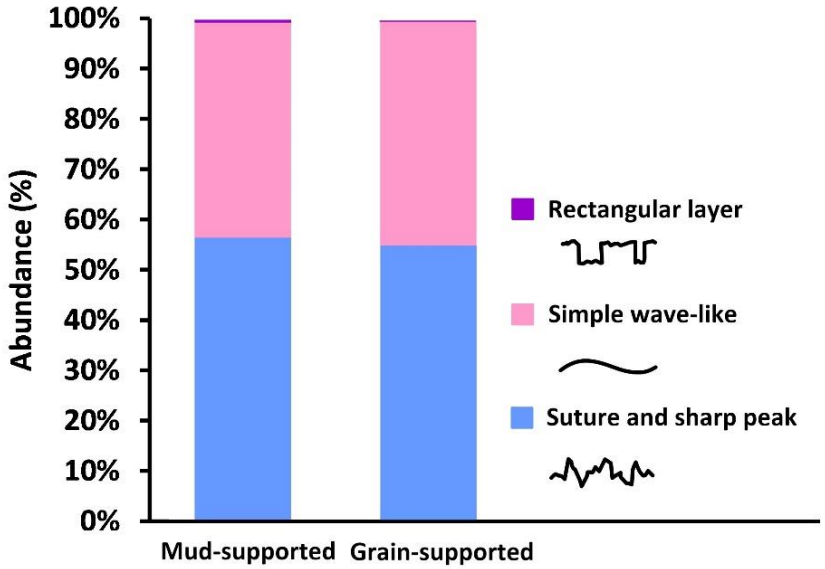

Fig. 7. Stylolite types (%) according to Koehn et al. (2016) classification in mud-supported (mudstone and wackestone) and grain-supported (packstone) lithofacies.

Statistical analysis of stylolite distribution (null hypothesis rejected at p-values < 0.05) indicates that the spacing, amplitude, and wavelength are most accurately represented by a log-normal distribution (Figs. 6 and 8). Utilizing a log-normal distribution of the stylolite spacing resulted in chi-squared values ranging from 22 to 32, indicating a diminished goodness of fit. The KS-test findings with a p-value exceeds 0.05 suggest a stronger level of agreement between the fitted distribution and the stylolite dataset, indicating a higher degree of goodness of fit. The p-values for both microfacies of spacing measurement for the log-normal distribution are found to be greater than 0.05 (Figs 6, and 8A).

The records of stylolite wavelength exhibit chi-squared values ranging from 47 to 50, as depicted in Fig. 8B. The chi-squared and p-value exhibit higher values in microfacies A when compared to the microfacies B. The p-value associated with the log-normal distribution for microfacies B remains much more than 0.05, suggesting a strong level of agreement between the observed data and the theoretical distribution. The readings of stylolite amplitude exhibit a wider range of chi-squared values (Fig. 6,

8C), ranging from 63 to 80. Additionally, the results of the KS test display a distribution of p-values above the significance threshold of 0.05, suggesting a satisfactory fit.

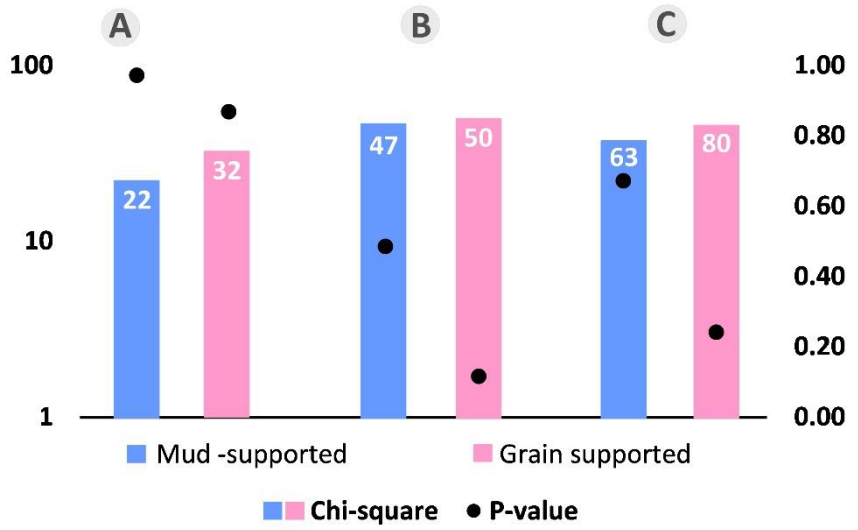

Fig. 8. Logarithmic distribution of the chi-squared and Kolmogorov-Smirnoff (KS) normality tests were used to fit stylolite measurements. (A) spacing. (B) Wavelength. (C) Amplitude.

X- and Y-type connections comprise 10.6% and 89.4% of microfacies A, respectively (Fig. 9A). About 7% of microfacies B have X-type connections. The junction intensity of microfacies A and B is 0.72 and 0.69 i/m respectively (Fig. 9B).

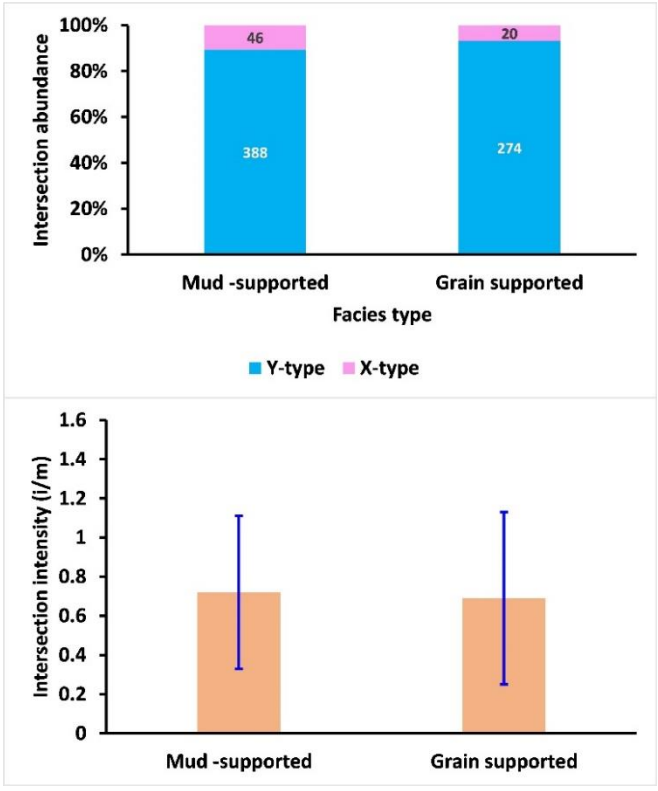

Fig. 9. (A) Stacked chart depicting the number of stylolite junctions within the microfacies under investigation. (B) junction intensity of stylolites for each microfacies.

4.3. Porosity and pore networking

The abundance of pores is higher in regions where stylolites are more pronounced, a feature easily discernible in both thin sections (Fig. 10) and SEM images (Fig. 11). Optical microscopy and SEM observations of the thin sections (Figs. 10, 11) reveal the primary focus on the stylolitic features and associated pore spaces. Stylolites create distinctive intergranular and intragranular pores within the limestone. Intergranular stylolites, visible in thin sections, exhibit linear dissolution seams along grain boundaries, while intragranular stylolites within individual calcite crystals are more prominently visualized in SEM images.

The features of stylolites are discernible under transmitted light analysis of thin sections embedded in blue resin (Fig. 10), providing insights into their morphology in two dimensions. Intergranular pores manifest as dark linear features against the blue background, displaying irregularities and steps along the stylolite surfaces. Intragranular pores within calcite crystals appear as small, dark voids within the crystal lattice. In SEM images (Fig. 11), the morphology of these pores is further highlighted, offering a more detailed perspective. Intergranular pores show complex dissolving patterns with uneven surfaces, like irregular shapes and steps. Intragranular pores inside calcite crystals have detailed forms and can be oriented differently. Stylolites tend to form preferentially along specific bedding planes or within layers with variations in composition, leading to a non-uniform distribution of intergranular and intragranular pores.

Quantitative analysis involves measuring the pore spaces in both intergranular and intragranular regions. The analysis of thin sections (Fig. 10) and SEM (Fig. 11) images reveal an average porosity of approximately 8.3% and 12.8%, respectively, indicating the percentage of void space within the stylolites. Pore size distribution based on SEM images revels values ranging from 0.008 to 2 millimeters (Fig. 11). SEM analysis of stylolized rock samples reveals a complex pore network indicative of localized pressure dissolution (Fig. 11). Residual materials in these pores include illite, kaolinite, montmorillonite, and iron oxide.

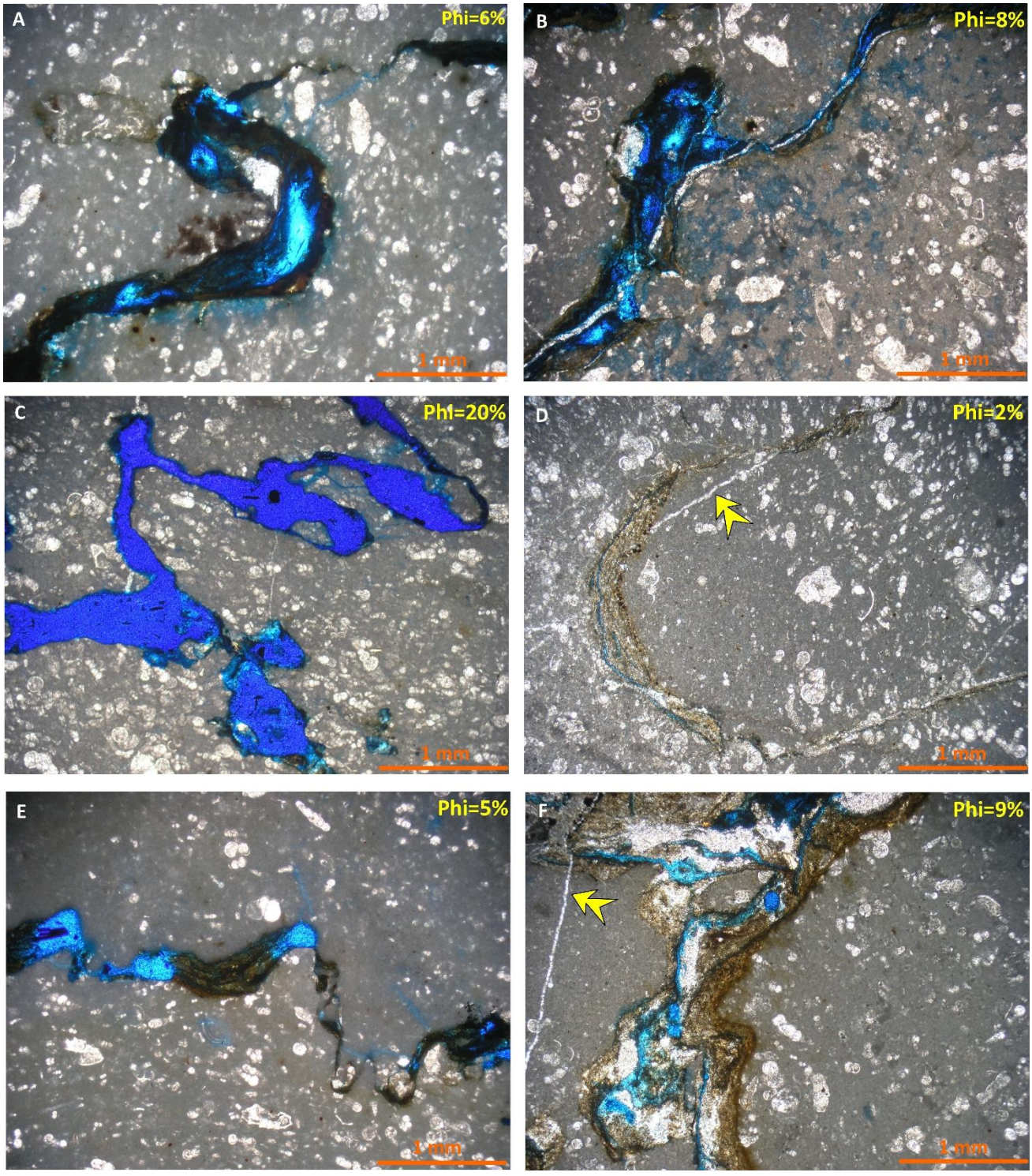

Fig. 10. Microphotograph of the Kometan Formation from the Zewe (A and B), Qamchuqa (C and D), and Dokan (E and F) sections showing pore shapes, sizes, distribution in the rock, relationship to stylolites, and quantification of porosity.

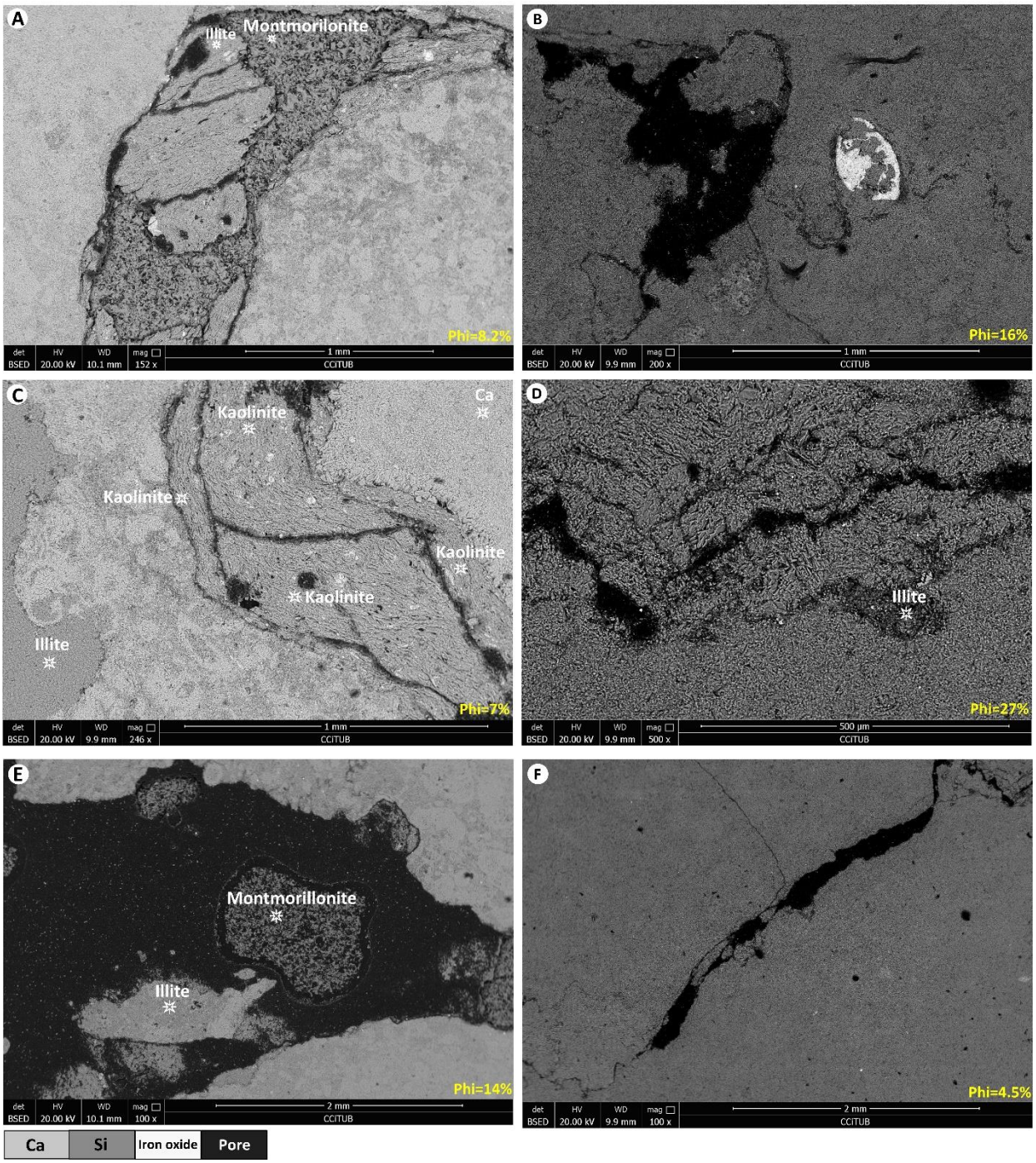

Fig.11 Microphotograph of scanning electron microscope (SEM) of Qamchuqa (A, C, and E) and Zewe (B, D, and F) sections showing materials in and outside of stylolite seams, dissolved area, and amount of pore spaces (Phi).

4.4 Element geochemistry of the studied carbonates

The elemental composition of bulk-rock samples (n = 246) of the studied sections is shown in Table S1 (Supplementary Material). The mean values (μ, wt. % / ppm) and coefficients of variations (CV, %) of the element concentrations are Ca (36.41 wt. %, 7.4 %), Si (2.99 wt. %, 43.3 %), P (1.23 % wt.

%, 4.7 %), Al (0.29 % wt. %, 101.0 %), Fe (0.13 wt. %, 111.3 %), K (0.1 wt. %, 177.5 %), Ti (0.04 wt. %, 68.7 %), Mn (0.01 wt. %, 74.6 %), Sr (658 ppm, 29.5 %), Zn (124 ppm, 1415,3 %), V (81 ppm, 731 %), Cu (18 ppm, 30.7 %), Ni (16 ppm, 28.3 %), Zr (10 ppm, 33.2 %), Pb (5 ppm, 77.0 %), Rb (5 ppm, 61.1 %), As (2 ppm, 27.1 %, and Mo (2 ppm, 72.9 %). Covariance patterns between elements generally reflect the composition of the sediment. Rubidium, titanium, silicon (Fig. 12), and other elements (K, Fe, Zr) show statistically significant covariance with aluminum. At the same time, these elements show negative covariance with Ca and P. This is explained by the mixing of two main mineral carriers, calcite for Ca and P, and detrital silicate minerals - phyllosilicates, quartz, feldspars, and heavy minerals for Al, Si, K, Ti, Rb, and Zr. The data points from different sections show relatively isolated clusters, e.g., for Rb:Al and Ca:Al (Fig. 12), but also for K:Al and Rb:K, indicating differences in the composition of the detrital minerals between the sections. As an example, the Rb/Al ratio is 13.6 in the Qamchuqa section and 17.3 in the Zewe section (Fig. 12). Silicon shows different patterns. The Qamchuqa section correlates with Al (R^2 = 0.61, Fig. 12, Si baseline), suggesting a similar mixing of calcite and detrital minerals as indicated above. However, Si shows a significant enrichment (points high above the baseline) in the Dokan and especially Zewe sections (Fig. 12), which can be attributed to biogenic (sponge spicules, radiolarians) and diagenetic (cherts) sources of silica. Similar patterns are observed for Ti.

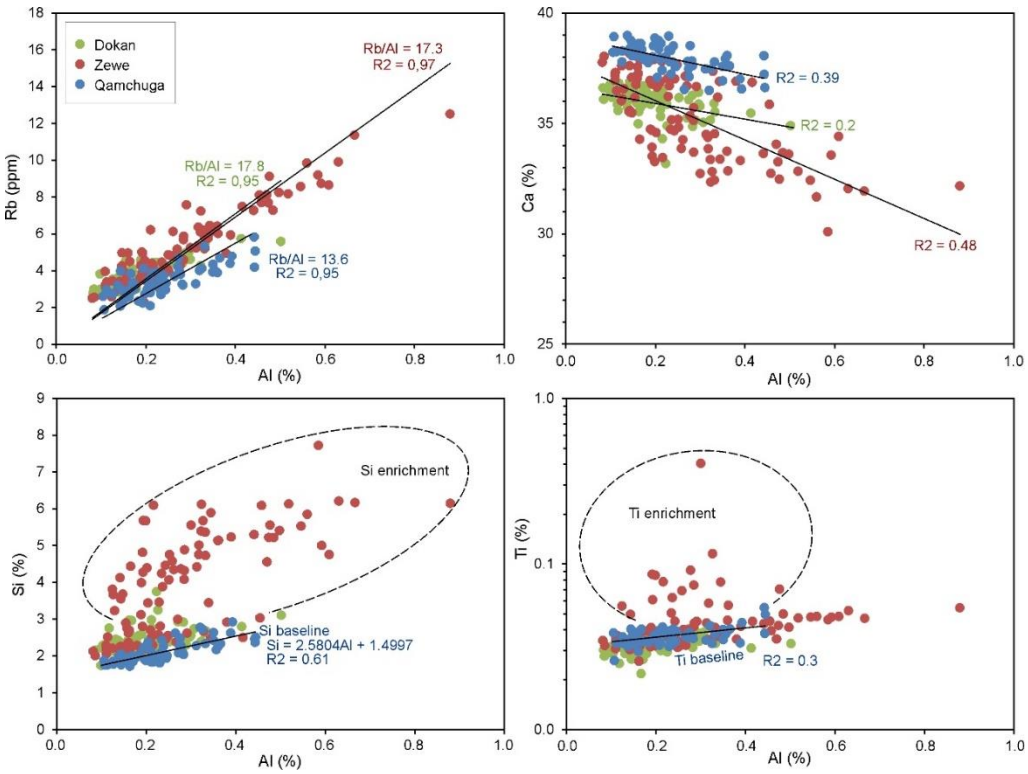

Fig. 12. Bivariate plots of element concentrations from the Kometan Formation from Dokan, Zewe, and Qamchuqa sections. Note the co-variance of lithogenic elements (Al, Rb, Ti, and Si from the Qamchuqa section). Also, note Si and Ti enrichment in the Zewe section.

The depth distribution of the element concentrations shows that most of the Si enrichment occurs in the Zewe section between 40 and 96 m, culminating 80 m above the section base (Fig. 13). The zone of silica enrichment can be correlated with the upper parts of the Qamchuqa section between 40 and 63 m above the section base, and partly with the top parts of the Dokan section between 45 and 65 m. These increased concentrations of Si partly coincide with increasing Al and decreasing Ca concentrations (Fig. 13). Across the dataset, instances can be found where an increase in Si concentration corresponds with an increase in total length per cubic meter, suggesting a positive correlation. However, this positive correlation is not universally observed, as there are instances where total length decreases despite higher Si levels. Similarly, while certain cases show a positive correlation between Ca concentration and the total length, others exhibit a decrease in total length despite elevated Ca concentrations (Fig. 13). In addition, the highest amount of stylolite is at depths (9 to 59 m above the section base) where Ca is high, and Si is low.

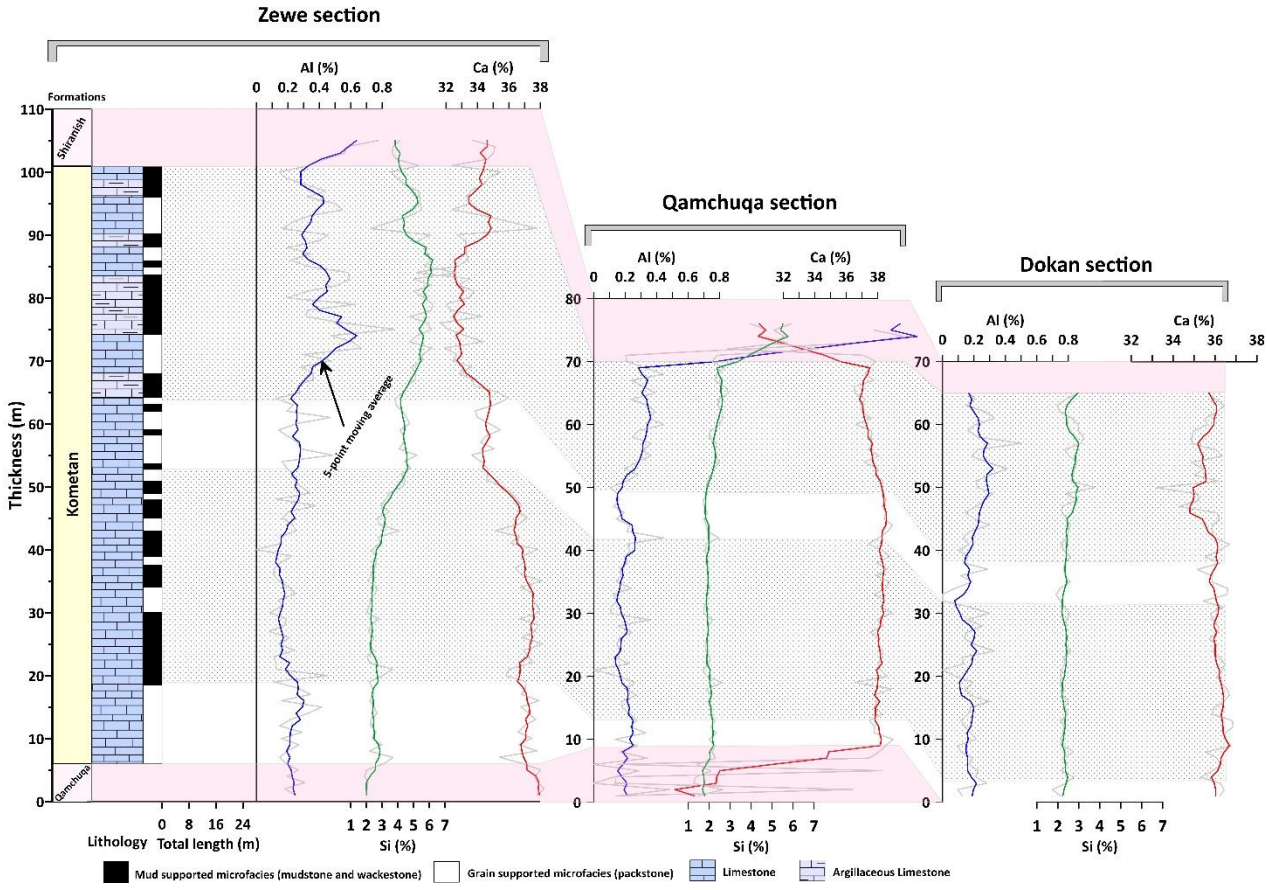

Fig.13. Total length of stylolite along different microfacies with elemental geochemistry (Al, Ca, and Si) for the studied sections (the lower contact of Kometan Formation in the Dokan section is not exposed).

5. Discussions

5.1. Correlation analysis of stylolite morphological parameters and their host rock characteristics

To effectively analyze the relationship between stylolite types and microfacies, it is crucial to initially define the microfacies criteria that facilitate the assessment of certain lithological and morphological characteristics. These variables have the potential to be integrated with stylolite shape characteristics to construct a matrix of correlations (Fig. 14). This matrix finds potential connections and impacts of lithology and elemental geochemistry on stylolite network geometries. The rock's complexity level, as shown by variations in composition, grain size, and grain size distribution, exhibits clear associations with important stylolite features. In the context of sedimentary facies, it has been shown that mud-supported microfacies with heterogeneous grain sizes exhibit stylolite networks characterized by high amplitudes and wavelengths, accompanied by relatively small vertical spacings. Conversely, microfacies characterized by moderately sorted grain support tend to create stylolites with lower amplitudes and wavelengths and greater vertical spacings (Humphrey et al., 2020).

5.1.1. Mud *vs* grain-dominated microfacies.

The identification of micrite and clay minerals has frequently been recognized as a significant factor contributing to heterogeneity and subsequent stylolite roughening (Wanless, 1979; Koehn et al., 2012; Paganoni et al., 2016; Morad et al., 2018). The increased surface area of micrite contributes to the enhanced solubility of the rock. The present work demonstrates that there is a significant correlation between the stylolite amplitudes, which refer to the degree of roughening, and the quantity of micrite. These associations result in greater amplitudes observed in mud-supported facies, as reported by Morad et al. Stylolites with greater amplitude and wavelength are found to promote a higher number of junctions, as evidenced by favorable associations with X- and Y-type crossings, as well as reduced vertical separation. It is noteworthy that the correlation matrix reveals contrasting morphological patterns in the development of stylolites within grain-supported facies (Fig. 14). The presence of clay minerals contributes to variability and rise in stylolite amplitude, hence facilitating the initiation and intersection of stylolites (Wanless, 1979; Koehn et al., 2012; Paganoni et al., 2016; Morad et al., 2018). The process is additionally helped by the feedback loop involving clay minerals and pressure solution, as suggested by Aharonov and Katsman (2009). In this mechanism, the buildup of clay minerals promotes dissolving, leading to the formation of stylolites, which in turn accumulate more clay minerals (Fig. 11).

5.1.2. Composition and grain size distribution

In addition to the occurrence of micrite and clay minerals, many lithological factors have been identified to contribute to carbonate heterogeneity, hence influencing the formation and resulting stylolite types. The presence of a bimodal particle size distribution results in an enhanced suturing process, mostly attributed to differences in dissolution and resistance to pressure solution (Railsback, 1993; Andrews and Railsback, 1997; Koehn et al., 2012). Stylolites tend to form preferentially in carbonates with a fine-grained texture (Rustichelli et al., 2012). This research has found a negative correlation between grain size and stylolite amplitudes (Fig. 14).

A combination of significant grain size variation and poor sorting leads to increased heterogeneity and, as a result, greater roughness (Koehn et al., 2012). There is a positive correlation between poorly sorted facies and larger amplitude stylolites (Fig. 14). Stylolites with larger amplitudes tend to exhibit smaller vertical spacings and a greater number of intersections. The occurrence of these situations is influenced by the changes in solubility resulting from particle size and spread variances. These dissimilarities lead to particle pinning and disparities in solubility rates, producing favorable situations for developing and roughening stylolites (Aharonov and Katsman, 2009; Koehn et al., 2016). The connection process can be facilitated by the phenomenon of stylolite cannibalism, which is induced by enhanced roughening and disintegration resulting from poor sorting, as proposed by Ben-Itzhak et al. (2014). The shape of stylolites is also influenced by the type of particles present in the rock. This is because the composition of these particles results in changes in dissolution, promoting the formation and binding of stylolites. According to Wanless (1979), magnesium (Mg) is recognized as an impurity that induces fluctuations in dissolution within the rock. Tucker and Wright (1991) demonstrate that low- and high-Mg calcite distribution may affect subsequent carbonate dissolution. As an illustration, it is observed that foraminifera generally have a magnesium (Mg) content of up to 25%, whereas other fossils, such as bivalves, display more restricted and lower ranges of 0-5%. The presence of either high or low magnesium (Mg) calcite and dolomite can contribute to variations in dissolution and pressure solution. Other factors that can influence dissolution include the calcite/aragonite content in bioclasts, the presence of non-soluble grains and silica, as well as the dissolution rate of mud (Dewers and Ortleva, 1994) (Fig. 11).

Si and Ca exhibit complex relationships with stylolite length. While Si concentrations vary widely, no clear linear trend with the stylolite total length emerges (Fig. 13). This scattered distribution shows that the influence of Si is complex and most likely controlled by other factors. Higher Si may sometimes correlate with greater mass loss, but not consistently. Similarly, despite some concentration variation, Ca lacks a straightforward linear relationship with stylolite length (Fig. 13). Higher Ca

values may generally coincide with increased mass loss, but not universally. Figure 13 clearly shows that pure carbonates (high Ca) have a higher total length. However, Ca is affected by the combined effects of Si and Al and other elements. These multifaceted responses emphasize the need for a more comprehensive understanding of factors influencing mass loss. Notably, Ca and Si show opposite correlations with stylolite length (Figs. 13, 14).

According to Wanless (1979), the primary determinant of the jagged or undulose waveform (identical to suture and sharp-peak and wave-like types) of stylolites is the particle size. This waveform is like the suture and sharp-peak, and simple wave-like types found in the stylolite categorization framework. Wanless (1979) argued that undulose waveforms are more likely to form in lithologies with large particles. In their study, Humphrey et al. (2020) documented a negative correlation between the prevalence of suture and sharp-peak stylolites and wave-like stylolites in facies characterized by particle sizes greater than 2 mm. Notably, wave-like stylolites were found to predominantly form in facies with lower grain size. The present study reveals a nearly identical relationship (Fig.7) between the abundance of suture and sharp-peak and wave-like type stylolites in mud-supported and grain-supported microfacies.

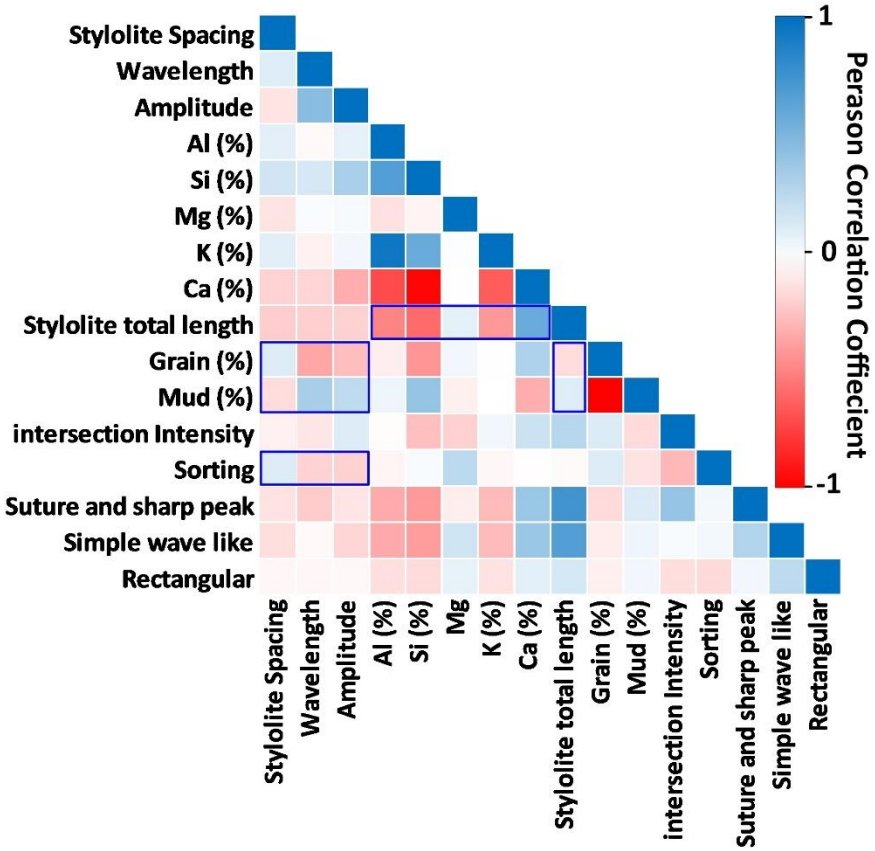

Fig. 14. Evaluation of the Pearson correlation coefficient between studied stylolite morphology and geological factors using a correlation matrix. Blue boxes show the most important connections.

5.2. Stylolite distribution

The log-normal distribution effectively represents the stylolite spacing, wavelength, and amplitude data in grain-supported microfacies (Figs. 6 and 8). Specifically, heterogeneities in the stylolite host rocks are influenced by the sorting of heterogenous grain compositions, which in turn govern the spatial distribution of pressure solution and following stylolite distribution. The log-normal spacing distribution accurately represents all the examined microfacies (Humphrey et al., 2020). This indicates that all microfacies possess a significant level of spatial heterogeneity, affecting the locations where stylolite nucleation occurs. Microfacies A exhibits comparatively lower chi-squared and higher K-S test outcomes in relation to spacing (Fig. 8A), suggesting a potential correlation with the elevated degree of sorting observed in the rock, thus leading to more heterogeneity. Nevertheless, it is important to acknowledge that the log-normal distributions of stylolite spacing may also be associated with reduction inclination, which is a form of sample inclination influenced by the precision of the sampling technique (Zeeb et al., 2013). In cases where the identification of a slender stylolite is impeded by either unfavorable outcrop situations or its clarity falls beyond the capability of pictures, two minor spacing values are omitted while a single bigger spacing value is included. This phenomenon may result in a disproportionate representation of larger spacings and a corresponding inadequate representation of smaller spacings, thereby altering the spread of spacings to a log-normal distribution.

The results of the chi-squared and K-S tests indicate that stylolite wavelength measurements exhibit greater strength in facies characterized by mud-supported rock (Figs. 6 and 8B). This observation may be attributed to the presence of clay content, leading to increased dissolution, as proposed by Aharonov and Katsman (2009). Consequently, spatial variations in solubility are influenced, thereby affecting amplitude growth. The log-normal amplitude values have been linked to an irregular growth process promoted by fluctuations in solubility and eventual grain "pinning" (i.e., the fixation of a stylolite plane to a grain or fossil) by Koehn et al. (2007) and Ebner et al. (2009). Microfacies A exhibits more robust chi-squared and K-S test outcomes regarding amplitude (Figs. 6 and 8C). This is linked to a mud-supported lithology characterized by various grains with varying compositions. Upon comparing the outcomes of distribution-fitting analysis with the primary lithological constituents in both facies, it becomes evident that there is a limited association between the heterogeneity of particle size and the extent of sorting concerning stylolite amplitude. The grain-supported facies exhibit a diminished level of fit in comparison to the mud-supported microfacies when evaluating the chi-squared and KS outcomes for log-normal stylolite distributions. The grain-supported facies exhibit a modest degree of sorting and display relatively low levels of compositional variation. The absence of heterogeneity could consequently underscore the significance of changes in solubility on the amplitude of stylolites,

as previously proposed by Ebner et al. (2009). In this context, the insufficient presence of particle "pinning" minimizes the non-linear amplitude increase.

5.3. Impact of stylolite on porosity and permeability

One of the most notable characteristics observed in this study pertains to the capacity of stylolites to improve the porosity and permeability of the formation under investigation. The dissolution of minerals along stylolite planes results in the formation of complex networks of channels and conduits (Figs.10 and 11). These pathways are crucial for the migration of fluids, as they offer paths through rock matrix that would otherwise be impermeable. Within the field of hydrocarbon exploration, stylolites are recognized as significant secondary migratory paths (Braithwaite, 1988; Peacock et al., 2017; Koehn et al., 2012). They facilitate the migration of oil and gas, ultimately resulting in their deposition and concentration within reservoir formations. The natural improvement of permeability can significantly impact the productivity and economic feasibility of petroleum reservoirs.

In their studies, Koehn et al. (2016) and Humphrey et al. (2019) established a correlation between the morphology of stylolites and their potential effectiveness as fluid flow barriers. They found that stylolites with low roughness exhibit greater continuity, making them more effective barriers than stylolites with irregular (rough) profiles. Gomez-Rivas et al. (2022) described a case study in which anastomosing stylolite networks collectively acted as baffles for diagenetic fluids. The fluid flow behavior of the material is also influenced by the nature of its filling material (Figure 11). Stylolites can serve as effective barriers when they are filled with impermeable substances such as clay, organic matter, and/or oxides (Figs. 10 and 11) (Mehrabi et al., 2016; Vandeginste and John, 2013). Furthermore, according to Heap et al. (2014), the presence of a stylolite can be deemed effective as a barrier if the material filling it spreads evenly and continuously throughout the seam and if the mix of insoluble materials is consistent throughout.

6. Conclusions

The extensive analysis of stylolites and their host rocks carried out in the Kometan Formation provides useful insights into stylolite formation and its role in terms of permeability. Firstly, the identification of microfacies, characterized by diverse lithologies ranging from mud-supported to grain-supported compositions, underscores the complex depositional environments prevalent during sedimentation within the formation. Secondly, the detailed scrutiny of stylolite morphology and distribution reveals subtle correlations with lithological characteristics, particle size distribution, and pressure dissolution processes. Additionally, the statistical assessment, particularly the recognition of log-normal distributions, emphasizes the inherent variability of stylolite development within the formation. Such statistical analyses provide a quantitative basis for

understanding the spatial diversity and distribution patterns of stylolites, crucial for predictive modeling and reservoir characterization. Moreover, the clarification of porosity and pore networking, combined with the evaluation of elemental geochemistry, provides valuable insights into the formation's petrophysical properties and diagenetic evolution. These findings not only advance our understanding of fluid migration pathways and reservoir connectivity but also hold significant implications for assessing reservoir quality and hydrocarbon recovery potential. In summary, the integrated approach employed in this study marks a notable advancement in our comprehension of carbonate reservoirs, offering valuable insights into their geological complexities and reservoir potential. These findings carry important implications for hydrocarbon exploration and development strategies, guiding decision-making processes and shaping future exploration efforts in similar geological contexts.

Acknowledgments

This research was partially funded by project number 22-15405S of the Czech Science Foundation (GACR), the Spanish Ministerio de Ciencia, Innovación y Universidades (PID2021-12246NB-C22), and the Grup Consolidat de Recerca Geologia Sedimentària (2021 SGR-Cat 00349). Hussein Hussein extends his appreciation for the significant financial support received through the Fischer PhD Scholarship Program at Palacky University Olomouc.

References:

Aharonov, E. and Katsman, R., 2009. Interaction between pressure solution and clays in stylolite development: Insights from modeling. American Journal of Science, 309(7), 607-632.

Alavi, M., 2004. Regional stratigraphy of the Zagros fold-thrust belt of Iran and its proforeland evolution. American journal of Science, 304(1), pp.1-20.

Al-Hamadani, A., 1986. Sedimentological and geochemical formation of khasib, tanuma and sadi (Doctoral dissertation, Ph. D. thesis, College of Science, University of Baghdad).

Alsharhan, A.S. and Sadd, J.L., 2000. Stylolites in Lower Cretaceous carbonate reservoirs, UAE.

Andrews, L.M. and Railsback, L.B., 1997. Controls on stylolite development: morphologic, lithologic, and temporal evidence from bedding-parallel and transverse stylolites from the US Appalachians. The Journal of Geology, 105(1), pp.59-73.

Aqrawi, A. A. M., J. C. Goff, A. D. Horbury, and F. N. Sadooni, 2010, The Petroleum Geology of Iraq: Beaconsfield, United Kingdom, Scientific Press Ltd., 424 p.

Bábek, O., Kumpan, T., Calner, M., Šimíček, D., Frýda, J., Holá, M., Ackerman, L. and Kolková, K., 2021. Redox geochemistry of the red 'orthoceratite limestone'of Baltoscandia: Possible linkage to mid-Ordovician palaeoceanographic changes. Sedimentary Geology, 420, p.105934.

Barnett, A.J., Wright, V.P., Chandra, V.S. and Jain, V., 2018. Distinguishing between eogenetic, unconformity-related and mesogenetic dissolution: a case study from the Panna and Mukta fields, offshore Mumbai, India. Geological Society, London, Special Publications, 435(1), pp.67-84.

Baron, M. and Parnell, J., 2007. Relationships between stylolites and cementation in sandstone reservoirs: Examples from the North Sea, UK and East Greenland. Sedimentary Geology, 194(1-2), pp.17-35.

Bathurst, R.G., 1991. Pressure-dissolution and limestone bedding: the influence of stratified cementation. Cycles and events in stratigraphy, pp.450-463.

Baud, P., Rolland, A., Heap, M., Xu, T., Nicolé, M., Ferrand, T., Reuschlé, T., Toussaint, R. and Conil, N., 2016. Impact of stylolites on the mechanical strength of limestone. Tectonophysics, 690, pp.4-20.

Bauerle, G., Bornemann, O., Mauthe, F. and Michalzik, D., 2000. Origin of stylolites in Upper Permian Zechstein anhydrite (Gorleben salt dome, Germany). Journal of Sedimentary Research, 70(3), pp.726-737.

Ben-Itzhak, L.L., Aharonov, E., Karcz, Z., Kaduri, M. and Toussaint, R., 2014. Sedimentary stylolite networks and connectivity in limestone: Large-scale field observations and implications for structure evolution. Journal of Structural Geology, 63, pp.106-123.

Bergen, D.V. and Carozzi, A.V., 1990. Experimentally-simulated stylolitic porosity in carbonate rocks. Journal of Petroleum Geology, 13(2), pp.179-192.

Bergen, D.V. and Carozzi, A.V., 1990. Experimentally-simulated stylolitic porosity in carbonate rocks. Journal of Petroleum Geology, 13(2), pp.179-192.

Bordenave, M.L., 2008. The origin of the Permo-Triassic gas accumulations in the Iranian Zagros foldbelt and contiguous offshore areas: a review of the Palaeozoic petroleum system. Journal of Petroleum Geology, 31(1), p.3.

Braithwaite, C.J.R., 1989. Stylolites as open fluid conduits. Marine and Petroleum Geology, 6(1), pp.93-96.

Bruna, P.O., Lavenu, A.P., Matonti, C. and Bertotti, G., 2019. Are stylolites fluid-flow efficient features? Journal of Structural Geology, 125, pp.270-277.

Burgess, C.J. and Peter, C.K., 1985, March. Formation, distribution, and prediction of stylolites as permeability barriers in the Thamama Group, Abu Dhabi. In SPE Middle East Oil and Gas Show and Conference (pp. SPE-13698). SPE.

Carozzi, A.V. and Bergen, D.V., 1987. Stylolitic porosity in carbonates: a critical factor for deep hydrocarbon production. Journal of Petroleum Geology, 10(3), pp.267-282.

Chandra, V., Wright, P., Barnett, A., Steele, R., Milroy, P., Corbett, P., Geiger, S. and Mangione, A., 2015. Evaluating the impact of a late-burial corrosion model on reservoir permeability and performance in a mature carbonate field using near-wellbore upscaling. Geological Society, London, Special Publications, 406(1), pp.427-445.

David, M.-E., 2016. Evaluation de la compaction chimique et des paléo-enfouissements des carbonates par l'étude des stylolites sédimentaires - Cas du Bassin de Paris. University Pierre et Marie Curie, Paris, pp. 42.

Dewers, T. and Ortoleva, P., 1994. Formation of stylolites, marl/limestone alternations, and dissolution (clay) seams by unstable chemical compaction of argillaceous carbonates. In Developments in Sedimentology (Vol. 51, pp. 155-216). Elsevier.

Dunham, R.J., 1962. Classification of carbonate rocks according to depositional textures.

Ebner, M., Koehn, D., Toussaint, R. and Renard, F., 2009. The influence of rock heterogeneity on the scaling properties of simulated and natural stylolites. Journal of Structural geology, 31(1), pp.72-82.

Ebner, M., Piazolo, S., Renard, F. and Koehn, D., 2010. Stylolite interfaces and surrounding matrix material: Nature and role of heterogeneities in roughness and microstructural development. Journal of Structural Geology, 32(8), pp.1070-1084.

Ehrenberg, S.N. and Nadeau, P.H., 2005. Sandstone vs. carbonate petroleum reservoirs: A global perspective on porosity-depth and porosity-permeability relationships. AAPG bulletin, 89(4), pp.435-445.

Ehrenberg, S.N., 2006. Porosity destruction in carbonate platforms. Journal of Petroleum Geology, 29(1), pp.41-52.

Ehrenberg, S.N., Morad, S., Yaxin, L. and Chen, R., 2016. Stylolites and porosity in a Lower Cretaceous limestone reservoir, onshore Abu Dhabi, UAE. Journal of Sedimentary Research, 86(10), pp.1228-1247.

English, J.M., Lunn, G.A., Ferreira, L. and Yacu, G., 2015. Geologic evolution of the Iraqi Zagros, and its influence on the distribution of hydrocarbons in the Kurdistan region. AAPG Bulletin, 99(2), pp.231-272.

Finkel, E.A. and Wilkinson, B.H., 1990. Stylolitization as source of cement in Mississippian Salem Limestone, west-central Indiana. AAPG bulletin, 74(2), pp.174-186.

Fletcher, R.C. and Pollard, D.D., 1981. Anticrack model for pressure solution surfaces. Geology, 9(9), pp.419-424.

Flügel, E. and Munnecke, A., 2010. Microfacies of carbonate rocks: analysis, interpretation and application (Vol. 976, p. 2004). Berlin: springer.

Folk, R.L. and Ward, W.C., 1957. Brazos River bar [Texas]; a study in the significance of grain size parameters. Journal of sedimentary research, 27(1), pp.3-26.

Gomez-Rivas, E., Martín-Martín, J.D., Bons, P.D., Koehn, D., Griera, A., Travé, A., Llorens, M.G., Humphrey, E. and Neilson, J., 2022. Stylolites and stylolite networks as primary controls on the geometry and distribution of carbonate diagenetic alterations. Marine and Petroleum Geology, 136, p.105444.

776 Gratier, J.P., Muquet, L., Hassani, R. and Renard, F., 2005. Experimental microstylolites in quartz and
777 modeled application to natural stylolitic structures. Journal of Structural Geology, 27(1), pp.89-100.

778 Groshong Jr, R.H., 1975. Strain, fractures, and pressure solution in natural single-layer
779 folds. Geological Society of America Bulletin, 86(10), pp.1363-1376.

780 Grove, C. and Jerram, D.A., 2011. jPOR: An ImageJ macro to quantify total optical porosity from
781 blue-stained thin sections. Computers & Geosciences, 37(11), pp.1850-1859.

782 Haddad, S.N.S. and Amin, M.A., 2007. Mid-Turonian–early Campanian sequence stratigraphy of
783 northeast Iraq. GeoArabia, 12(2), pp.135-176.

784 Haines, T.J., Neilson, J.E., Healy, D., Michie, E.A. and Aplin, A.C., 2015. The impact of carbonate
785 texture on the quantification of total porosity by image analysis. Computers & Geosciences, 85,
786 pp.112-125.

787 Harris, N.B., 2006. Low-porosity haloes at stylolites in the feldspathic Upper Jurassic Ula sandstone,
788 Norwegian North Sea: an integrated petrographic and chemical mass-balance approach. Journal of
789 Sedimentary Research, 76(3), pp.444-459.

790 Harris, P.M., 2010. Delineating and quantifying depositional facies patterns in carbonate reservoirs:
791 Insight from modern analogs. AAPG bulletin, 94(1), pp.61-86.

792 Hassan, T.H. and Wada, Y., 1981. Geology and development of Thamama zone 4, Zakum
793 field. Journal of Petroleum Technology, 33(07), pp.1327-1337.

794 Heap, M., Reuschlé, T., Baud, P., Renard, F. and Iezzi, G., 2018. The permeability of stylolite-bearing
795 limestone. Journal of structural geology, 116, pp.81-93.

796 Heap, M.J., Baud, P., Reuschlé, T. and Meredith, P.G., 2014. Stylolites in limestones: Barriers to fluid
797 flow? Geology, 42(1), pp.51-54.

798 Humphrey, E., Gomez-Rivas, E., Koehn, D., Bons, P.D., Neilson, J., Martín-Martín, J.D. and
799 Schoenherr, J., 2019. Stylolite-controlled diagenesis of a mudstone carbonate reservoir: A case study
800 from the Zechstein_2_Carbonate (Central European Basin, NW Germany). Marine and Petroleum
801 Geology, 109, pp.88-107.

802 Humphrey, E., Gomez-Rivas, E., Neilson, J., Martín-Martín, J.D., Healy, D., Yao, S. and Bons, P.D.,
803 2020. Quantitative analysis of stylolite networks in different platform carbonate facies. Marine and
804 Petroleum Geology, 114, p.104203.

805 Hussein, H.S., Bábek, O., Mansurbeg, H. and Shahrokhi, S., 2024. Outcrop-to-subsurface correlation
806 and sequence stratigraphy of a mixed carbonate–siliciclastic ramp using element geochemistry and
807 well logging; Upper Cretaceous Kometan Formation, Zagros Foreland, NE Iraq. Sedimentary
808 Geology, 459, p.106547.

809

810 Hussein, H.S., Mansurbeg, H. and Bábek, O., 2024. A new approach to predict carbonate lithology
811 from well logs: A case study of the Kometan formation in northern Iraq. Heliyon.

812 Jassim, S.Z. and Goff, J.C. eds., 2006. Geology of Iraq. DOLIN, sro, distributed by Geological Society
813 of London.

814 Koehn, D., Ebner, M., Renard, F., Toussaint, R. and Passchier, C.W., 2012. Modelling of stylolite
815 geometries and stress scaling. Earth and Planetary Science Letters, 341, pp.104-113.

816 Koehn, D., Renard, F., Toussaint, R. and Passchier, C.W., 2007. Growth of stylolite teeth patterns
817 depending on normal stress and finite compaction. Earth and Planetary Science Letters, 257(3-4),
818 pp.582-595.

819 Koehn, D., Rood, M.P., Beaudoin, N., Chung, P., Bons, P.D. and Gomez-Rivas, E., 2016. A new
820 stylolite classification scheme to estimate compaction and local permeability variations. Sedimentary
821 Geology, 346, pp.60-71.

822 Lind, I., Nykjaer, O., Priisholm, S. and Springer, N., 1994. Permeability of stylolite-bearing
823 chalk. Journal of Petroleum Technology, 46(11), pp.986-993.

824 Lucia, F.J., Kerans, C. and Jennings Jr, J.W., 2003. Carbonate reservoir characterization. Journal of
825 Petroleum Technology, 55(06), pp.70-72.

826 Manzocchi, T., 2002. The connectivity of two-dimensional networks of spatially correlated
827 fractures. Water Resources Research, 38(9), pp.1-1.

828 Martin, A.Z., 2001. Late Permian to Holocene paleofacies evolution of the Arabian Plate and its
829 hydrocarbon occurrences. GeoArabia, 6(3), pp.445-504.

830 Martín-Martín, J.D., Gomez-Rivas, E., Gómez-Gras, D., Travé, A., Ameneiro, R., Koehn, D. and Bons,
831 P.D., 2018. Activation of stylolites as conduits for overpressured fluid flow in dolomitized platform
832 carbonates. Geological Society, London, Special Publications, 459(1), pp.157-176.

833 Massey Jr, F.J., 1951. The Kolmogorov-Smirnov test for goodness of fit. Journal of the American
834 statistical Association, 46(253), pp.68-78.

835 Mehrabi, H., Mansouri, M., Rahimpour-Bonab, H., Tavakoli, V. and Hassanzadeh, M., 2016.
836 Chemical compaction features as potential barriers in the Permian-Triassic reservoirs of Southern
837 Iran. Journal of Petroleum Science and Engineering, 145, pp.95-113.

838 Morad, D., Nader, F.H., Morad, S., Al Darmaki, F. and Hellevang, H., 2018. Impact of stylolitization
839 on fluid flow and diagenesis in foreland basins: evidence from an Upper Jurassic Carbonate gas
840 reservoir, Abu Dhabi, United Arab Emirates. Journal of Sedimentary Research, 88(12), pp.1345-1361.

841 Muttoni, G., Gaetani, M., Kent, D.V., Sciunnach, D., Angiolini, L., Berra, F., Garzanti, E., Mattei, M.
842 and Zanchi, A., 2009. Opening of the Neo-Tethys Ocean and the Pangea B to Pangea A transformation
843 during the Permian. GeoArabia, 14(4), pp.17-48.

844 Neilson, J.E., Oxtoby, N.H., Simmons, M.D., Simpson, I.R. and Fortunatova, N.K., 1998. The
845 relationship between petroleum emplacement and carbonate reservoir quality: examples from Abu
846 Dhabi and the Amu Darya Basin. Marine and Petroleum Geology, 15(1), pp.57-72.

847 Nenna, F. and Aydin, A., 2011. The formation and growth of pressure solution seams in clastic rocks:
848 A field and analytical study. Journal of Structural Geology, 33(4), pp.633-643.

849 Paganoni, M., Al Harthi, A., Morad, D., Morad, S., Ceriani, A., Mansurbeg, H., Al Suwaidi, A., Al-
850 Aasm, I.S., Ehrenberg, S.N. and Sirat, M., 2016. Impact of stylolitization on diagenesis of a Lower
851 Cretaceous carbonate reservoir from a giant oilfield, Abu Dhabi, United Arab Emirates. Sedimentary
852 Geology, 335, pp.70-92.

853 Palermo, D., Aigner, T., Nardon, S. and Blendinger, W., 2010. Three-dimensional facies modeling of
854 carbonate sand bodies: Outcrop analog study in an epicontinental basin (Triassic, southwest
855 Germany). AAPG bulletin, 94(4), pp.475-512.

856 Peacock, D.C.P., Korneva, I., Nixon, C.W. and Rotevatn, A., 2017. Changes of scaling relationships
857 in an evolving population: the example of "sedimentary" stylolites. Journal of Structural Geology, 96,
858 pp.118-133.

859 Railsback, L.B., 1993. Lithologic controls on morphology of pressure-dissolution surfaces (stylolites
860 and dissolution seams) in Paleozoic carbonate rocks from the mideastern United States. Journal of
861 Sedimentary Research, 63(3), pp.513-522.

862 Rashid, F., Glover, P.W.J., Lorinczi, P., Collier, R. and Lawrence, J., 2015. Porosity and permeability
863 of tight carbonate reservoir rocks in the north of Iraq. Journal of Petroleum Science and
864 Engineering, 133, pp.147-161.

865 Ronchi, P., Giulio, A.D., Ceriani, A. and Scotti, P., 2010. Contrasting fluid events giving rise to
866 apparently similar diagenetic products; late-stage dolomite cements from the Southern Alps and central
867 Apennines, Italy. Geological Society, London, Special Publications, 329(1), pp.397-413.

868 Rustichelli, A., Tondi, E., Agosta, F., Cilona, A. and Giorgioni, M., 2012. Development and
869 distribution of bed-parallel compaction bands and pressure solution seams in carbonates (Bolognano
870 Formation, Majella Mountain, Italy). Journal of Structural Geology, 37, pp.181-199.

871 Rustichelli, A., Tondi, E., Korneva, I., Baud, P., Vinciguerra, S., Agosta, F., Reuschlé, T. and Janiseck,
872 J.M., 2015. Bedding-parallel stylolites in shallow-water limestone successions of the Apulian
873 Carbonate Platform (central-southern Italy). Italian Journal of Geosciences, 134(3), pp.513-534.

874 Sadooni, F.N. and Alsharhan, A.S., 2004. Stratigraphy, lithofacies distribution, and petroleum
875 potential of the Triassic strata of the northern Arabian plate. AAPG bulletin, 88(4), pp.515-538.

876 Sanderson, D.J. and Nixon, C.W., 2015. The use of topology in fracture network
877 characterization. Journal of Structural Geology, 72, pp.55-66.

878 Scholle, P.A. and Ulmer-Scholle, D.S., 2003. A color guide to the petrography of carbonate rocks:
879 grains, textures, porosity, diagenesis, AAPG Memoir 77 (Vol. 77). AAPG.

880 Schultz, R.A., Fossen, H., 2008. Terminology for structural discontinuities. AAPG (American
881 Association Petroleum Geology) Bull. 92, 15.

Simpson, J., 1985. Stylolite-controlled layering in an homogeneous limestone: pseudo-bedding produced by burial diagenesis. Sedimentology, 32(4), pp.495-505.

Szabo, F. and Kheradpir, A., 1978. Permian and Triassic stratigraphy, Zagros basin, south-west Iran. Journal of Petroleum Geology, 1(2), pp.57-82.

Toussaint, R., Aharonov, E., Koehn, D., Gratier, J.P., Ebner, M., Baud, P., Rolland, A. and Renard, F., 2018. Stylolites: A review. Journal of Structural Geology, 114, pp.163-195.

Tucker, M.E. and Wright, V.P., 2009. Carbonate sedimentology. John Wiley & Sons.

Vandeginste, V. and John, C.M., 2013. Diagenetic implications of stylolitization in pelagic carbonates, Canterbury Basin, offshore New Zealand. Journal of Sedimentary Research, 83(3), pp.226-240.

Wanless, H.R., 1979. Limestone response to stress; pressure solution and dolomitization. Journal of Sedimentary Research, 49(2), pp.437-462.

Zeeb, C., Gomez-Rivas, E., Bons, P.D. and Blum, P., 2013. Evaluation of sampling methods for fracture network characterization using outcrops. AAPG bulletin, 97(9), pp.1545-1566.

Palacký University
Olomouc

Palacky University Olomouc

Faculty of Science

Department of Geology

Study programme: Geological Sciences (P0532D330004)

Sequence Stratigraphic Framework and Hydrocarbon Potential of Stylolite Distribution in Upper Cretaceous Kometan Formation, Western Zagros, Iraqi Kurdistan

Doctoral Dissertation Summary

Hussein Suad Hussein M.Sc.

Supervisor: prof. Mgr. Ondřej Bábek, Dr.

Consultant: Dr. Howri Mansurbeg

Olomouc 2024

Abstract

Surface analogues are suitable tools to link reservoir models to real facies, but they require a robust outcrop-to-subsurface correlation. This Dissertation thesis aims to characterize reservoir quality by statistically predicting electrofacies, fracture identification, statistically analyzing stylolite morphology and network distribution, and linking the reservoir to sequence stratigraphy from different Oil Fields in the Upper Cretaceous Kometan Formation, a prolific carbonate reservoir of northern Iraq. Conventional well logs (caliper, gamma ray, neutron, density, and sonic), along with geochemical data, were used in this study. Laboratory spectral gamma-ray measurements were also conducted. A multivariate regression approach was used to analyze electrofacies. Various interpretations, including porosity analysis and fracture identification, were employed. Field sampling quantified stylolite networks, and thin sections with scanning electron microscopy were used for pore estimation. The correlation was done between well logs and geochemical data from surface analogues. The results indicate that the Kometan Formation predominantly comprises limestone, marl, marly limestone, and argillaceous limestone. A statistically significant correlation (R^2 = 0.83–0.85) between described and predicted lithology was established. The model with a higher coefficient of determination (0.85) was tested for further predictions in other wells. Six microfacies composed of mudstones to packstone with planktonic, and benthic foraminifers were identified in the outcrop, and interpreted as middle ramp, outer ramp, and basin deposits. The K+Al logs are correlated for 33 km, and the subsurface GR logs for over 100 km distance, but both reflect detrital admixture in biogenic carbonate. However, the outcrop- and subsurface log patterns show opposite vertical trends across the lower, middle, and upper parts of the formation. Such opposite log trends are interpreted as jointly reflecting landward and seaward shifts of the middle ramp carbonate factory within the mixed carbonate–siliciclastic system during transgressions and regressions, respectively. The inner ramp GR maxima and minima, and the outer ramp K+Al minima and maxima, are interpreted as maximum regression surfaces (mrs) and maximum flooding surfaces (mfs), respectively, in the T-R sequence-stratigraphic model. Neutron-density and sonic logs indicate that the best reservoir quality is achieved in fractured pure carbonates, which are controlled by these T-R cycles. Good secondary porosity has been Identified from the Secondary Porosity Index (SPI), which has reached a maximum value of 17%, and the average is 4% for Kz40. The maximum value is 30%, and the average is 8% for K216. In facies primarily composed of grain-supported packstone with moderate sorting, where grains are dispersed within a finer matrix, predominant stylolites typically exhibit weak connectivity and considerable vertical spacing. Conversely, mud-supported facies, marked by poor sorting and heterogeneity, display well-developed intersection stylolite networks. Stylolites in mud-supported facies demonstrate closer spacing, heightened amplitudes, and intensified junctions, with prevalent morphologies of the suture and sharp-peak varieties. Notably, this study unveils that stylolite significantly enhances porosity and permeability in the studied formation. Dissolution of minerals along stylolite seams forms intricate networks of channels and conduits. The results highlight the importance of the outcrop-to-subsurface correlation of well log data and elemental geochemistry in stratigraphic correlation and reservoir quality.

Keywords: sequence stratigraphy, stylolite, fracture, well logs, element geochemistry, Kometan Formation

Table of Contents

1. Introduction

1.1. Lithological Controls on Carbonate Reservoir Properties

The lithology of carbonate succession controls porosity and permeability heterogeneity. Thus, understanding spatial and vertical lithological differences is essential for characterizing petrophysical and mechanical properties of carbonate reservoirs (Li et al., 2006; Sun et al., 2018; Wang et al., 2018; Al-Dujaili et al., 2021). Rock density, strength, and hydraulic fracturing depend on lithology (Vipulanandan and Mohammed, 2018; Mohammed, 2019; Mahmood et al., 2020). The core description is the easiest approach to determine lithology, but it takes time and is limited to well intervals (Chang et al., 2000; Li et al., 2006; Mahmoodi et al., 2016; Tian et al., 2016; Zhang et al., 2017). Thus, lithology identification requires well log analysis. Well logging methods were used to study subsurface reservoir lithology, petrophysics, and facies interpretation (Killeen, 1997; Chang et al., 2000; Sfidari et al., 2014; Abdelmaksoud and Radwan, 2022; Abdullah et al., 2022). Bar graphs and bivariate statistical analysis have been widely used to determine lithology from well log data (Guiwen et al., 2015). Qualitative techniques can benefit from geologists' knowledge but have disadvantages such ambiguity, excessive work, ineffectiveness, and geologist-introduced artifacts (Li et al., 2006; Zhang et al., 2017). Recently, computer methods have been used to estimate lithology from well log data. In logging-based lithology categorization, the ANN is commonly used as an unpredictable automated estimator. Supervised (Baldwin, et al., 1989; Rogers, et al., 1992), unsupervised (Kohonen, 1982; Ripley, 2007; Chang et al., 2000), and adaptive resonance theory (Doveton, 1994; Chang et al., 2000) have been used to predict lithology. Backpropagation neural networks and Kohonen self-organizing maps are supervised and unsupervised ANNs. Studies examined clustering theory in lithology recognition (Sfidari et al., 2014). Various clustering studies predicted lithology (Tian et al., 2016; Pabakhsh et al., 2012; Nouri-Taleghani et al., 2015). Computerized well log evaluation has lately used random forest (Cracknell and Reading, 2014; Harris and Grunsky, 2015), support vector machine (Elkatatny and Mahmoud, 2018), deep recurrent neural networks (Wu et al., 2018), and deep convolutional neural networks (Imamverdiyev and Sukhostat, 2019). In the preceding methods, the lithology is established only by examining several log readings at the relevant depth, without considering the combined lithologies' geological properties. The response properties of log curves of different lithologies are difficult to distinguish, especially close to the transition surface, and no mathematical solution can adequately integrate log data to create an accurate underground lithology pattern (Li et al., 2006; Mahmoodi et al., 2016). Accordingly, the results may disagree with accepted geologic principles.

1.2. Carbonate Reservoir Modeling and Sequence Stratigraphy

Outcrop analogues can aid subsurface reservoir modeling. Outcrops allow direct study of facies, stacking patterns, diagenesis, and petrophysical properties, unlike exploratory wells. Even though outcrop research has several benefits, the lack of quantitative logging procedures makes subsurface correlation challenging. Facies stacking patterns and diagenetic traits inherited from sea-level variations during deposition are often linked to reservoir attributes (Westphal et al., 2004; Ehrenberg et al., 2006; Stadtműller, 2019; Zhang et al., 2024). Transgressive and regressive cycles may be linked to the primary and secondary porosity of carbonate

rock (Morad et al., 2000; Flügel, 2004). Cementation during regression fills significant inter- or intra-particle pores, reducing primary porosity (Read and Horbury, 1993; Tucker, 1993; Flügel, 2004). Sea-level variations affect diagenesis and secondary porosity (Morad et al., 2012). Porosity chemistry differs in near-surface water, hypersaline, brackish, and meteoric depositional situations. At the sediment/water contact, sea-level changes can modify the pore water chemistry in carbonate sediments (Morad et al., 2012). Transgressive/regressive cycles also determine diagenetic process duration and modulation magnitude. Slow sedimentation during transgression exposes sediments to marine pore water diagenesis, while high sedimentation during regression leads to widespread meteoric diagenesis (Morad et al., 2012). Changing sea levels affect organic matter amount and type (Cross, 1988; Whalen et al., 2000). Biochemically generated methane exhalation impacts carbonate matrix dissolution (Flügel, 2004). In sequence stratigraphy, primary and secondary diagenetic porosity are controlled (Tucker and Wright, 1990; Posamentier and Allen, 1999). North Iraq's Upper Cretaceous Kometan Formation carbonate rocks provide gas in the Jambur oil field and oil in the Kirkuk structure's Avanah and Baba Domes and Bai Hassan field. Recoverable reserves of 700–750 million barrels and production rates of 200,000–250,000 barrels per day are predicted for the fractured Kometan Formation, which produces light oil (41 API). The Kometan Formation's sedimentology, stratigraphy, paleontology, and structure have been examined by various investigators. Stylollites, chert nodules, and high secondary porosity characterize the Kometan Formation's foraminiferal oligostiginid wackestone to grainstone. It was deposited in an open marine, low energy, middle to outer ramp depositional context partly governed by shallow-water eroded components. Deep burial diagenesis created stylolite and chert nodules, according to Al-Barzinjy (2008). The formation contains transgressive and highstand systems tracts of a complete third-order sequence separated by type-2 sequence boundaries (Haddad and Amin, 2007; Balaky et al., 2016).

Rashid et al. (2015a, 2015b, 2017) examined the surface and subsurface porosity, permeability, and reservoir quality of the Kometan Formation. Although outcrop investigations reveal the Kometan Formation's depositional contexts, sequence stratigraphy, and diagenetic history, its underground production potential is unknown. To turn well-log lithology data into genetic packages for assessing delicate stratigraphic reservoirs, reservoir basin analysis must use sequence stratigraphy. This approach correlates well lithostratigraphy (Omigie and Alaminiokuma, 2020). However, quantitative procedures in reservoir outcrop analogues and subsurface well log correlation are difficult. Gamma-ray spectrometry can link petrophysical characteristics to facies (Rider, 1999) and enable quantitative sequence-stratigraphic interpretations in outcrop studies (Bábek et al., 2018). One more fast, cheap method for quantifying stratigraphic correlation in outcrop is X-ray fluorescence spectroscopy (XRF) of powdered samples. It can detect changes in lithology and paleoenvironmental conditions in carbonates. Although sediment geochemistry is seldom used in hydrocarbon exploration and production, it is hypothesized here that outcrop geochemistry and subsurface lithology well logs can be mutually correlated and the XRF technique provides a quantitative link between reservoirs and their outcrop analogues.

1.3. Stylolites and Fractures in Carbonate Reservoirs

Subsurface reservoir features of carbonate rocks are difficult to predict due to depositional rock textural variability and post-depositional diagenetic overprints. Petrophysical characteristics and carbonate textures fluctuate vertically, laterally, and over time along diagenetic pathways. Therefore, reservoir quality, especially permeability, is hard to assess. In otherwise homogenous carbonate rocks, stylolites are common diagenetic characteristics (Bathurst et al., 1991). Pressure dissolution can form thin, undulating tooth-like stylolites with concentrated insoluble residue parallel to bedding planes. Stylolites may exaggerate the original bedding planes defined by changes in lithology, or even form new, so-called pseudo-bedding surfaces, which do not coincide with original bedding, and which separate units of the same lithology (Simpson, 1985). Targeted contractional strain affected stylolite orientation (Fletcher and Pollard, 1981; Schultz and Fossen, 2008). According to Groshong (1975), stylolite peaks align with the highest primary stress ($\sigma 1$). Slickolites have skewed stylolite planes when they move (Gratier et al., 2005). Normal sedimentary stylolites are parallel to bedding and perpendicular to burial stress. Pressure-dissolution at grain and crystal interfaces nucleates and grows stylolites. The chemical dissolution of rock-forming minerals and localized physical stress-induced grain compaction at a fluid-filled interface occur. Because it provides the solubility contrast needed to generate stylolite surfaces, rock mineralogical heterogeneity governs this process. On localized less-soluble heterogeneous material, the "proto-stylolite plane" becomes sharp and roughens (Koehn et al., 2012). Stylolites have been shown to affect fluid flow and petrophysical parameters in several research (Paganoni et al., 2016; Martín-Martín et al., 2018; Heap et al., 2018; Toussaint et al., 2018; Bruna et al., 2019; Humphrey et al., 2019; Gomez-Rivas et al., 2022). Even though stylolite shaves are prevalent in carbonate rocks, they attracted less attention than fracture networks. Stylolite morphology and orientation can determine compressive stress distribution, amplitude, and orientation in a region (Koehn et al., 2012). Amplitude, wavelength, spacing, and connectivity combine to create a variety of stylolite network designs. Stylolite networks' effects on fluid flow have largely been studied due to their diverse fluid behavior. Based on field and microscopy observations, stylolites and their networks may act as fluid flow barriers (Burgess and Peter, 1985; Finkel and Wilkinson, 1990; Alsharhan and Sadd, 2000; Martín-Martín et al., 2018; Gomez-Rivas et al., 2022). Stylolites may increase permeability parallel to their planes, like in carbonate reservoirs and outcrops (Carozzi and Bergen 1987; Bergen and Carozzi, 1990; Lind et al., 1994; Harris, 2006; Chandra et al., 2015; Barnett et al., 2018; Paganoni et al., 2016; Martín-Martín et al., 2018; Morad et al., 2018; Gomez-Rivas et al., 2022). Preferred dissolving along stylolite planes leads to limited porosity around stylolites (Bergen and Carozzi, 1990) and larger pore throats (Baud et al., 2016). Despite various research on stylolites' significance in local fluid flow, little is known about how depositional facies and carbonate rock components affect stylolite morphology, type, and growth. There is also growing interest in how host rock variety impacts stylolite shape, distribution, and size (Toussaint et al., 2018; Morad et al., 2018; Humphrey et al., 2020). While these authors recognized lithology as the key factor for stylolitization, Koehn et al. (2016) stressed the importance of lithological controls interacting to create stylolite. Fluids' role in stylolite production and evolution is also unclear. Petroleum emplacement could prevent stylolitization (Neilson et al., 1998; Morad, 2018). Many hydrocarbon-bearing limestones include broad lateral stylolite networks that compartmentalize reservoirs and

modify fluid movability (Hassan and Wada, 1981; Ehrenberg et al., 2016). The discontinuous shape of stylolites only affects petrophysical properties locally, according to Heap et al. (2014). Stylolites can also cause permeability heterogeneities, where permeability increases throughout the surface, according to Heap et al. (2018). Numerous studies have examined stylolites in carbonate rocks (Koehn et al. 2007; Ebner et al. 2010; Paganoni et al., 2016; Martín-Martín et al., 2018; Heap et al., 2018; Toussaint et al., 2018; Bruna et al., 2019; Humphrey et al., 2020; Gomez-Rivas et al., 2022), as well as sandstones (Baron and Parnell, 2007; Nenna and Aydin, 2011), and evaporites (Bauerle et al., 2000). There is a lack of studies on the formation of stylolites in carbonates with a mixed carbonate/silica composition, which are quite common in carbonate reservoirs and in which the silica enrichment results from accumulation and diagenesis of siliceous organisms (diatoms, radiolarians, sponge spicules).

Carbonate reservoirs are fractured and complex due to varied depositional textures and diagenetic effects throughout a wide part of Northern Iraq's geology, making reservoir quality evaluation difficult. Natural fractures cause carbonate rocks' complexity and heterogeneity. Fractures improve reservoir quality, fluid movability, and production (Roehl and Choduette, 1985). Fractures can be identified directly from core samples and indirectly from seismic sections, well logs, well tests, and drilling mud losses (Thompson, 2000; Nelson, 2001; Martinez-Torres, 2002; Dutta et al., 2007). The most qualified fracture identification methods are the Borehole Acoustic Televiewer, Formation Micro scanner (FMS), Formation Micro-Imager (FMI), and Electric Micro Imaging (EMI), however, they are pricey and only provide images at defined intervals. On the other hand, the Conventional well log tools can be evaluated without limitations. In addition, open and fluid-filled fractures are also sensitive to conventional logging approaches (Laongsakul and Durrast, 2011). Fractures increase permeability in carbonate reservoirs, especially low-pore Carbonates, hence fracture networks must be identified.

This study proposes an innovative approach to predict lithology in carbonate rocks from the Kometan Formation, Northern Iraq, integrating well log data with geological information. Simultaneously, we investigate the correlation between sequence stratigraphy and reservoir properties in ramp carbonates of the same formation, analyzing both outcrop and subsurface data. Additionally, we explore the relationship between stylolites and microfacies within the formation, aiming to quantify their impact on reservoir characteristics. Furthermore, we demonstrate the capability of conventional well logging tools to identify fractures and detect fracture zones in the Kometan Formation, enhancing understanding of reservoir quality and distribution.

2. Geological Background

The type locality of the Kometan Formation (upper Turonian to lower Campanian) is located in the Kometan Village, north-east of the town of Ranya near the city of Sulaimani, the Kurdistan region of Iraq (Fig. 1) (Van Bellen et al., 1959; Dunnington, 2005). The type locality exposes thin-bedded, white to light grey globigerinid–oligosteginid limestone containing locally abundant chert nodules, especially near the base of the section, and occasional glauconite-rich layers. The Kometan Formation was observed in many outcrop sections and in the subsurface of the Imbricated Zone, High Folded Zone, and Low Folded Zone of the Zagros Foreland Basin,

Kurdistan Region, Iraq; its thickness ranges from 63 to 185 m (Aqrawi et al., 2010). In different parts of the basin, the Kometan Formation rests either conformably or unconformably on the oligosteginid limestone facies of the Balambo Formation and limestones and dolomites of the Dokan, Gulneri, and Qamchuqa Formations of Early Cretaceous to Coniacian ages (Fig. 2) (Buday, 1980; Kaddouri, 1982; Jassim and Goff, 2006; Al-Qayim, 2010). The Kometan Formation is either conformably or unconformably overlain by the Shiranish Formation and Tanjero Formation of Campanian to Maastrichtian age (Buday, 1980; Jassim and Goff, 2006). A distinct, glauconite-rich layer at the base of the Shiranish Formation can be used as a lithostratigraphic marker bed (van Bellen et al., 1959; Dunnington, 2005). Field observations suggest that in places the basal and top boundaries of the Kometan Formation are cut off by post-depositional (early Miocene to Pliocene) faults accompanying the anticlinal structures of the north-western Zagros in the Kurdistan region (cf., László et al., 2012). A variety of fine-grained carbonate lithologies of the Kometan Formation were deposited in shallow marine shelf, restricted settings (oligosteginid facies), and open marine settings (globigerinid facies) (Buday, 1980; Abawi and Mahmood, 2005; Jassim and Goff, 2006). Towards the west and southwest of Iraq, the globigerinid and oligosteginid facies laterally pass into more argillaceous facies and marls fully corresponding to the oligosteginid biofacies (van Bellen et al., 1959; Dunnington, 2005). The Kometan Formation of the Imbricated, High Folded, and Low Folded Zones passes laterally into bioturbated chalky limestone, shale and marly limestone of the Khasib Formation, lagoonal shale, and carbonate of the Tanuma Formation, and open shelf globigerinid limestone of the Sa'di Formation in the Mesopotamian Zone and the Stable Platform of central Iraq and south Iraq (Figs. 1, 2) (Aqrawi, 1996; Al-Qayim, 2010).

3. Methods

The well-log dataset comprises gamma ray, caliper, sonic, density, and neutron logs from nine wells (J-37, BR-1, BH-13, Kz-13, Kz-29, Kz-40, K-216, and K-218, K-243 wells) from the Khabbaz, Kirkuk, Jambur, Bai Hasan, and Barda Rash oil fields (Fig.1), provided by the North Oil Company, Iraq. The Get Data Digitizer 2.2 was used to digitize the analog logs with 0.2 m reading interval.

The gamma-ray log used as indicator of formation shaliness, or the volume of shale (Oberto, 1984). The first step in the calculation of the shale volume was the gamma-ray index (I_{GR}), which was calculated using equation (1):

$$I_{GR} = (GR_{log} - GR_{min}) / (GR_{max} - GR_{min}) \quad (1)$$

The gamma-ray index is denoted by I_{GR}, the gamma-ray reading from the log is denoted by GR_{log}, the clean zone gamma-ray reading is denoted by GR_{min}, and the maximum gamma-ray reading from the log is denoted by GR_{max} (shale zone). The following equation was used to determine the shale volumes (Vsh), as proposed by Larionov (Oberto, 1984) (Eq. 2):

$$Vsh = 0.33[2^{2*IGR} - 1.0] \quad (2)$$

Input parameters for multivariate regression included ρb, Δt, and neutron porosity values from digitized logs are used to predict lithology. Multivariate regression combines independent factors to predict dependent values (Mohaghegh et al., 1997). Multivariate linear regression analyses connect several variable predictors (X-variables) to a single response variable (Y-vector). Linear regression between well log response (X-variables) and formation rock lithology (Y-vector) is used in this method. Fig. 3 shows the general methodology: Using rock sample lithology and regression analysis with well logs (ρb, Δt, and neutron) can achieve linear best-fit parameters for lithology prediction. For regression analysis to a continuous lithology log of the examined formation in the same and other wells in the same drilling environment, the coefficient of determination (R^2) between lithology from rock samples and well log readings should be 0.8 or better. This study's multivariate regression used lithology codification and fuzzy logic (Eq. 3).

If $X < P \leq Y$, then S (3)

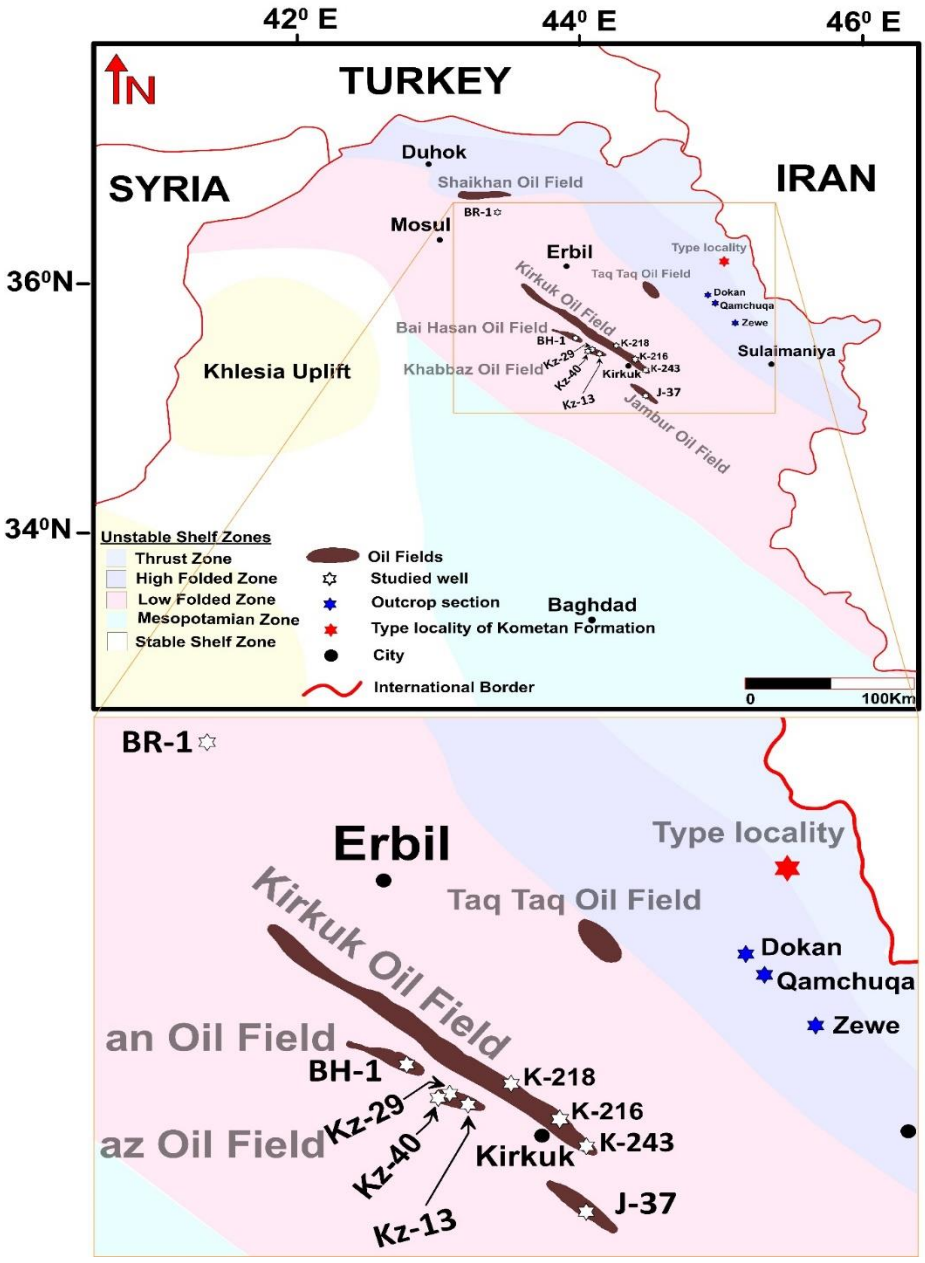

Fig. 1. Location, and tectonic subdivisions of the study area (Adopted from Hussein et al., 2024).

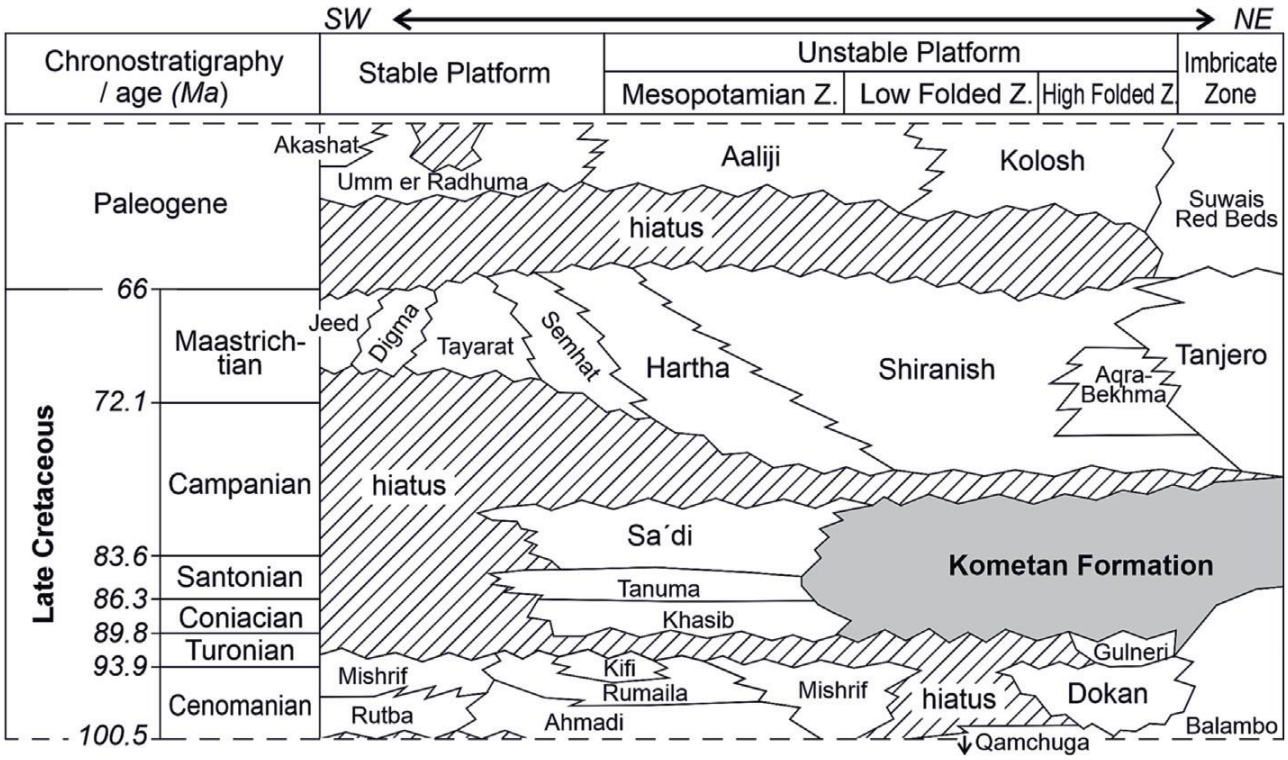

Fig. 2. Chronostratigraphic division of Upper Cretaceous lithostratigraphic units in NE Iraq. (Adopted from Hussein et al., 2024).

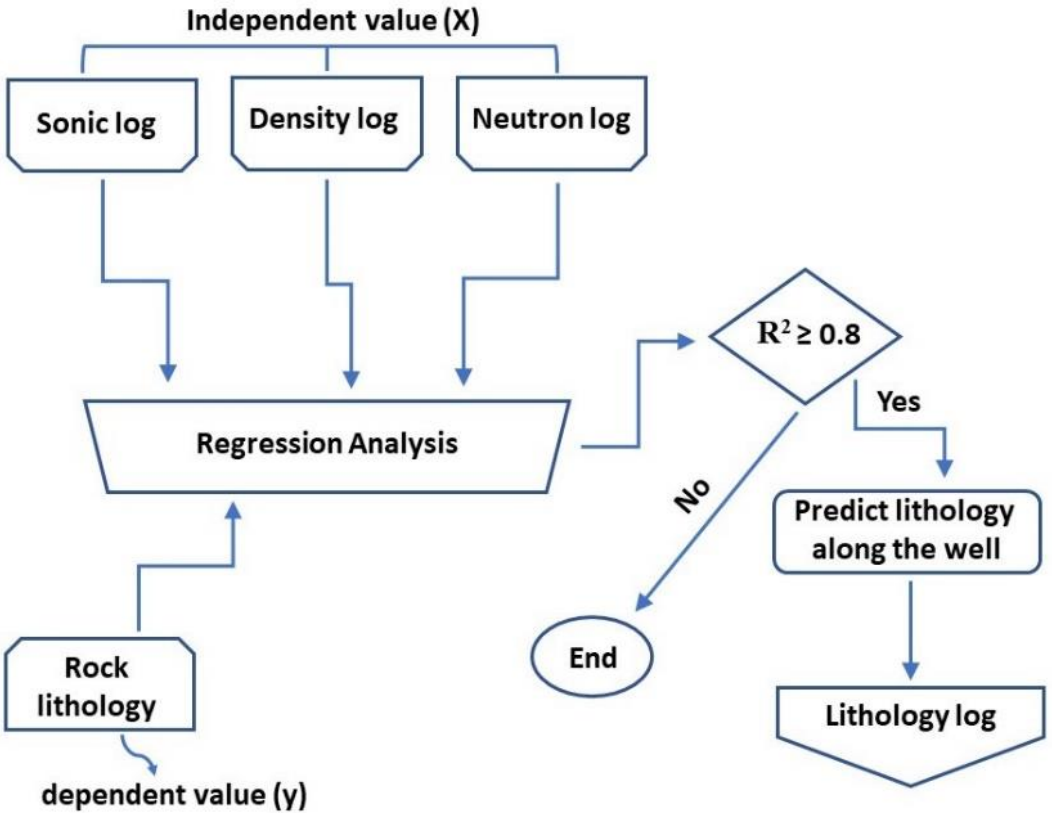

Fig. 3. Proposed quantitative methodology workflow for predicting lithology (Adopted from Hussein et al., 2024).

Porosity cross-plot has been used to identify the fracture zones. Neutron, density, sonic, caliper, and total gamma-ray logs have been used qualitatively to detect fractures. total porosity (neutron-density combination) with sonic porosity can be proposed for the identification of secondary porosity (Eq.4) (Rider, 1999; Lyon, 2010).

$$SPI = \Phi_{total} - \Phi_{sonic} \quad (4)$$

Where:

SPI: Secondary Porosity Index

Φ_{total}: Total Porosity ((Neutron Porosity + Density Porosity) / 2)

Φ_{sonic}: Sonic porosity

Three outcrop sections of the Kometan Formation, Zewe (96 m thick) (35.73535° N, 45.2371° E), Qamchuqa (63 m) (35.897196° N, 45.01338° E), and Dokan (65 m) (35.944634° N, 44.983866° E) (Fig.1) were sampled and documented using bed-by-bed descriptions of bed thickness, bed geometry, sedimentary structures, and grain size using the approach summarized by Graham (1988). The outcrop sampling was conducted for thin section analysis. A qualitative microfacies analysis following the principles summarized in Scholle and Ulmer-Scholle (2003) and Flügel (2004) was carried out on a total of 50 thin sections using the Dunham classification scheme (Dunham, 1962).

Following Humphrey et al. (2020), the abundance, and various size and morphology parameters of the stylolites and their networks were measured in the field using 1m x 1m sized sampling frames, which were placed next to each other bottom side parallel with the bedding to minimize the effects of stratigraphic variation. The framed outcrop sections were marked, photographed, and rectified to maintain a uniform scale and vertical-to-horizontal aspect. To minimize the effects of vegetation and noise from the background, line drawings of all stylolites present were made from each scaled frame picture. The stylolite spacing, amplitudes, wavelengths, intersection angles, and types of interaction were measured from the scaled pictures (Fig. 4). Three vertical lines (dashed lines, Fig. 4A) with a lateral offset of 50 cm were drawn in each frame picture perpendicular to the stylolites, to measure the stylolite spacing. The perpendicular spacing values taken from every line were added up for each frame, and the heights between stylolite crossing were documented (Fig. 4B). Thus, the biggest vertical stylolite spacing that can be measured is one meter, but in all frames, the spacing was lower than one meter. The central vertical line in each sampling frame was used to record the stylolite wavelength and amplitude. We recorded every stylolite that crossed the measuring line. The wavelength was measured as a horizontal separation between the nearest two positive peaks located along the measuring line (Fig. 4C), whereas amplitudes were measured as a vertical distance between positive and negative stylolite peaks located nearest to the scanline (Fig. 4D). Selecting the nearest amplitude observations to the measuring line minimized the effects of inclination. The junction angles were calculated between the two intersecting lines (Fig. 4E).

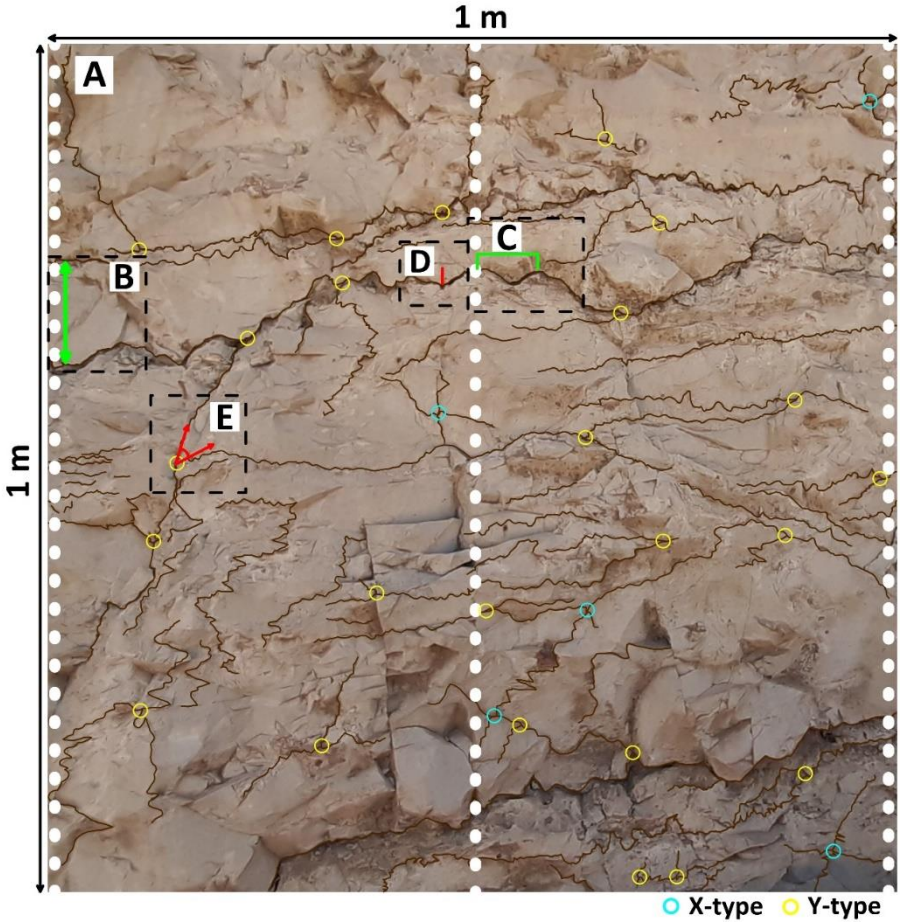

Fig. 4. Example frame size and positions of three scanlines (A) used for recording stylolite spaces (B), wavelength (C) (middle scanline), amplitude (D) (middle scanline), junction angle (E), and labeled image identifying the X-type (Cyan) or Y-type (yellow)of stylolite junction.

Stylolite spacing, wavelength, and amplitude were measured and graphically represented using Past 4.04 software. stylolite data was fitted with log-normal distributions. The Kolmogorov-Smirnov (KS) normality testing and chi-squared tests were employed to determine the goodness of fit (Massey, 1951). The null hypothesis for KS test was p-value < 0.05. Using stylolite length, junction forms were calculated. The stylolite junction intensity per meter (m) for each frame was calculated. To calculate microfacies ratios (Eq. 5), this was averaged:

$$JI\ (/m) = (Jt\ /\ (SLt) \quad (5)$$

where JI (/m) is the junction intensity per meter, Jt is the total amount of junctions in the sample frame, and SLt is the total stylolite length per frame.

Use optical microscope images to identify and measure porosity in thin sections impregnated with blue-dyed epoxy resins. Textural analysis was done with a scanning electron microscope (SEM QUANTA 200 FEI with an EDS detector). The grain area of a thin piece was quantified using ImageJ. Folk and Ward (1957) formulae determined Mean grain size (Mz) and standard deviation or sorting from grain.

Measured element concentrations in 246 powdered rock samples from three outcrop sections and 28 samples from four wells using a Delta Premium EDXRF (Energy Dispersive X-Ray Fluorescence) spectrometer (Innov-X, U.S.A.) with a large-area silicon-drift detector. The acquisition time was 2 × 120 s at 15 kV and 40 kV accelerating voltages. The samples were pulverized to analytical fineness and stored in Mylar-sealed plastic cells before EDXRF analysis. In each sample, Al, Si, P, S, K, Ca, Ti, Mn, Fe, Ni, Cu, Zn, As, Rb, Sr, Zr, Mo, Pb, and Th concentrations were measured. Calibrated EDXRF concentrations with ICPMS/OES data (Table S1, Appendix 6). We chose 76 geochemically similar limestones, marls, and shales from the Lower Devonian mixed carbonate–siliciclastic ramp system in the Prague Basin, Czechia (Bábek et al., 2021) for calibration. ICP-MS/OES and EDXRF were used, followed by a statistical correlation. Linear or polynomic regression techniques calibrated analysed EDXRF data for ICP-MS/OES. High regression coefficients ($R2 \geq 0.99$) were observed for Si, Al, Fe, Ca, K, Ti, Mn, Zr, Rb, and Zn, somewhat lower for As, Sr, and Pb, and much lower but acceptable for Cu, Ni, and Mo. Not calibrated: sulphur and phosphorus.

An RT-50 shielded laboratory spectrometer (Georadis, s.r.o., Czech Republic) with a 3 x 300" (350 cm^3) NaI (Tl) detector was used to study the gamma-ray spectra of 17 rock samples from the Kz-29 (7) and Kz-40 (10) wells. Based on calibrations utilizing calibration standards provided by the manufacturer, the instrument converted the counts per second from 512 energy windows to K (%), U (ppm), and Th (ppm) concentrations. The declared sensitivity was 0.7 ppm for Th, 0.4 ppm for U, and 0.12% for K. Each sample was ground into a powder, put in a 250 cm^3 plastic container, and measured for 30 minutes.

A Panalytical X'Pert PRO MPD diffractometer with reflection geometry, cobalt tube ($\lambda K\alpha = 0.17903$ nm), Fe filter, and X'Celerator 1-D RTMS detector (Masaryk University Brno, Czechia) was used to analyze the mineralogy of 16 powdered samples from outcrops and well-cuttings. Analytical setup includes step size: 0.033° 2Θ, 160 s per step, angular range: 4–100° 2Θ, and 3702 s total scan duration. Bruker AXS Diffrac + Topas 4 and Panalytical HighScore 4.8 plus processed XRD data. The Rietveld method quantified only crystalline phases in 8 samples.

4. Results

4.1. Lithological Aspect and Shale Content

4.1.1. Outcrop Lithology

In the outcrop sections especially the Qamchuqa and Zewe sections (Fig. 1), the upper boundary of the Kometan Formation is overlain by the marl and marly limestone of the Shiranish Formation, and the lower boundary is defined by the limestone and dolomitic limestone of the Qamchuqa Formation. In outcrop, the lithology of the Kometan Formation is very uniform, corresponding to thin-bedded to medium-bedded, very fine grained, bioturbated limestone and argillaceous limestone that ranges from light grey (lower part) to light brown (upper part) colour. The beds contain poorly identifiable trace fossils. Bed thickness usually ranges from ~15 cm to ~60 cm. The beds are separated by thin marly laminae, very often modified by stylolitization. In all measured sections, the carbonate is highly fractured and contains abundant stylolites which are often

very large having up to 4 cm amplitude. The limestones locally contain abundant chert nodules arranged parallel with the bedding planes, which are in places concentrated on the stylolites (Figs. 5, 6).

All samples from the Kometan Formation in the outcrop sections (Zewe, Qamchuqa, and Dokan) (Fig. 1) with low concentrations of Al (<1 wt%), Rb, Si, and K correspond to pure carbonates. In outcrop, the Kometan Formation can be roughly subdivided into a lower part, characterized by low K (~0.05 to 0.12 wt%) and Al (~0.1 to 0.4 wt%) concentrations, middle part featuring even little bit lower K (~0 to 0.1 wt%) and Al (~0.1 to 0.4 wt%) concentrations and relatively high Zr/Al ratios, and an upper part with relatively high K (~0.05 to 0.25 wt%) and Al (~0.2 to 0.8 wt%) concentrations and low Zr/Al ratios (Figs. 6, 7). The K, and Al concentrations show well constrained lows and highs, which can be correlated between the Zewe, Qamchuqa, and Dokan sections over the distance of 33 km parallel with the tectonic strike (Fig. 7).

The XRD analyses from 6 samples from the Qamchuqa and Zewe sections (Fig. S1, Appendix 5) show that the limestones contain abundant calcite (up to 96 %), quartz and chert (up to 12 %), clay minerals (illite, illite/smectite and smectite, up to 2 %) and trace amounts of K-feldspars and dolomite.

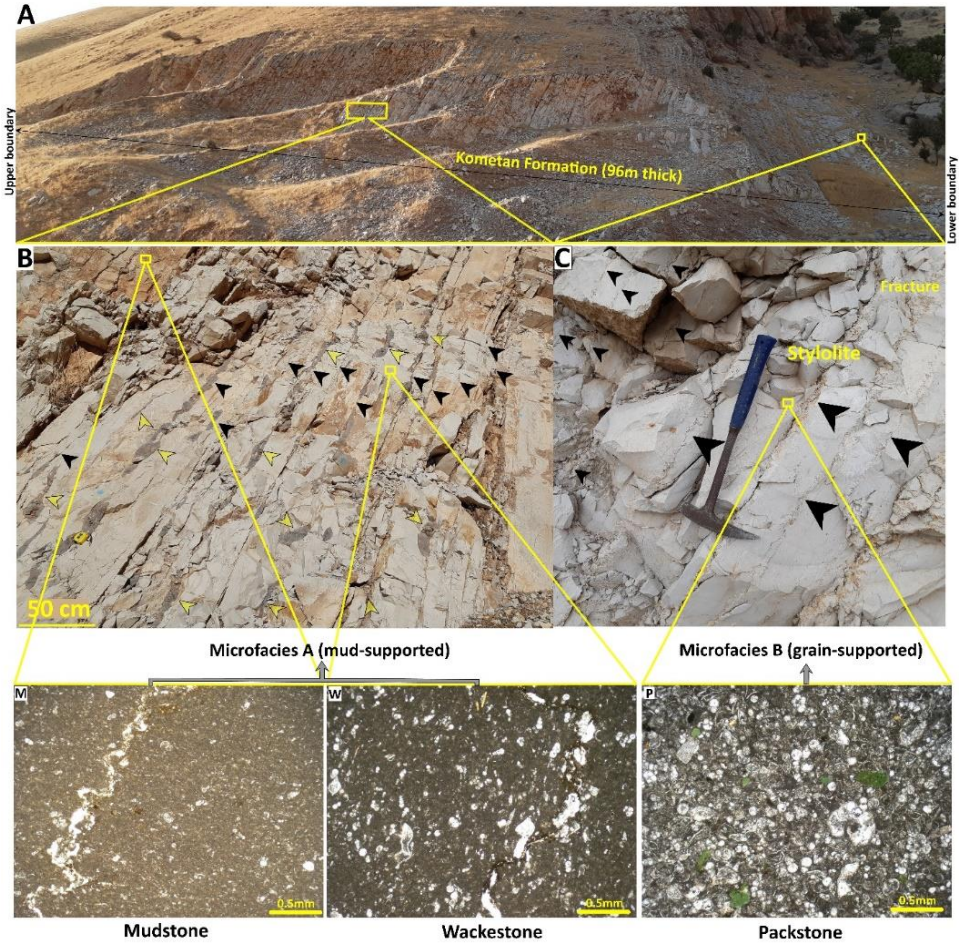

Fig. 5. Field photos of the studied formation in the Zewe section (A) and a close view of bed observations show chert nodules (yellow arrow) and stylolites (black arrow) (B, C). Photomicrographs showing the microfacies: M) planktonic foraminiferal mudstone W) planktonic foraminiferal wackestone, and P) planktonic foraminiferal packstone with glauconite (green particles).

4.1.2. Subsurface Lithology

For subsurface lithology, the description of the available rock samples (well cuttings) from the Kometan Formation could be subdivided into four lithologies: limestone, argillaceous limestone, marly limestone, and marl (Fig. 8). The well log intervals from 2870 to 2885 m in the Kz-29 well (Fig. 8) and 2786 to 2830 m in the Kz-40 well (Fig.4 in Appendix 1) were used as the anchor points (trained samples) in which each lithology was transformed into a code number used in the multivariate regression analysis. The codes ranged from 0.6 to 1.3 (Table 1).

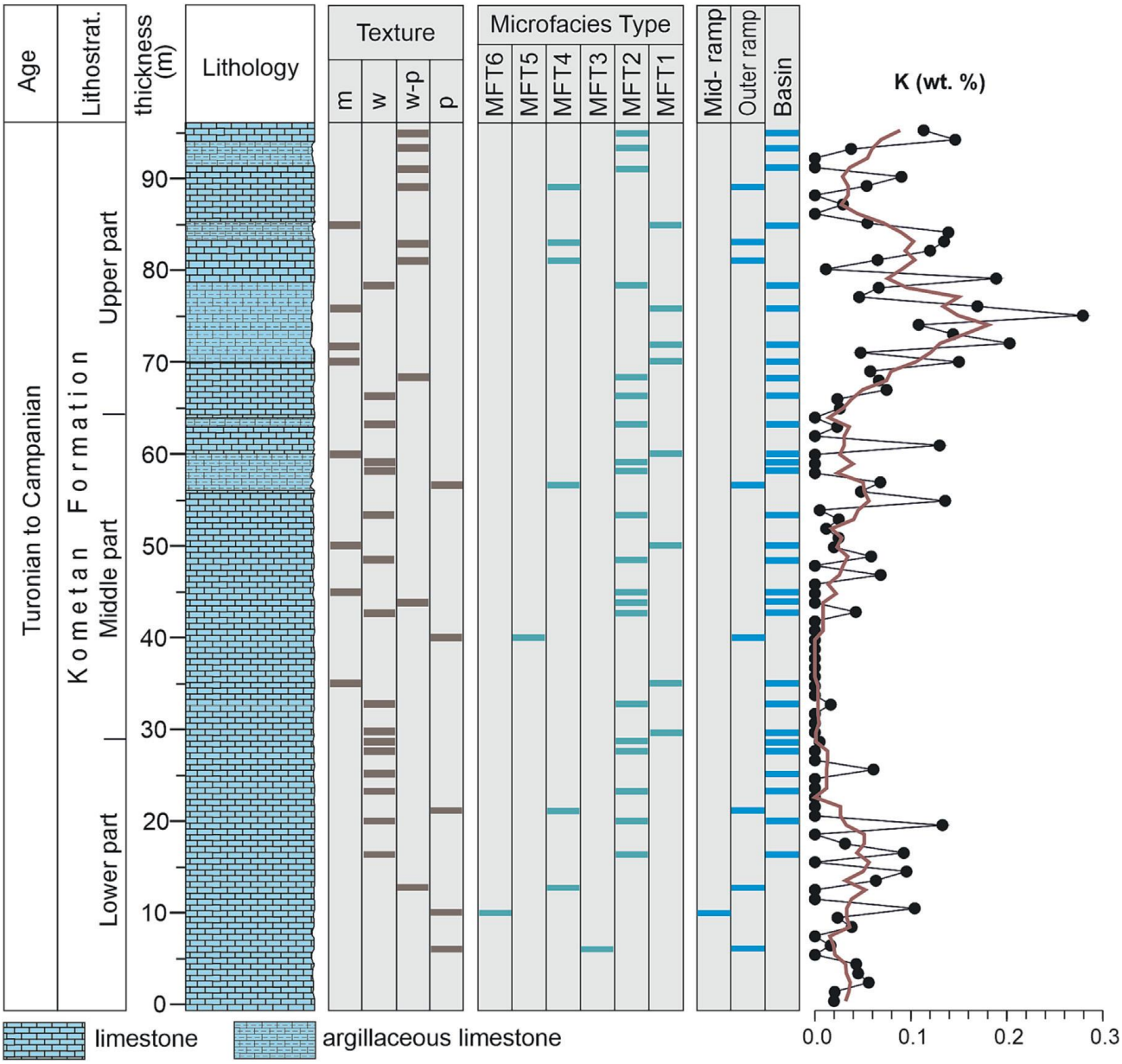

Fig. 6. Stratigraphic log showing lithology, distribution of microfacies, their corresponding depositional settings, and concentration of K (wt%; red line shows the 5-point running mean) in the Kometan Formation at the Zewe section (Adopted from Hussein et al., 2024).

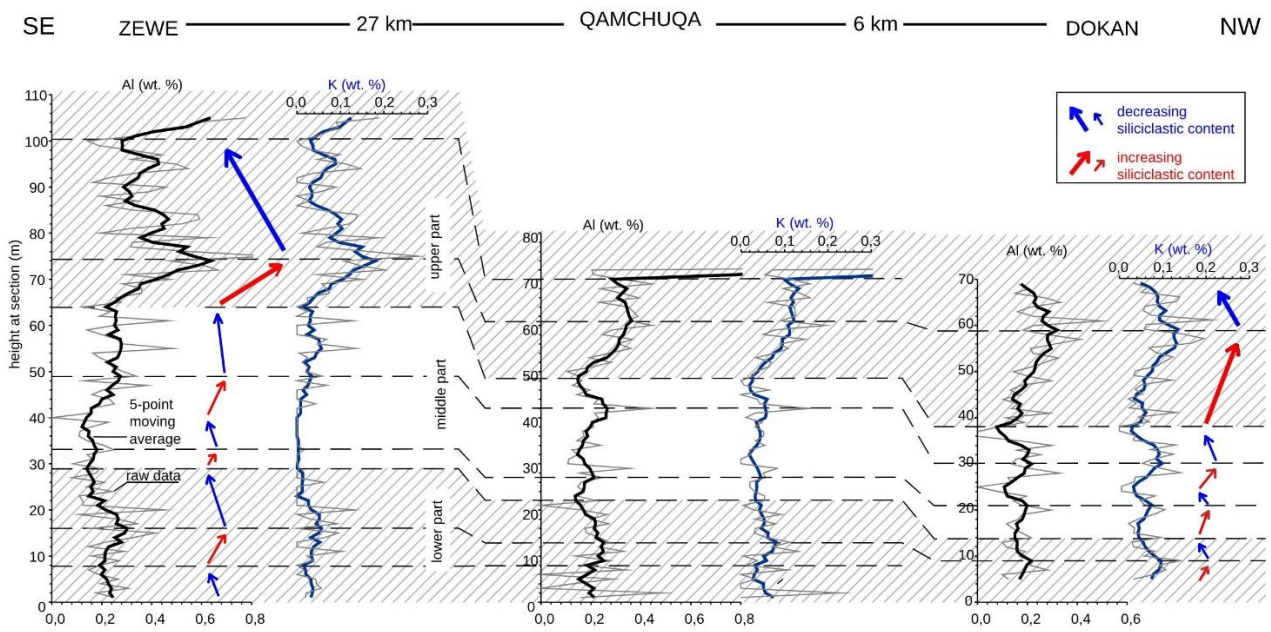

Fig. 7. Geochemical log correlation of the Al (wt%), and K (wt%) logs at the Zewe, Qamchuqa, and Dokan outcrop sections (Adopted from Hussein et al., 2024).

Table 1. Matrix and mineral density values for common types of rocks (Asquith et al., 2004; Derder and Geo, 2016), shale content ranges, and codification for the most common rocks.

Lithology	Density (g/cm^3)	Shale content (%)	Code Number
Anhydrite	2.98	0	1.3
Dolomite	2.87	0-5	1.2
Dolomitic limestone	2.79	0-5	1.1
Limestone	2.71	0-5	1.0
Argillaceous limestone	2.69	15-25	0.9
Marly limestone	2.67	25-35	0.8
Marl	2.66	35-65	0.7
Sandstone	2.65	0-5	0.6

The following equations were derived from the multivariate regressions of bulk density, interval transit time, and neutron porosity log data as independent values to identify the log lithology (dependent value) (Eqs. 6 and 7):

$$\text{Log (Lithology)} = (0.7 + 0.19 * \rho b - 0.0035 * \Delta t + 0.002 * \text{NPHI}) \quad (6)$$

$$\text{Log (Lithology)} = (0.7 + 0.06 * \rho b + 0.0033 * \Delta t - 0.012 * \text{NPHI}) \quad (7)$$

The equations 7 and 8 were generated and applied to the Kz-29 and Kz-40 wells, respectively. The resulting log lithologies varied from limestone to marly limestone in the Kz-29 well (Fig. 8), and from limestone to marl in the Kz-40 well (Fig. 4 in Appendix 1). Statistical correlations were made between the log lithologies and the rock lithologies (cores and cuttings) by using the coefficient of determination (Fig. 5A in Appendix 1), root

mean square error (RMSE), mean absolute error (MAE), and error bar (Fig. 5B in Appendix 1) to show model performance, as well as the error percentage line (Error%) to show the percentages of error between actual and predicted values (Fig. 8). A good match was obtained, with the coefficient of determination equalling 0.85 and 0.83 for the Kz-29 and Kz-40 wells, respectively (Fig.5A in Appendix 1). The values for MAE and RMSE for Kz-29 well are 0.00002 and 0.0007, and 0.000021 and 0.0007 for Kz-40, respectively.

The error bar graph (Fig.5 in Appendix 1) shows the average and standard deviation of each of the measured (rock lithology) and predicted (log lithology) values for the Kz-29 well and Kz-40 well. The graph showed that the models are well-performing and can be used to predict the lithology. However, there are some errors presented between the actual and predicted lithology in Fig. 8 (green-filled line). The average errors are 4 % and 8 % in the Kz-29 and Kz-40 wells, respectively.

Based on the average of the error percentage line, equation 7 (Fig. 8) provides a more accurate identification of all lithology classes during the performance validation of the multivariate system than Equation 8 (Fig.4 in Appendix 1). Finally, the models were applied to predict the log lithology for the entire thickness of the Kometan Formation in both wells and compared with the observed lithologies (Fig. 8).

The shale volumes determined from the gamma-ray log (Fig. 8) showed that the studied formation can be divided into three zones: 2802 to 2868 m, with shale volumes ranging from 5.4% to 18% (mean: 8.8%), 2868 to 2920 m, with volumes ranging from 3.7% to 23% (mean: 16%), and 2920 to 2948 m, with volumes from 3.7% to 21.5% (mean: 7.4%) in Kz-29 well. In Kz-40 well, these three intervals corresponded to depths of 2711 to 2792 m, 2792 to 2861 m, and 2862 to 2898 m, with mean shale volume values of 7% (from 4% to 11.4%), 12.6% (3.2% to 22%), and 8% (3.6% to 21.9%), respectively. In both wells, the middle "shaly" part contained more shale than the "clean" upper and lower parts (Fig. 8). Gamma rays computed and measured from the available rock samples (Fig. 8) validated this. A good correlation between the gamma-ray log and gamma-ray rock was represented by the correlation coefficients equalling 0.70 and 0.82 for wells Kz-29 and Kz-40 wells, respectively (Fig.6 in Appendix 1). The distribution of the elemental proxies shows a relationship with the principal lithologies. The limestone in the Kz-40 well (depth 2711 to 2790 m) has low Al concentrations (1.0 wt.%) and relatively high K/Al (0.4 to 0.6) and Ti/Al (0.08 to 0.12) ratios. On the other hand, marls and argillaceous limestone from the same well have distinctly higher Al concentrations (2.0 to 6.0 wt.%) and lower K/Al (0.2) and Ti/Al (0.06) ratios (Fig. 10B in Appendix 1). The Al concentrations correlated with the shale volumes as determined from the gamma-ray logs, and they could be considered an independent proxy of the shale contents in the Kometan Formation (Fig. 8). The concentrations of Al increased in the shaly intervals between 2868–2920 m and 2792–2861 m depths for the Kz-29 (Fig. 9A) and Kz-40 (Fig.10B in Appendix 1) wells, respectively, as demonstrated by the gamma-ray values, which contrasted with those of the overlying and underlying clean units (Fig. 8).

The derived model (Eq. 6) with a coefficient of determination (R^2) higher than 0.8 has been tested to predict the lithology for the Kometan Formation in other wells (Kirkuk 216 (K-216) and Kirkuk 218 (K-218)) (Fig.

1). The lithology estimated by the equation mainly consists of limestone and argillaceous limestone (Fig. 11 in Appendix 1). The thickness of the argillaceous limestone is higher in the K-216 well than in the K-218 well (Fig. 11 in Appendix 1), which is about 25m. The result could be accepted because the Kometan Formation mainly consists of limestone with a small thickness of marly or argillaceous limestone in different locations.

The XRD analyses from 10 subsurface samples (Fig. S1, Appendix 5) show that the rocks are composed of calcite (from 44 to 89 %), illite, illite/smectite and smectite (from 3 to 19 %), kaolinite (from 0 to 22 %), quartz (from 2 to 7 %), K-feldspars (up to 5 %), dolomite (up to 3 %), and minor (<2 %) proportion of siderite, pyrite, hematite, gypsum, anhydrite, baryte and anatase. They show a distinct vertical arrangement: the upper parts of Kometan Formation in Kz- 40 (2710 to 2790 m), Kz-29 (2780 to 2860 m) and K-216 (1440 to 1558 m) are composed of pure limestone and marly limestone; the middle parts in Kz-40 (2810 to 2850 m) and Kz-29 (2880 to 2940 m) are composed of marls, shale and marly limestone, and the lower parts in Kz-40 (2870 to 2888 m) and Kz-29 (2950 m) are composed of marly limestone and pure limestone. The siliciclastic lithologies are fine-grained but any other lithological observations cannot be obtained from the cuttings.

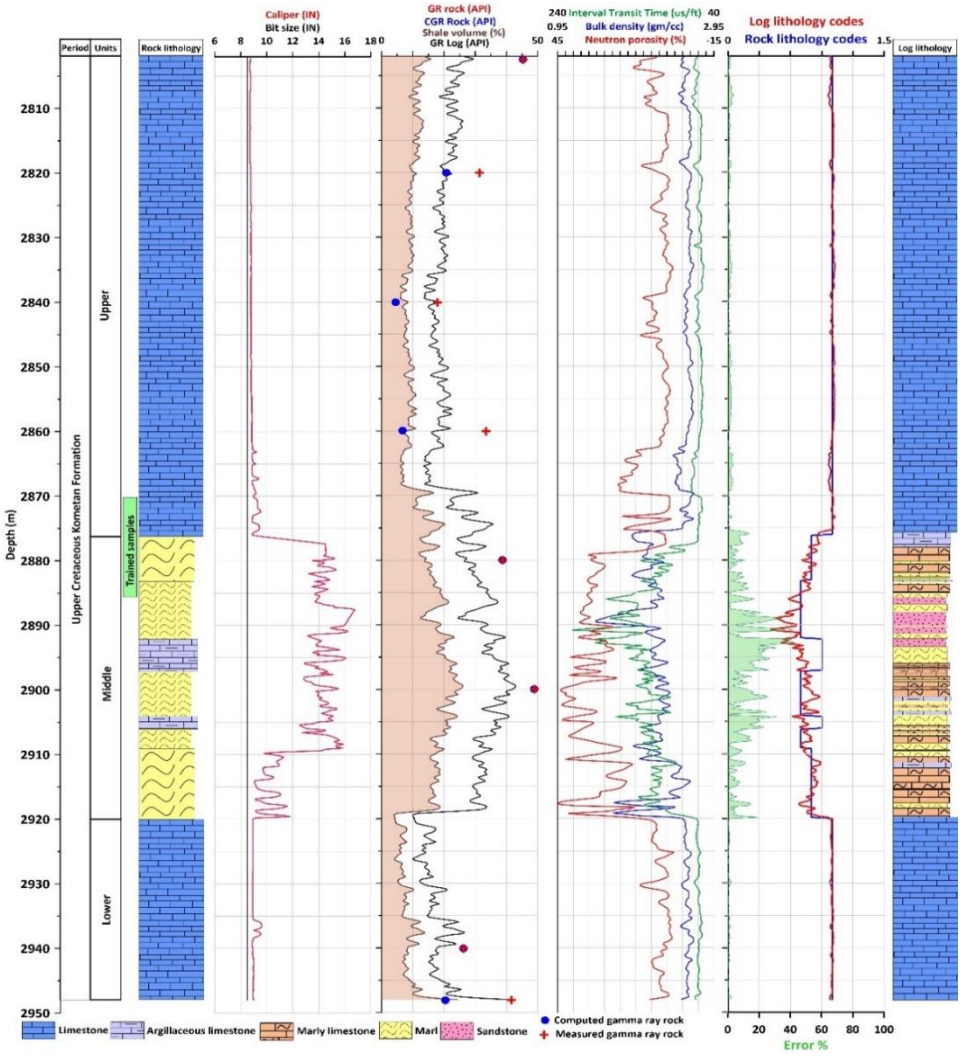

Fig. 8. Log data (caliper, gamma-ray log (GR log), gamma-ray rock (GR rock), computed gamma-ray rock (CGR), sonic (Interval transit time), density (bulk density), and neutron log (neutron porosity)), rock lithology codes (blue line), log lithology codes (red line) computed from multivariate regression, and error percent line (green-filled line) for Kz-29 well (Adopted from Hussein et al., 2024).

The well log data show very similar (correlatable) patterns in both the Kz-29 and Kz-40 wells, but especially the gamma-ray logs can be used for long-distance (>100 km) correlation. The middle, "shaly" interval is well-constrained by blocky patterns at the base and the top, and upwards-increasing and then decreasing GR values in BH-13, Kz-40, Kz-29, Kz-13, and partly K-2018 wells. The middle interval in the K-218, K-216, K-243, and J-37 wells is delimited by a distinct GR peak at the base, which is followed by upwards-decreasing values. In contrast, the lower and upper intervals have lower and more uniform GR values. The correlation results (Fig. 10) show that the middle, shaly interval attains a maximum thickness of ~68 m (Kz40 well) whilst it laterally pinches out to a minimum thickness of ~12 m towards NW (BR-1 well) and to ~15 m towards SE (J-37 well). The gamma-ray values generally decrease consistently with the decreasing thickness of the shaly interval, from maximum values in Kz-40 (~30 to ~70 API) to J-37 wells (~22 to ~35 API, but with a few outliers reaching up to 75 API).

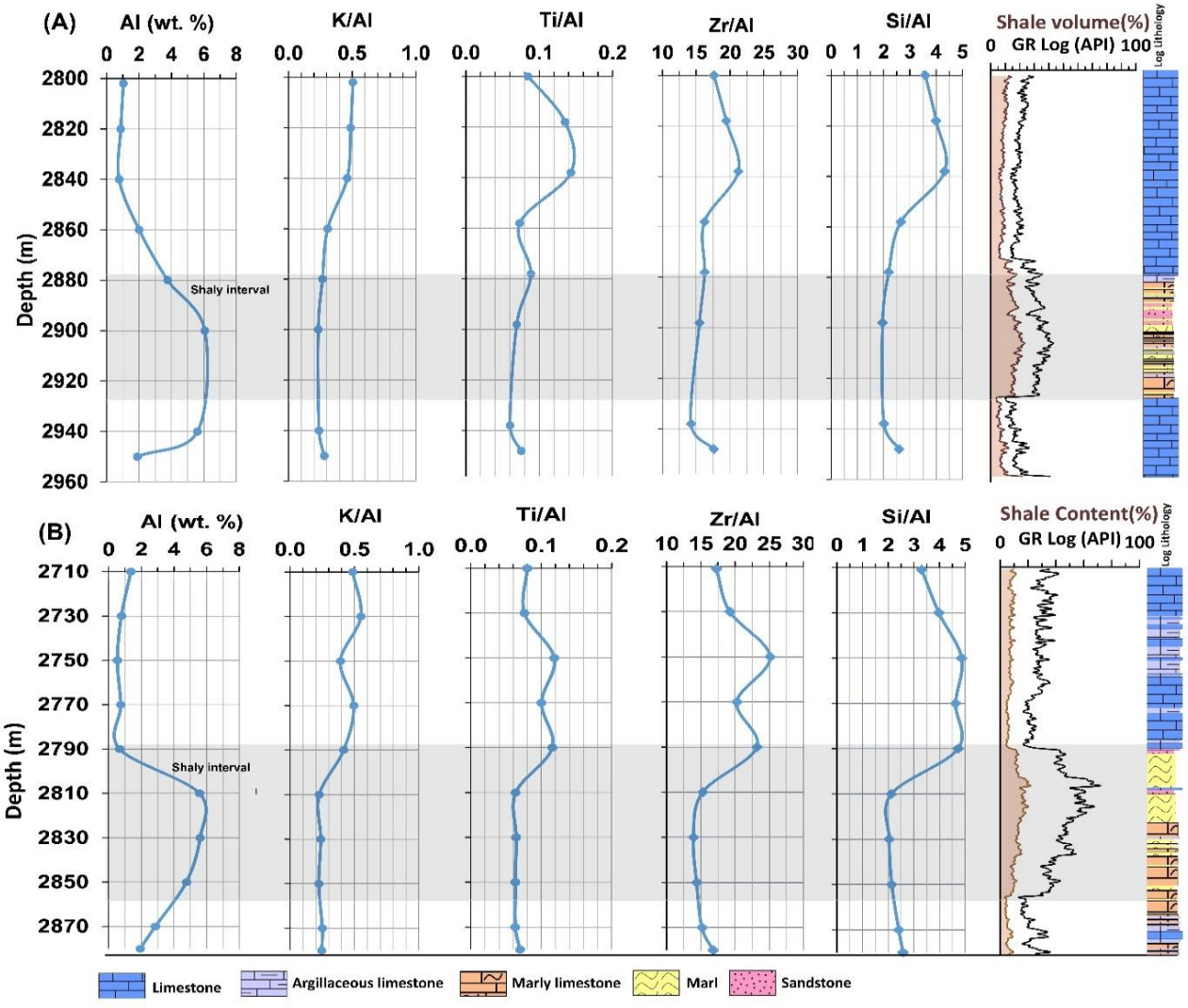

Fig. 9. Vertical distribution of selected elemental proxies and their correlation with selected log data (gamma ray and shale content) in the Kz-29 well (A) and Kz-40 wells (B) (Adopted from Hussein et al., 2024).

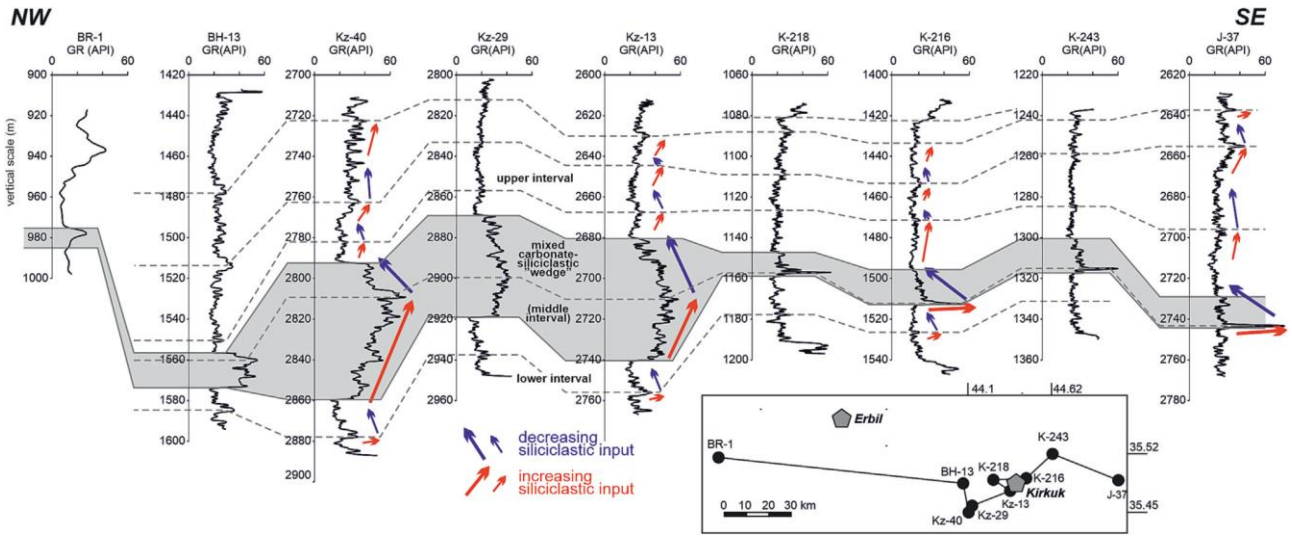

Fig. 10. Well log correlation of the Kometan Formation based on total gamma-ray logs; note the presence of middle, shaly interval (wedge of mixed carbonate–siliciclastic sediment) laterally pinching out (Adopted from Hussein et al., 2024).

4.2. Microfacies Identification

The microfacies analysis is based on thin sections from the Qamchuqa and Zewe sections (Fig. 11). The composition of the Kometan Formation is relatively uniform, but the texture is more variable. Subtle changes in texture and composition of skeletal grains allowed us to classify six microfacies, MFT1–MFT6 (Figs. 6, 11). The MFT1 microfacies is a mudstone including planktonic foraminifers (*Globigerina*, *Heterohelix*, and oligosteginids) and sparse calcispheres (Fig. 11a). The MFT2 microfacies is a wacke-packstone with abundant foraminifers such as *Hedbergella*, *Heterohelix*, and oligosteginids, sparse calcispheres and sponge spicules (Fig. 11b). The MFT3 microfacies is a densely packed, moderately sorted packstone with abundant planktonic foraminifers such as *Globotruncana*, and *Dicarinella*, less abundant *Hedbergella* and *Heterohelix*, sparse calcispheres, fragments of ostracod shells, and relatively large grains of glauconite (Fig. 11c). The MFT4 is a packstone with abundant (35 to 40 %) oligosteginids and less abundant planktonic foraminifers (Fig. 11d). The MFT5 microfacies is a fine-grained, well sorted packstone with oligosteginid planktonic foraminifers, *Hedbergella*, *Heterohelix*, *Globigerina*, and *Globotruncana* (Fig. 11e). The MFT6 microfacies is packstone with benthic foraminifers (e.g., *Textularia*), echinoderm fragments, oligosteginids and sparse ostracods (Fig. 11f).

Analyzing the distribution of these facies, we observe that all six types (MFT1-MFT6) (Fig. 11) are categorized into three main groups: packstone, wackestone, and mudstone. Subsequently, stylolite measurements were conducted for each of these three groups. These groups are further subdivided into Groups A (mud-supported) and B (grain-supported) (Fig. 5B, C), encompassing wackestone and mudstone in group A, while Group B solely comprises packstone. All stylolite analyses are conducted based on these delineated groupings.

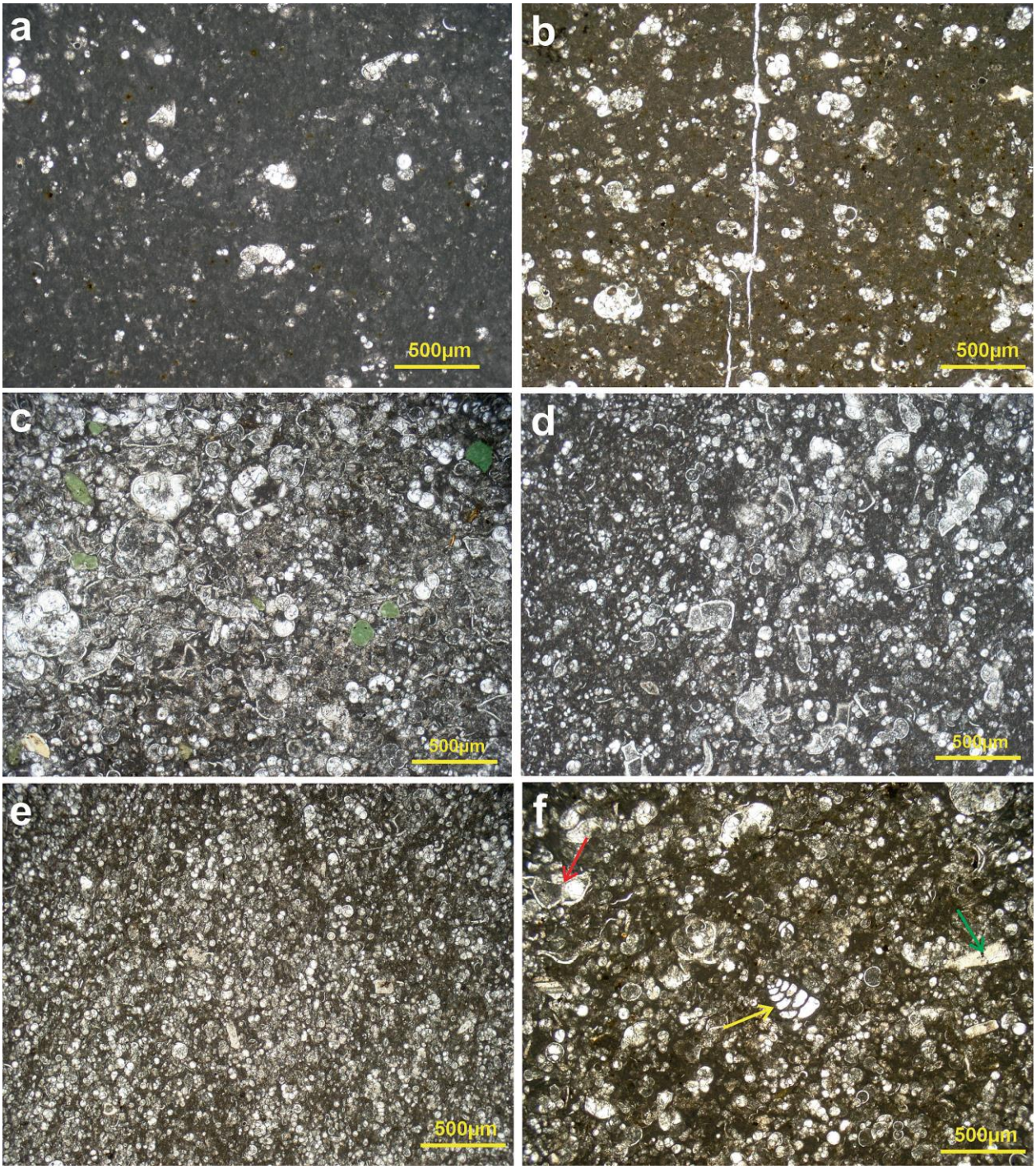

Fig. 11. Photomicrographs of microfacies of the Kometan Formation; a) planktonic foraminiferal mudstone (MFT1); b) *Heterohelix/Hedbergella* wackestone–packstone (MFT2); c) planktonic foraminiferal packstone with glauconite (MFT3); d) oligosteginid packstone (MFT4); e) planktonic foraminiferal wackestone-packstone with oligosteginids (MFT5); f) packstone with benthic foraminifers, echinoderms, and oligosteginids (MFT6), yellow arrow: benthic foraminifer (*Textularia*), green arrow: echinoderm fragments; red arrow: ostracod (Adopted from Hussein et al., 2024)..

4.3. Stylolitization and Pore Networking

4.3.1. Stylolitization

The examined thin sections revealed the presence of lime mudstone, wackestone, and packstone microfacies. They are divided into mud-supported (mudstone and wackestone) (microfacies A) and grain-supported (packstone) (microfacies B) microfacies (Fig. 5). The microfacies, A and B, with relatively uniform allochem composition but different texture, have been identified from petrographic analysis of thin sections from the Qamchuga and Zewe sections. The microfacies A is a poorly sorted mudstone and wackestone with abundant planktonic foraminifers such as *Hedbergella*, *Heterohelix*, oligosteginid forams, sparse calcispheres, and sponge spicules. The matrix is composed of micrite with silt-sized, unidentifiable calcite fragments (Figs. 5B, 11a, b, e). The microfacies B which is a moderately sorted packstone with numerous planktonic foraminifers including *Globotruncana* and *Dicarinella*, less abundant *Hedbergella* and *Heterohelix*, scarce calcispheres, remnants of ostracod shells, and abundant grains of glauconite (Figs. 5C, 11c, d, f). Both microfacies indicate distal, basinal/pelagic environment, reworked, and sorted by current activity, as evidenced by their lime mudstone/wackestone/packstone texture and the dominance of planktonic foraminifers. The microfacies A volumetrically prevails.

Well-developed stylolites in microfacies A (Fig. 5B) show little weathering. The stylolites in pure carbonate beds are evenly distributed and parallel to the bedding plane. Stylolites are mostly suture and sharp-peak varieties, with many basic wave-like features. The structures' horizontal and vertical connections form intricate anastomosing networks. At junctions, stylolites create Y-type arrangements with occasional X-type configurations. As a result, the stylolite networks exhibit a branching morphology. The maximum thickness of the stylolite seams is 9.5 cm which is filled by clay and chert nodules. The stylolites of microfacies B (Fig. 5C) exhibit comparable outcrop characteristics and formation patterns to those of microfacies A but at a lower frequency and thinner stylolite seams (maximum = 5.4 cm).

The characterization of stylolite populations was initially conducted by measuring stylolite morphology at the outcrop scale, to define the statistical characteristics of stylolites within any facies analyzed. The morphological variables employed for the statistical characterization of stylolites encompassed vertical spacing, amplitude, wavelength, junction type, and junction intensity (Table 2).

The microfacies A has less vertical stylolite spacing than the microfacies B (Fig. 6 in Appendix 4). Specifically, nearly 50% of these spacings are in the range of 0.7 to 7.4 cm, while 40% are in the range of 9.4 to 77.6 cm. Most spacing sizes (60%) between stylolites in this microfacies range between 2.9 and 14.7 cm. The highest spacing frequency of microfacies A in total frequency numbers (683) is equal to 68 (mode = 2.7 cm, 10% of total). In comparison, 50% of the recorded measures in microfacies B show a progressive increase from 0.9 to 9.4 cm. Forty percent of the space ranges from 11.9 to 77.6 cm. Most of the spacings (60%) between stylolites in this microfacies vary from 3.7 to 19 cm. Ten percent of the total measurements are between 9.75 and 12.25 cm, resulting in a maximum frequency of 43 in total frequency numbers of 423 (mode = 3 cm, 6% of total).

The microfacies A exhibits the highest wavelength with a mode equal to 3.31 cm (73 measurements, 30 % of total) (Fig. 6 in Appendix 4). Fifty percent of the measured data ranges from 3.8 to 20 cm. The microfacies B has a shorter wavelength, with approximately half of the recorded values falling within the range of 3.1 to 16.6 cm. The mode is equal to 3.73 cm whereby 22% of the total wavelength (244).

Regarding amplitude, microfacies A shows the largest values (6.17 cm) and the higher mean value (0.66 cm) (Table. 2). The minimum value recorded in this microfacies is 0.2 cm. Contrary to microfacies A, the maximum amplitude recorded in microfacies B is 2.8 cm. The mode value of the amplitude for both microfacies is equal to 0.5 cm (35% of the total measured amplitude (359)) and 0.77 cm respectively (32% of the total measured amplitude (242)).

Table 2. Summary of the statistical properties (mean values) of stylolite networks for microfacies A (mud-supported) and B (grain-supported).

microfacies	Characteristic component	Spacing (cm)	Wavelength (cm)	Amplitude (cm)	Junction intensity (i/m)	Junction angle (°)
A	planktonic foraminiferal mudstone and wackestone	6.92	3.39	0.66	0.73	37.5
B	planktonic foraminiferal packstone with glauconite	8.91	3.09	0.65	0.69	27.5

According to the classification of Koehn et al. (2016), the suture and sharp-peak type, as well as the simple wave-like type stylolites predominate in the Kometan Formation (Fig. 7 in Appendix 4). Stylolites of the suture and sharp-peak type constitute about 55% of the stylolites identified in microfacies A and B. The simple wave-like type stylolites represent about 43% of the stylolites found in microfacies A. Simple wave-like stylolites are found in a slightly higher quantity in microfacies B in contrast to microfacies A, with percentages of 44%. Rectangular layer-type stylolites exhibit the lowest occurrence among various stylolite morphologies, with proportions ranging from 0.5 to 0.1% for microfacies A and B, respectively.

Statistical analysis of stylolite distribution (null hypothesis rejected at p-values < 0.05) indicates that the spacing, amplitude, and wavelength are most accurately represented by a log-normal distribution (Figs. 6, 8 in Appendix 4). The utilization of a log-normal distribution of the stylolite spacing resulted in chi-squared values ranging from 22 to 32, indicating a diminished level of goodness of fit. The KS-test findings with a p-value beyond 0.05 suggest a stronger level of agreement between the fitted distribution and the stylolite dataset,

indicating a higher degree of goodness of fit. The p-values for both microfacies of spacing measurement for the log-normal distribution are found to be greater than 0.05 (Figs. 6, 8 in Appendix 4).

The records of stylolite wavelength exhibit chi-squared values ranging from 47 to 50 (Fig. 8B in Appendix 4). The chi-squared and p-value exhibit higher values in microfacies A when compared to microfacies B. The p-value associated with the log-normal distribution for microfacies B remains much more than 0.05, suggesting a strong level of agreement between the observed data and the theoretical distribution. The readings of stylolite amplitude exhibit a wider range of chi-squared values (Figs. 6, 8C in Appendix 4), ranging from 63 to 80. Additionally, the results of the KS test display a distribution of p-values above the significance threshold of 0.05, suggesting a satisfactory fit.

X- and Y-type connections make up 10.6% and 89.4% of microfacies A, respectively (Fig. 9A in Appendix 4). About 7% of microfacies B have X-type connections. The junction intensity of microfacies A and B is 0.72 and 0.69 i/m respectively (Fig. 9B in Appendix 4).

4.3.2. Pore Networking

Observations from optical microscopy and SEM of the thin sections (Figs. 12, 13) reveal the primary focus on the stylolite features and associated pore spaces. Stylolites create distinctive intergranular and intragranular pores within the limestone. Intergranular stylolites, visible in thin sections, exhibit linear dissolution seams along grain boundaries, while intragranular stylolites within individual calcite crystals are more prominently visualized in SEM images.

In thin sections embedded in blue resin (Fig. 12), the stylolite features are discernible under transmitted light, providing insights into their morphology in two dimensions. Intergranular pores manifest as dark linear features against the blue background, displaying irregularities and steps along the stylolite surfaces. Intragranular pores within calcite crystals appear as smaller, darker voids within the crystal lattice. In SEM images (Fig. 13), the morphology of these pores is further highlighted, offering a more detailed perspective. Intergranular pores show complex dissolving patterns with uneven surfaces, like irregular shapes and steps. Intragranular pores inside calcite crystals have detailed forms and can be oriented in different directions. Stylolites tend to form preferentially along specific bedding planes or within layers with variations in composition, leading to a non-uniform distribution of intergranular and intragranular pores. The concentration of pores is higher in regions where stylolites are more pronounced, a feature easily discernible in both thin sections (Fig. 12) and SEM images (Fig. 13).

Quantitative analysis involves measuring the pore spaces in both intergranular and intragranular regions. Image analysis software applied to thin sections (Fig. 12) and SEM (Fig. 13) images reveal an average porosity of approximately 8.3% and 12.8% respectively, indicating the percentage of void space within the stylolites. SEM images show an estimation of the size distribution of pores, with pores ranging from 0.008 to 2 millimeters (Fig. 13).

SEM analysis of carbonate rock with stylolites reveals a complex pore network, indicative of localized pressure dissolution (Fig. 13). Residual materials in these pores include illite, kaolinite, montmorillonite, and iron oxide. These secondary minerals suggest intricate alterations during diagenesis, with clay precipitation and potential involvement of oxidation and phosphate mineral formation. This SEM-based exploration offers a nuanced understanding of the dynamic interplay among dissolution, precipitation, and alteration within stylolite seams in carbonate rocks.

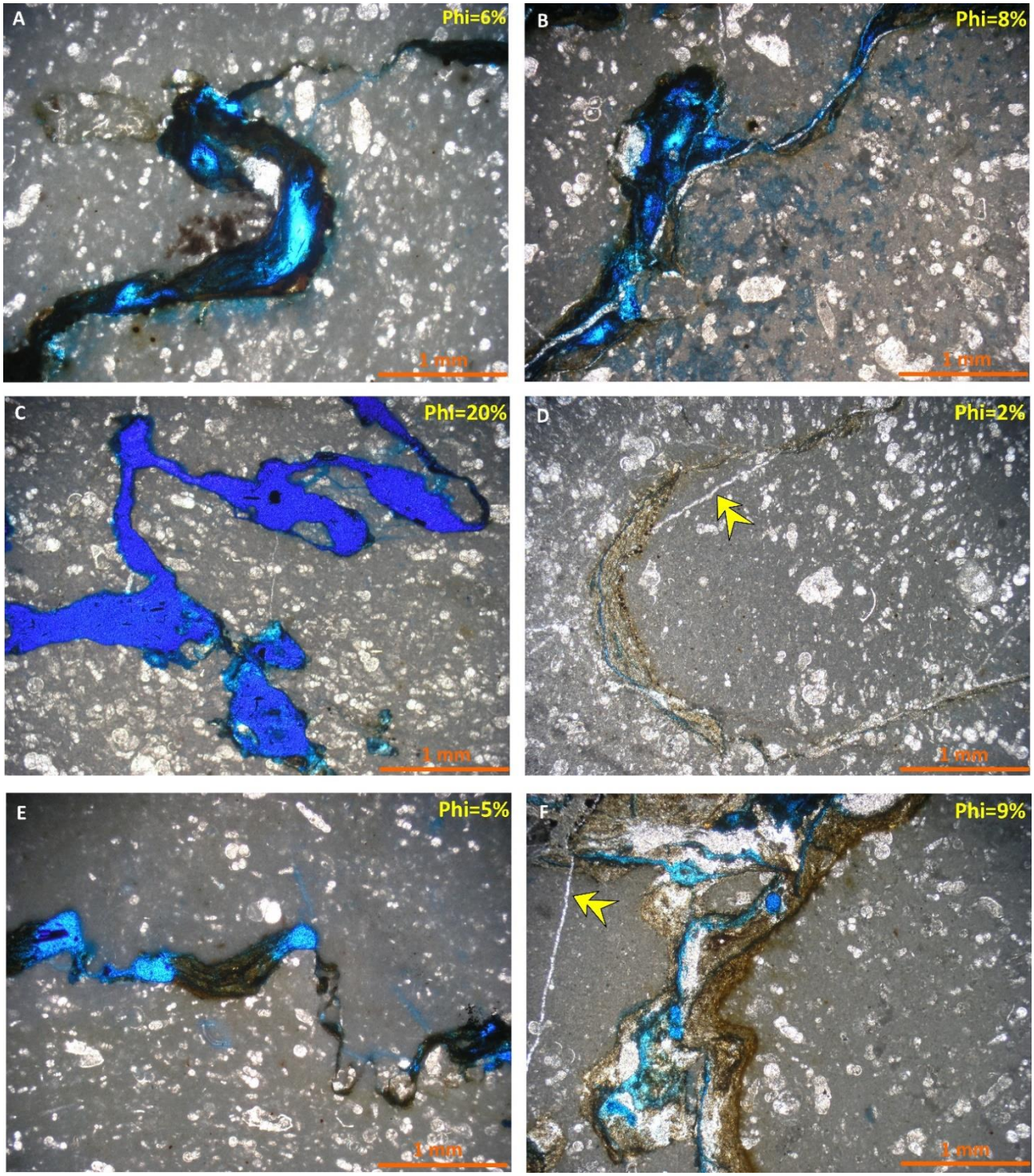

Fig. 12. Microphotograph of the Kometan Formation from the Zewe (A and B), Qamchuqa (C and D), and Dokan (E and F) sections showing pore shapes, sizes, distribution in the rock, relationship to stylolites, and quantification of porosity.

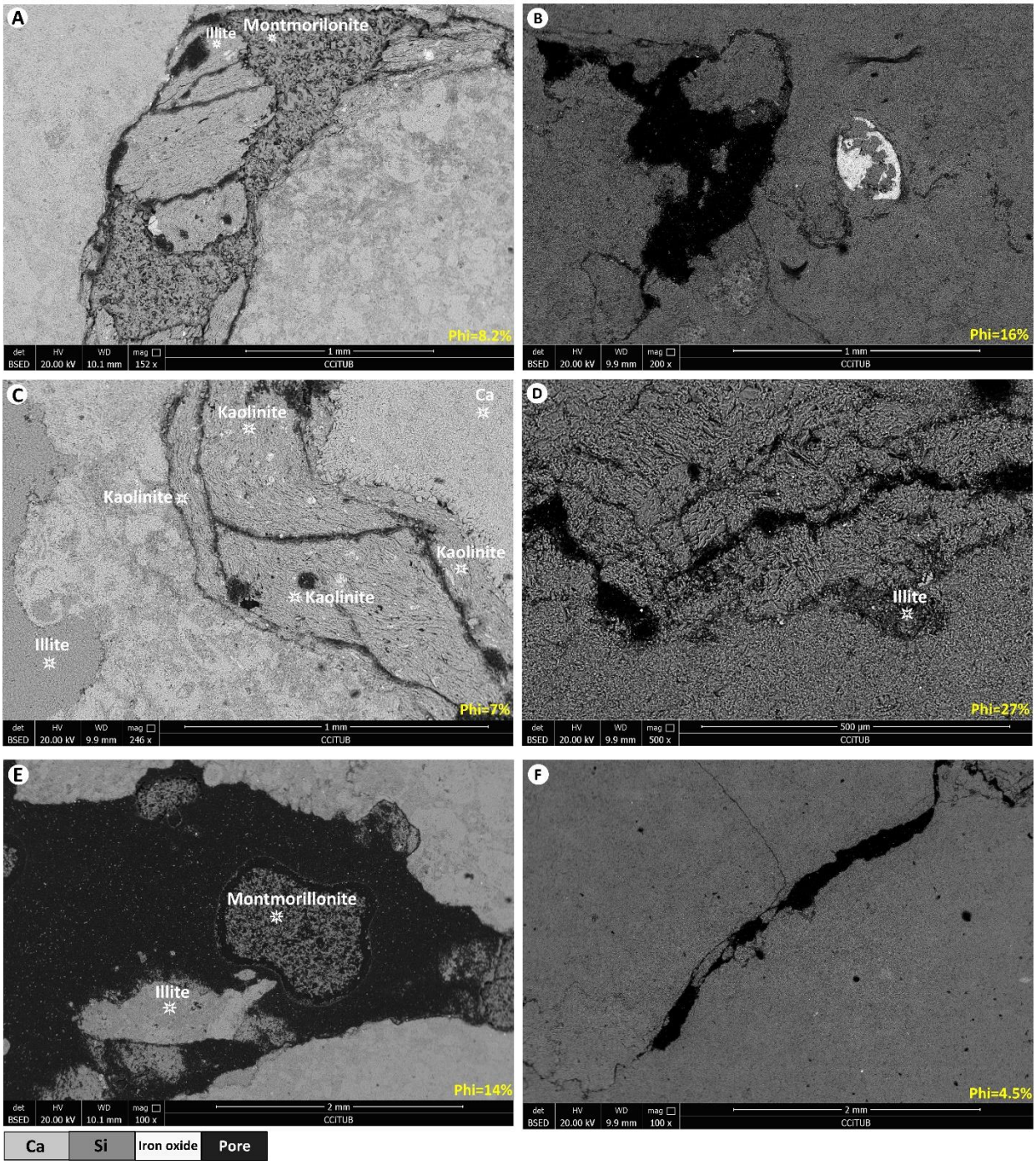

Fig. 13. Microphotograph of scanning electron microscope (SEM) of Qamchuqa (A, C, and E) and Zewe (B, D, and F) sections showing materials in and outside of stylolite seams, dissolved area, and amount of pore spaces (Phi).

The depth distribution of the element concentrations shows that most of the Si enrichment occurs in the Zewe section between 40 and 96 m (Fig. 14). The zone of silica enrichment can be correlated with the upper parts of the Qamchuqa section between 40 and 63 m above the section base, and partly with the top parts of the Dokan section between 45 and 65 m. These increased concentrations of Si partly coincide with increasing Al and decreasing Ca concentrations (Fig. 14). Across the dataset, instances can be found where an increase in Si

concentration corresponds with an increase in total length per cubic meter, suggesting a positive correlation. However, this positive correlation is not universally observed, as there are instances where total length decreases despite higher Si levels. Similarly, while certain cases show a positive correlation between Ca concentration and the total length, others exhibit a decrease in total length despite elevated Ca concentrations (Fig. 14). In addition, the highest amount of stylolite is at depths (9 to 59 m above the section base) where Ca is high, and Si is low.

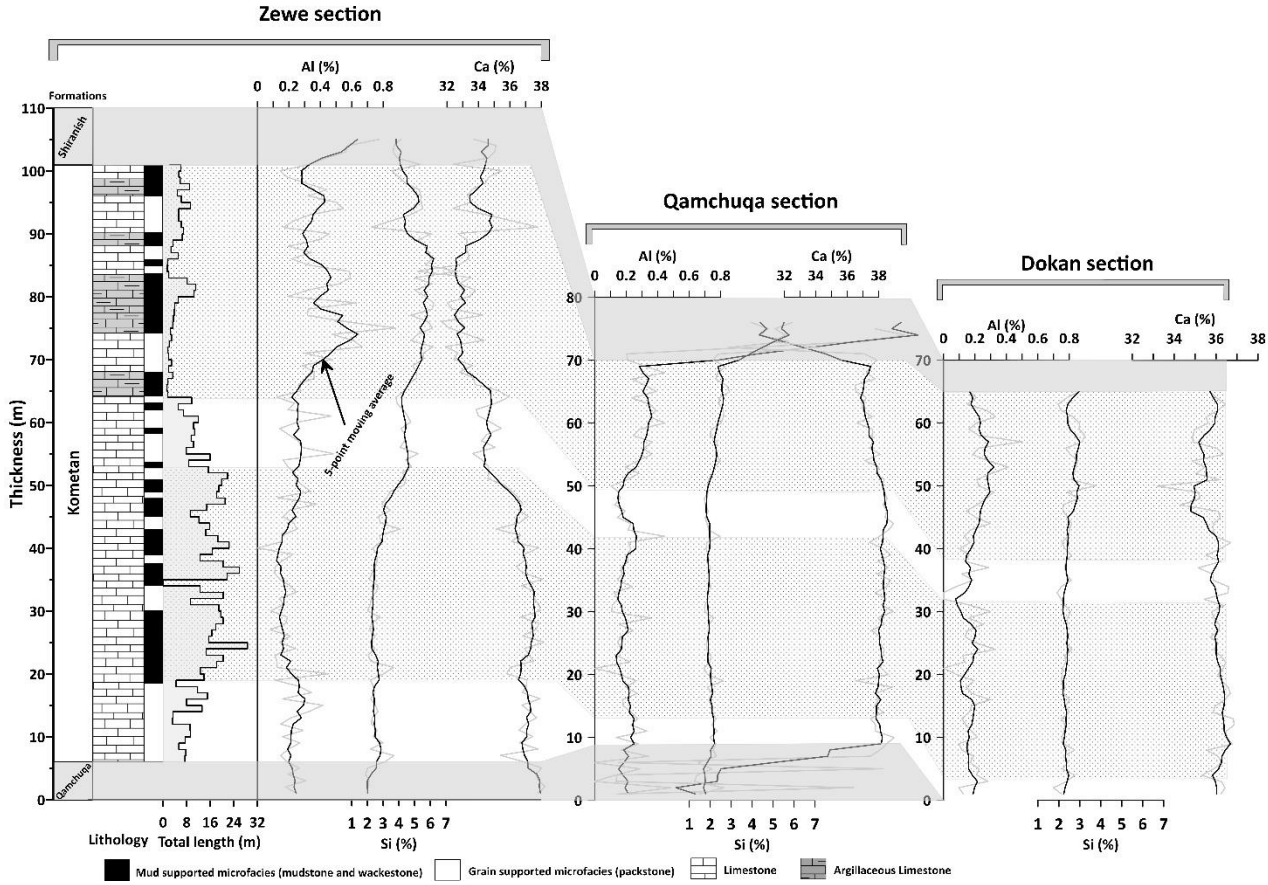

Fig. 14. Total length of stylolite along different microfacies with elemental geochemistry (Al, Ca, and Si) for the studied sections (the lower contact of Kometan Formation in the Dokan section is not exposed).

4.4. Porosity and Fractures

The Fig. 15 demonstrates the porosity structure between total porosity derived from neutron and density on the horizontal (X) axis and sonic porosity on the vertical (Y) axis in the studied wells. The plotted data are equally spread between primary and secondary porosity. There are many points plotted in the secondary zone, which can assume that good secondary porosity is anticipated from the Kometan Formation in the studied wells.

The Secondary Porosity Index (SPI) for the inspected interval, reached a maximum value of 17%, and the average is 4% for Kz40 (Fig. 16A), the maximum value is 30%, and the average is 8% for K216 (Fig. 16B). The SPI results in Fig. 16A indicated that four zones are fractured at the specific depths 2792–2803, 2832–2837, 2841–2873, and 2879–2898. In addition, three high and three low fractured zones of K216 are presented

in Fig. 16B, in which the high fractured zones are 1420–1452, 1452–1485, and 1485–1498. The porosity cross-plot and SPI methods (Figs. 15A, 16B) do not indicate a fracture zone in 2711–2792 intervals of Kz40, but the

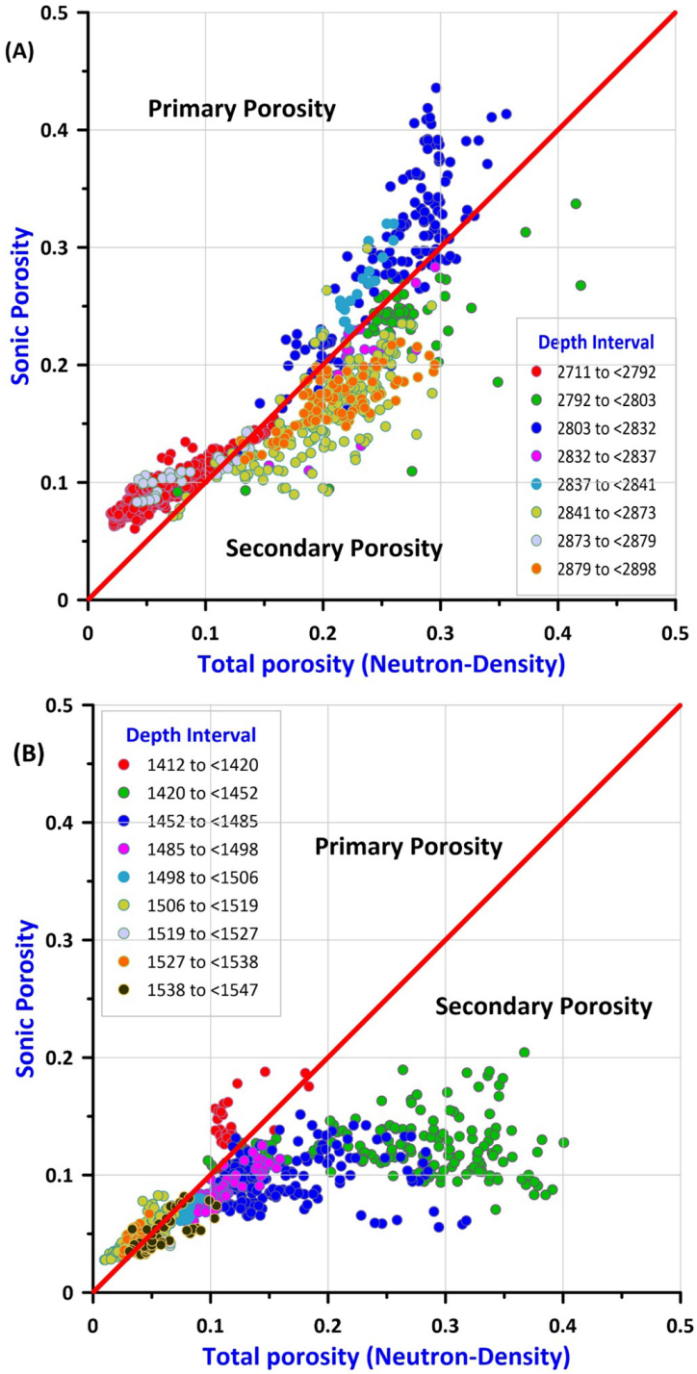

Fig. 15. Secondary porosity is indicated from porosity cross-plots, A in Kz40 and B in K216 wells (Adopted from Hussein, 2022).

caliper log (Fig. 5A in Appendix 3) shows mud cake of this interval which can reveal the presence of permeable zones and open fractures. Density and neutron log are more affected by mudcake than sonic log, so according to Eq. 1 in Appendix 3, the result of SPI in this interval would be negative (no fracture) (Fig. 16A), and on the cross plot the data plotted on the primary porosity area (Fig. 15A). All other intervals and fracture zones suggested from cross-plot and SPI (Figs. 15, 16) are supported by a caliper log which shows borehole

enlargement (Fig. 5A, B in Appendix 3), which can be a good indicator for fractures of competent formation. The behavior of other logs (density, neutron, and sonic) can be applied qualitatively to support the evidence relevant to fractures. Spikes of the sonic log (Fig. 5 in Appendix 3), which indicate the presence of fractures. Spikes for the sonic log are primarily observed in enlarged intervals, but the density spikes also indicate fractures, observed at a depth of 1477, which is not indicated by the neutron log (Fig. 5B in Appendix 3). The enlargement also caused an abrupt increase and decrease in neutron and density log. It is due to the increasing mud thickness in enlarged intervals, and it has been considered during interpretation to identify fractures.

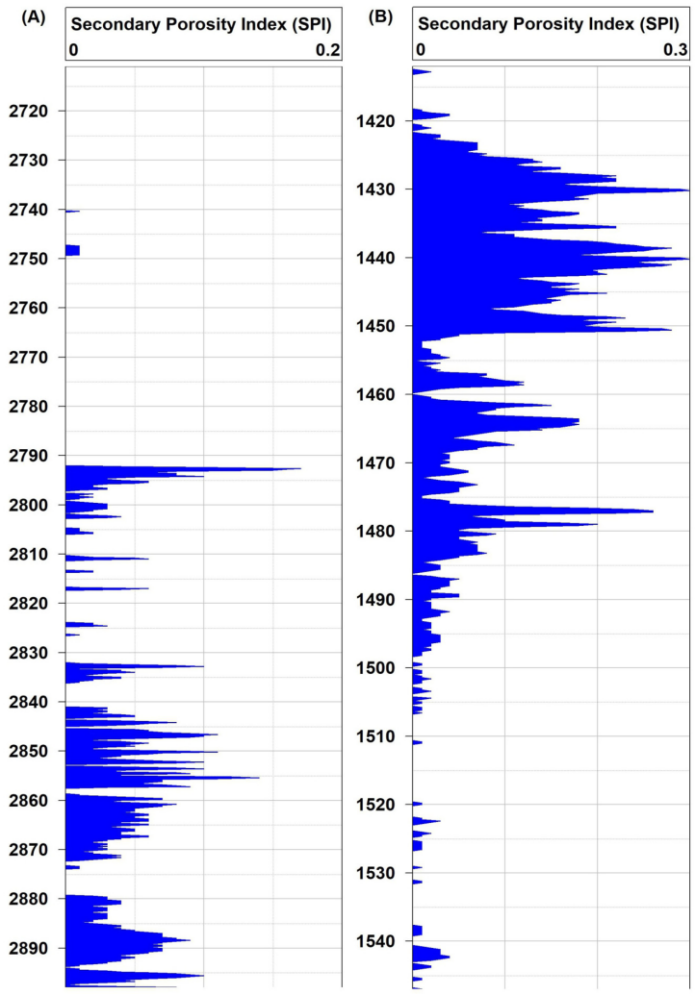

Fig. 16. Secondary Porosity Index (SPI) demonstrating the availability of fractures, A in Kz40 and B in K216 wells (Adopted from Hussein, 2022).

The available gamma-ray log (total gamma-ray) (Fig. 5 in Appendix 3) and spectral gamma-ray from available subsurface rock samples (Fig. 6 in Appendix 3) demonstrate an increment of uranium content against fractures. It can be noticed when the uranium precipitates in the fractures, which the fluid movement may endorse (Rider, 1999). Since the total gamma ray measures combined radioactive elements (uranium, thorium, and potassium) and the spectral gamma ray log is not available, the shale content from the total gamma ray (Fig. 5 in Appendix 3) can be combined with that from the neutron-density log (Fig. 17) to validate either the gamma ray log reading is due to uranium or other elements (potassium and thorium). In addition, the available spectral gamma ray of rock samples also can be used (Fig. 6 in Appendix 3). The positive difference between gamma ray shale

to neutron-density shale (Vsh gamma ray – Vsh neutron-density) may refer to uranium content, and consequently, fractures in the formation. Fig. 17 shows the calculated shale volume from different approaches (gamma ray and neutron-density log) and the differences between them to distinguish fracture zones. The technique was successfully applied especially in K216 (Fig. 17B) which is perfectly comparable with other approaches to fracture identification in this study (Figs. 15B, 16B). However. It couldn't depict the fractures in Kz40 in the 2793–2846 m interval due to the borehole effect which enlarged in this interval. Neutron and density logs are impaired in this interval because the thickness of drilling mud increases, and the tools stay away from the borehole wall. Fresh base mud was used to drill these wells (Kz40 and K216) which is a high hydrogen index, so the value of the neutron log in enlarged interval would be high. The density log value in this interval would be low because the depth of investigation of this log is shallow, so the porosity is overestimated. The computed gamma ray (CGR) also can be used decisively to identify uranium in the formation (Fig. 5 in Appendix 3). Since the total gamma ray (GR) combined uranium, thorium, and potassium and the computed gamma ray (CGR) combined only thorium and potassium, the difference between the total gamma ray to computed gamma ray is equal to uranium content (Fig. 5 in Appendix 3).

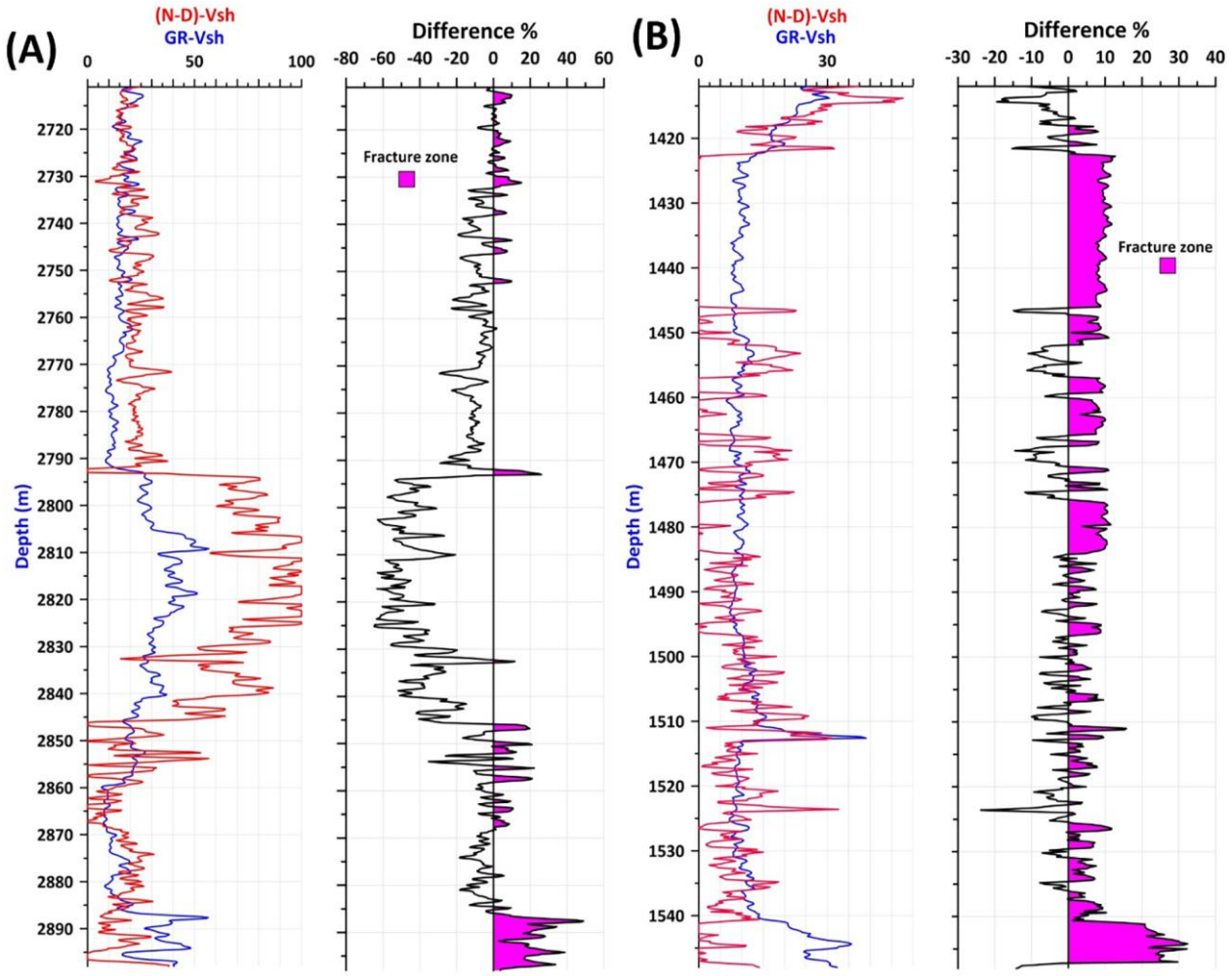

Fig. 17. Shale volume from neutron-density and gamma-ray, and their differences to demonstrate fracture zones in Kz40 (A) and in K216 (B) wells (Adopted from Hussein, 2022).

5. Discussion

5.1. Sequence Stratigraphy and Depositional Environment

5.1.1. Depositional Environment and Sedimentary Trends in Outcrop

The abundance of planktonic foraminifera such as *Hedbergella, Heterohelix, Globigerinoides, Rotallipora, Praeglobotruncana* and *Daicarinella* along with numerous species of *Oligostegina*, and the scarcity of other skeletal/nonskeletal grains suggest relatively a uniform, deep-water depositional environment for the outcrop sections. The similarity of pelagic facies is very high, and the exact separation of the mentioned facies with conventional petrographic methods is difficult. For this reason, the methodology of planktonic foraminifer morphotypes (Keller, 1993) was adopted in this study. The MFT1 microfacies is mainly composed of planktonic foraminifers of the morphotype 3 (Keller, 1993). The abundance of planktonic foraminifers, and abundant micrite indicate deposition in the calm, deep marine environment (Wilson, 1975; Bernaus et al., 2002). This microfacies corresponds to the RMF 5 of Flügel (2004), which belongs to the basinal environment. The MFT2 and MFT3 microfacies containing glauconite also correspond to RMF5 (Flügel, 2004) products of a basinal/pelagic environment, in which glauconite grains and pure carbonate lithology indicate low sedimentation rates, sub-oxic to reducing conditions, and a lack of detrital input (Amorosi, 1995). The grain-supported texture of the MFT4 and especially MFT5 microfacies along with the abundance of planktonic foraminifers, indicates low- to medium-energy water activity, presumably due to bottom currents, in relatively deep marine environments, well below the fair-weather wave base (Scholle and Ulmer-Scholle, 2003; Flügel, 2004). These microfacies are comparable with the open marine facies zones (FZ1, FZ2, FZ3) of Wilson (1975), and the RMF 5 of Flügel (2004), which can be attributed to the outer ramp environment. Due to the predominance of the oligosteginid planktonic foraminifers and other planktonic foraminifers, it can be said that the MFT1 to MFT5 microfacies represent pelagic open marine conditions (Keller et al., 2002). Echinoderm fragments are found in shallow-marine limestones as well as in deep-marine limestone (Flügel, 2004); in addition, ostracod and benthic foraminifera are observed in middle ramp environments (Flügel, 2004). The MFT6 microfacies containing more abundant echinoderms, ostracods, and benthic foraminifers are interpreted as corresponding to the RMF3 microfacies reflecting shallower, middle ramp environments (Flügel, 2004). The general lack of sliding, slumping and resedimented facies such as turbidites indicates predominant basin floor/deep shelf bottom with flat topography with predominant sedimentation from suspension settling, only partly affected by bottom currents. The studied outcrop part of the Kometan Formation was likely deposited in outer ramp rather than in a basin adjacent to carbonate shelf. This is supported by the absence of shelf-derived cortoids, oncoids, and aggregate grains, which are commonly found in age-equivalent carbonates in other parts of the Zagros basin (Ilam Formation; Adabi and Mehmandosti, 2008).

5.1.2. Facies Stacking Patterns

The microfacies stacking patterns are more difficult to interpret. The model of MFT1 to MFT6 microfacies likely represents a gradual transition from open marine/pelagic environments to middle ramp environments but the microfacies do not show distinct vertical trends (Fig. 6). Although, at a first glance, it seems that there

are no relationships between the carbonate geochemistry and microfacies stacking patterns (Fig. 6), the bivariate statistics of the microfacies vs. element geochemistry shows the opposite. When plotted against the microfacies type, the mean Al concentrations show statistically significant (R^2=0.58) decreasing trends from more distal (MFT1) to more proximal (MFT6) microfacies, whilst the Ca concentrations show an opposite, increasing trend (R2 = 0.69) (Fig. 18). This suggests that the slightly more proximal open shelf microfacies are purer carbonate whereas the more distal ones are more argillaceous, exactly the opposite as what we see in the more proximal parts of the basin.

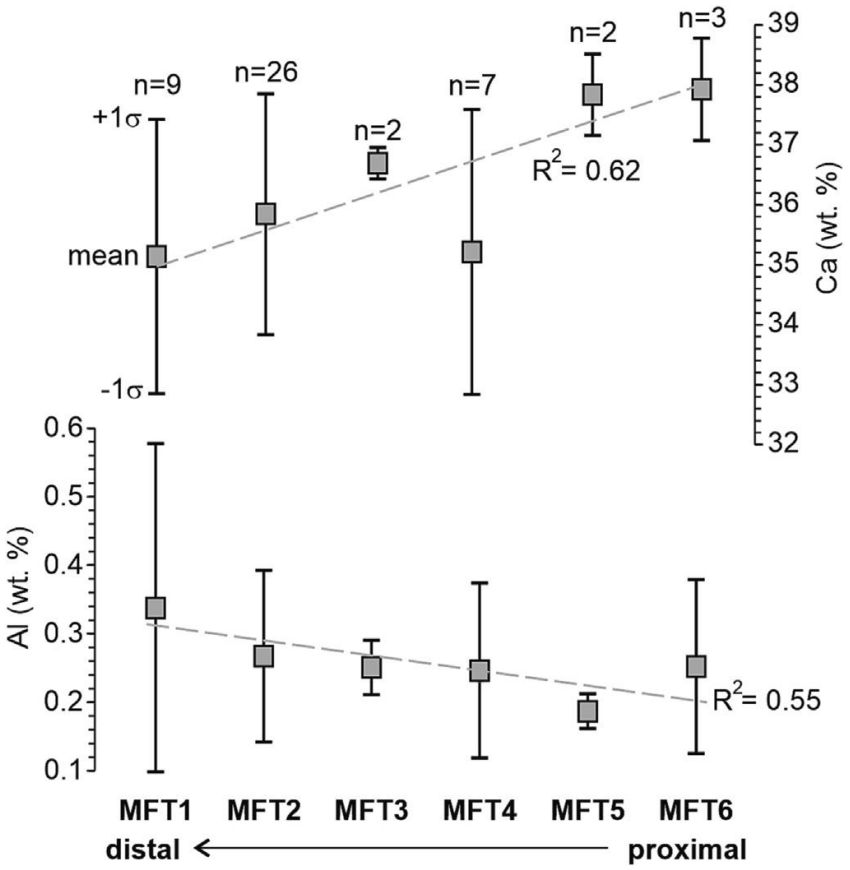

Fig. 18. Trends of decreasing mean Al concentrations and increasing mean Ca concentrations (mean value ± 1 standard deviation) in a microfacies series from MFT1 (open shelf/pelagic environment) to MFT6 (restricted shelf environment) in the Zewe and Qamchuqa sections (total 49 samples) (Adopted from Hussein et al., 2024).

The carbonate production on carbonate ramps can extend well into bathyal and abyssal depths (De Mol et al., 2002; Schlager, 2005). However, in mixed carbonate–siliciclastic depositional systems, the autochthonous carbonate facies (as well as their chemistry and well-log response) are mixed with allochthonous sediment from detrital sources generally located landwards from the carbonate factory. Bábek et al. (2013) described a carbonate ramp profile in Lower Carboniferous of the British Isles showing that from the mid ramp carbonate factory, the CaCO3 contents decrease, and the computed gamma-ray values, based on K and Th concentrations increase both up-dip towards more proximal lagoonal settings, and down-dip towards the deep basin. Trends of increasing gamma-ray values and magnetic susceptibility from a proximal carbonate factory to distal basinal settings have been described from the Devonian mixed carbonate–siliciclastic systems of the Prague Basin,

Czechia, and Eifel Mts., Germany (Mabille et al., 2008; Bábek et al., 2018). Such mixing of biogenic carbonate and detrital siliciclastic sediment, and proximal-to-distal spatial distribution are typical for a hybrid, mixed carbonate–siliciclastic depositional system (Sarg, 1988; Dolan, 1989; Page et al., 2003). Consistently with these examples, the concentrations of Al, K, and Rb (and possibly other elements bound to detrital phyllosilicates) tend to slowly increase basin wards in the distal, outcrop parts of the Kometan Formation (Figs. 18, 19).

5.1.3. Depositional Environment and Sedimentary Trends in Subsurface

The depositional environment of the subsurface parts of the Kometan Formation is more difficult to interpret owing to the lack of lithology and biofacies data. However, published foraminifer data suggest that the Kometan Formation in the Jambur oil field composed of argillaceous limestones and marls corresponds to oligosteginid biofacies deposited in a restricted shelf (Abawi and Mahmood, 2005; Jassim and Goff, 2006). The regional patterns suggest that the open shelf limestone facies of the Kometan Formation of the Zagros foreland basin pass laterally towards W and SW into bioturbated chalky limestone, shale and marly limestone of the Khasib Formation deposited in a restricted shelf, and further into lagoonal shale, and carbonate of the age-equivalent Tanuma Formation (Fig. 2) (Van Bellen et al., 1959; Buday, 1980; Dunnington, 2005; Al-Qayim, 2010). The Kometan Formation in the Jambur, Khabbaz, and Kirkuk oil fields is therefore considered a shallow-water equivalent of the studied outcrop sections.

The average concentrations of Al, Si, K, Ti, Fe, Rb, and Zr in the well samples are 1.8 times to 8.8 times higher than in the outcrops. These elements are associated with the detrital minerals identified from the XRD data: illite, illite/smectite, smectite, kaolinite, quartz, and K-feldspars. In contrast, the concentrations of Ca in subsurface samples are lower than in outcrops (Fig. S1 in Appendix 5; Table S1 in Appendix 6). The mineralogy and geochemistry of the subsurface samples support the interpretation of the Kometan as a mixed carbonate–siliciclastic ramp (Dolan, 1989; Bábek et al., 2013), in which the siliciclastic admixture decreases from more proximal (inner ramp) towards more distal parts (middle ramp). In the same direction, the Ca concentrations tend to increase to attain a maximum in the mid-ramp carbonate factory, and then slowly decrease with reduced carbonate production in the most distal basinal settings as indicated by the geochemical trends in the microfacies (Figs. 18, 19). According to the well-log (especially gamma-ray log) characteristics, the Kometan Formation is subdivided into three distinct intervals in subsurface, the lower clean interval (low GR), the middle shaly interval (high GR) and the upper clean interval (low GR) (Fig.10). We assume that the wedge of mixed carbonate–siliciclastic sediments represented by the middle shaly interval (Fig.10) represents a progradation of more proximal ramp deposits onto the open shelf/pelagic deposits. Thus the upwards increasing gamma-ray trends in the proximal settings (Khabbaz, Kirkuk, Jambur, Bai Hasan, and Barda Rash oil fields) represent progradation (regression) whereas the upwards decreasing ones represent retrogradation (transgression).

Sequence-stratigraphic interpretation of the Kometan Formation is determined by three factors: (i) the predominance of deep-water sediments in outcrop, with low facies variability that predetermines well log and

geochemical data as the only meaningful data source for stratigraphic correlation, (ii) the layer-cake stratigraphic geometry with invisible (or absent) clinoforms as inferred from such correlation, and (iii) lack of lithology data from shallow-water parts of the depositional system. Previous attempts to interpret the sequence stratigraphy of lithologically uniform deep-marine carbonates relied on the presence of specific lithological

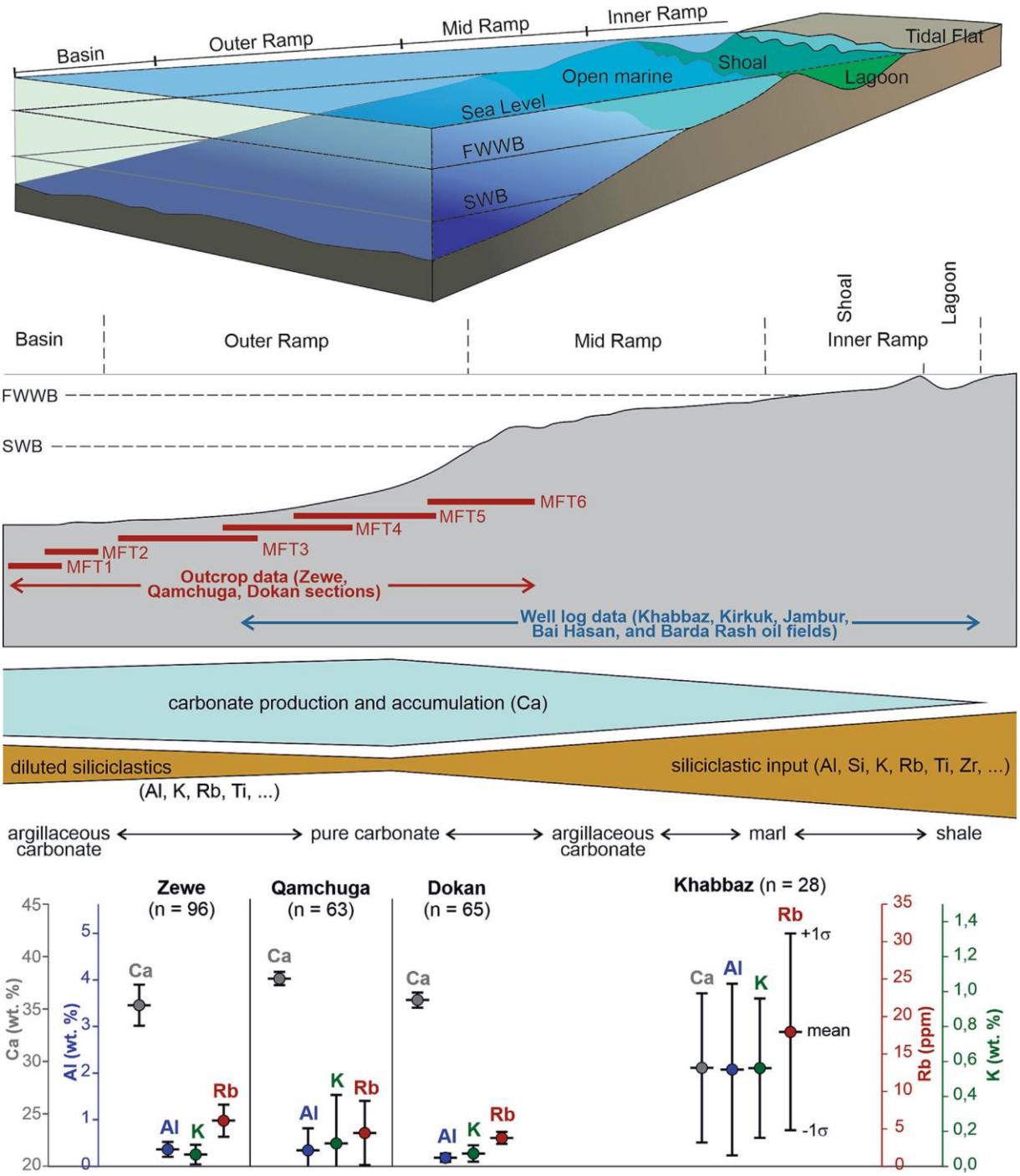

Fig. 19. Depositional model showing the interpreted mixed siliciclastic–carbonate ramp depositional environments of the Kometan Formation, distribution of selected elements (mean± standard deviation of Ca, Al, K, Rb) along the ramp profile, and a schematic distribution of biogenic carbonate (Ca) and detrital elements (Al, Si, K, Rb, Ti, and Zr) along the ramp profile (Adopted from Hussein et al., 2024).

features such as hardgrounds and bioturbated horizons (Martire, 1992), element geochemistry and outcrop gamma-ray logs (Halgedahl et al., 2009; Ver Straeten et al., 2011; Bábek et al., 2016), and stable isotope geochemistry (Jarvis et al., 2001; Mabrouk et al., 2007). The gamma-ray data supported by facies can be extremely useful in sequence stratigraphic correlations. Using the sequence-stratigraphic model of Hunt and Tucker (1993), Bábek et al. (2013) interpreted the upwards-decreasing computed gamma-ray (CGR) trends, supported by facies analysis, as normal and forced regression during highstand (HST) and falling stage (FSST) systems tracts in the distal carbonate ramp. They conversely interpreted the upwards increasing CGR trends as transgression (TST), the peak CGR values as maximum flooding surfaces (mfs), and the rapid drops in CGR values as basal surfaces of forced regression (bsfr).

Our interpretation of the distal part of the Kometan Formation in outcrop follows similar principles: the peak Al and K concentrations are assumed to represent the overturn from transgression (T) to normal regression (R) i.e., the maximum flooding surface (mfs), whilst the end of regression and passage to transgression (maximum regression surface, mrs) are associated with Al and K concentration minima (Fig. 13 in Appendix 3). In contrast, the well log patterns in the more proximal, subsurface part of the Kometan Formation were primarily controlled by basinwards and landwards shifts of the proximal siliciclastic system onto the more distal ramp carbonates. Consequently, the peak gamma-ray values represent maximum regression surfaces whereas the gamma-ray minima represent maximum flooding surfaces. It is assumed here that the T–R cycles in outcrop were synchronous with the T–R cycles in subsurface. In this rather simplistic model, we use the maxima and minima on the curves as the only reliable correlation points. This approach is close to the "inductive" sequence-stratigraphic concept of Embry and Johannessen (2017) identifying the maximum flooding surfaces as separating underlying, upwards deepening strata from overlying, upwards shallowing ones (and vice versa for maximum regressive surfaces). Using just two easily identifiable surfaces, the T–R sequences of Embry and Johannessen (1993, 2017) consist of just two systems tracts, transgressive (TST) and regressive (RST). Under the conditions defined at the beginning of this section, this model is applicable. The Kometan Formation consists of four T–R sequences, ranging in thickness from ~10 to ~45 m.

5.2. Remarks on Reservoir Quality

The relationship between the wireline log characteristics reveals that the matrix porosity (sonic porosity) decreases with depth, from about 10–20 % at the top to about 5 % at the bottom of the Kometan Formation (Fig. 13A in Appendix 2). However, the reservoir quality is largely given by the fracture porosity, which can be inferred from the residues between the neutron-density (N-D) porosity and sonic porosity. The N-D porosities reach up to 40 % in the upper interval of the Kometan Formation whilst they drop down to about 5 % in its lower interval (Fig. 13 in Appendix 2). There are four depth segments in the upper interval, in which the N-D minus sonic porosity residues increase. All of them coincide with the passages from transgressive to regressive systems tracts (maximum flooding surface) which corresponds to the pure carbonates. In general, the Zagros foreland oil reservoirs in northern Iraq, including the Kirkuk embayment, the Avanah and Baba Domes, the Bai Hassan field as well as the gas reservoirs in the Jambur oil field all produce from fractured

reservoirs of the Kometan Formation (Aqrawi, 1996). Light oils (41 API) are produced from the Kometan Formation, a fractured reservoir in the Taq oil field with estimated recoverable reserves of 700–750 million barrels. When the field is fully established, it is anticipated that it will yield 200,000–250,000 barrels per day (Rashid et al., 2015a, 2015b). Fractures that increase the formation's porosity and permeability are principally responsible for controlling the productivity of carbonate rock in the Kometan Formation (Rashid et al., 2015a, 2015b). In addition, the fractured reservoir quality inferred from well-log data has been supported by rock samples from outcrops (Hussein, 2022). Rheology of the carbonate likely changes with shale content, resulting in higher susceptibility of the pure carbonates to brittle deformation and development of fracture systems, compared to argillaceous carbonates and marls. It is assumed that in mixed carbonate–siliciclastic ramps, the sea-level driven transgressive–regressive, upwards cleaning and dirtying sequences control the post-depositional development of fracture systems and affect the reservoir quality.

In a subsurface geological context, the interplay between shale content and porosity is crucial for understanding the porosity variations at different depths. Fig. 20 illustrates a clear relationship between increasing shale content and decreasing density porosity, especially in crossovers (cyan-filled color) within specific depth intervals. In the Kz-29 well (Fig. 20A), at 2819 meters depth, with a relatively low shale content of 9.8%, the density porosity is 8%. As we descend to 2830 meters, encountering a moderate shale content of 11%, the density porosity decreases to 3.5%. Further, at a depth of 2870 meters, where shale content is higher at 14%, the density porosity diminishes to 2.3%. In the shallower depth of Kz-40 (2711-2747m) (Fig. 20B), characterized by decreasing shale content (e.g., from 20-13%), density porosity values tend to be higher, ranging from 2.4% to 12%. This suggests a more porous and less dense subsurface in these intervals. However, as we progress to greater depths (2762m) where shale content becomes more pronounced (e.g., 13%-20%), there is a consistent decline in density porosity, dropping to the range of 12% to 3%. In the K-216 well (Fig 20C), the range of density porosity spans from a minimum of 0.01% to a maximum of 53%, indicating considerable heterogeneity in reservoir quality. The shale content ranges from 6.5% to 39%. This illustrates a discernible inverse relationship, where an increase in shale content correlates with a reduction in density porosity.

One of the most notable characteristics observed in this study pertains to the capacity of stylolites to improve the porosity and permeability of the formation under investigation. The dissolution of minerals along stylolite planes results in the formation of complex networks of channels and conduits (Figs.12, and 13). These pathways are crucial for the migration of fluids, as they offer paths through rock matrix that would otherwise be impermeable. Within the field of hydrocarbon exploration, stylolites are recognized as significant secondary migratory paths (Braithwaite, 1988; Peacock et al., 2017; Koehn et al., 2012). They facilitate the transportation of oil and gas, ultimately resulting in their deposition and concentration within reservoir formations. The natural improvement of permeability can have a significant impact on the productivity and economic feasibility of petroleum reservoirs.

In their studies, Koehn et al. (2016) and Humphrey et al. (2019) established a correlation between the morphology of stylolites and their potential effectiveness as fluid flow barriers. They found that stylolites with low roughness tend to exhibit greater continuity, making them more effective barriers compared to stylolites with irregular (rough) profiles. The fluid flow behavior of the material is also influenced by the nature of its filling material (Fig. 13). Stylolites can serve as effective barriers when they are filled with impermeable substances such as clay, organic matter, and/or oxides (Figs. 12, 13) (Mehrabi et al., 2016; Vandeginste and John, 2013). Furthermore, according to Heap et al. (2014), the presence of a stylolite can be deemed effective as a barrier if the material filling it spreads evenly and continuously throughout the seam, and if the mix of insoluble materials is consistent throughout.

5.3. Stylolite and Microfacies Correlation

To effectively analyze the relationship between stylolite types and microfacies, it is crucial to initially define the microfacies criteria that facilitate the assessment of certain lithological and morphological characteristics. These variables have the potential to be integrated with stylolite shape characteristics to construct a matrix of correlations (Fig. 21). This matrix finds potential connections and impacts of lithology and elemental geochemistry on stylolite network geometries. The rock's complexity level, as shown by variations in composition, grain size, and grain size distribution, exhibits clear associations with important stylolite features. In the context of sedimentary facies, it has been shown that mud-supported microfacies with heterogeneous grain sizes exhibit stylolite networks characterized by high amplitudes and wavelengths, accompanied by relatively small vertical spacings. Conversely, microfacies characterized by moderately sorted grain support tend to create stylolites with lower amplitudes and wavelengths and greater vertical spacings.

5.3.1. Mud as Opposed to Grain-Dominated Microfacies.

The identification of micrite and clay minerals has frequently been recognized as a significant factor contributing to heterogeneity and subsequent stylolite roughening (Wanless, 1979; Koehn et al., 2012; Paganoni et al., 2016; Morad et al., 2018). The increased surface area of micrite contributes to the enhanced solubility of the rock. The present work demonstrates that there is a significant correlation between the stylolite amplitudes, which refer to the degree of roughening, and the quantity of micrite. These associations result in greater amplitudes observed in mud-supported facies. Stylolites with greater amplitude and wavelength are found to promote a higher number of junctions, as evidenced by favorable associations with X- and Y-type crossings, as well as reduced vertical separation. It is noteworthy that the correlation matrix reveals contrasting morphological patterns in the development of stylolites within grain-supported facies (Fig. 21). The presence of clay minerals contributes to variability and rise in stylolite amplitude, hence facilitating the initiation and intersection of stylolites (Wanless, 1979; Koehn et al., 2012; Paganoni et al., 2016; Morad et al., 2018). The process is additionally helped by the feedback loop involving clay minerals and pressure solution, as suggested by Aharonov and Katsman (2009). In this mechanism, the buildup of clay minerals promotes dissolving, leading to the formation of stylolites, which in turn accumulate more clay minerals (Fig. 13).

5.3.2. Composition and Grain Size Distribution

In addition to the occurrence of micrite and clay minerals, many lithological factors have been seen to contribute to heterogeneity in carbonate host rocks, hence influencing the formation and type of stylolites. The presence of bimodal particle size distribution results in an enhanced suturing process, mostly attributed to differences in dissolution and resistance to pressure solution (Railsback, 1993; Andrews and Railsback, 1997; Koehn et al., 2012). Stylolites tend to form preferentially in carbonates with a fine-grained texture (Rustichelli et al., 2012). This research has found a negative correlation between grain size and stylolite amplitudes (Fig. 21).

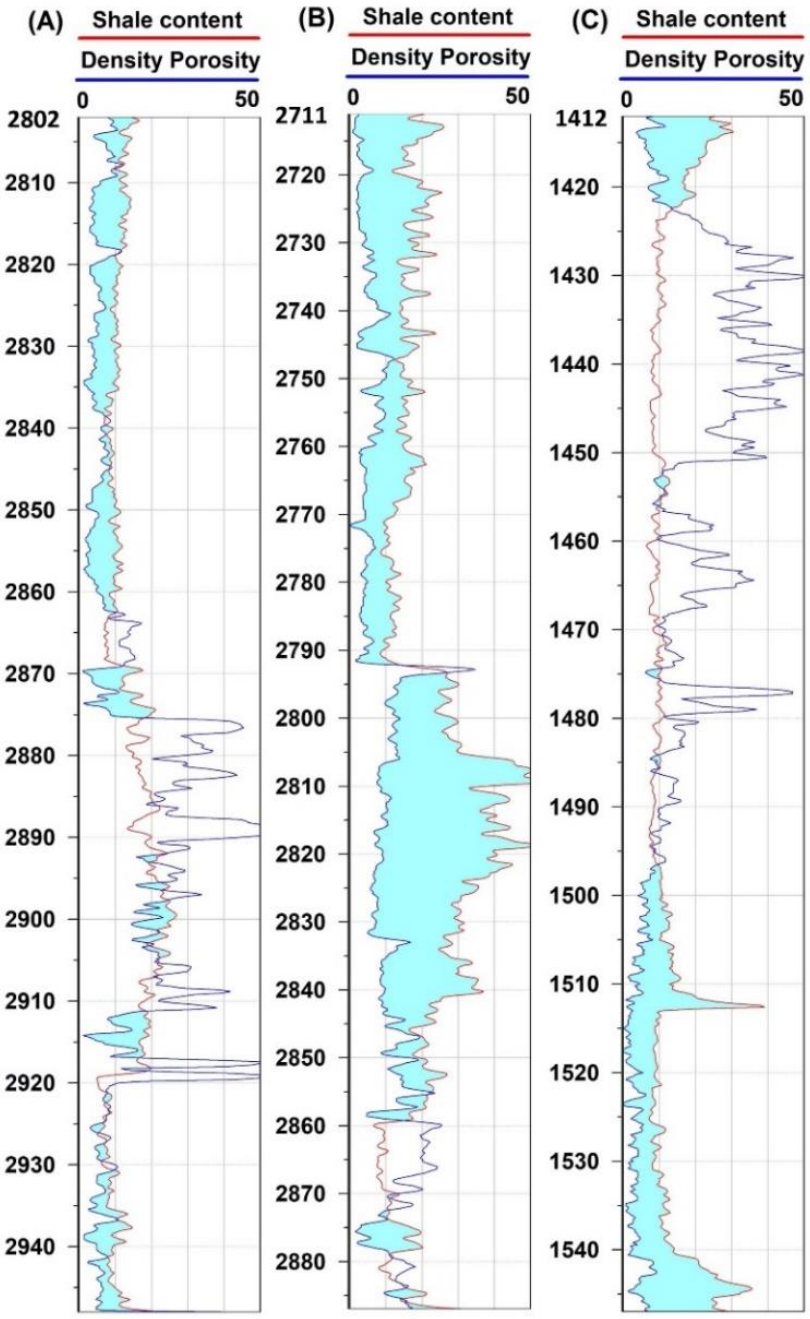

Fig. 20. Density porosity and shale content relationship in percent for wells Kz-29 (A), Kz-40 (B), and K-216 (C). Note the crossover sections (cyan colour) in which the shale contents impact the density porosity (Adopted from Hussein et al., 2024).

In stylolitized rock, variations in grain size are directly linked to the sorting level. A combination of significant grain size variation and poor sorting leads to increased heterogeneity and, as a result, greater roughness. (Koehn et al., 2012). There is a positive correlation between poorly sorted facies and larger amplitude stylolites (Fig. 21). Stylolites with larger amplitudes tend to exhibit smaller vertical spacings and a greater number of intersections. The occurrence of these situations is influenced by the changes in solubility resulting from variances in particle size and spread. These dissimilarities lead to particle pinning and disparities in solubility rates, which in turn produce favorable situations for the development and roughening of stylolites (Aharonov and Katsman, 2009; Koehn et al., 2016). The process of connection can be facilitated by the phenomenon of stylolite cannibalism', which is induced by enhanced roughening and disintegration resulting from poor sorting, as proposed by Ben-Itzhak et al. (2014). The shape of stylolites is also influenced by the type of particles present in the rock. This is because the composition of these particles results in changes in dissolution, which in turn promotes the formation and binding of stylolites. According to Wanless (1979), magnesium (Mg) is recognized as an impurity that induces fluctuations in dissolution within the rock. Tucker and Wright (1991) demonstrate that the distribution of low- and high-Mg calcite may affect subsequent carbonate dissolution. As an illustration, it is observed that foraminifera generally have a magnesium (Mg) content of up to 25%, whereas other fossils, such as bivalves, display more restricted ranges of 0-5%. The presence of either high or low magnesium (Mg) calcite and dolomite can contribute to variations in dissolution and pressure solution. Other factors that can influence dissolution include the calcite/aragonite content in bioclasts, the presence of non-soluble grains and silica, as well as the dissolution rate of mud (Dewers and Ortleva, 1994) (Fig. 13).

Si and Ca exhibit complex relationships with stylolite length. While Si concentrations vary widely, no clear linear trend with total length emerges (Fig. 14). This scattered distribution shows that the influence of Si is complex and most likely controlled by other factors. Higher Si may sometimes correlate with greater mass loss, but not consistently. Similarly, Ca, despite some concentration variation, lacks a straightforward linear relationship with stylolite length (Fig. 14). Higher Ca values may generally coincide with increased mass loss, but not universally. Figure 17 clearly shows that pure carbonates (high Ca) have a higher total length. However, Ca is affected by the combined effects of Si and Al and other elements. These multifaceted responses emphasize the need for a more comprehensive understanding of factors influencing mass loss. Notably, Ca and Si show opposite correlations with stylolite length (Figs. 14, 21).

According to Wanless (1979), the primary determinant of the jagged or undulose waveform (identical to suture and sharp-peak and wave-like types) of stylolites is the particle size. This waveform is like the suture and sharp-peak, and simple wave-like types found in the stylolite categorization framework. Wanless (1979) argued that undulose waveforms are more likely to form in lithologies with large particles. In their study, Humphrey et al. (2020) documented a negative association between the prevalence of suture and sharp-peak stylolites, as well as wave-like stylolites, in larger facies characterized by a particle size greater than 2 mm. Notably, the wave-like stylolites were found to predominantly form in smaller facies. The present study examines the link between the abundance of suture and sharp-peak and wave-like type stylolites in mud-supported and grain-supported microfacies, revealing a nearly identical relationship (Fig.7 in Appendix 4).

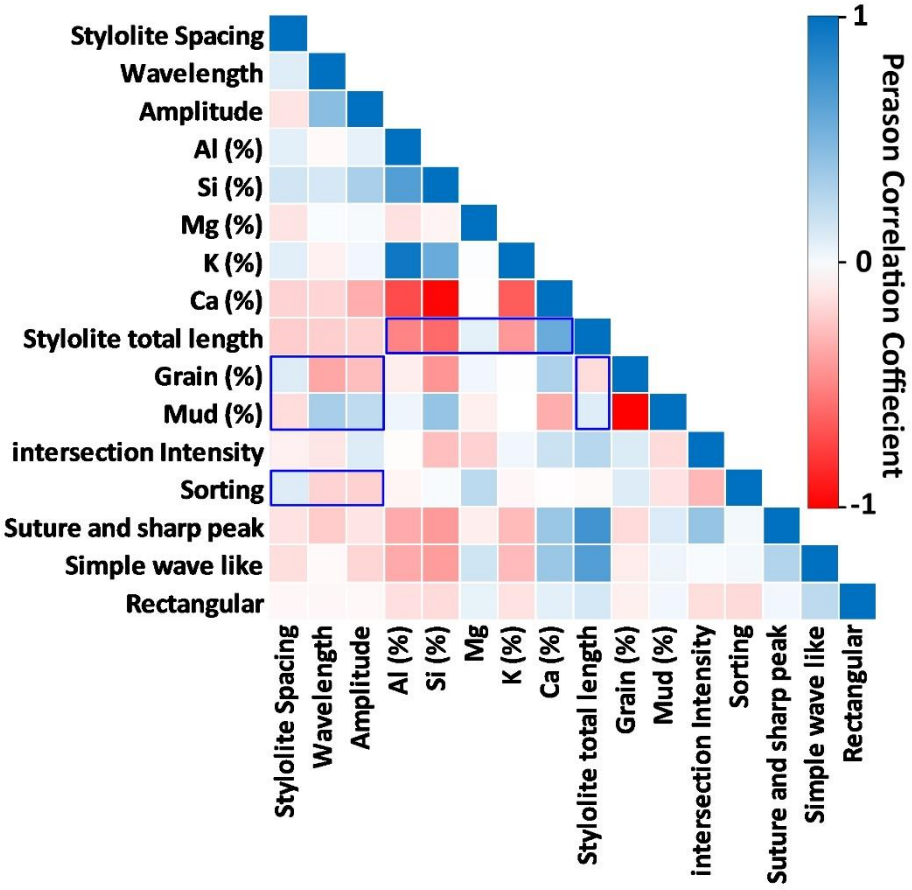

Fig. 21. Evaluation of the Pearson correlation coefficient between studied stylolite morphology and geological factors using a correlation matrix. Blue boxes show the most important connections.

6. Conclusions

The multivariate regression of well log data with fuzzy logic indicates that mixed carbonate-siliciclastic lithologies in reservoir rocks can be identified and quantified from the neutron, sonic, and density logs without a rock sample. All studied wells can employ the model created using the applied approach with the greater coefficient of determination. Calculations from wire-line logging data validated the Kometan Formation's lithologic sequence of limestone, argillaceous limestone, marls, and marly limestone.

In outcrop, the Kometan Formation comprises mudstones to packstones hosting planktonic and benthic foraminifers, divided into six microfacies (MF1 to MF6) found in basinal, outer ramp, and middle ramp environments. Subsurface drilling in northern Iraq reveals limestones, marls, and shales with benthic foraminifers, believed to be inner ramp to middle ramp equivalents of outcropped ramp carbonates. Geochemical logs and gamma-ray patterns exhibit contrasting trends across the formation's lower, middle, and upper parts. Subsurface gamma-ray maxima in the inner ramp, notably in the middle Kometan Formation, signal maximum regression surfaces (mrs), while gamma-ray minima indicate maximum flooding surfaces (mfs). Conversely, in outcropped outer to middle ramp sections, Al and K log minima in the middle Kometan signify mrs, while Al and K minima denote mfs. These opposing log trends are attributed to shifts in the middle

ramp carbonate factory during transgressions and regressions within the mixed carbonate–siliciclastic ramp system.

The Kometan Formation serves as a fractured reservoir, with notable variations in neutron-density and sonic porosity logs suggesting superior reservoir quality in pure carbonates. It's postulated that transgressive–regressive sequences, along with sedimentary cleaning and dirtying, may influence fracture system development and reservoir quality in mixed carbonate–siliciclastic ramps.

High-amplitude stylolites, characterized by tight spacing and extensive connections, are shaped primarily by particle size, grain composition, and sorting levels. They're prevalent in mud-supported facies like mudstone and wackestone. In contrast, less connected stylolites with greater spacing and uniform amplitude are common in grain-supported facies such as packstone. The degree of connection among stylolites, crucial for fluid flow, is dictated by host microfacies attributes. Stylolites significantly enhance rock porosity and permeability, forming intricate networks of channels and conduits through mineral dissolution.

References:

Abawi, T., Mahmood, S., 2005. Biostratigraphy of the Kometan and Gulneri Formations (Upper Cretaceous) in Jambur well No. 46, Northern Iraq. Iraqi Journal of Earth Science 5, 1–8.

Abdelmaksoud, A. and Radwan, A.A., 2022. Integrating 3D seismic interpretation, well log analysis and static modelling for characterizing the Late Miocene reservoir, Ngatoro area, New Zealand. *Geomechanics and Geophysics for Geo-Energy and Geo-Resources*, *8*(2), p.63.

Abdullah, E.A., Abdelmaksoud, A. and Hassan, M.A., 2022. Application of 3D static modelling in reservoir characterization: a case study from the qishn Formation in sharyoof oil field, masila basin, Yemen. *Acta Geologica Sinica-English Edition*, *96*(1), pp.348-368.

Adabi, M.H. and Mehmandosti, E.A., 2008. Microfacies and geochemistry of the Ilam Formation in the Tang-E Rashid area, Izeh, SW Iran. *Journal of Asian Earth Sciences*, *33*(3-4), pp.267-277.

Aharonov, E. and Katsman, R., 2009. Interaction between pressure solution and clays in stylolite development: Insights from modeling. *American Journal of Science*, *309*(7), pp.607-632.

Al-Barzinjy, S.T., 2008. Origin of chert nodules in Kometan Formation from Dokan area, Northeast Iraq. *Iraqi Bulletin of Geology and Mining*, *4*(1), pp.95-104.

Al-Dujaili, A.N., Shabani, M. and AL-Jawad, M.S., 2021. Characterization of flow units, rock and pore types for Mishrif Reservoir in West Qurna oilfield, Southern Iraq by using lithofacies data. *Journal of Petroleum Exploration and Production Technology*, *11*, pp.4005-4018.

Al-Qayim, B., 2010. Sequence stratigraphy and reservoir characteristics of the turonian-coniacian Khasib Formation in central Iraq. *Journal of Petroleum Geology*, *33*(4), pp.387-403.

Alsharhan, A.S. and Sadd, J.L., 2000. Stylolites in Lower Cretaceous carbonate reservoirs, UAE.

Amorosi, A., 1995. Glaucony and sequence stratigraphy; a conceptual framework of distribution in siliciclastic sequences. *Journal of sedimentary research*, *65*(4b), pp.419-425.

Andrews, L.M. and Railsback, L.B., 1997. Controls on stylolite development: morphologic, lithologic, and temporal evidence from bedding-parallel and transverse stylolites from the US Appalachians. *The Journal of Geology*, *105*(1), pp.59-73.

Aqrawi, A.A., 1996. Carbonate-siliciclastic sediments of the upper cretaceous (Khasib, Tanuma and Sa'di formations) of the Mesopotamian basin. *Marine and Petroleum Geology*, *13*(7), pp.781-790.

Aqrawi, A.A., 1996. Carbonate-siliciclastic sediments of the upper cretaceous (Khasib, Tanuma and Sa'di formations) of the Mesopotamian basin. *Marine and Petroleum Geology*, *13*(7), pp.781-790.

Aqrawi, A.A., Goff, J.C., Horbury, A.D. and Sadooni, F.N., 2010. *The petroleum geology of Iraq*. Scientific press.

Asquith, G.B., Krygowski, D. and Gibson, C.R., 2004. *Basic well log analysis* (Vol. 16, pp. 305-371). Tulsa: American Association of Petroleum Geologists.

Bábek, O., Faměra, M., Šimíček, D., Weinerová, H., Hladil, J. and Kalvoda, J., 2018. Sea-level changes vs. organic productivity as controls on Early and Middle Devonian bioevents: Facies-and gamma-ray based sequence-stratigraphic correlation of the Prague Basin, Czech Republic. *Global and Planetary Change*, *160*, pp.75-95.

Bábek, O., Kalvoda, J., Cossey, P., Šimíček, D., Devuyst, F.X. and Hargreaves, S., 2013. Facies and petrophysical signature of the Tournaisian/Viséan (Lower Carboniferous) sea-level cycle in carbonate ramp to basinal settings of the Wales-Brabant massif, British Isles. *Sedimentary Geology*, *284*, pp.197-213.

Bábek, O., Kumpan, T., Kalvoda, J. and Grygar, T.M., 2016. Devonian/Carboniferous boundary glacioeustatic fluctuations in a platform-to-basin direction: A geochemical approach of sequence stratigraphy in pelagic settings. *Sedimentary geology*, *337*, pp.81-99.

Bábek, O., Vodrážková, S., Kumpan, T., Kalvoda, J., Holá, M. and Ackerman, L., 2021. Geochemical record of the subsurface redox gradient in marine red beds: A case study from the Devonian Prague Basin, Czechia. *Sedimentology*, *68*(7), pp.3523-3548.

Balaky, S.M., Asaad, I.S. and Al-Juboury, A.I., 2016. Facies analysis and sequence stratigraphy of Kometan Formation (Upper Cretaceous) in the imbricated zone, northeastern Iraq. *Arabian Journal of Geosciences*, *9*, pp.1-17.

Baldwin, J.L., Otte, D.N. and Wheatley, C.L., 1989, October. Computer emulation of human mental processes: Application of neural network simulators to problems in well log interpretation. In *SPE Annual Technical Conference and Exhibition?* (pp. SPE-19619). SPE.

Barnett, A.J., Wright, V.P., Chandra, V.S. and Jain, V., 2018. Distinguishing between eogenetic, unconformity-related and mesogenetic dissolution: a case study from the Panna and Mukta fields, offshore Mumbai, India. *Geological Society, London, Special Publications*, *435*(1), pp.67-84.

Baron, M. and Parnell, J., 2007. Relationships between stylolites and cementation in sandstone reservoirs: Examples from the North Sea, UK and East Greenland. *Sedimentary Geology*, *194*(1-2), pp.17-35.

Bathurst, R.G., Einsele, G., Ricken, W. and Seilacher, A., 1991. Pressure-dissolution and limestone bedding: the influence of stratified cementation. *Cycles and events in stratigraphy*, pp.450-463.

Baud, P., Rolland, A., Heap, M., Xu, T., Nicolé, M., Ferrand, T., Reuschlé, T., Toussaint, R. and Conil, N., 2016. Impact of stylolites on the mechanical strength of limestone. Tectonophysics, 690, pp.4-20.

Bauerle, G., Bornemann, O., Mauthe, F. and Michalzik, D., 2000. Origin of stylolites in Upper Permian Zechstein anhydrite (Gorleben salt dome, Germany). *Journal of Sedimentary Research*, *70*(3), pp.726-737.

Ben-Itzhak, L.L., Aharonov, E., Karcz, Z., Kaduri, M. and Toussaint, R., 2014. Sedimentary stylolite networks and connectivity in limestone: Large-scale field observations and implications for structure evolution. *Journal of Structural Geology*, *63*, pp.106-123.

Bergen, D.V. and Carozzi, A.V., 1990. Experimentally-simulated stylolitic porosity in carbonate rocks. *Journal of Petroleum Geology*, *13*(2), pp.179-192.

Bernaus, J.M., Arnaud-Vanneau, A. and Caus, E., 2002. Stratigraphic distribution of Valanginian–Early Aptian shallow-water benthic foraminifera and algae, and depositional sequences of a carbonate platform in a tectonically-controlled basin: the Organyà Basin, Pyrenees, Spain. *Cretaceous Research*, *23*(1), pp.25-36.

Braithwaite, C.J.R., 1989. Stylolites as open fluid conduits. *Marine and Petroleum Geology*, *6*(1), pp.93-96.

Bruna, P.O., Lavenu, A.P., Matonti, C. and Bertotti, G., 2019. Are stylolites fluid-flow efficient features? *Journal of Structural Geology*, *125*, pp.270-277.

Buday, T., 1980. *The regional geology of Iraq: stratigraphy and paleogeography* (Vol. 1). State Organization for Minerals, Directorate General for Geological Survey and Mineral Investigations.

Burgess, C.J. and Peter, C.K., 1985, March. Formation, distribution, and prediction of stylolites as permeability barriers in the Thamama Group, Abu Dhabi. In *SPE Middle East Oil and Gas Show and Conference* (pp. SPE-13698). SPE.

Carozzi, A.V. and Bergen, D.V., 1987. Stylolitic porosity in carbonates: a critical factor for deep hydrocarbon production. *Journal of Petroleum Geology*, *10*(3), pp.267-282.

Chandra, V., Wright, P., Barnett, A., Steele, R., Milroy, P., Corbett, P., Geiger, S. and Mangione, A., 2015. Evaluating the impact of a late-burial corrosion model on reservoir permeability and performance in a mature carbonate field using near-wellbore upscaling. *Geological Society, London, Special Publications*, *406*(1), pp.427-445.

Chang, H.C., Kopaska-Merkel, D.C. and Chen, H.C., 2002. Identification of lithofacies using Kohonen self-organizing maps. *Computers & Geosciences*, *28*(2), pp.223-229.

Chang, H.C., Kopaska-Merkel, D.C., Chen, H.C. and Durrans, S.R., 2000. Lithofacies identification using multiple adaptive resonance theory neural networks and group decision expert system. *Computers & Geosciences*, *26*(5), pp.591-601.

Cracknell, M.J. and Reading, A.M., 2014. Geological mapping using remote sensing data: A comparison of five machine learning algorithms, their response to variations in the spatial distribution of training data and the use of explicit spatial information. *Computers & Geosciences*, *63*, pp.22-33.

Cross, T.A., 1988. Controls on coal distribution in transgressive-regressive cycles, Upper Cretaceous, Western Interior, USA.

De Mol, B., Van Rensbergen, P., Pillen, S., Van Herreweghe, K., Van Rooij, D., McDonnell, A., Huvenne, V., Ivanov, M., Swennen, R. and Henriet, J.P., 2002. Large deep-water coral banks in the Porcupine Basin, southwest of Ireland. *Marine Geology*, *188*(1-2), pp.193-231.

Derder, O.M. and Geo, P., 2016. Lithology and mineralogy estimation from matrix density utilizing wireline logs in glauconitic sandstone, Blackfoot area, alberta, Canada. *Can. J. Explor. Geophys*, *41*(1), pp.1-8.

Dewers, T. and Ortoleva, P., 1994. Formation of stylolites, marl/limestone alternations, and dissolution (clay) seams by unstable chemical compaction of argillaceous carbonates. In *Developments in Sedimentology* (Vol. 51, pp. 155-216). Elsevier.

Dolan, J.F., 1989. Eustatic and tectonic controls on deposition of hybrid siliciclastic/carbonate basinal cycles: discussion with examples. *AAPG Bulletin*, *73*(10), pp.1233-1246.

Doveton, J.H., 1994. Applications of Artificial Intelligence in Log Analysis: Chapter 7.

Dunham, R.J., 1962. Classification of carbonate rocks according to depositional textures.

Dunnington, H.V., 2005. Generation, migration, accumulation, and dissipation of oil in Northern Iraq. *GeoArabia*, *10*(2), pp.39-84.

Dutta, P., Singh, S.K., Al-Genai, J., Akhtar, A. and Akbar, M., 2007. A novel approach to fracture characterization utilizing borehole seismic data. In *SPE Middle East Oil and Gas Show and Conference* (pp. SPE-105427). SPE.

Ebner, M., Piazolo, S., Renard, F. and Koehn, D., 2010. Stylolite interfaces and surrounding matrix material: Nature and role of heterogeneities in roughness and microstructural development. *Journal of Structural Geology*, *32*(8), pp.1070-1084.

Ehrenberg, S.N., Eberli, G.P., Keramati, M. and Moallemi, S.A., 2006. Porosity-permeability relationships in interlayered limestone-dolostone reservoirs. *AAPG bulletin*, *90*(1), pp.91-114.

Ehrenberg, S.N., Morad, S., Yaxin, L. and Chen, R., 2016. Stylolites and porosity in a Lower Cretaceous limestone reservoir, onshore Abu Dhabi, UAE. *Journal of Sedimentary Research*, *86*(10), pp.1228-1247.

Elkatatny, S. and Mahmoud, M., 2018. Development of new correlations for the oil formation volume factor in oil reservoirs using artificial intelligent white box technique. Petroleum, 4(2), pp.178-186.

Embry, A.F. and Johannessen, E.P., 1993. T–R sequence stratigraphy, facies analysis and reservoir distribution in the uppermost Triassic–Lower Jurassic succession, western Sverdrup Basin, Arctic Canada. In Norwegian petroleum society special publications (Vol. 2, pp. 121-146). Elsevier.

Embry, A.F. and Johannessen, E.P., 2017. Two approaches to sequence stratigraphy. In Stratigraphy & Timescales (Vol. 2, pp. 85-118). Academic Press.

Finkel, E.A. and Wilkinson, B.H., 1990. Stylolitization as source of cement in Mississippian Salem Limestone, west-central Indiana. *AAPG bulletin*, *74*(2), pp.174-186.

Fletcher, R.C. and Pollard, D.D., 1981. Anticrack model for pressure solution surfaces. *Geology*, *9*(9), pp.419-424.

Flügel, E., 2004. Microfacies of Carbonate Rocks: Analysis, Interpretation, and Application. Springer-Verlag, Berlin Heidelberg (976 pp.).

Folk, R.L. and Ward, W.C., 1957. Brazos River bar [Texas]; a study in the significance of grain size parameters. *Journal of sedimentary research*, *27*(1), pp.3-26.

Gomez-Rivas, E., Martín-Martín, J.D., Bons, P.D., Koehn, D., Griera, A., Travé, A., Llorens, M.G., Humphrey, E. and Neilson, J., 2022. Stylolites and stylolite networks as primary controls on the geometry and distribution of carbonate diagenetic alterations. *Marine and Petroleum Geology*, *136*, p.105444.

Graham, J. and Tucker, M., 1988. Collection and analysis of field data. *Techniques in sedimentology*, pp.5-62.

Gratier, J.P., Muquet, L., Hassani, R. and Renard, F., 2005. Experimental microstylolites in quartz and modeled application to natural stylolitic structures. *Journal of Structural Geology*, *27*(1), pp.89-100.

Groshong Jr, R.H., 1975. Strain, fractures, and pressure solution in natural single-layer folds. *Geological Society of America Bulletin*, *86*(10), pp.1363-1376.

Guiwen, W.A.N.G., Zhongchun, S.U.N., Jianwei, F.U., Xingping, L.U.O., Xianling, Z.H.A.O. and Tuo, P.A.N., 2015. Control factors and logging evaluation method for glutenite reservoir in Mabei area, Junggar Basin. *Xinjiang Petroleum Geology*, *36*(1), p.1.

Haddad, S.N.S. and Amin, M.A., 2007. Mid-Turonian–early Campanian sequence stratigraphy of northeast Iraq. *GeoArabia*, *12*(2), pp.135-176.

Halgedahl, S.L., Jarrard, R.D., Brett, C.E. and Allison, P.A., 2009. Geophysical and geological signatures of relative sea level change in the upper Wheeler Formation, Drum Mountains, West-Central Utah: A perspective into exceptional preservation of fossils. *Palaeogeography, Palaeoclimatology, Palaeoecology*, *277*(1-2), pp.34-56.

Harris, J.R. and Grunsky, E.C., 2015. Predictive lithological mapping of Canada's North using Random Forest classification applied to geophysical and geochemical data. *Computers & geosciences*, *80*, pp.9-25.

Harris, N.B., 2006. Low-porosity haloes at stylolites in the feldspathic Upper Jurassic Ula sandstone, Norwegian North Sea: an integrated petrographic and chemical mass-balance approach. *Journal of Sedimentary Research*, *76*(3), pp.444-459.

Hassan, T.H. and Wada, Y., 1981. Geology and development of Thamama zone 4, Zakum field. *Journal of Petroleum Technology*, *33*(07), pp.1327-1337.

Heap, M., Reuschlé, T., Baud, P., Renard, F. and Iezzi, G., 2018. The permeability of stylolite-bearing limestone. *Journal of structural geology*, *116*, pp.81-93.

Heap, M.J., Baud, P., Reuschlé, T. and Meredith, P.G., 2014. Stylolites in limestones: Barriers to fluid flow? *Geology*, *42*(1), pp.51-54.

Humphrey, E., Gomez-Rivas, E., Koehn, D., Bons, P.D., Neilson, J., Martín-Martín, J.D. and Schoenherr, J., 2019. Stylolite-controlled diagenesis of a mudstone carbonate reservoir: A case study from the Zechstein_2_Carbonate (Central European Basin, NW Germany). *Marine and Petroleum Geology*, *109*, pp.88-107.

Humphrey, E., Gomez-Rivas, E., Neilson, J., Martín-Martín, J.D., Healy, D., Yao, S. and Bons, P.D., 2020. Quantitative analysis of stylolite networks in different platform carbonate facies. *Marine and Petroleum Geology*, *114*, p.104203.

Hussein, H.S., 2022. Carbonate fractures from conventional well log data, Kometan Formation, Northern Iraq case study. *Journal of Applied Geophysics*, *206*, p.104810.

Hussein, H.S., Bábek, O., Mansurbeg, H. and Shahrokhi, S., 2024. Outcrop-to-subsurface correlation and sequence stratigraphy of a mixed carbonate–siliciclastic ramp using element geochemistry and well logging; Upper Cretaceous Kometan Formation, Zagros Foreland, NE Iraq. *Sedimentary Geology*, *459*, p.106547.

Hussein, H.S., Mansurbeg, H. and Bábek, O., 2024. A new approach to predict carbonate lithology from well logs: A case study of the Kometan formation in northern Iraq. Heliyon.

Imamverdiyev, Y. and Sukhostat, L., 2019. Lithological facies classification using deep convolutional neural network. *Journal of Petroleum Science and Engineering*, *174*, pp.216-228.

Jarvis, I.A.N., Murphy, A.M. and Gale, A.S., 2001. Geochemistry of pelagic and hemipelagic carbonates: criteria for identifying systems tracts and sea-level change. *Journal of the Geological Society*, *158*(4), pp.685-696.

Jassim, Z.J., Goff, J.C., 2006. The Geology of Iraq. Dolin, Prague (341 pp.).

Kaddouri, N., 1982. Tel Hajar: A new Cenomanian-lower Turonian stratigraphic unit from north-west Iraq. *Cretaceous Research*, *3*(4), pp.391-395.

Keller, G., 1993. The Cretaceous-Tertiary boundary transition in the Antarctic Ocean and its global implications. *Marine Micropaleontology*, *21*(1-3), pp.1-45.

Keller, G., Adatte, T., Stinnesbeck, W., Luciani, V., Karoui-Yaakoub, N. and Zaghbib-Turki, D., 2002. Paleoecology of the Cretaceous–Tertiary mass extinction in planktonic foraminifera. *Palaeogeography, Palaeoclimatology, Palaeoecology*, *178*(3-4), pp.257-297.

Killeen, P.G., 1997. Borehole geophysics: exploring the third dimension. In *Proceedings of Exploration* (Vol. 97, pp. 31-42).

Koehn, D., Ebner, M., Renard, F., Toussaint, R. and Passchier, C.W., 2012. Modelling of stylolite geometries and stress scaling. *Earth and Planetary Science Letters*, *341*, pp.104-113.

Koehn, D., Renard, F., Toussaint, R. and Passchier, C.W., 2007. Growth of stylolite teeth patterns depending on normal stress and finite compaction. *Earth and Planetary Science Letters*, *257*(3-4), pp.582-595.

Koehn, D., Rood, M.P., Beaudoin, N., Chung, P., Bons, P.D. and Gomez-Rivas, E., 2016. A new stylolite classification scheme to estimate compaction and local permeability variations. *Sedimentary Geology*, *346*, pp.60-71.

Kohonen, T., 1988. Self-organized function of topologically correct feature maps. *Biological Cybernetics*, (43), pp.43-69.

Laongsakul, P., 2010. Characterization of reservoir fractures using conventional geophysical logging (Doctoral dissertation, Prince of Songkla University Faculty of Science (Geophysics)).

László, C., Ágoston, S., Tamás, P., László, K., Salae, A.T. and Athar, A., 2012. Structural evolution of the northwestern Zagros, Kurdistan Region, Iraq: Implications on oil migration. GeoArabia, 17(2), pp.81-116.

Leyon, W.C., 2010. Working Guide to Reservoir Engineering. Elsevier, 129p.

Li, Y. and Anderson-Sprecher, R., 2006. Facies identification from well logs: A comparison of discriminant analysis and naïve Bayes classifier. *Journal of Petroleum Science and Engineering*, *53*(3-4), pp.149-157.

Lind, I., Nykjaer, O., Priisholm, S. and Springer, N., 1994. Permeability of stylolite-bearing chalk. *Journal of Petroleum Technology*, *46*(11), pp.986-993.

Mabille, C., Pas, D., Aretz, M., Boulvain, F., Schröder, S. and Da Silva, A.C., 2008. Deposition within the vicinity of the Mid-Eifelian High: detailed sedimentological study and magnetic susceptibility of a mixed ramp-related system from the Eifelian Lauch and Nohn formations (Devonian; Ohlesberg, Eifel, Germany). *Facies*, *54*, pp.597-612.

Mabrouk, A., Jarvis, I., Belayouni, H., Murphy, A. and Moody, R.T., 2007. Sequence stratigraphy, sea level change and palaeoenvironments via chemostratigraphy: Regional to global correlations. *American Association of Petroleum Geologists Search and Discovery, article*, *40244*.

Mahmood, W., Mohammed, A. and HamaHussein, S., 2020. Predicting mechanical properties and ultimate shear strength of gypsum, limestone and sandstone rocks using Vipulanandan models. *Geomechanics and Geoengineering*, *15*(2), pp.90-106.

Mahmoodi, O., Smith, R.S. and Tinkham, D.K., 2016. Supervised classification of down-hole physical properties measurements using neural network to predict the lithology. *Journal of Applied Geophysics*, *124*, pp.17-26.

Martinez-Torres, L.P., 2002. *Characterization of naturally fractured reservoirs from conventional well logs* (Doctoral dissertation, University of Oklahoma).

Martín-Martín, J.D., Gomez-Rivas, E., Gómez-Gras, D., Travé, A., Ameneiro, R., Koehn, D. and Bons, P.D., 2018. Activation of stylolites as conduits for overpressured fluid flow in dolomitized platform carbonates. *Geological Society, London, Special Publications*, *459*(1), pp.157-176.

Martire, L., 1992. Sequence stratigraphy and condensed pelagic sediments. An example from the Rosso Ammonitico Veronese, northeastern Italy. *Palaeogeography, Palaeoclimatology, Palaeoecology*, *94*(1-4), pp.169-191.

Massey Jr, F.J., 1951. The Kolmogorov-Smirnov test for goodness of fit. *Journal of the American statistical Association*, *46*(253), pp.68-78.

Mehrabi, H., Mansouri, M., Rahimpour-Bonab, H., Tavakoli, V. and Hassanzadeh, M., 2016. Chemical compaction features as potential barriers in the Permian-Triassic reservoirs of Southern Iran. *Journal of Petroleum Science and Engineering*, *145*, pp.95-113.

Mohaghegh, S., Balan, B. and Ameri, S., 1997. Permeability determination from well log data. *SPE formation evaluation*, *12*(03), pp.170-174.

Mohammed, A.S., 2019. Vipulanandan models to predict the mechanical properties, fracture toughness, pulse velocity and ultimate shear strength of shale rocks. *Geotechnical and Geological Engineering*, *37*(2), pp.625-638.

Morad, D., Nader, F.H., Morad, S., Al Darmaki, F. and Hellevang, H., 2018. Impact of stylolitization on fluid flow and diagenesis in foreland basins: evidence from an Upper Jurassic Carbonate gas reservoir, Abu Dhabi, United Arab Emirates. *Journal of Sedimentary Research*, *88*(12), pp.1345-1361.

Morad, S., Ketzer, J.M. and De Ros, L.F., 2000. Spatial and temporal distribution of diagenetic alterations in siliciclastic rocks: implications for mass transfer in sedimentary basins. *Sedimentology*, *47*, pp.95-120.

Morad, S., Ketzer, J.M. and De Ros, L.F., 2013. Linking diagenesis to sequence stratigraphy: an integrated tool for understanding and predicting reservoir quality distribution. *Linking diagenesis to sequence stratigraphy*, pp.1-36.

Neilson, J.E., Oxtoby, N.H., Simmons, M.D., Simpson, I.R. and Fortunatova, N.K., 1998. The relationship between petroleum emplacement and carbonate reservoir quality: examples from Abu Dhabi and the Amu Darya Basin. *Marine and Petroleum Geology*, *15*(1), pp.57-72.

Nelson, R.A., 2001. Geologic Analysis of Naturally Fractured Reservoirs, 2nd edn. Gulf Professional Publishing, Houston, p. 332.

Nenna, F. and Aydin, A., 2011. The formation and growth of pressure solution seams in clastic rocks: A field and analytical study. *Journal of Structural Geology*, *33*(4), pp.633-643.

Nouri-Taleghani, M., Kadkhodaie-llkhchi, A. and Karimi-Khaledi, M., 2015. DETERMINING HYDRAULIC FLOW UNITS USING A HYBRID NEURAL NETWORK AND MULTI-RESOLUTION GRAPH-BASED CLUSTERING METHOD: CASE STUDY FROM SOUTH PARS GASFIELD, IRAN. *Journal of Petroleum Geology*, *38*(2), pp.177-191.

Oberto, S., 1984. Fundamentals of Well-Log Interpretation/the Acquisition of Logging Data. Elsevier Publishers, Amsterdam, 1984, p. 435

Omigie, J.I. and Alaminiokuma, G.I., 2020. Well log sequence stratigraphic analyses for reservoir delineation and hydrocarbon distribution in the eastern part of the central swamp depobelt, Niger Delta. *Journal of Earth Sciences and Geotechnical Engineering*, *10*(5), pp.1-14.

Pabakhsh, M., Ahmadi, K., Riahi, M.A. and Shahri, A.A., 2012. Prediction of PEF and LITH logs using MRGC approach. *Life Science Journal*, *9*(4), pp.974-982.

Paganoni, M., Al Harthi, A., Morad, D., Morad, S., Ceriani, A., Mansurbeg, H., Al Suwaidi, A., Al-Aasm, I.S., Ehrenberg, S.N. and Sirat, M., 2016. Impact of stylolitization on diagenesis of a Lower Cretaceous carbonate reservoir from a giant oilfield, Abu Dhabi, United Arab Emirates. *Sedimentary Geology*, *335*, pp.70-92.

Page, M.C., Dickens, G.R. and Dunbar, G.B., 2003. Tropical view of Quaternary sequence stratigraphy: siliciclastic accumulation on slopes east of the Great Barrier Reef since the Last Glacial Maximum. *Geology*, *31*(11), pp.1013-1016.

Peacock, D.C.P., Korneva, I., Nixon, C.W. and Rotevatn, A., 2017. Changes of scaling relationships in an evolving population: the example of "sedimentary" stylolites. *Journal of Structural Geology*, *96*, pp.118-133.

Posamentier, H.W., Allen, G.P., 1999. Siliciclastic Sequence Stratigraphy: Concepts and Applications. Society for Sedimentary Geology, Tulsa, Oklahoma (193 pp.).

Railsback, L.B., 1993. Lithologic controls on morphology of pressure-dissolution surfaces (stylolites and dissolution seams) in Paleozoic carbonate rocks from the mideastern United States. *Journal of Sedimentary Research*, *63*(3), pp.513-522.

Rashid, F., Glover, P.W.J., Lorinczi, P., Collier, R. and Lawrence, J., 2015a. Porosity and permeability of tight carbonate reservoir rocks in the north of Iraq. *Journal of Petroleum Science and Engineering*, *133*, pp.147-161.

Rashid, F., Glover, P.W.J., Lorinczi, P., Hussein, D. and Lawrence, J.A., 2017. Microstructural controls on reservoir quality in tight oil carbonate reservoir rocks. *Journal of Petroleum Science and Engineering*, *156*, pp.814-826.

Rashid, F., Glover, P.W.J., Lorinczi, P., Hussein, D., Collier, R. and Lawrence, J., 2015. Permeability prediction in tight carbonate rocks using capillary pressure measurements. *Marine and Petroleum Geology*, *68*, pp.536-550.

Rashid, F., Glover, P.W.J., Lorinczi, P., Hussein, D., Collier, R. and Lawrence, J., 2015b. Permeability prediction in tight carbonate rocks using capillary pressure measurements. *Marine and Petroleum Geology*, *68*, pp.536-550.

Read, J.F. and Horbury, A.D., 1993. Eustatic and Tectonic Controls on Porosity Evolution Beneath Sequence-Bounding Unconformities and Parasequence Disconformities on Carbonate Platforms: Chapter 11: DIAGENESIS, SEQUENCE STRATIGRAPHY, AND CHANGES IN RELATIVE SEA LEVEL.

Rider, M.H., 1999. The Geological Interpretation of Well Logs.Whittles Publishing Services (288 pp.).

Ripley, B.D., 2007. *Pattern recognition and neural networks*. Cambridge university press.

Roehl, P.O., Choduette, P.W., 1985. Carbonate Petroleum Reservoirs. Spring-Verlag, New York, p. 622.

Rogers, S.J., Fang, J.H., Karr, C.L. and Stanley, D.A., 1992. Determination of lithology from well logs using a neural network. *AAPG bulletin*, *76*(5), pp.731-739.

Rustichelli, A., Tondi, E., Agosta, F., Cilona, A. and Giorgioni, M., 2012. Development and distribution of bed-parallel compaction bands and pressure solution seams in carbonates (Bolognano Formation, Majella Mountain, Italy). *Journal of Structural Geology*, *37*, pp.181-199.

Sarg, J.F., 1988. carbonate sequence stratigraphy. In: Wigus, C.K. (Ed.), Sea-level Change: An Integrated Approach. Society of Economic Paleontologists and Mineralogists, Special Publicationvol. 42, pp. 155–181.

Schlager, W., 2005. *Carbonate sedimentology and sequence stratigraphy* (No. 8). SEPM Soc for Sed Geology.

Scholle, P.A. and Ulmer-Scholle, D.S., 2003. *A color guide to the petrography of carbonate rocks: grains, textures, porosity, diagenesis, AAPG Memoir 77* (Vol. 77). AAPG.

Schultz, R.A., Fossen, H., 2008. Terminology for structural discontinuities. AAPG (American Association Petroleum Geology) Bull. 92, 15.

Sfidari, E., Kadkhodaie-Ilkhchi, A., Rahimpour-Bbonab, H. and Soltani, B., 2014. A hybrid approach for litho-facies characterization in the framework of sequence stratigraphy: a case study from the South Pars gas field, the Persian Gulf basin. *Journal of Petroleum Science and Engineering*, *121*, pp.87-102.

Simpson, J., 1985. Stylolite-controlled layering in an homogeneous limestone: pseudo-bedding produced by burial diagenesis. Sedimentology, 32(4), pp.495-505.

Stadtműller, M., 2019. Well logging interpretation methodology for carbonate formation fracture system properties determination. *Acta Geophysica*, *67*(6), pp.1933-1943.

Sun, Z., Lin, C., Zhu, P. and Chen, J., 2018. Analysis and modeling of fluvial-reservoir petrophysical heterogeneity based on sealed coring wells and their test data, Guantao Formation, Shengli oilfield. *Journal of Petroleum Science and Engineering*, *162*, pp.785-800.

Taq Taq Operation Company (TTOPCO), 2007. Geological Report.

Thompson, L.B., 2000. Fractured reservoirs: Integration is the key to optimization. *Journal of petroleum technology*, 52(02), pp.52-54.

Tian, Y., Xu, H., Zhang, X.Y., Wang, H.J., Guo, T.C., Zhang, L.J. and Gong, X.L., 2016. Multi-resolution graph-based clustering analysis for lithofacies identification from well log data: Case study of intraplatform bank gas fields, Amu Darya Basin. *Applied Geophysics*, *13*, pp.598-607.

Toussaint, R., Aharonov, E., Koehn, D., Gratier, J.P., Ebner, M., Baud, P., Rolland, A. and Renard, F., 2018. Stylolites: A review. Journal of Structural Geology, 114, pp.163-195.

Tucker, M.E., 1993. Carbonate diagenesis and sequence stratigraphy. *Sedimentology Review/1*, pp.51-72.

Tucker, M.E., Wright, V.P., 1990. Carbonate Sedimentology. Wiley-Blackwell, Oxford (484 pp.).

Van Bellen, R.C., Dunnington, H.V.G.,Wetzel, R., Morton, D.M., 1959. Lexique Stratigraphique international, III, Asie, fasc.10a, Iraq. Centre national de la recherché scientifique, Paris (333 pp.).

Vandeginste, V. and John, C.M., 2013. Diagenetic implications of stylolitization in pelagic carbonates, Canterbury Basin, offshore New Zealand. *Journal of Sedimentary Research*, *83*(3), pp.226-240.

Ver Straeten, C.A., Brett, C.E. and Sageman, B.B., 2011. Mudrock sequence stratigraphy: A multi-proxy (sedimentological, paleobiological and geochemical) approach, Devonian Appalachian Basin. *Palaeogeography, Palaeoclimatology, Palaeoecology*, *304*(1-2), pp.54-73.

Vipulanandan, C. and Mohammed, A., 2018. New Vipulanandan failure model and property correlations for sandstone, shale and limestone rocks. In *IFCEE 2018* (pp. 365-376).

Wang, X., Hou, J., Song, S., Wang, D., Gong, L., Ma, K., Liu, Y., Li, Y. and Yan, L., 2018. Combining pressure-controlled porosimetry and rate-controlled porosimetry to investigate the fractal characteristics of full-range pores in tight oil reservoirs. *Journal of Petroleum Science and Engineering*, *171*, pp.353-361.

Wanless, H.R., 1979. Limestone response to stress; pressure solution and dolomitization. *Journal of Sedimentary Research*, *49*(2), pp.437-462.

Westphal, H., Eberli, G.P., Smith, L.B., Grammer, G.M. and Kislak, J., 2004. Reservoir characterization of the Mississippian Madison formation, Wind river basin, Wyoming. *AAPG bulletin*, *88*(4), pp.405-432.

Whalen, M.T., Eberli, G.P., Van Buchem, F.S., Mountjoy, E.W. and Homewood, P.W., 2000. Bypass margins, basin-restricted wedges, and platform-to-basin correlation, Upper Devonian, Canadian Rocky Mountains: implications for sequence stratigraphy of carbonate platform systems. *Journal of Sedimentary* Research, 70(4), pp.913-936.

Wilson, J.L., 2012. *Carbonate facies in geologic history*. Springer Science & Business Media.

Wu, P.Y., Jain, V., Kulkarni, M.S. and Abubakar, A., 2018, October. Machine learning-based method for automated well-log processing and interpretation. In *SEG International Exposition and Annual Meeting* (pp. SEG-2018). SEG.

Zhang, C., Zhang, Z., Chen, Y., Xing, Y. and Li, C., 2014. Logging lithology identification of tight sandy conglomerate and its application. *Technology Review*, *32*(25), pp.59-62.

Zhang, J., Liu, S., Li, J., Liu, L., Liu, H. and Sun, Z., 2017. Identification of sedimentary facies with well logs: an indirect approach with multinomial logistic regression and artificial neural network. *Arabian Journal of Geosciences*, *10*, pp.1-9.

Appendices:

Appendix 1: Hussein, H.S., Mansurbeg, H. and Bábek, O., 2024. A new approach to predict carbonate lithology from well logs: A case study of the Kometan formation in northern Iraq. *Heliyon*, *10*(3).

Appendix 2: Hussein, H.S., Bábek, O., Mansurbeg, H. and Shahrokhi, S., 2024. Outcrop-to-subsurface correlation and sequence stratigraphy of a mixed carbonate–siliciclastic ramp using element geochemistry and well logging; Upper Cretaceous Kometan Formation, Zagros Foreland, NE Iraq. *Sedimentary Geology*, *459*, p.106547.

Appendix 3: Hussein, H.S., 2022. Carbonate fractures from conventional well log data, Kometan Formation, Northern Iraq case study. *Journal of Applied Geophysics*, *206*, p.104810.

Appendix 4: Hussein S.H., Bábek, O., Mansurbeg H., Juan Diego Martín-Martín3, Enrique Gomez-Rivas3, Marten-Marten. J.D., Gomez-Rivas, E., 2024 Impact of stylolitization on porosity and permeability of carbonate rocks: the Upper Cretaceous Kometan Formation, Zagros Forland Basin in Iraqi Kurdistan, (**Submitted to Journal of Marine and Petroleum Geology**).

Appendix 5: Fig. S1. X-ray diffractograms with results of quantitative and qualitative phase analyses from the Kometan Formation.

https://ars.els-cdn.com/content/image/1-s2.0-S0037073823002191-mmc1.pdf

Appendix 6: Table S1. Bulk-rock X-ray fluorescence (XRF) concentrations (both raw data and calibrated data) from the Zewe, Qamchuqa and Dokan sections, and calibration equations.

https://ars.els-cdn.com/content/image/1-s2.0-S0037073823002191-mmc2.xlsx

Appendix 7: Table S2. Total gamma-ray logs from Kometan Formation in nine wells from the Khabbaz, Kirkuk, Jambur, Bai Hasan, and Barda Rash oil fields.

https://ars.els-cdn.com/content/image/1-s2.0-S0037073823002191-mmc3.xlsx

Appendix 8: Table S3. Density porosity, neutron porosity, neutron-density porosity and sonic porosity logs from Kometan Formation in K-216 and K-218 wells.

https://ars.els-cdn.com/content/image/1-s2.0-S0037073823002191-mmc4.xlsx

Appendix 9: Table S4. Measured data of stylolite spacing, wavelength, amplitude, junction angle, junction density, and classification of stylolite.